

Bayesian Constraints on Dark Energy and Cosmic Structure

from supernovae, galaxy clusters and other probes

Martin Sahlén



Submitted for the degree of Doctor of Philosophy
University of Sussex
September 2008

Declaration

I hereby declare that this thesis, either in the same or different form, has not been previously submitted to this or any other University for a degree.

Signature:

Martin Sahlén

UNIVERSITY OF SUSSEX

MARTIN SAHLÉN, DOCTOR OF PHILOSOPHY

BAYESIAN CONSTRAINTS ON DARK ENERGY AND COSMIC STRUCTUREFROM SUPERNOVAE, GALAXY CLUSTERS AND OTHER PROBESSUMMARY

Constraints on quintessence dark energy models are obtained from a combination of recent observational data, including Type Ia supernovae, the distance to the surface of last scattering as encoded by the cosmic microwave background, and the angular size of baryon acoustic oscillations as encoded by the power spectrum of luminous red galaxies. Focus is given to the Bayesian framework for parameter estimation and model selection, for assessing the observational support for particular model classes and data set consistency. Calculations are done exactly using Monte Carlo Markov Chain methods. We find that although the models that fit the data best are highly dynamical, the data set strengthens the preference of the cosmological constant over evolving quintessence models compared to previous studies. The data also show some signs of favouring tracker models over non-tracker models under our assumptions. Forecasted constraints on the matter content and the matter-field dispersion, and astrophysical galaxy cluster parameters, expected from the ongoing *XMM* Cluster Survey (XCS) are obtained. The treatment is the most detailed yet of an X-ray galaxy cluster survey. Specifically, a simulated selection function and X-ray temperature errors are included, and also typical photometric redshift errors and scatter in the mass–observable relations. We introduce a new estimate of expected constraints, and perform an exact analysis using Monte Carlo Markov Chain methods, with and without mass–observable self-calibration and possible systematic errors. Under the assumption of a spatially flat Λ CDM model, we find that the XCS should measure Ω_m to ± 0.03 and σ_8 to ± 0.05 , also constraining the normalization and slope of the luminosity–temperature relation to $\pm 6\%$ and $\pm 13\%$ (at 1σ) respectively in the process. Self-calibration fails to jointly constrain the scatter and redshift evolution of the luminosity–temperature relation significantly. We do not expect measurement errors or imperfect knowledge of their distribution to degrade constraints significantly.

Acknowledgements

This thesis bears my name, and in terms of the intellectual effort I have done the work. However, as with any human pursuit, it has been a collective effort in a broader sense. These words could not have been written without the collective scientific knowledge of generations, the collective striving for opportunity over generations, and the collective of individuals I am fortunate to call relations, friends and family. I am indebted to many, but could not possibly do them all justice here. That said, I would like to mention and thank some that particularly come to mind in this context.

My mother Eleonor, who is always there and without whom nothing would be possible. Her integrity and work ethic have been a model for me, not forgetting that a bit of silliness sometimes goes a long way too. *Tack*. My father Kenneth, for the good times. My dear Pelin, for loving and living with me, and for seeing with clarity the things that I can't. I am fortunate that she came along for the journey. *Seni seviyorum*. And I mustn't forget my elongated four-legged friend Morrgan, for doing what dogs do, and don't do. *Vov!*

There are also those no longer among us. My grandmother Astrid, from whom perhaps came the joy of singing, which has helped me also during my studies. Rudolf, the grandfather I never knew in person, but so much more as an inspiration from old stories retold. My great-uncle Linus and great-aunt Astrid, whose life-long hard work and frugality surpasses generations. Uncle Henryk, whose life experiences taught me not to second-guess life nor people, a very valuable reminder. I will treasure our time in Poland forever. Uncle Roland, the most generous and joyful spirit I can imagine, come rain or shine. Aunt Mariana, who went where no-one had gone before. Her courage inspires strength and audacity. And all others who came before me – thanks to their hard work, I have received opportunities unavailable to them.

Thanks to Birgitta, for the good times we've spent, in the mountains, in the cottage, in England, and elsewhere. There's always a joke around the corner with her. I hope to hear them more often soon. Alf, who has a special place in my heart. And Ingegerd, one tough cookie, but hers are the sweetest cookies you can imagine. I am so grateful for all her tender thoughtfulness. During my studies, I have benefited from a peaceful haven in

the Swedish countryside, thanks to the generosity of Märta and Sture. The summers (and other times) in Torgesta remain with me. The friends and colleagues who made my time in Brighton a very enjoyable one: Anthony, Bianca, Ben, Bruno, Cédric, Céline, Claudia, Cosmin, David, Ed, Erandy, Friedel, Hide, Irit, Isaac, Jon, Kayvon, Laura, Leon, Leslie, Luis, Lucia, Maria, Marina, Mark, Mirona, Mike, Monica, Nghia, Nicola, Owain, Petja, Pia, Riccardo, Rich, Robert, Seb, Serena, Sooa, and many others I met in Cambridge, Brighton and conferences around the world, but might be overlooking just now. Jon, a generous friend unlike any other. Katie, who taught me about risk. The students I had the privilege of teaching. I have to also acknowledge the musical genius of Stevie Wonder, which kept me going many times when I could have given up.

Part of this work was written in Sahilleralti, Dikili, Turkey, at the house of Yasemin and Abidder Yükselci. I thank them, Deniz, Okan and Ozan for their hospitality and the wonderful time we spent there. *Ellerinize sağlık!*

My supervisor Andrew Liddle has been a good and supportive guide through the sometimes labyrinthine workings of academia, while leaving me to figure things out for myself too. The most valuable things I have learned from him is the importance of distilling the essence of things, to carefully examine your assumptions, and to hurry slowly, as we would say in Swedish. Kathy Romer, my 2nd supervisor and PI for the XCS project, has been very generous with her time. I have truly appreciated her directness and good sense of humour, which has been refreshing. Through my involvement in the XCS, I have spent time working at CAUP, University of Porto in Portugal. Kind thanks to Pedro Viana for having me over, to what is a most beautiful city. As I discovered by getting lost! I spent three months at Syracuse University in Syracuse, USA, at the end of 2006, and had the pleasure of working mainly with Cristian Armendáriz-Picón, Alessandra Silvestri, Mark Trodden and Eric West. Their and the Physics Department's hospitality, and the support of Syracuse University, was much appreciated. The Department of Physics at Stockholm University has been very supportive of me, and for that I am truly grateful. Especially Lars Bergström and Ove Appelblad have given guidance and helped ensure my academic freedom and opportunity. Things would have been much different without their help. While in Cambridge, before starting my doctoral studies, I benefited from the academic and pastoral support of Fernando Quevedo and Bobbie Wells, at Clare Hall, which made life much easier during a testing time. Thanks also to Roger Powe, for introducing new perspectives that have led me to new understanding.

Directly relating to the science content of this thesis, I particularly thank Dominique Fouchez, Ariel Goobar, Irit Maor, Ben Maughan, David Parkinson, Mark Trodden and Jochen Weller for useful discussions, and also all the collaborators in the XCS. Especially, Mark Hosmer who provided the selection function (Sect. 6.2.2), Nicola Mehrrens who helped with some data checks, and Ed Lloyd–Davies who performed the temperature-error simulations (Sect. 6.3.5). I am grateful to Edvard Mörtzell for providing the SNLS supernova data used, and to Ronald Cools and the NINES group at KU Leuven for making the numerical integration package CUBPACK (Cools & Haegemans, 2003) available. Some analysis and plotting was made using a modified version of GETDIST provided with COSMOMC (Lewis & Bridle, 2002). The research presented herein was conducted in cooperation with SGI/Intel utilizing the Altix 4700 supercomputer (COSMOS), also funded by HEFCE and STFC. The work is based in part on data obtained by *XMM–Newton*, an ESA science mission funded by contributions from ESA member states and from NASA. The research also made indirect use of the NASA/GSFC-supported XSPEC software. The preparation of the thesis was much helped thanks to Anthony Smith’s L^AT_EX template. I am grateful to Antigone Dimas and David Parkinson for helping me with the Ancient Greek in the last Chapter.

Opportunity has been afforded me through the generous financial support of the following organisations: the Gunvor and Josef Anér Foundation, Cambridge European Trust, Clare Hall – Cambridge, the EU Commission, the Gälö Foundation, the KTH Donation Foundations, the Carl Erik Levin Foundation, the Dr. Félix Neubergh Foundation, NORDITA, the Rhodin Memorial Fund (Stockholm University), the Sir Richard Stapley Educational Trust, the Swedish Physical Society, the Gustaf Söderberg Foundation and the University of Sussex (Department of Physics and Astronomy, School of Science and Technology). Their support has taken me around the world, physically and intellectually, and broadened my cultural horizons; I have visited conferences and research centres in more than ten countries. I shall remain forever grateful and endeavour to make their investment worthwhile by contributing constructively to our common good through knowledge, skill and ability.

M. S.

Brighton/Cambridge, UK

September 2008

Contents

List of Tables	xi
List of Figures	xiii
1 Introduction	1
1.1 Κόσμological Contexts: Epistemology, Psychology and Sociology	1
1.2 Physical Cosmology	7
1.3 Synopsis	7
2 Foundations of Physical Cosmology	11
2.1 The Standard Model of Cosmology	11
2.2 Background – Geometric Expansion – Friedmann Equation	12
2.3 Perturbations – Structure Formation – Perturbation Equation	16
3 Observational Tests	21
3.1 Cosmological Observations	21
3.1.1 Observing the Universe	21
3.1.2 Luminosity and Angular Diameter Distance	22
3.1.3 Power Spectra – Perturbation Growth	23
3.1.4 Complementarity	27
3.2 Geometric Probes	29
3.2.1 Type Ia Supernovae (SNIa)	29
3.2.2 Baryon Acoustic Oscillations (BAO)	33
3.3 Structural Probes	36
3.3.1 Cosmic Microwave Background (CMB)	36
3.3.2 Number Counts (Clusters of Galaxies)	44
3.4 Data Analysis	47
3.4.1 Frequentists and Bayesians	47

3.4.2	Bayesian Parameter Estimation	49
3.4.3	Bayesian Model Selection	49
3.4.4	The Monte Carlo Markov Chain Method	51
3.5	Current Status	52
3.5.1	Type Ia Supernovae	54
3.5.2	Cosmic Microwave Background	54
3.5.3	Large-Scale Structure	54
3.5.4	Joint Constraints	59
3.6	Future Prospects	61
4	Selected Theoretical Challenges	66
4.1	Dark Energy	66
4.1.1	Observational Concordance – Theoretical Discordance	66
4.1.2	Coincidence Problem	68
4.1.3	Fine-Tuning Problem	68
4.2	Priors: Measures, Multiverses, and the Knowable	69
5	Reconstruction of Quintessence	72
5.1	Introduction	72
5.1.1	Quintessence	72
5.1.2	Tracker Potentials	74
5.1.3	Reconstructing $V(\phi)$	77
5.2	Formalism	78
5.2.1	Cosmological Model	78
5.2.2	Potential Parameterizations	79
5.3	Observables	81
5.3.1	SNIa Luminosity–Redshift Relation	81
5.3.2	CMB Peak-Shift and Acoustic-Scale Parameters	82
5.3.3	Baryon Acoustic Peak	83
5.3.4	Big Bang Nucleosynthesis	84
5.4	Data Analysis	84
5.4.1	Parameter Estimation	84
5.4.2	Model Selection	85
5.4.3	Tracker Viability	86
5.5	Results	88

5.5.1	Parameter Estimation	88
5.5.2	Model Comparison	100
5.5.3	Tracker Viability	103
5.6	Conclusions	105
6	Forecast Constraints from Galaxy Clusters in the XCS	107
6.1	Introduction	107
6.2	The <i>XMM</i> Cluster Survey (XCS)	109
6.2.1	Background and Current Status	109
6.2.2	The XCS Selection Function	111
6.3	From X-ray Observables to Mass	114
6.3.1	Modelling Summary	114
6.3.2	The X-ray Temperature to Mass Relation	115
6.3.3	The X-ray Luminosity to Temperature Relation	116
6.3.4	Photometric Redshifts	119
6.3.5	X-ray Temperature	122
6.4	From Mass to Cosmology and Constraints	124
6.4.1	The Mass Function	124
6.4.2	Cosmology	124
6.4.3	Combining Observables and Cosmology	125
6.4.4	Likelihood	126
6.5	Results	129
6.5.1	Labelling	129
6.5.2	Expected Cluster Distributions	129
6.5.3	Constraints: Without Measurement Errors	136
6.5.4	Constraints: With Measurement Errors	142
6.5.5	Constraints: Systematic Biases	146
6.6	Conclusions	149
6.6.1	The XCS Forecast	149
6.6.2	Measurement Errors	150
6.6.3	Cluster Scaling Relations	151
6.6.4	Other Systematic Errors	152
6.6.5	Sensitivity to Fiducial Model and Priors	153
6.6.6	Survey Specifications	154
6.6.7	Future Surveys and Outlook	154

7 Summary and Outlook	156
Bibliography	158
A Reconstruction of Quintessence	191
A.1 Uncertainty in Tracker Bayes Factor Estimates	191
A.2 Tracker Probability Distributions	192
B Forecast Constraints from Galaxy Clusters in the XCS	195
B.1 Cluster Number Count Equations	195
B.1.1 Ideal Measurements	195
B.1.2 Measurement Errors	196
B.2 Expected Likelihood	197

List of Tables

1.1	A brief outline of the history of the Universe.	9
3.1	The Jeffreys evidence scale.	50
3.2	Cosmic microwave background constraints on standard parameters.	57
3.3	Joint constraints on standard parameters.	60
5.1	Constraints and BIC values for Taylor series. Flat. ‘Basic’ data.	90
5.2	Constraints and BIC values for Taylor series. Flat. ‘Extended’ data.	96
5.3	Constraints and BIC values for Taylor series. Non-flat. ‘Extended’ data.	97
5.4	Constraints and BIC values for Padé series. Flat. ‘Basic’ data.	99
6.1	<i>XMM</i> Cluster Survey specifications.	110
6.2	Fiducial cosmological parameters, and estimation priors.	125
6.3	Measurement error assumptions and their labelling.	129
6.4	Cluster scaling-relation assumptions and their labelling.	130
6.5	Self-calibration constraints. Scaling-relation scatter and no meas. errors.	140
6.6	Constraints with accounted-for meas. errors. No scaling-relation scatter.	144
6.7	Constraints with unaccounted-for meas. errors. No scaling-relation scatter.	145
B.1	Temperature error specifications.	197
B.2	Redshift error specifications.	198

List of Figures

1.1	Rock carvings.	4
1.2	World trees.	5
1.3	Zodiac/plenisphere.	6
1.4	A physical-cosmology history of the Universe.	8
3.2	Survey weight functions.	28
3.3	Cosmic complementarity.	29
3.4	Supernova SN1994D.	30
3.5	Raw and fitted supernova lightcurves.	32
3.6	The Union sample Hubble diagram.	33
3.7	Explanation of baryon acoustic oscillations.	34
3.8	The galaxy distribution in the Two-degree Field Galaxy Redshift Survey.	36
3.9	Correlation function of luminous red galaxies in the SDSS.	37
3.10	The cosmic microwave background as seen by <i>WMAP</i>	39
3.11	The CMB TT power spectrum from <i>WMAP</i> +ACBAR+Boomerang+CBI.	40
3.12	Explanation of cosmic microwave background anisotropies.	41
3.13	Dark energy shift-effect on the CMB power spectrum.	42
3.14	CMB spectra with and without dark energy perturbations.	43
3.15	Galaxy cluster distribution in the Red-Sequence Cluster Survey.	46
3.16	The galaxy cluster XMMXCS J092018.9+370618.0 in X-ray and optical.	47
3.17	Monte Carlo Markov Chain in action.	53
3.18	Supernova constraints on non-flat Λ CDM and flat w CDM models.	55
3.19	Cosmic microwave background constraints on non-flat Λ CDM model.	56
3.20	Baryon acoustic oscillation constraints on flat Λ CDM and w CDM models.	58
3.21	Galaxy cluster f_{gas} constraints on non-flat Λ CDM and flat w CDM models.	58
3.22	Galaxy cluster abundance constraints on σ_8 and Ω_m	59
3.23	Joint constraints on non-flat Λ CDM and flat w CDM models.	62

3.24	Joint constraints on Ω_k and w in the non-flat w CDM model.	63
3.25	Joint constraints on σ_8 and w in the flat w CDM model.	63
5.1	Examples of the dynamical behaviour of tracker quintessence.	76
5.2	Constraints on flat cosmological constant (Λ CDM) model.	89
5.3	Constraints on non-flat cosmological constant (Λ CDM) model.	91
5.4	Constraints on ‘skater’ model.	92
5.5	Constraints on ‘skater’ model from only SNLS data.	93
5.6	Constraints on linear-potential model.	94
5.7	Constraints on Padé $M = 0, N = 1$ ($R_{0/1}$) model.	98
5.8	Best-fitting $V(\phi)$, $\phi(z)$ and $V(z)$	101
5.9	Best-fitting Ω_ϕ and w_ϕ	102
5.10	Model average of $\ln(B_{12})$ for tracking required between redshift 1 and 10.	104
6.1	The <i>XMM</i> Cluster Survey selection function.	113
6.2	Realistic redshift error distributions at various redshifts.	121
6.3	Mean fractional temperature errors from simulations.	122
6.4	Realistic temp. error distributions at various redshifts and temperatures.	123
6.5	Flowchart for cluster predictions and forecast parameter estimation.	127
6.6	Comparison of average-catalogue and Poisson random-catalogue constraints.	128
6.7	Expected cluster number count redshift–temp. distributions for ^{500}XCS	131
6.8	Expected cluster number count redshift distributions for ^{500}XCS	132
6.9	Expected observational limits for the ^{500}XCS	133
6.10	Changes in total number of clusters due to different measurement errors.	134
6.11	Expected ^{500}XCS constraints on Ω_m and σ_8 . No measurement errors.	137
6.12	Comparison of ^{500}XCS and all-detections constraints.	138
6.13	Self-calibration constraints. Scaling-relation scatter and no meas. errors.	139
6.14	Constraints with measurement errors. No scaling-relation scatter.	143
6.15	Constraints for various scaling-relation assumptions inconsistent with data.	147
B.1	The probability density function for s_{rel} for a typical XCS catalogue.	203

Cover illustration:

A depiction of the Rebis, the ‘divine child’ which symbolizes the union of the spiritual and the physical. From *Viatorium spagyricum* (Jamsthaler, 1625).

Chapter 1

Introduction

Av kaos blir kosmos på andens bud.

Det gudaborna är lusten att forma.

Så skänk mig, du höga, du strålande gud,

din klarhets kraft när barbarerna storma!

/Of chaos becomes cosmos on the spirit's nod.

The godgiven is the desire to form.

So grant me, thou high, thou radiant god,

the power of your clarity when the barbarians storm!/
/

from Trots allt /In spite of everything/ (1931), Bo Bergman (1869–1967) ¹

1.1 Κόσμological Contexts: Epistemology, Psychology and Sociology

Cosmos, in its ancient-Greek² meaning, refers to an orderly, harmonious arrangement. The anti-thesis to this is chaos. In this very general sense, cosmology is the study (scientific or otherwise) of how and/or why orderly arrangement of any sort exists, as opposed to pure randomness (whatever meaning is given to that term). Why is there somethingness rather than nothingness? The questions are broad and unspecific, and have been addressed within many epistemic contexts, such as philosophy, religion, physical science and psychology. One thing that appears to unify these approaches is the human desire to understand and endure her existence; the emotional, social and physical order to which she is subject. But why is this so? Why are these considered problems? Why do we attach meaning to them?

¹My translations from the Swedish original (Bergman, 1931).

²Κόσμος

I will attempt to illustrate one point of view with some examples from history, with the caveat that these are one cosmologist's personal reflections on this topic.

The different aspects of the conditions of existence have often become intertwined in cosmological discussions throughout history. A central theme is the duality of mind/spirit/life and body/matter/death, which has pre-occupied humans for thousands of years. It can be traced back to, among other places, the first lines of one of the first known creation myths, the 4000-year-old Babylonian *Enûma Eliš* (King, 2002):

When in the height heaven was not named,
And the earth beneath did not yet bear a name,
[...]
Then were created the gods in the midst of heaven

This passage captures neatly the conceptual division of reality into physical and spiritual as fundamental cognitive categories. Today, this can be seen represented in the duality between e.g. religion and science (perhaps not surprising, as the Judæo-Christian creation myth appears to be based on the earlier Babylonian one). The Babylonian creation myth describes how the gods Anshar (sky lining) and Kishar (earth lining) that form the horizon, were created from the mixing of the salt water of the chaotic primeval ocean and the fresh water of the underground sea. These gods constitute the boundary between heaven and earth. In a modern interpretation, the salt water could represent the subconscious mind and the fresh water the conscious mind. Through the joining of subconscious and conscious, the emotions are formed, and constitute the intersection between the two. The parallel image is that the horizon constitutes the boundary between tangible earth and intangible heaven. As this example shows, there is thus a clear duality between what we are 'in charge of' internally and externally (also paralleling life and death), which is negotiated by way of our emotions (my interpretation is close to the perceptual theory of emotion, see e.g. Prinz, 2004, but I do not enter into details here). We may attach notions of 'spiritual'/'mind'/etc. and 'material'/'body'/etc. to these experiences in different ways. Another example expressing this dualism can be found in the Stoic Marcus Aurelius' *Meditations* from around 170–180 A.D. (Aurelius, 1909),

He who does not know what the world is does not know where he is, and he who does not know for what purpose the world exists, does not know who he is, nor what the world is.

Arguably, one of the most basic conscious and subconscious processes in humans is manifested in the fear of being alone, particularly the possible complete desolation in death.

It would appear natural that such a principle, balancing two competing needs for survival, would have developed in a successful life form: on the one hand, the need for learning, and on the other the need for avoiding unknown dangers. That is, we need to expose ourselves to unfamiliar situations so as to learn, which promotes the chances of survival, but not to the point of seriously risking death. Here we also touch upon a fundamental reason for the existence of processes to understand ‘somethingness’: considering such questions appears, at some level, intrinsically linked to life itself. Recognizing and responding to patterns are at the heart of differentiating and manipulating an environment, a basic requirement for any life form (see e.g. [Schrödinger, 1944](#)).

In managing our fears, we may thus be led to interpret the external world in spiritual terms, assigning internal meaning to external objects (teleology)³, as in e.g. animistic or hylozoistic traditions such as alchemy (the cover illustration shows an alchemical metaphor, including the ‘3+1=4’ mysticism which might be traced to the spatial-temporal dimensionality). Equally, we may be drawn to construct our spiritual reality by way of external objects, deriving internal meaning from them. An example of this would be the extreme versions of empiric/positivistic and materialistic philosophy. Such processes can of course be both explicit and implicit, but as they involve subconscious dynamics presumably predominantly implicit. The work in [Jung \(2003, part III\)](#) explores this in quite some detail. David Hume (himself empiricist) echoes this critique in *Dialogues concerning Natural Religion* from 1779 ([Hume, 1935](#)):

What peculiar privilege has this little agitation of the brain which we call thought, that we must thus make it the model of the whole universe? Our partiality in our own favour does indeed present it on all occasions; but sound philosophy ought carefully to guard against so natural an illusion.

Philo to Cleanthes, Part II

Subscribing to a particular conceptual organization of the external world, can thus for the individual also provide an internal organization that purportedly ensures him/her from loneliness/death. Belonging to a group of people sharing such a framework can have the additional effects of confirming the validity of the framework, and also in itself provide a community through which the individual is not alone. This might explain to some extent how and why conceptual paradigms form and are sustained.

The first known cosmological theories are, to the extent we understand them, largely rudimentary depictions of the main preoccupations in hunter-gatherer societies (men,

³A current example, in my opinion, is also [Tipler \(1994, 2007\)](#).



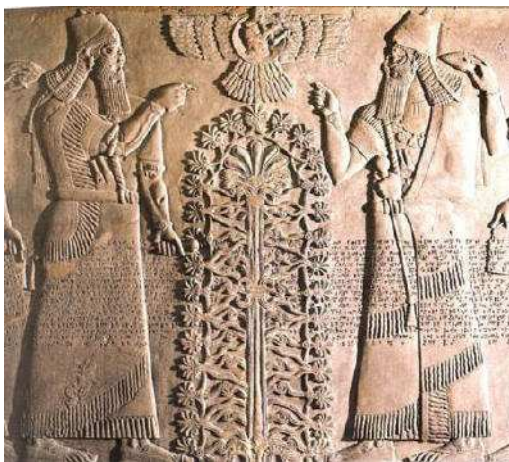
Figure 1.1: Rock carvings (1800–500 B.C.) at Fossum, Tanum, Sweden. Reproduced from [Blomberg \(2006\)](#).

women, animals and hunting tools). An example of this type is shown in Fig. 1.1. Another world-organizing principle, which appears to have developed in more settled communities, is that of the ‘world tree’ or ‘tree of life’, which connects the underground world with the heavens. This theme is very similar to that in the *Enûma Eliš*, described above. Some have interpreted this concept as a representation of the Milky Way. A collection of world trees from three different continents is shown in Fig. 1.2. In ancient Greco–Roman culture in particular, the heavenly bodies became synonymous with gods and creatures of varying dispositions. This created the basis for astrology as a theory of world events, through the movements of the ‘wandering stars’ we now call planets. These were illustrated on traditional sky maps, zodiacs, or plenispheres, an example of which is shown in Fig. 1.3 (p. 6).

In summary, as a prerequisite to and consequence of being alive we are drawn to study and learn patterns. A balancing force to this behaviour is provided by our fear of death. What we cannot control/understand induces this emotion (at some level of consciousness). We respond to it by achieving concordance between our conceptual organizations of our internal and the external world (assuming there is such a thing). This can potentially lead to affective and defective statements, and conceptual paradigms, about the external world. These can take both the form of abstract theses, and of concrete shaping of the external world.



(a) The world tree 'Yggdrasil', an ash tree housing the nine realms of the world, from Norse mythology. Detail from rune stone (c. 1000 A.D.) in Ockelbo, Sweden. Reproduced from [Berig \(2008\)](#).



(b) Relief: Sacred Tree Attended by Winged Beings; Neo-Assyrian period, reign of Ashurnasirpal II (r. 883-859 B.C.) Mesopotamia; excavated at Nimrud (ancient Kalhu). Alabaster (gypsum). Gift of John D. Rockefeller Jr., 1932 (32.143.3). Reproduced from [MetropolitanMuseum \(2008\)](#).



(c) The Olmec 'Tree of Life' (Mesoamerica). The lineage founder, 2 Grass, is being born from a twisting world tree. Detail from *Selden Codex*, p. 2. Reproduced from [FAMSI \(2008\)](#).

Figure 1.2: World trees.

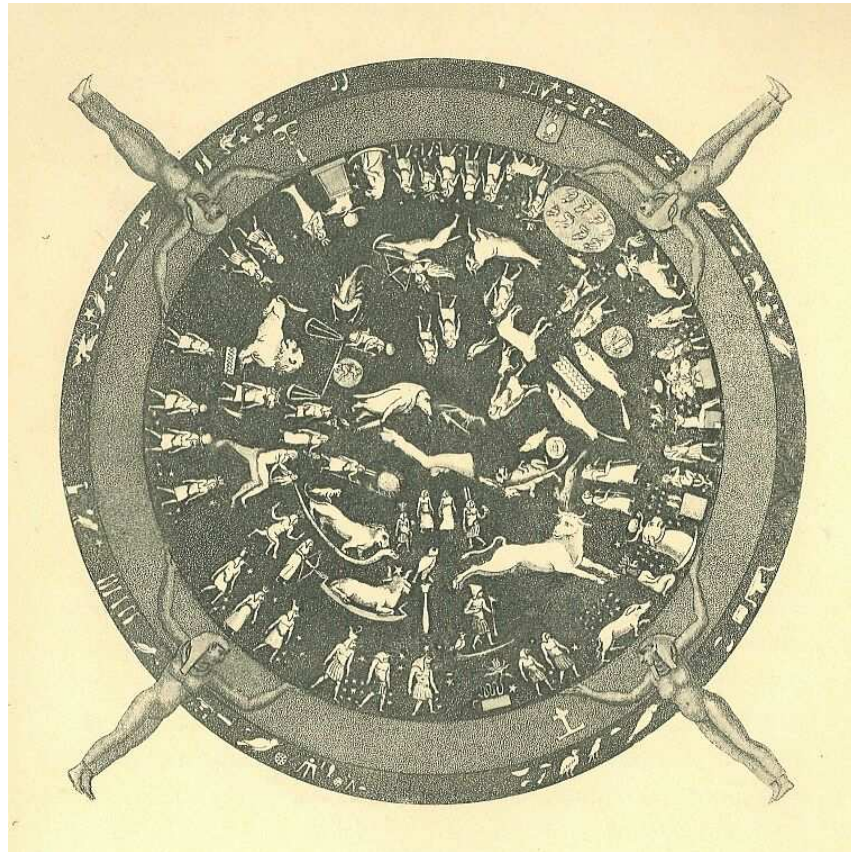


Figure 1.3: Plensphere, or zodiac, from around 100 B.C. found in Hathor temple, Dendera temple complex, Egypt. Reproduced from [Maspero \(1906\)](#).

Only in the last one hundred years, through the application of the scientific method, have we developed what this author considers to be a sufficient scientific language with which to address the physical Cosmos in its entirety in a well-defined and, arguably, objective way.

1.2 Physical Cosmology

Physical cosmology is the scientific study of the large-scale properties of the Universe within the context of physics. Hereafter, by cosmology we shall mean physical cosmology. The current understanding of how the Universe began agrees well with the ancient-Greek opposites chaos and cosmos: out of an apparently random and featureless initial state, order was realized based on one or a few principles of harmony. Very broadly, the main aim of contemporary physics is the identification of these principles. Cosmology plays a crucial part in this endeavour, as such principles only become manifest under extreme conditions in certain distant physical systems or in the very early Universe.

The refinement of General Relativity and Elementary Particle Physics/Quantum Field Theory over the last hundred years, together with observational leaps forward, has led to a radically improved understanding of the early Universe and the evolution and structure of the Universe as a whole. The picture we have of the history of the Universe is quite detailed, and stretches back to the time when the Universe was only a fraction of a second old. An outline of the sequence of events described by modern physical cosmology is shown in Fig. 1.4 – a modern-day ‘world tree’ – and explained further in Table 1.1, p. 9 (any discrepancies in the time scale are due to uncertainty in our current understanding). Nevertheless, several fundamental components, and also details, are missing. In the coming decades, a range of new observational facilities will provide precision tests of the zoo of theoretical models purporting to explain many of the mysterious features of the Universe.

1.3 Synopsis

This thesis examines the current level of understanding of dark energy and large-scale structure (ultimately from the initial conditions seeding structure), and investigates future prospects for gaining new, robust knowledge about these properties of the Universe.

The remainder of the thesis is structured as follows. We start by introducing the theoretical framework that forms the foundation of modern cosmology in Chapter 2. After that, in Chapter 3, we present theory and techniques of observational tests, and review

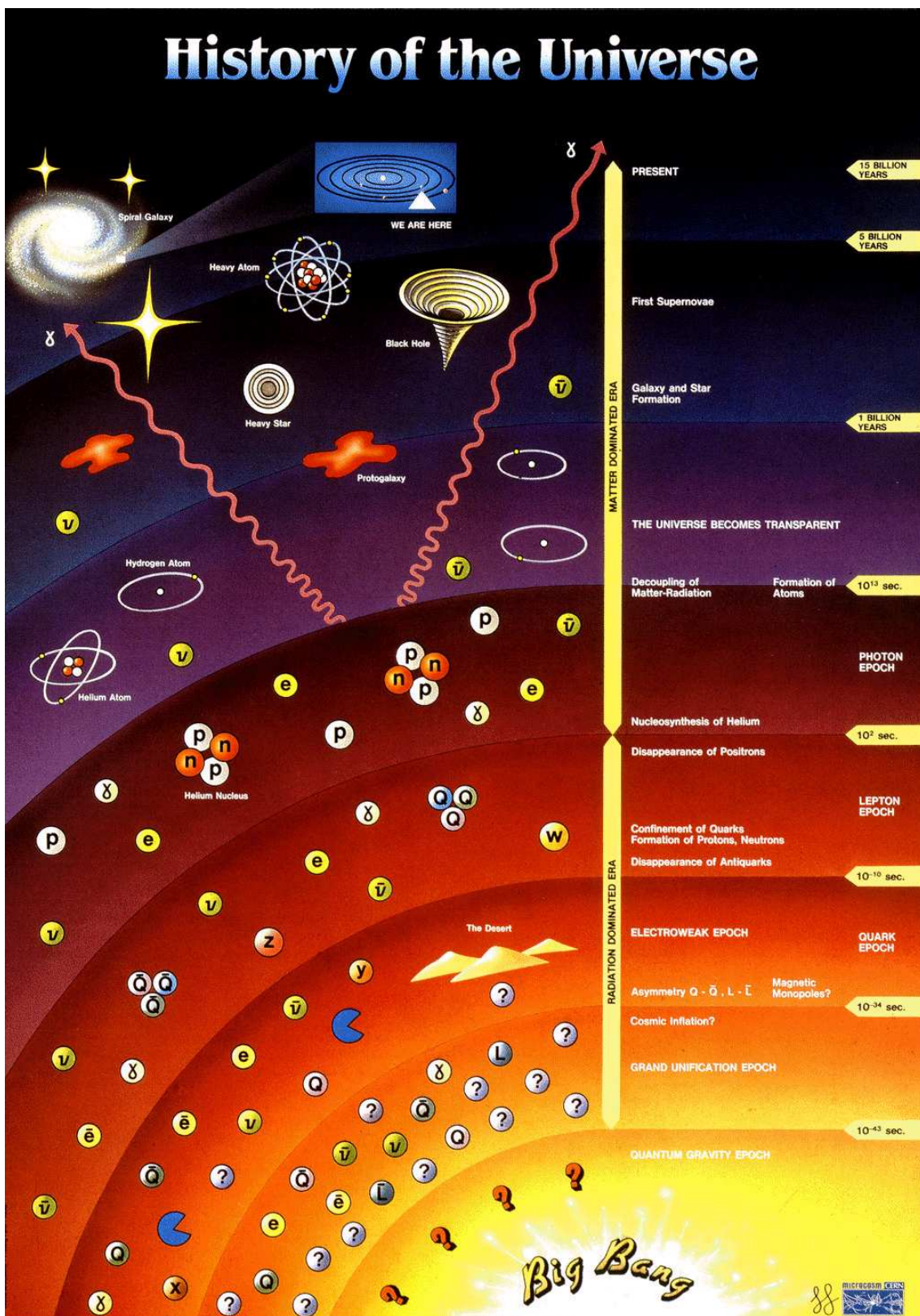


Figure 1.4: A history of the Universe, based on modern physical cosmology. Reproduced from a poster produced by the European Organization for Nuclear Research (CERN).

Time after initial singularity	Description
10^{-43} seconds	The Planck time. After this time, quantum gravity ‘turns off’.
10^{-42} seconds	Inflation begins.
10^{-32} seconds	Inflation ends. Thousandfold-magnified quantum fluctuations seed structure.
10^{-18} seconds	The Hot Big Bang begins.
10^{-10} seconds	Electroweak phase transition. Baryogenesis, the formation of baryons, occurs around this time.
10^{-4} seconds	Quark–hadron phase transition.
10^{-2} seconds	Leptons, photons, protons and neutrons in thermal equilibrium.
1 second	Neutrinos decouple. Electron–anti-electron annihilation.
100 seconds	Nucleosynthesis. Hydrogen, helium, lithium and beryllium nuclei form.
10^4 years	Matter–radiation equality. Dark matter inhomogeneities start collapsing into clumps.
10^5 years	Atoms form, photons decouple. The ‘dark ages’ begin. Baryonic matter starts falling into the dark matter clumps.
10^8 years	The first stars appear and reionize the Universe. ‘Dark ages’ end. First supernovae explode and spread the heavier elements.
10^9 years	First bound structures form. Galaxies and clusters of galaxies appear.
10^{10} years	Dark energy starts to dominate. The Solar System forms.
1.4×10^{10} years	You are reading this.

Table 1.1: A brief outline of the sequence of events in the history of the Universe, as described by modern physical cosmology. Further back than about 10^{-2} seconds, the detailed understanding of the picture is incomplete. Most concepts are described in later Chapters.

current and future experimental results. Then follows in Chapter 4, a discussion of some pressing theoretical challenges that these observations bring, as well as more philosophical problems facing cosmology and physics. After these introductory Chapters, we explore the application of two of the principal current and future cosmological probes detailed by the Dark Energy Task Force (Albrecht et al., 2006), Type Ia supernovae and galaxy clusters, for studying dark energy and cosmic structure. First, the methodology described is applied in Chapter 5 to reconstructing the self-interaction potential of a hypothesized scalar field, quintessence, from observational data. This is a candidate for explaining dark energy, and we also test to what extent such a dynamical model is favoured by the data. Chapter 6 presents forecast measurement results for the *XMM* Cluster Survey, an X-ray galaxy cluster survey probing the initial conditions and formation of structure in the Universe. It is the most detailed such study to date, including large amounts numerical simulation. These two Chapters also have additional background material in the Appendix. Although Chapters 5 & 6 have their own concluding Sections, we also make some final summary and forward-looking remarks in Chapter 7.

We will assume natural units, where $c = \hbar = 1$, throughout, and will generally also use *reduced Planck units*, in which the *reduced Planck mass* $M_{\text{P}} \equiv \sqrt{\hbar c/8\pi G} = 1$. As a consequence of this, some equations may appear different from how they are commonly presented. We use a space-time signature $(+ - - -)$. In General-Relativistic contexts, Greek indices (μ, ν , etc.) take values 0, 1, 2, 3. Likewise, Latin indices (i, j , etc.) take values 1, 2, 3.

Chapter 2

Foundations of Physical Cosmology

2.1 The Standard Model of Cosmology

The standard model of cosmology has been developed over the last 100 years, alongside the revolution in gravitational and particle physics that took place during the 20th century. During the past two decades, it has been tested experimentally to high accuracy and gradually refined. A highly readable introduction to the historical development of cosmology can be found in [Singh \(2004\)](#). Further details on the physical models themselves are given in e.g. [Peebles 1993](#); [Liddle & Lyth 2000](#); [Liddle 2003](#); [Dodelson 2003](#); [Bergström & Goobar 2004](#); [Mukhanov 2005](#).

The standard model of cosmology rests on three assumptions:

1. General Relativity (GR; [Einstein, 1916](#))
2. homogeneity and isotropy (the Cosmological Principle; [Einstein, 1917](#))
3. the constituents of the Universe are effectively perfect fluids (Weyl's Postulate; [Weyl, 1923](#))

In addition, the Standard Model of Particle Physics, or an extension thereof, is usually assumed. Likewise, a period of rapid exponential expansion, inflation, before the Hot Big Bang is part of the standard model.

In the following two Sections, we apply the above principles and review briefly the General-Relativistic framework describing the expansion of a homogeneous universe, and the first-order perturbations to this solution. These form the basis for the observational

tests we will consider in Chapter 3. In doing so, we also present the components of the standard model of cosmology.

2.2 Background – Geometric Expansion – Friedmann Equation

The standard basis for describing the physical Universe is General Relativity (Einstein, 1916, or Stewart, 1993 for a concise modern treatment), which can be summarized in the *Einstein equation*,

$$G_{\mu\nu} = 8\pi GT_{\mu\nu}, \quad (2.1)$$

where $G_{\mu\nu}$ is the *Einstein tensor*, defined by $G_{\mu\nu} = R_{\mu\nu} - g_{\mu\nu}R/2$, and $T_{\mu\nu}$ is the *energy–momentum tensor*. The *Ricci tensor* $R_{\mu\nu}$ and *Ricci scalar* R are ultimately (complicated) functions of the *metric* $g_{\mu\nu}$ and its derivatives. It is practical to work in units of the *reduced Planck mass* $M_{\text{P}} = \sqrt{\hbar c/8\pi G}$, and we shall generally adopt such units in this thesis. The expression above, Eq. (2.1), can also be modified to (now in reduced Planck units)

$$G_{\mu\nu} = T_{\mu\nu} + \Lambda g_{\mu\nu}, \quad (2.2)$$

where Λ is a constant. Originally, this was suggested by Einstein (1917), since it is mathematically consistent and allows for a static-universe solution (which he at the time thought desirable based on e.g. philosophical principles of Mach). The extra term can be viewed either as an additional energy–momentum contribution or a gravitational term (in this interpretation space-time would be curved also when $T_{\mu\nu} = 0$). However, there is nothing that *a priori* dictates that the additional term in Einstein’s equations has to be a constant. We might therefore also consider models with a time-dependent component. In the following, we shall absorb this possible term into the definition of $T_{\mu\nu}$, and generically call it *dark energy*, using subscript ‘DE’ to denote it. Dark energy is discussed further particularly in Chapters 4 & 5.

The static universe was soon abandoned, following theoretical work by Friedmann (1922, 1924); Lemaître (1927); Einstein & de Sitter (1932); Robertson (1935, 1936a,b); Walker (1937) and the decisive observations of Hubble (1929), showing that the Universe is expanding and could have originated in an ultra-dense singularity (the Big Bang; Lemaître, 1931). Applying the cosmological principle, the Friedmann–Lemaître–Robertson–Walker (FLRW) form of the metric,

$$ds^2 \equiv g_{\mu\nu}dx^\mu dx^\nu = dt^2 - a^2(t) \left(\frac{dr^2}{1 - kr^2} + r^2 d\Omega^2 \right), \quad (2.3)$$

can be derived. We will often assume that we are working in a flat universe ($k = 0$) since an initial period of inflation should produce an approximately flat universe (which is consistent with observation). We return to inflation in the next Section. Now consider a perfect fluid with energy–momentum tensor

$$T_{\mu\nu} = (\rho + p) u_\mu u_\nu - p g_{\mu\nu}, \quad (2.4)$$

where ρ and p are the energy density and pressure of the fluid, respectively, and u^μ is the 4-velocity of the fluid (note that the fluid in question here is the combination of all constituents of the universe). A *comoving* frame is defined as one in which

$$u^\mu = (1, 0, 0, 0), \quad (2.5)$$

which also implies

$$T^{0i} = 0. \quad (2.6)$$

We normally choose to work in coordinates comoving with the expansion of the universe, i.e. with a Euclidean line element

$$ds^2 = dt^2 - a^2(t) \delta_{ij} dx^i dx^j. \quad (2.7)$$

We will call this the *cosmic frame*. This frame is generally identified with the comoving frame of the dominant energy component in the universe, and the comoving frames of other fluid components are in turn identified with the same since any peculiar velocities with respect to the cosmic frame should decay (to validate our homogeneity–isotropy requirement).

Evaluating the energy–momentum tensor, Eq. (2.4), in the cosmic frame we find

$$\begin{aligned} T_{00} &= \rho, \\ T_{ii} &= 3a^2 p, \\ T_{0i} &= 0. \end{aligned} \quad (2.8)$$

Inserting the energy–momentum tensor, Eq. (2.4), in Einstein’s equations and using our above assumptions gives the *Friedmann equation* and the *acceleration equation*:

$$3H^2 = \rho \quad (2.9)$$

$$2\frac{\ddot{a}}{a} + H^2 = -p \quad (2.10)$$

where $H \equiv \dot{a}/a$ ($\equiv d/dt$) is called the *Hubble parameter*, and $\rho = \sum_i \rho_i$, $p = \sum_i p_i$ are sums over the constituents of the universe, indexed by i . Combining these equations, or

equivalently by the contracted Bianchi identities,

$$G_{;\nu}^{\mu\nu} = T_{;\nu}^{\mu\nu} = 0, \quad (2.11)$$

we get the continuity equation

$$\frac{d}{dt}(\rho a^3) + p \frac{d}{dt}(a^3) = 0. \quad (2.12)$$

For a perfect fluid with an *equation of state*,

$$p = w\rho, \quad (2.13)$$

this becomes

$$\dot{\rho} + 3(1+w)H\rho = 0, \quad (2.14)$$

which has the solution

$$\rho = \rho_0 \left(\frac{a}{a_0} \right)^{-3(1+w_{\text{eff}}(a))} \quad (2.15)$$

where subscript ‘0’ denotes the present time, and

$$w_{\text{eff}}(a) \equiv \frac{1}{\ln a} \int_0^{\ln a} (1 + w(\hat{a})) d \ln \hat{a} \quad (2.16)$$

is the *effective equation of state*. For a constant w this reduces to

$$\rho = \rho_0 \left(\frac{a}{a_0} \right)^{-3(1+w)} = \rho_0 (1+z)^{3(1+w)}, \quad (2.17)$$

where $1+z \equiv a_0/a$ defines the *redshift* z . We will assume in the following that $a_0 = 1$ without loss of generality, so that $1+z = a^{-1}$. Plugging these expressions for ρ back in Eq. (2.10), and combining with Eq. (2.9), we find that

$$\frac{\ddot{a}}{a} = -\frac{1}{6}\rho(1+3w), \quad (2.18)$$

so if the dominant component in the universe has $w < -1/3$, the expansion will accelerate.

There are four standard components: non-relativistic matter (subscript ‘m’), radiation (subscript ‘r’), spatial curvature (subscript ‘k’), and dark energy (subscript ‘DE’). These are required by observations, except curvature, as will be described further in Chapter 3.

The components evolve as

$$\rho_m \propto a^{-3} \quad \text{non-relativistic matter, } w_m = 0, \quad (2.19)$$

$$\rho_r \propto a^{-4} \quad \text{radiation, } w_r = 1/3, \quad (2.20)$$

$$\rho_k \propto a^{-2} \quad \text{curvature, } w_k = -1/3, \quad (2.21)$$

and the dark energy component in the case of a cosmological constant obeys

$$\rho_\Lambda \propto a^0 \quad \text{cosmological constant, } w_\Lambda = -1. \quad (2.22)$$

More general, time-varying equations of state $w_{\text{DE}}(a)$ are also allowed by observations.

With these components, we can write the Friedmann equation in a sometimes more useful form,

$$E^2(z) = \Omega_r(1+z)^4 + \Omega_m(1+z)^3 + \Omega_k(1+z)^2 + \Omega_{\text{DE}}(1+z)^{3(1+w_{\text{eff}}^{\text{DE}}(z))}, \quad (2.23)$$

where $E^2(z) \equiv (H/H_0)^2$, H_0 is the Hubble parameter at the present time (the *Hubble constant*) and $\Omega_i = \rho_{i,0}/3H_0^2$ is the present fraction of the critical energy density,

$$\rho_c = 3H^2, \quad (2.24)$$

in component i at the present time. The curvature density parameter $\Omega_k \equiv k/H_0^2 = 1 - (\Omega_m + \Omega_r + \Omega_{\text{DE}})$, since $\sum_i \Omega_i = 1$ by definition. In the standard *Cold Dark Matter* (CDM) model, the non-relativistic matter is made up of baryons (sometimes separated out as Ω_b) and barely-interacting cold dark matter (sometimes denoted by Ω_c), and the radiation is made up of photons (density Ω_γ) and neutrinos (density Ω_ν). The radiation density

$$\Omega_r = \Omega_\gamma(1 + 0.2271N_{\text{eff}}), \quad (2.25)$$

where N_{eff} is the effective number of neutrino species. The standard value is $N_{\text{eff}} = 3.04$.

In summary, the geometric expansion (or background evolution) of the universe in the standard Λ CDM *model* of cosmology (cosmological constant + cold dark matter), can be described by four numbers:

$$\{H_0, \Omega_r, \Omega_m, \Omega_\Lambda\}. \quad (2.26)$$

From observations, the concordance model is the flat Λ CDM model, which is thus described by three parameters. The extended model where the dark energy equation of state is allowed to differ from $w_\Lambda = -1$ typically has one or two more parameters to describe that. Most common is a constant equation of state, thus just one more parameter, and we will refer to that as the w CDM *model*. Often, the Hubble constant H_0 is exchanged for the dimensionless parameter $h \equiv H_0/100 \text{ km/s/Mpc}$.

2.3 Perturbations – Structure Formation – Perturbation Equation

On top of the homogeneous perfect-fluid background, there will also be density perturbations (since there clearly is structure in the Universe). This is a topic in many ways pioneered by [Bardeen \(1980\)](#). The following presents an outline of linear perturbation theory as applied to non-relativistic matter, relevant for the formation of structure on sub-horizon scales from the matter era (or rather, photon decoupling) onwards. Excellent extended introductions are given in e.g. [Peacock \(1999\)](#); [Liddle & Lyth \(2000\)](#); [Coles & Lucchin \(2002\)](#). We do not consider vector or tensor perturbations, as they have little relevance to the later thesis.

By perturbing the equations of General Relativity, we can find that matter perturbations $\delta_m \equiv (\rho_m - \bar{\rho}_m)/\bar{\rho}_m$ obey the equation

$$\ddot{\delta}_m + 2H\dot{\delta}_m + \left(\frac{k}{a}\right)^2 \frac{\delta P_{m,\mathbf{k}}}{\rho_m} = \frac{3}{2}\rho\delta. \quad (2.27)$$

to linear order (see e.g. [Liddle & Lyth, 2000](#)). Note that in the above, the background value is now written as $\bar{\rho}_m$, with ρ_m here the exact inhomogeneous density. In the equation, ρ and δ is the total energy density and its perturbation, respectively, and $\delta P_{m,\mathbf{k}}$ the matter pressure perturbation. In this context, \mathbf{k} denotes the comoving momentum of the perturbation, obtained by Fourier-transforming the real-space equation, and k is its magnitude. The cold-dark-matter part of the matter content lacks pressure perturbations as its interaction rate must be extremely small, whereas baryonic matter does exhibit pressure perturbations. For scales above the *Jeans scale* $k_J = \sqrt{3\rho/2}/c_s$, where c_s is the sound speed of baryons, the pressure is negligible. Below the Jeans scale, the pressure is highly relevant and inhibits perturbation growth, and this primarily applies to small scales before matter–radiation equality. Additionally, dissipative interactions including photons and neutrinos, that we will not specify explicitly, affect small-scale perturbations. On sufficiently large scales, we can therefore neglect these effects, also coinciding with the long-wavelength limit ($k \rightarrow 0$) of the equation. This thus ignores causal physics inside the *horizon* of size H^{-1}/a , which particularly plays a role in creating the perturbation structure of the cosmic microwave background, and the baryon density contrast. We will come back to the inclusion of these effects through a transfer function, below. These physical processes are also discussed further in Sects. [3.2.2](#) & [3.3.1](#).

With this assumption ($k = 0$ – comoving momentum now, not spatial curvature), the

perturbation equation takes the form

$$\ddot{\delta}_m + 2H\dot{\delta}_m - \frac{3}{2}\rho\delta = 0. \quad (2.28)$$

We will restrict ourselves to a flat universe in the following, which is typically a good approximation to the late matter era which we will consider. For a flat cosmology with matter and dark energy, Eq. (2.28) becomes (Ma et al., 1999)

$$\ddot{\delta}_m + 2H\dot{\delta}_m = \frac{3}{2}(\rho_m\delta_m + \delta\rho_{\text{DE}} + 3\delta p_{\text{DE}}), \quad (2.29)$$

where we now included dark energy perturbations explicitly. A cosmological constant does not exhibit perturbations by construction. A general dark energy component may, such as quintessence (see Sect. 5.1.1). However, quintessence will only cluster on very large scales, and therefore its perturbations are negligible compared to the matter perturbation at the sub-horizon scales we are interested in (Ma et al., 1999; Dave et al., 2002). We discuss some of the effects of dark energy perturbations in Sect. 3.3.1. In this approximation (i.e. with dark energy homogeneous), the equation thus becomes

$$\ddot{\delta}_m + 2H\dot{\delta}_m - \frac{3}{2}\Omega_m(a)H^2\delta_m = 0. \quad (2.30)$$

Expanding this expression in terms of the dark energy equation of state $w_{\text{DE}}(a)$ gives (Linder & Jenkins, 2003)

$$\delta'' + \frac{3}{2}\left[1 - \frac{w_{\text{DE}}(a)}{1 + X(a)}\right]\frac{\delta'}{a} - \frac{3}{2}\frac{X(a)}{1 + X(a)}\frac{\delta}{a^2} = 0, \quad (2.31)$$

where

$$X(a) = \frac{\Omega_m}{1 - \Omega_m}a^{3w_{\text{eff}}(a)}, \quad (2.32)$$

and the prime now indicates differentiation with respect to a . The quantity w_{eff} is defined in Eq. (2.16). The general solution for δ is a superposition of a growing and a decaying solution. Normally one considers only the growing solution $D_1(a)$, as the decaying mode will be entirely negligible for perturbations originating from the primordial vacuum perturbations.

It is also practical to work with the function $g(a) \equiv D_1(a)/a$, as this normalizes the evolution to that in a critical-density ($\Omega_m = 1$) universe, $\delta \propto a$. Such evolution will generically take place in the matter-dominated epoch, and therefore normalizing to this time evolution is convenient. One therefore speaks of the *growth suppression factor* g , measuring the suppression of perturbation growth relative to that in a critical-density universe. The equation for g becomes (Linder & Jenkins, 2003)

$$g'' + \left[\frac{7}{2} - \frac{3}{2}\frac{w_{\text{DE}}(a)}{1 + X(a)}\right]\frac{g'}{a} - \frac{3}{2}\frac{1 - w_{\text{DE}}(a)}{1 + X(a)}\frac{g}{a^2} = 0. \quad (2.33)$$

This equation thus most importantly describes the suppression of linear matter perturbations at sub-horizon scales after matter–radiation equality, relative to those in a critical-density universe. In a Λ CDM universe, the solution to this equation is given by (Heath, 1977)

$$g_{\Lambda\text{CDM}}(a) = \frac{D_1^{\Lambda\text{CDM}}(a)}{a} = \frac{5}{2}\Omega_m \frac{H}{a} \int_0^a \frac{d\hat{a}}{[\hat{a}H(\hat{a})]^3}. \quad (2.34)$$

The normalization here is chosen so that $g(a) = 1$ in a critical-density universe. This function is well-approximated by (Lightman & Schechter, 1990; Lahav et al., 1991; Carroll et al., 1992)

$$g_{\Lambda\text{CDM}}(a=1) \approx \frac{5}{2}\Omega_m \left[\Omega_m^{4/7} - \Omega_\Lambda + \left(1 + \frac{1}{2}\Omega_m\right) \left(1 + \frac{1}{70}\Omega_\Lambda\right) \right]^{-1}, \quad (2.35)$$

which can be straightforwardly extended to other redshifts, letting the Ω 's depend on a . For other cosmologies, the differential equation must generally be solved numerically.

As touched upon, the perturbation equation so far presented, describes only the linear evolution due to self-gravity alone. The additional physical effects due to pressure and dissipative interactions is usually encoded by a *transfer function* $T(k)$. The transfer function describes how a perturbation of scale k is modified by these effects. It can be found through solving a *Boltzmann hierarchy* of connected Boltzmann equations, linking the different species in the early Universe (essentially photons, baryons, dark matter and neutrinos) – see e.g. Liddle & Lyth (2000), or Bernstein (1988) for a general introduction to non-equilibrium thermodynamics in cosmology. The coupled system will include a model for how radiation and matter perturbations are related, the standard case of which is *adiabatic* perturbations for which $\delta_r = 3\delta_m/4$, independent of time. This relation is expected to hold also on small scales (tight-coupling approximation). The alternative is called *isocurvature* perturbations, but is unfavoured by data. Generically, the additional physical processes lead to a suppression of perturbations on small scales. The transfer function thus describes the part of the perturbation evolution due to causal physics inside the horizon, and the long-wavelength perturbation equation the collisionless Boltzmann evolution. The transfer function is therefore defined as (e.g. Eisenstein & Hu, 1998)

$$T(k) \equiv \frac{\delta_k(z=0)}{\delta_k(z=\infty)} \frac{\delta_{k=0}(z=\infty)}{\delta_{k=0}(z=0)}. \quad (2.36)$$

Matter transfer functions (including with hot dark matter, neutrinos, baryons and photons) have been studied particularly by Bond & Szalay (1983); Bond & Efstathiou (1984); Efstathiou & Bond (1986); Bardeen et al. (1986); Holtzman (1989); Hu & Sugiyama (1995); Eisenstein & Hu (1998, 1999); Ma et al. (1999). The CDM transfer function can

be reasonably well approximated by (Bardeen et al., 1986)

$$T_{\text{CDM}}(q) \approx \frac{\ln(1 + 2.34q)}{2.34q} [1 + 3.89q + (16.1q)^2 + (5.46q)^3 + (6.71q)^4]^{-1/4}, \quad (2.37)$$

for a ΛCDM universe, applicable when the baryon density is small and with adiabatic perturbations. Here, $q = k/h\Gamma \text{ Mpc}^{-1}$, with

$$\Gamma \approx \Omega_{\text{m}} h \exp \left[-\Omega_{\text{b}} \left(1 + \frac{\sqrt{2h}}{\Omega_{\text{m}}} \right) \right] \quad (2.38)$$

the *shape parameter* of the transfer function (Efstathiou et al., 1992; Peacock & Dodds, 1994; Sugiyama, 1995). The shape parameter describes the effect of baryon pressure perturbations (but here does not incorporate the photon–baryon acoustic oscillations prior to decoupling), which determines the overall shape of the power spectrum. For applications where percent or higher precision is required, the Boltzmann hierarchy must be solved numerically, with a software package such as CMBFAST (Seljak & Zaldarriaga, 1996).

Putting the pieces together, the overall evolution of a matter perturbation $\delta_{\text{m},\mathbf{k}}$ is given by

$$\delta_{\text{m},\mathbf{k}}(z) = T_{\text{m}}(k) \frac{g(z)}{g(z=0)} \frac{\delta_{\mathbf{k}}^i}{1+z} \quad (2.39)$$

where $T_{\text{m}}(k)$ specifically relates to the matter perturbations and $\delta_{\mathbf{k}}^i$ are the energy-density perturbations at $z = \infty$, or at least some initial time well before all the scales of interest entered the horizon ($k = aH$).

The perturbations must ultimately originate in the initial conditions for the GR evolution of the Universe. The currently most favoured scenario is that these primordial perturbations were provided by a pre-Hot-Big-Bang period of inflation, during which the Universe expanded exponentially (see e.g. Guth, 1981; Linde, 1982; Liddle & Lyth, 2000). Through this expansion, quantum fluctuations in the vacuum are stretched to classical scales and frozen during the inflationary epoch. These perturbations then provide the primordial seeds of structure in the Universe. The primordial scalar perturbations are usually described by the normalization σ_8 and scalar spectral index n_s of their power-law power spectrum, and as such in terms of the statistical properties of the perturbations (see Sect. 3.1.3). Inflation models generically predict adiabatic primordial perturbations with a near-scale-invariant power spectrum, $n_s \approx 1$ (Bardeen et al., 1983). A scale-invariant spectrum with $n_s = 1$ is often called a *Harrison–Zel’dovich* spectrum. The first-order matter perturbations are thus in the standard model described by three numbers,

$$\{\Gamma \text{ (or } \Omega_{\text{b}}), \sigma_8, n_s\}, \quad (2.40)$$

in addition to those describing also the background expansion, with so-far indecisive observational evidence for the need of n_s rather than a Harrison–Zel’dovich spectrum. Perturbations in the photon distribution, the cosmic microwave background, will in addition depend on the optical depth through the reionization era, which is usually parameterized in terms of the *reionization optical depth* τ . This is discussed further in Sect. 3.3.1.

A period of inflation is the leading explanation for the observational fact that regions in the cosmic microwave background (see Sect. 3.3.1) that appear to have been in causal contact could not have been so in a universe without any such mechanism (this is called the Horizon Problem). It can further explain why the Universe has a flat geometry to such high accuracy (the Flatness Problem), and why no relic abundance of theoretically predicted magnetic monopoles is found (the Monopole Problem), since they would be exponentially diluted away. The unique success of inflation in explaining the observed structure of the Universe and the range of problems described above make it the preferred model (class) for primordial perturbations.

For non-linear perturbations (i.e. when $\delta \gtrsim 1$), the evolution equations of the gravitational theory (e.g. GR) must generally be solved numerically using some type of N -body simulation. This applies to comoving scales smaller than approximately $10h^{-1}$ Mpc. See e.g. [Bertschinger \(1998\)](#); [Bernardeau et al. \(2002\)](#) for more on non-linear perturbations.

Chapter 3

Observational Tests

3.1 Cosmological Observations

3.1.1 Observing the Universe

Because of the immense distances involved, the Universe does not lend itself to direct physical examination beyond our Solar System. Instead, we have to rely on whatever information reaches us from distant sources. This primarily takes the form of electromagnetic radiation, neutrinos and gravitational radiation (the existence of which has not yet been experimentally verified) travelling to us from the Cosmos. Out of these, only observations using electromagnetic radiation have reached maturity. All current and most future observational methods rely on observing the electromagnetic radiation from gas, stars, galaxies, clusters of galaxies and the cosmic microwave background. From this radiation, geometric and structural properties of the Universe can be inferred, sometimes involving complex modelling of the interaction history of the photons.

Observations of the electromagnetic radiation from the Universe have a long history, starting with studies of the occurrence of stars and solar-system objects such as planets and comets. From the proto-astronomy of the Chaldaeans in Mesopotamia, and the Chinese, around 4000 years ago, this gradually led via the Copernican and Newtonian revolutions to what is now considered celestial mechanics, and then extragalactic astronomy and cosmology via Hubble. The current observational methods and results in cosmology will be discussed in the following Sections.

Since it appears that a dominant part of the content of the Universe is ‘dark’, i.e. does not emit or absorb electromagnetic radiation, observations of this ‘dark side’ of the Universe are indirect and convoluted – constituting the most significant challenge in cosmology.

An important part of observational cosmology is the understanding of possible systematic effects, i.e. effects that may not be modelled accurately and can lead to bias in the estimates of parameter values. This includes understanding selection (i.e. the probability of detecting objects given their physical properties), foreground emission, and uncertainty in the theoretical description of transfer functions and photon interaction history (however, such ‘noise’ can also be ‘signal’ for testing alternative such models).

We discuss a number of particular cosmological quantities, as well as current and future experiments probing them, below.

3.1.2 Luminosity and Angular Diameter Distance

Cosmological observations often measure the *luminosity distance* d_L and/or the *angular diameter distance* d_A . From measuring these quantities, we may constrain cosmological parameters. These observables are geometric, only telling us about the geometry of the Universe as described by the Friedmann equation, but not the structure from perturbations.

The electromagnetic flux \mathcal{F} measured by a telescope on Earth from a light source at comoving radial coordinate r at redshift z with an absolute luminosity L is

$$\mathcal{F} = \frac{L}{4\pi d_L^2}, \quad (3.1)$$

where

$$d_L(z) \equiv a_0(1+z)r(z) \quad (3.2)$$

defines the *luminosity distance*. Since the photons will have traveled to us from the position r , we can find by considering a null geodesic that

$$r(z) = \frac{1}{H_0\sqrt{|\Omega_{k,0}|}} \mathcal{S} \left(\sqrt{|\Omega_{k,0}|} \int_0^z \frac{1}{E(z')} dz' \right), \quad (3.3)$$

where $E(z)$ is given by the Friedmann equation, Eq. (2.23) on p. 15, and

$$\mathcal{S}(x) = \begin{cases} \sin(x), & \Omega_k < 0; \\ \sinh(x), & \Omega_k > 0; \\ x, & \Omega_k = 0. \end{cases} \quad (3.4)$$

Here, the factors $\sqrt{|\Omega_k|}$ in Eq. (3.3) cancel for $\Omega_k = 0$. Hence

$$d_L(z) = \frac{1+z}{H_0\sqrt{|\Omega_k|}} \mathcal{S} \left(\sqrt{|\Omega_k|} \int_0^z \frac{1}{E(z')} dz' \right), \quad (3.5)$$

and we can thus theoretically predict this quantity, as well as measure it from the flux \mathcal{F} and intrinsic luminosity L of a source.

The *angular diameter distance* d_A is defined as

$$d_A \equiv \frac{D}{\theta}, \quad (3.6)$$

where D is the proper size of an object and θ is the angular size of the object. From the FLRW metric we can find that

$$d_A = \frac{d_L}{(1+z)^2}, \quad (3.7)$$

which in fact also applies in any metric theory of gravity where the photon phase-space density is conserved (Etherington, 1933; Linder, 1988).

3.1.3 Power Spectra – Perturbation Growth

The theory of initial conditions is in practice always a statistical statement, i.e. *some* random realization of a statistical distribution of primordial perturbations occurs in the very early universe. Observational tests probing the large-scale structure in the Universe must therefore by necessity be based on statistical properties of the matter distribution.

The statistical properties of any distribution p can be fully and systematically described in terms of the *irreducible moments* of the distribution,

$$\begin{aligned} \xi_n(\mathbf{x}_1, \mathbf{x}_2, \dots, \mathbf{x}_n) = \\ \int_{-\infty}^{\infty} d\delta_1 \int_{-\infty}^{\infty} d\delta_2 \cdots \int_{-\infty}^{\infty} d\delta_n \delta_1 \delta_2 \cdots \delta_n p(\delta_1, \delta_2, \dots, \delta_n | \mathbf{x}_1, \mathbf{x}_2, \dots, \mathbf{x}_n) \end{aligned} \quad (3.8)$$

For practical and computational reasons, it is often convenient to work with the Fourier transform of the correlation function. In practice, the correlation function always fulfils the conditions of Fourier's Theorem and hence its Fourier transform contains the same information as the correlation function itself. Fourier transforming gives

$$\begin{aligned} \xi_n(\mathbf{k}_1, \mathbf{k}_2, \dots, \mathbf{k}_n) = \frac{1}{(2\pi)^{3n/2}} \int_{-\infty}^{\infty} d^3\mathbf{x}_1 \cdots \int_{-\infty}^{\infty} d^3\mathbf{x}_n \xi(\mathbf{x}_1, \mathbf{x}_2, \dots, \mathbf{x}_n) \times \\ \exp\left(-i \sum_{j=1}^n \mathbf{k}_j \cdot \mathbf{x}_j\right) \end{aligned} \quad (3.9)$$

The Fourier transform of ξ_2 is called the *power spectrum* P , and provided that the patch of the Universe we are looking at is statistically homogeneous, then

$$p(\delta_1, \delta_2 | \mathbf{x}_1, \mathbf{x}_2) = p(\delta_1, \delta_2 | \mathbf{x}_1 - \mathbf{x}_2) \quad (3.10)$$

and hence

$$\begin{aligned}
P(\mathbf{k}_1, \mathbf{k}_2) &= \xi_2(\mathbf{k}_1, \mathbf{k}_2) \\
&= \frac{1}{(2\pi)^3} \int_{-\infty}^{\infty} d^3\mathbf{x}_1 \int_{-\infty}^{\infty} d^3\mathbf{x}_2 \xi_2(\mathbf{x}_1 - \mathbf{x}_2) \exp[-i(\mathbf{k}_1 \cdot \mathbf{x}_1 + \mathbf{k}_2 \cdot \mathbf{x}_2)] \\
&= \frac{1}{(2\pi)^3} \int_{-\infty}^{\infty} d^3\mathbf{u} \int_{-\infty}^{\infty} d^3\mathbf{x}_2 \xi_2(\mathbf{u}) \exp[-i(\mathbf{k}_1 \cdot \mathbf{u} + (\mathbf{k}_1 + \mathbf{k}_2) \cdot \mathbf{x}_2)] \\
&= \frac{1}{(2\pi)^3} \delta_D(\mathbf{k}_1 + \mathbf{k}_2) \int_{-\infty}^{\infty} d^3\mathbf{u} \xi_2(\mathbf{u}) \exp[-i(\mathbf{k}_1 \cdot \mathbf{u})] \\
&= \frac{1}{(2\pi)^3} \delta_D(\mathbf{k}_1 + \mathbf{k}_2) P(\mathbf{k}_1), \tag{3.11}
\end{aligned}$$

where $\delta_D(\cdot)$ is the Dirac delta function, and $\mathbf{u} = \mathbf{x}_1 - \mathbf{x}_2$.

Adding isotropy means $\xi_2(\mathbf{x}_2 - \mathbf{x}_1) = \xi_2(|\mathbf{x}_2 - \mathbf{x}_1|)$. Choosing a right-handed coordinate system aligned with \mathbf{k}_1 in the z -direction, and changing to spherical coordinates, we get

$$\begin{aligned}
P(\mathbf{k}_1, \mathbf{k}_2) &= \frac{1}{(2\pi)^3} \delta_D(\mathbf{k}_1 + \mathbf{k}_2) \int_{-\infty}^{\infty} d^3\mathbf{u} \xi_2(\mathbf{u}) e^{-i(\mathbf{k}_1 \cdot \mathbf{u})} \\
&= \frac{1}{(2\pi)^3} \delta_D(\mathbf{k}_1 + \mathbf{k}_2) \int_0^{\infty} dr \int_{-1}^1 d(\cos\theta) \int_0^{2\pi} d\phi \xi_2(r) r^2 e^{-i|\mathbf{k}_1|r \cos(\theta)} \\
&= \frac{1}{2\pi^2} \delta_D(\mathbf{k}_1 + \mathbf{k}_2) \int_0^{\infty} dr \xi_2(r) r^2 j_0(|\mathbf{k}_1|r) \\
&= \frac{1}{2\pi^2} \delta_D(\mathbf{k}_1 + \mathbf{k}_2) P(|\mathbf{k}_1|), \tag{3.12}
\end{aligned}$$

which also defines $P(|\mathbf{k}_1|)$. The power spectrum where homogeneity and isotropy applies thus only depends on the magnitude of the momenta. We see that it can be written in the form $P(\mathbf{k}_1, \mathbf{k}_2) \propto \delta_D(|\mathbf{k}_1| - |\mathbf{k}_2|) P(|\mathbf{k}_1|)$. Therefore, we only need to consider the function $P(k)$ to fully describe $P(\mathbf{k}_1, \mathbf{k}_2)$.

Now consider a Gaussian probability distribution p with covariance matrix $C(r)$:

$$p(\delta_1, \delta_2 | r) = \frac{1}{2\pi \sqrt{|C(r)|}} \exp \left[-\frac{1}{2} \sum_{i,j=1}^2 \delta_i (C^{-1}(r))_{ij} \delta_j \right]. \tag{3.13}$$

Inserting this gives

$$\begin{aligned}
\xi_2(r) &= \int_{-\infty}^{\infty} d\delta_1 \int_{-\infty}^{\infty} d\delta_2 \delta_1 \delta_2 p(\delta_1, \delta_2 | r) \\
&= \frac{1}{2\pi \sqrt{|C(r)|}} \int_{-\infty}^{\infty} d\delta_1 \int_{-\infty}^{\infty} d\delta_2 \delta_1 \delta_2 \exp \left[-\frac{1}{2} \sum_{i,j=1}^2 \delta_i (C^{-1}(r))_{ij} \delta_j \right] \\
&= \sqrt{|C(r)|}, \tag{3.14}
\end{aligned}$$

where $|\cdot|$ denotes matrix determinant. Clearly, a Gaussian perturbation field is completely described by its mean and power spectrum. There are good reasons why near-Gaussian perturbations described by $P(k)$ are expected in the Universe:

- homogeneity and isotropy in the primordial perturbations are expected from quantum field theory, due to the invariance of the vacuum state (Liddle & Lyth, 2000)
- because the perturbations ultimately result from an average of many independent random processes, the Central Limit Theorem implies that a density field will asymptotically be Gaussian (Hamilton, 2005)

The power spectrum $P(k)$ should therefore be ideal for studying density perturbations.

Combining these statistics with the perturbation evolution described in Sect. 2.3, the power spectrum of matter density perturbations will be related to the power spectrum of initial density perturbations $P^i(k)$ through Eq. (2.39) on p. 19. It can therefore be written

$$P_m(k) = \delta_H^2 T_m^2(k) \frac{g^2(z)}{g^2(z=0)} \frac{P^i(k)}{(1+z)^2}. \quad (3.15)$$

Other authors use other notations and definitions for some of these quantities; in particular, δ_H^2 is sometimes a function a time, and other pre-factors occur. The initial power spectrum $P^i(k)$ is usually related to the primordial curvature perturbation \mathcal{R}_k^i . This is a practical quantity to work with, as it freezes shortly after horizon exit ($k = aH$), unlike the actual primordial density perturbations themselves, and is well-defined also after the same perturbations have decayed. It can be computed from the inflationary dynamics at horizon exit. The primordial power spectrum of \mathcal{R}_k is usually modeled as a power-law,

$$\mathcal{P}_{\mathcal{R}}(k) = A \left(\frac{k}{k_0} \right)^{n_s - 1}, \quad (3.16)$$

around some pivot scale k_0 . Such a power-law is expected to be a good approximation, as the primordial perturbations quickly freeze out during the exponential expansion of inflation, and therefore undergo very limited dynamics (Liddle & Lyth, 2000). The initial perturbations $\delta_k^i \propto k^2 \mathcal{R}_k^i$, so the initial power spectrum can be written

$$P^i(k) = A \left(\frac{k}{k_0} \right)^{n_s}, \quad (3.17)$$

with a renormalization of A , or using the more commonly used $\mathcal{P}_\delta(k) \equiv k^3 P(k)/2\pi^2$,

$$\mathcal{P}_\delta^i(k) = A \left(\frac{k}{k_0} \right)^{n_s + 3}, \quad (3.18)$$

for mathematical convenience.

Very commonly, the dispersion on some particular length-scale is used as the observable (at least for matter fields), rather than the power spectrum itself. This is largely because the range of length scales accessible with any particular probe is limited. This is usually encoded with a window function $W(kR)$, a type of selection function, which picks out

length scales around R , analogous to a Fourier frequency filter. The most common choice is a *top hat* window function in real space, which translates to

$$W_{\text{TH}}(q) = 3 \left(\frac{\sin(q)}{q^3} - \frac{\cos(q)}{q^2} \right) \quad (3.19)$$

in Fourier space. Using the window function, we can then calculate the dispersion of the perturbation field on a particular length scale R as

$$\sigma^2(R) = \int_0^\infty W^2(kR) \mathcal{P}_\delta(k) \frac{dk}{k}, \quad (3.20)$$

having taken care to normalize appropriately. By Eq. (2.39) on p. 19, we can write the time evolution of this dispersion as

$$\sigma(R, z) = \sigma(R, z=0) \frac{g(z)}{g(z=0)} \frac{1}{1+z}, \quad (3.21)$$

and can use $\sigma(R, z=0)$ for some R to parameterize the normalization of the power spectrum. By tradition, the choice has been $R = 8h^{-1}$ Mpc, and so the normalization given as $\sigma_8 \equiv \sigma(8h^{-1} \text{ Mpc}, z=0)$.

A reasonable approximation to $\sigma(R, z=0)$ is given by (Viana & Liddle, 1999; Viana, 2006)

$$\sigma(R, z=0) = \sigma_8 \left(\frac{R}{8h^{-1} \text{ Mpc}} \right)^{-\gamma(R)}, \quad (3.22)$$

with

$$\gamma(R) = (0.3\Gamma + 0.2) \left[2.89 + \frac{0.12h \text{ Mpc}^{-1}}{R} + \log_{10} \left(\frac{R}{8h^{-1} \text{ Mpc}} \right) \right], \quad (3.23)$$

which is accurate to within two percent for the range of halo masses relevant for this work (Chapter 6), compared to the exact expression employing the BBKS transfer function, Eq. (2.37) on p. 19. As before, Γ is the shape parameter associated with the transfer function, see Eq. (2.38). This expression is also generally a good approximation for other dark energy models than the cosmological constant, particularly standard quintessence models, except at large comoving scales $\gtrsim 100h^{-1}$ Mpc (Ma et al., 1999).

Thus, the large-scale structure of the Universe is commonly described using three basic parameters; the normalization σ_8 and exponent n_s of the power spectrum of primordial scalar density perturbations, and the shape parameter Γ of the transfer function (see also Sect. 2.3). These are then constrained by measuring the power spectrum or the dispersion of perturbation fields, around some particular length scale. Inflation predicts a close-to-scale-invariant power spectrum, $n_s \approx 1$ (see further in Sect. 2.3). An illustration of the power spectrum of density fluctuations in the Universe, and the corresponding structures, is shown in Fig. 3.1.

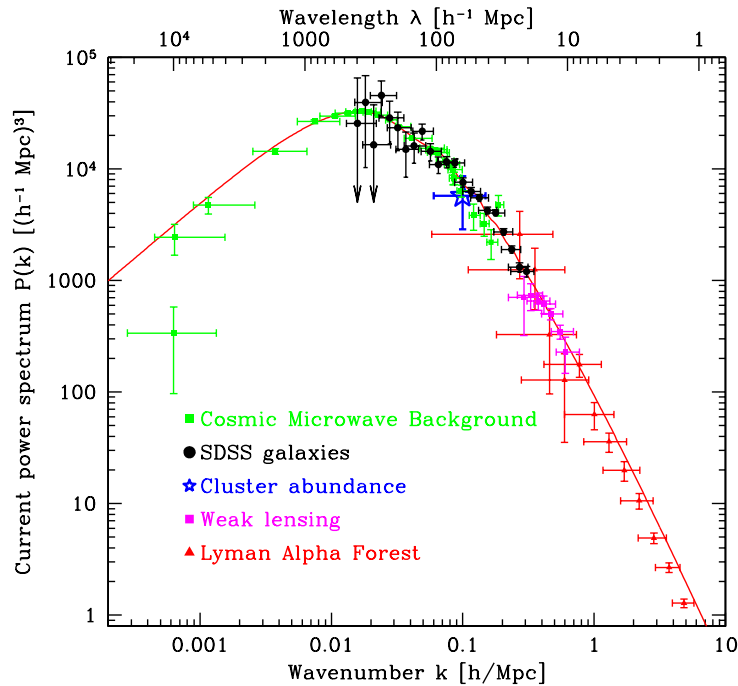


Figure 3.1: The current perturbation power spectrum as measured by various observational probes at different structure scales. Reproduced from Tegmark et al. (2004).

As indicated above, higher-order statistics are needed to fully describe any distribution which is not Gaussian. Testing for such non-Gaussianity is now becoming increasingly popular and feasible, as experimental accuracy improves. No conclusive detection of non-zero three-point (bispectrum) or higher-order correlation functions has been made to date, although some tentative indications exist (most recently Jeong & Smoot, 2007; Yadav & Wandelt, 2008). We shall not consider these further in this work, but refer the reader to Bartolo et al. (2005) for a comprehensive discussion of theory and applications.

3.1.4 Complementarity

Since in the analysis of cosmological data we are essentially faced with a set of under-determined equations, there will in general be multiple ways of arranging model parameter values to fit the data in the same way. Such interchangeability is called parameter degeneracy, and cannot be overcome by increasing measurement precision. The data is said to be sensitive only to particular model-parameter combinations, or more generally particular eigenfunctions of a model–survey combination.

The description of such sensitivity can be formalized through looking at the eigenvec-

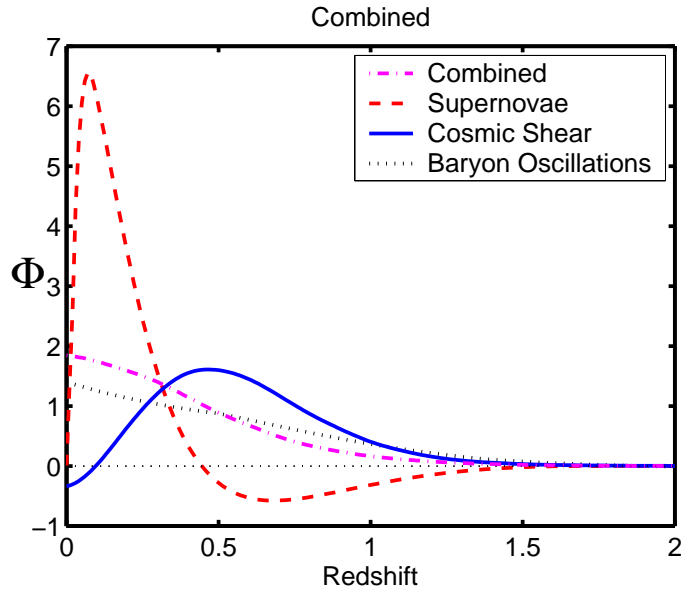


Figure 3.2: Weight functions for different sample probes/surveys, and their combination. The weight function Φ is a measure of the observational sensitivity of the survey to the dark energy equation of state at each redshift. Reproduced from [Simpson & Bridle \(2006\)](#).

tors of the covariance matrix of the model parameters, given some data. This provides a useful measure of which parameter combinations the data is sensitive to, and for Gaussian distributions is a complete description. It is also possible to derive eigenfunctions through what is called principal component analysis (PCA, [Huterer & Starkman, 2003](#); [Huterer & Cooray, 2005](#); [Crittenden & Pogosian, 2005](#); [Stephan-Otto, 2006](#)) or weight function methodology ([Saini et al., 2003](#); [Saini, 2003](#); [Simpson & Bridle, 2005, 2006](#)). Without going into precise detail, these usually describe (relative to some fiducial model) the sensitivity of different observational probes/surveys to the dark energy equation of state, as a function of redshift. An example of this is shown in Fig. 3.2.

To overcome the obstacle of limited data sensitivity, one can combine different types of data, all sensitive to different combinations of model parameters or eigenfunctions, in a joint analysis (see the combined weight function in Fig. 3.2). In this way, parameter degeneracies can be broken, leading to significant leverage over each data set considered separately ([Tegmark et al., 1998](#)). A classic illustration of this is shown in Fig. 3.3. The strongest leverage generally comes from combining geometric probes with perturbation-sensitive probes, as these are based on different evolution equations – Eq. (2.9) on p. 13 and Eq. (2.39) on p. 19 – corresponding to zeroth and first-order approximations of the energy density field of the universe.

The most important application of cosmic complementarity for the future is in con-

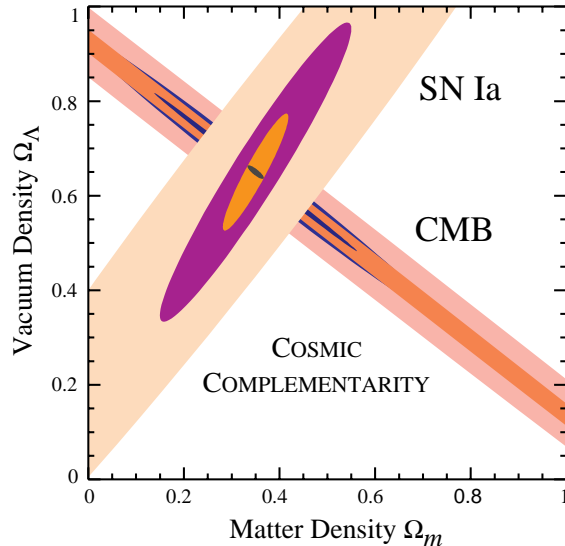


Figure 3.3: Cosmic complementarity of geometric and perturbation-based probes. Independently, neither SNIa nor CMB data can achieve very narrow parameter constraints. When they are combined in a joint analysis, the resulting constraints are dramatically smaller (small black oval). Reproduced from [Tegmark et al. \(1998\)](#).

straining the equation of state w_{DE} of dark energy ([Upadhye et al., 2005](#)), and to distinguish scalar-field dark energy from modified-gravity dark energy ([Ishak et al., 2006](#); [Bertschinger & Zúkin, 2008](#)) – see further discussion in Sect. 4.1. This is particularly so, since distance measures only are sensitive to an averaged, effective dark energy equation of state ([Maor et al., 2001a,b, 2002](#)).

3.2 Geometric Probes

3.2.1 Type Ia Supernovae (SNIa)

Type Ia supernovae (SNIa) are thought to be stars undergoing thermonuclear explosions which occur when a carbon–oxygen white dwarf is pushed above its maximum mass of 1.4 solar masses (the Chandrasekhar limit) owing to mass transfer from a companion star (most likely a giant star). This leads to the complete disruption of the two stars. Such an explosion will typically shine with the same brightness as the whole of its host galaxy. An example is shown in Fig. 3.4. The characteristics of the supernova explosion depend on its progenitor system, and the detailed physics of the explosion process. Although all the details of supernova progenitors and explosion physics are still not clear, Type Ia supernovae appear to be sufficiently homogeneous so as to be used as standard candles, i.e. they all share the same intrinsic magnitude to good accuracy. From observations



Figure 3.4: The supernova SN1994D. Reproduced from [NASA/ESA \(2008\)](#).

there is a now well-known relation between the peak luminosity and the shape of the light curve in the initial phase of the supernova explosion, the *Phillips relation* ([Phillips, 1993](#)). More precisely, the peak luminosity is tightly correlated with the rate at which the luminosity drops after the explosion. A sometimes preferred terminology is that SNIa are *standardizable candles*, currently to around 7%.

The first steps towards using supernovae as observational distance indicators were taken by [Kulikovskij \(1944\)](#), in classifying them according to the shape of their light curve. [Lundmark \(1956\)](#) first explicitly suggested actually using supernovae as extra-galactic distance indicators, although [Wilson \(1939\)](#) first suggested using supernovae to extend the velocity–distance relation of galaxies. Pskovskii and Kowal built up evidence in the 1960s in support of the homogeneity of Type I supernovae (e.g. [Pskovskii, 1962, 1967](#); [Kowal, 1968](#)). During the following decades, additional evidence was slowly accumulated (e.g. [Elias et al., 1985](#)), leading up to the [Branch & Tammann \(1992\)](#) review of data that consolidated the usefulness of Type Ia supernovae as extra-galactic distance indicators and cosmological probes. One of the first serious proposals for surveys to utilize Type I supernovae as cosmological standard candles was set forth by [Colgate \(1979\)](#), and a detailed feasibility study focusing on measuring Ω_m and Ω_Λ was presented by [Goobar & Perlmutter \(1995\)](#). For introductions to Type Ia supernova physics and their use in cosmology, see

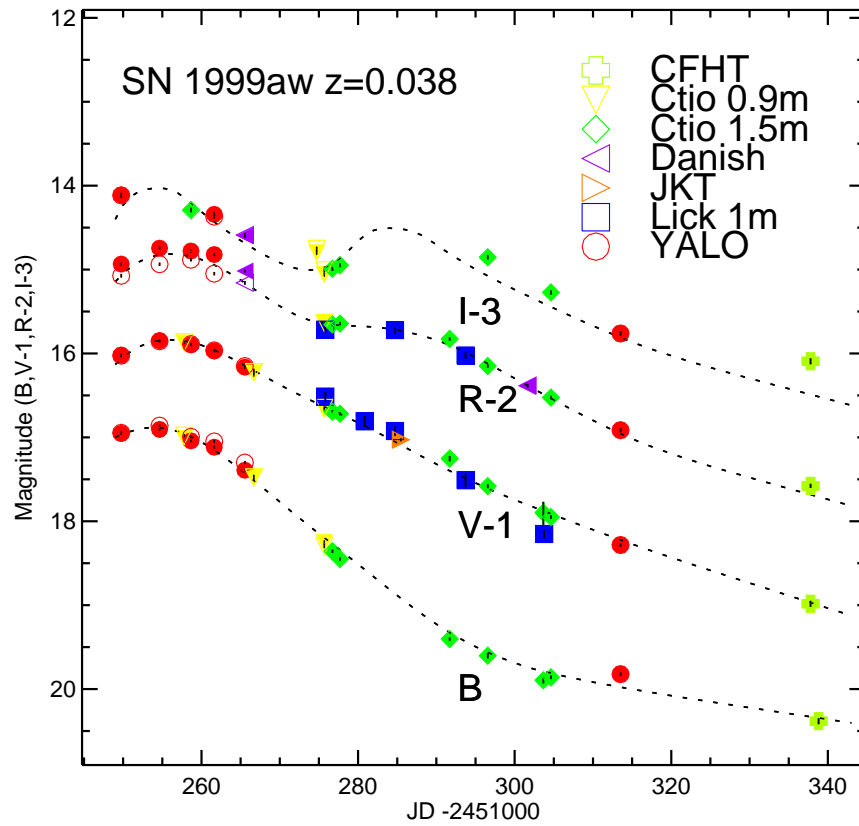
e.g. [Hillebrandt & Niemeyer 2000](#); [Perlmutter & Schmidt 2003](#); [Leibundgut 2008](#).

The first major survey of Type Ia supernovae for cosmological purposes was the Calán–Tololo survey ([Hamuy et al., 1993](#)). These were low-redshift supernovae with $z \sim 0.02$, and the Calán–Tololo sample still constitutes a majority of the known low-redshift supernovae. However, the major breakthrough for supernova cosmology came in 1998, when the Supernova Cosmology Project (SCP) and the High- z Supernova Search Team announced the findings that their observations require a dark energy component with high statistical significance ([Perlmutter et al., 1998](#); [Riess et al., 1998](#)). This led to Science’s ‘Breakthrough of the Year’ award, and later the Gruber Cosmology Prize in 2007. Since then, numerous surveys have been performed confirming the results, with several ongoing ([Garnavich et al., 1998](#); [Schmidt et al., 1998](#); [Riess et al., 1998](#); [Perlmutter et al., 1999](#); [Tonry et al., 2003](#); [Knop et al., 2003](#); [Barris et al., 2004](#); [Riess et al., 2004, 2007](#); [Astier et al., 2006](#); [Wood–Vasey et al., 2007](#); [Davis et al., 2007](#)). Recently, the combination of essentially all Type Ia supernova data to date was uniformly analyzed from lightcurve level, to produce as homogeneous a sample as possible ([Kowalski et al., 2008](#)). This data set constitutes the Union sample.

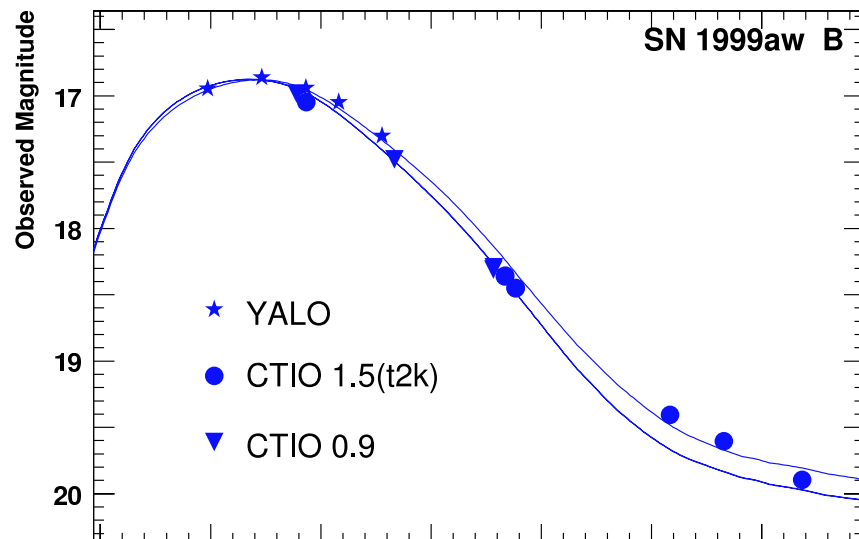
The experimental methodology of supernova cosmology involves three main steps:

- supernova detection and photometry
- lightcurve fitting
- cosmology fitting

The first of these is the serendipitous detection of a supernova explosion, by repeatedly observing the same patch of sky, and taking multi-band photometric and possibly also spectroscopic data over a period of time from the supernova once detected. This gives a set of measurements of the supernova luminosity over time, its lightcurve. An example is shown in [Fig. 3.5a](#). Redshift measurements are also taken from the host galaxy. The data is then processed by fitting to standard lightcurve templates, which typically have three free parameters: the normalization of the curve, the ‘stretch’ factor (a measure of intrinsic luminosity), and the colour of the supernova. [Fig. 3.5b](#) shows the lightcurve in [Fig. 3.5a](#) after lightcurve fitting. From this fitting, the overall apparent magnitude m of the supernova is obtained. The supernovae can then be plotted on a *Hubble diagram* with magnitude vs. redshift (after the velocity–distance plots of [Hubble, 1929](#)), as in [Fig. 3.6](#) (p. 33). This can be used to fit the cosmological parameters using the expression for the



(a) Raw measured lightcurves.



(b) The lightcurve in Fig. 3.5a after fitting. The diverging curves have now been fitted to the lightcurve template and an apparent magnitude can be derived.

Figure 3.5: Raw and fitted lightcurves for one of the Union sample supernovae. Reproduced from [Kowalski et al. \(2008\)](#).

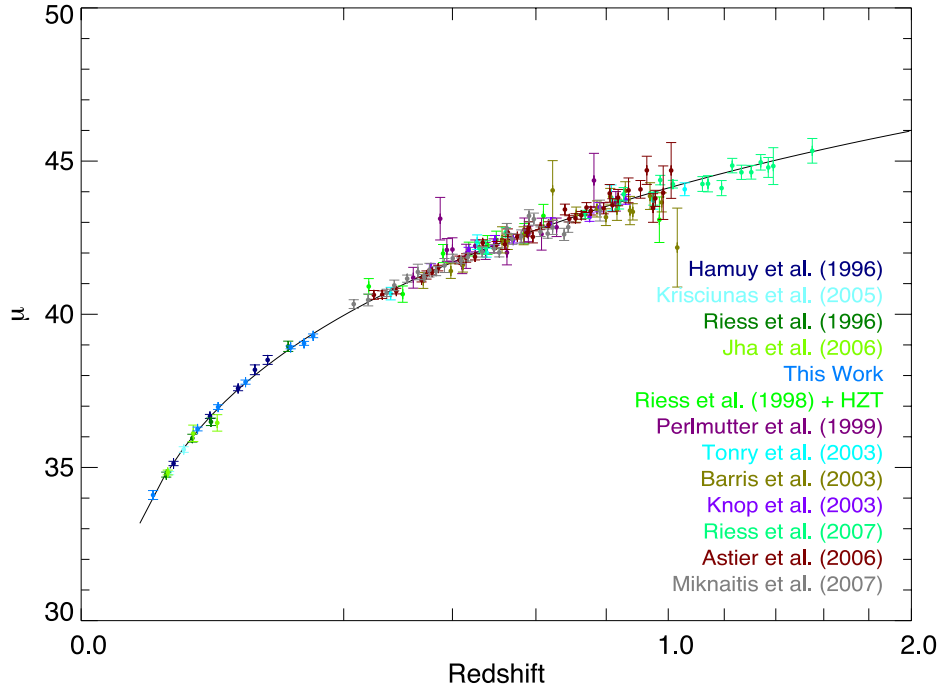


Figure 3.6: The Union sample Hubble diagram. The quantity $\mu(z) \equiv m(z) - M$. Reproduced from [Kowalski et al. \(2008\)](#).

luminosity distance, Eq. (3.5). It is related to the apparent magnitude as

$$m(z) = M + 5 \log_{10} \frac{d_L(z)}{\text{Mpc}} + 25, \quad (3.24)$$

where M is the absolute magnitude of Type Ia supernovae. This parameter should be taken as a free parameter in cosmological fitting. The expression is often also parameterized as

$$m(z) = \mathcal{M} + 5 \log_{10} \mathcal{D}_L(z), \quad (3.25)$$

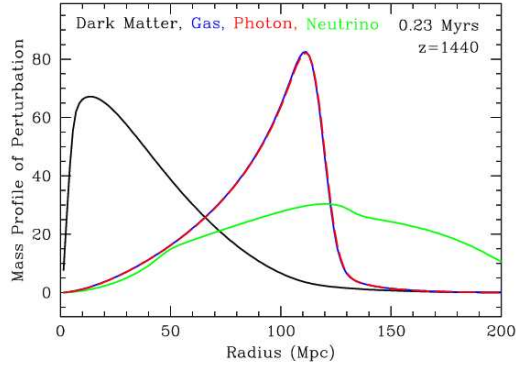
where $\mathcal{D}_L \equiv H_0 d_L$ is the *Hubble-reduced* luminosity distance, and

$$\mathcal{M} \equiv M - 5 \log_{10} (H_0 \text{ Mpc}) + 25 = M - 5 \log_{10} (h_{70}) + 43.16, \quad (3.26)$$

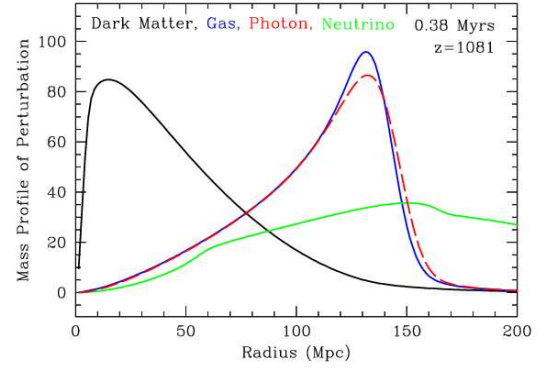
where $h_{70} = H_0 / (70 \text{ km/s/Mpc})$. Note that some authors define \mathcal{M} somewhat differently.

3.2.2 Baryon Acoustic Oscillations (BAO)

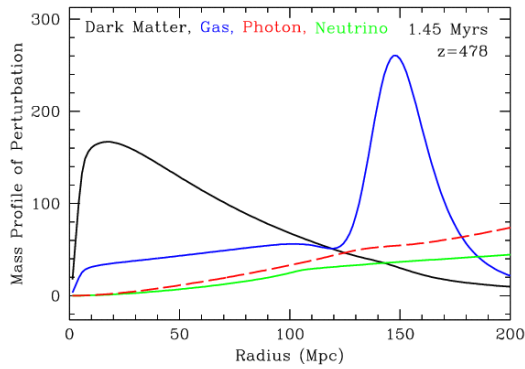
The standard Big Bang scenario predicts that close to the surface of last scattering, baryons and photons act as a fluid with acoustic oscillations from the competition between gravitational attraction and radiation pressure (Fig. 3.7a). As the photons decouple, these acoustic oscillations should be frozen in the baryonic matter distribution (Figs. 3.7b & 3.7c), and gradually also transferred to the dark matter distribution through its gravitational



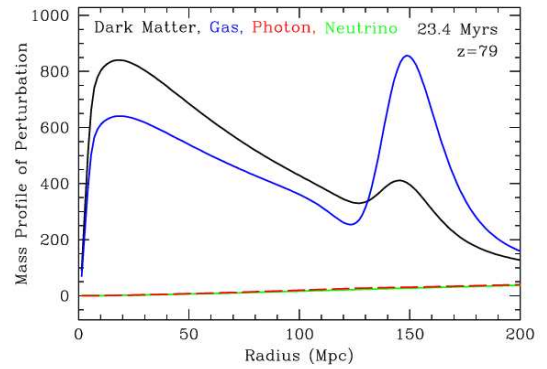
(a) Baryons and photons act as a fluid with acoustic oscillations and share the same perturbation profile.



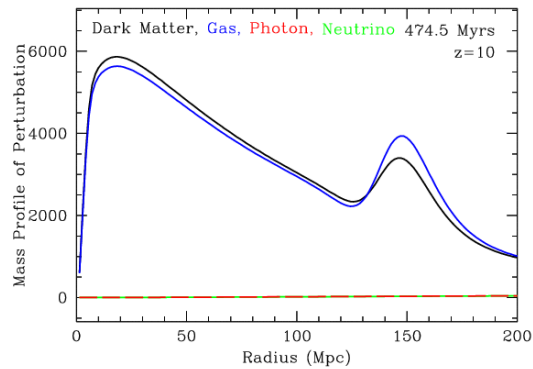
(b) Photons decouple and start free-streaming.



(c) Baryon perturbation is frozen.



(d) The dark matter and baryon overdensities gravitate towards each other, imprinting their respective features onto each other.



(e) The dark matter and baryon overdensities finally converge to very similar distributions.

Figure 3.7: The sequence of imprinting a characteristic-scale overdensity in the matter distribution from the baryon acoustic oscillations at recombination. The particular choice of initial perturbations makes the illustration clear; in general, initial perturbations are random. Reproduced from [Eisenstein \(2008\)](#).

interaction with the baryons (Figs. 3.7d & 3.7e, p. 34). One would thus expect a rise in the power spectrum of matter at a scale corresponding to the acoustic scale, i.e. the sound horizon, at recombination (see e.g. Sunyaev & Zeldovich 1970; Peebles & Yu 1970; Bond & Efstathiou 1984; Holtzman 1989; Hu & Sugiyama 1996; Eisenstein & Hu 1998; Blake & Glazebrook 2003). See also Sect. 2.3 for a discussion about perturbation evolution. The relevant comoving length scale is thus

$$r_s^{\text{BAO}} \equiv H_0^{-1} \int_0^{1/(1+z_{\text{dr}})} \frac{c_s(a)}{E(a)} da = \frac{1}{\sqrt{3}} \int_0^{1/(1+z_{\text{dr}})} \frac{da}{a^2 H(a) \sqrt{1 + (3\Omega_b/4\Omega_\gamma)a}}, \quad (3.27)$$

where $c_s(z)$ is the sound speed at redshift z , and z_{dr} is the redshift of the drag epoch when baryons were released from the photons. It can be approximated as (Eisenstein & Hu, 1998)

$$z_{\text{dr}} = \frac{1291(\Omega_m h^2)^{0.251}}{1 + 0.659(\Omega_m h^2)^{0.828}} \left[1 + b_1(\Omega_b h^2)^{b_2} \right], \quad (3.28)$$

with

$$b_1 = 0.313(\Omega_m h^2)^{-0.419} \left[1 + 0.607(\Omega_m h^2)^{0.674} \right], \quad (3.29)$$

$$b_2 = 0.238(\Omega_m h^2)^{0.223}. \quad (3.30)$$

Evaluating the integral, Eq. (3.27), one finds that $r_s^{\text{BAO}} \approx 100 h^{-1} \text{Mpc}$.

Independent first detections of this baryon acoustic peak were made by the Sloan Digital Sky Survey (SDSS, Eisenstein et al., 2005; Tegmark et al., 2006b) and the Two-degree Field Galaxy Redshift Survey (2dFGRS or 2dF; Cole et al., 2005). A joint analysis was also recently published (Percival et al., 2007). These surveys construct maps of the distribution of galaxies, sometimes referred to as *cosmography*, and then analyze them with the help of statistical methods such as those described in Sect. 3.1.3.

An illustration of the observed distribution of galaxies in the 2dFGRS is shown in Fig. 3.8. The SDSS measurement of the correlation function of luminous red galaxies is shown in Fig. 3.9 (p. 37).

The SDSS team defined an effective distance measure

$$d_V(z) \equiv \left[r^2(z) \frac{z}{H(z)} \right]^{1/3}, \quad (3.31)$$

which can be thought of as a spherical average of radial and perpendicular clustering scales in the galaxy distribution. They also used it to define the dimensionless quantity

$$A \equiv \frac{\sqrt{\Omega_m} H_0}{z_{\text{BAO}}} d_V(z_{\text{BAO}}) = \sqrt{\Omega_m} \left[\frac{H_0^2 r^2(z_{\text{BAO}})}{z_{\text{BAO}}^2 E(z_{\text{BAO}})} \right]^{1/3}. \quad (3.32)$$

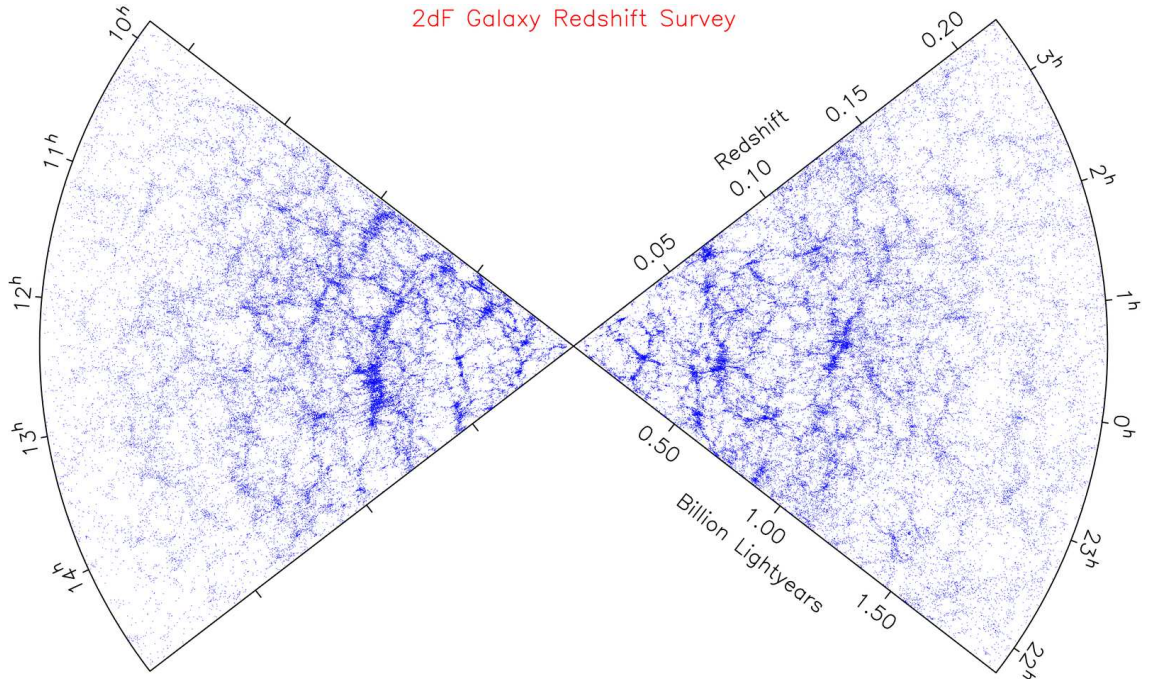


Figure 3.8: The distribution of galaxies observed by the 2dF Galaxy Redshift Survey. Reproduced from [2dFGRS \(2008\)](#).

with, for SDSS, $z_{\text{BAO}} = 0.35$. These can be thought of as measures of the position of the BAO peak. As such, they are purely geometric quantities, although the correlation function as a whole depends on the history of perturbation growth. In this sense, they are similar to the CMB peak-shift parameter, discussed in Sect. 3.3.1.

Additionally, measurements have been published of the ratio of the recombination BAO scale to the BAO scale at redshift z , $r_s^{\text{BAO}}/d_V(z)$, for two redshifts from the 2dF and SDSS data ([Percival et al., 2007](#)), although concern has been expressed over the consistency of these results (see e.g. [Percival et al., 2007](#); [Kowalski et al., 2008](#)).

3.3 Structural Probes

3.3.1 Cosmic Microwave Background (CMB)

The cosmic microwave background (CMB) is the residual radiation from the Big Bang ([Lemaître, 1931](#)), first predicted by [Alpher et al. \(1948\)](#); [Alpher & Herman \(1948\)](#). Around 13.4 billion years ago at $z \sim 1090$, photons stopped interacting with the electrons in the particle soup in the very early Universe, due to the gradual cooling as the Universe expanded. As such, they were then able to travel freely without interruption (statistically speaking), and now engulf us from all directions. The CMB was first measured

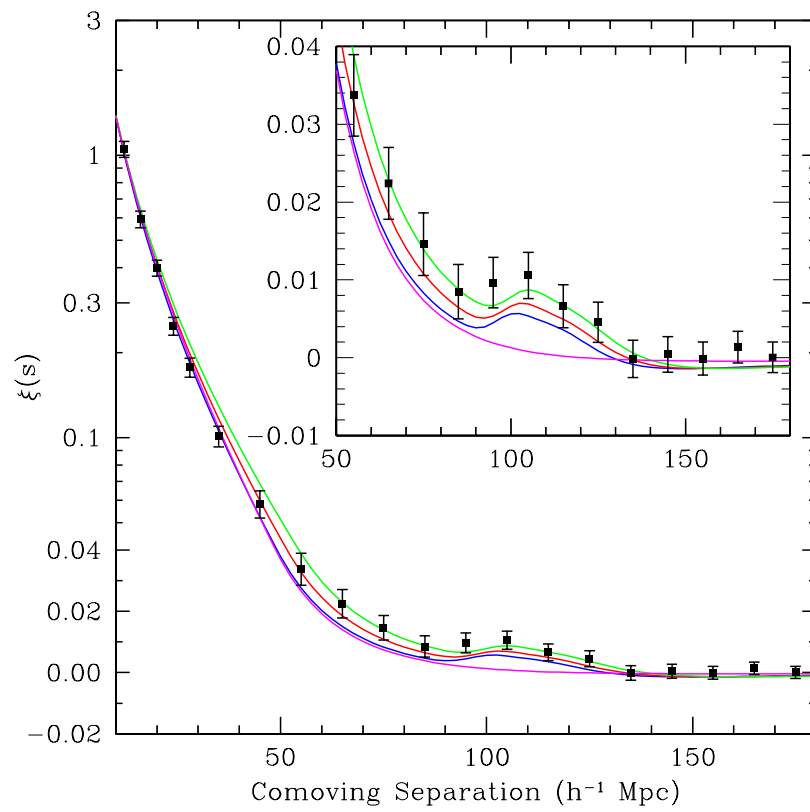


Figure 3.9: The correlation function of luminous red galaxies measured by the Sloan Digital Sky Survey. The expected peak at $\sim 100 h^{-1}$ Mpc is clearly visible. Reproduced from [Eisenstein et al. \(2005\)](#).

by Penzias & Wilson (1965), who were duly awarded the Nobel Prize for their discovery (although Dicke et al., 1965 also deserve recognition for interpreting the results, as do a number of researchers who made direct or indirect detections of the CMB but failed to interpret them – see Naselsky et al., 2006, chap. 1). This essentially made the Hot Big Bang model the only viable option. The CMB has a current average temperature of approximately 2.7 K, and also exhibits tiny anisotropies in the temperature, on the order of 1 in 10^5 , first described in some detail by Sachs & Wolfe (1967); Silk (1967, 1968). These anisotropies carry information about the conditions in the very early Universe and the subsequent expansion; foremost the individual constituents and the initial conditions. The theoretical predictions were elaborated upon in many of the references on perturbations evolution/transfer functions, listed in Sect. 2.3. A number of experiments over the past decade or so have been very successful in measuring this anisotropy. They include COBE (Smoot et al., 1992; Bennett et al., 1994, 1996), that first detected the anisotropy, MAT/TOCO and QMAP (Miller et al., 1999, 2002), Boomerang (de Bernardis et al., 2000; Netterfield et al., 2002; Ruhl et al., 2003; Jones et al., 2006; Montroy et al., 2006; Piacentini et al., 2006), MAXIMA (Hanany et al., 2000), DASI (Halverson et al., 2002; Kovac et al., 2002; Leitch et al., 2005), CBI (Mason et al., 2003; Sievers et al., 2003, 2007; Pearson et al., 2003; Readhead et al., 2004), WMAP (Spergel et al., 2003, 2007; Komatsu et al., 2008), VSA (Scott et al., 2003; Dickinson et al., 2004) and ACBAR (Kuo et al., 2004, 2007; Reichardt et al., 2008). In these experiments, the anisotropies of the CMB have been confirmed and measured with increasingly high accuracy. The latest all-sky map from the *Wilkinson Microwave Anisotropy Probe* (WMAP) is shown in Fig. 3.10. As a result, the discovery of the CMB anisotropy was also recently rewarded through the Nobel Prize to Smoot and Mather. Good introductions to the physics of the CMB are given in Hu & Dodelson (2002); Dodelson (2003); Mukhanov (2005). Naselsky et al. (2006) also contains a review of the history of CMB science and many technical details.

The temperature anisotropy distribution of the CMB can be written as

$$\frac{\Delta T(\theta, \phi)}{T} = \sum_{l,m} a_{lm} Y_{lm}(\theta, \phi), \quad (3.33)$$

where ΔT is the deviation from the background value T and we have expanded in spherical harmonics on the spherical surface of last scattering (LSS). The expansion coefficients a_{lm} are determined by the physics prior to last scattering and the subsequent propagation history, and can thus be calculated using expansion and perturbation formalism described in Chapter 2. The simplest statistical quantity to consider, and so far the main one

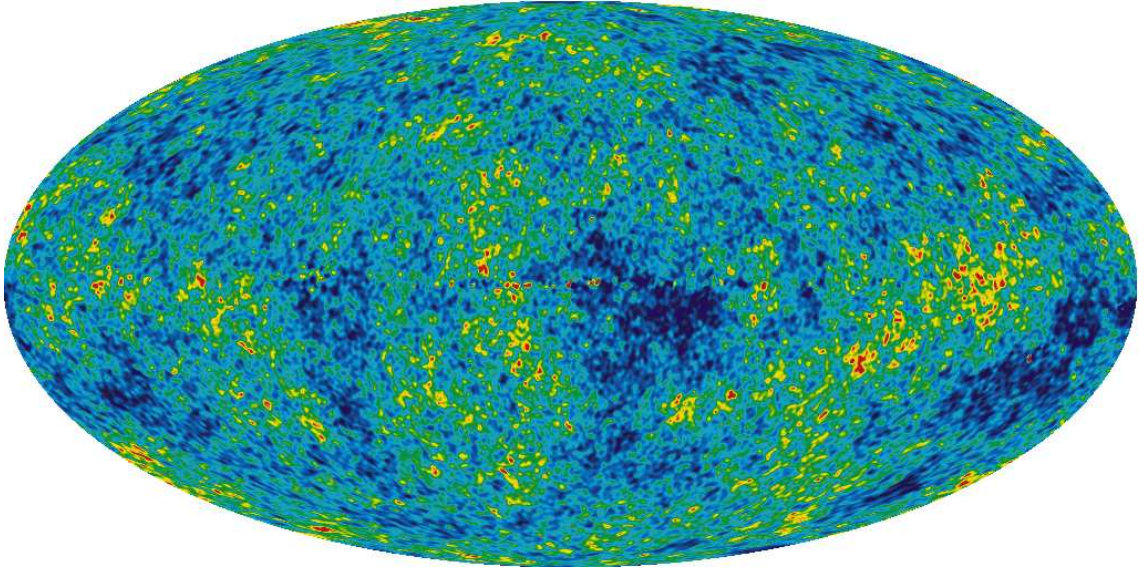


Figure 3.10: The CMB temperature anisotropy as measured by *WMAP* (Komatsu et al., 2008).

studied, is the two-point TT correlation function

$$C(\theta) \equiv \left\langle \frac{\Delta T(\mathbf{m})}{T} \frac{\Delta T(\mathbf{n})}{T} \right\rangle = \sum_{l,m,l',m'} \langle a_{lm} a_{l'm'}^* \rangle Y_{lm}(\mathbf{m}) Y_{l'm'}^*(\mathbf{n}), \quad (3.34)$$

where \mathbf{m} , \mathbf{n} are two directions in the sky an angle θ apart. A standard assumption is that the a_{lm} 's are random fields (see Sect. 3.1.3) so that we can write $\langle a_{lm} a_{l'm'}^* \rangle = C_l \delta_{ll'} \delta_{mm'}$, and hence one can represent

$$C(\theta) = \sum_l \frac{2l+1}{4\pi} C_l P_l(\cos \theta), \quad (3.35)$$

where the addition theorem for spherical harmonics was used in an intermediate step. The coefficients C_l is the standard representation of the CMB anisotropy, and is essentially the *angular power spectrum*. One can thus fit cosmological models against the measured coefficients to constrain cosmological parameters and physical theories that have an effect on the anisotropies. An example of this TT angular power spectrum is shown in Fig. 3.11.

The main effects producing the anisotropies are

1. the Sachs–Wolfe (SW) effect,
2. the intrinsic anisotropy on the Last-Scattering Surface (LSS),
3. the Doppler shift effect, and,
4. the Integrated Sachs–Wolfe (ISW) effect.

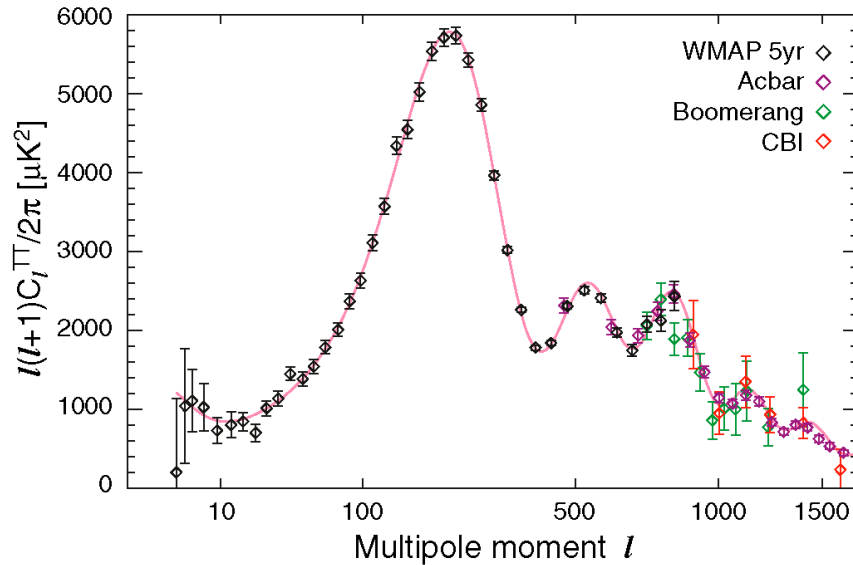


Figure 3.11: The CMB TT angular power spectrum as measured by $WMAP+ACBAR+Boomerang+CBI$. Reproduced from [Komatsu et al. \(2008\)](#).

The contributions of these effects to the angular power spectrum are shown in Fig. 3.12. The Sachs–Wolfe effect is due to perturbations in the gravitational potential at the LSS producing slightly red/blue-shifted photons. The intrinsic anisotropy is determined by the cosmological scenario (e.g. Λ CDM, adiabatic perturbations). The Doppler shift referred to is that occurring when the photons last Thomson-scatter off an electron. The Integrated Sachs–Wolfe effect is due to changes in the gravitational potential along the line of sight. On large scales (small l), particularly the two Sachs–Wolfe effects dominate, whereas on small scales the Doppler and intrinsic anisotropies dominate. In addition to these effects, the Universe will be very opaque after recombination, consisting largely of neutral hydrogen atoms. Photon absorption will therefore damp small-scale perturbations (see Fig. 3.12). This continues through to the reionization epoch, around $z \sim 10$, when quasar and star formation is thought to reionize the hydrogen, making the Universe effectively transparent to the photons. The effect is usually parameterized by the *reionization optical depth* τ , which is a measure of the probability of a photon to scatter on its way us.

For the case of a dark energy component, this will primarily affect the CMB anisotropies through a linear shift of the C_l 's in l -space measured by the CMB *peak-shift parameter* ([Bond et al., 1997](#); [Zaldarriaga et al., 1997](#); [Efstathiou & Bond, 1999](#); [Melchiorri et al., 2003b](#))

$$\mathcal{R}(z_{\text{dec}}) = \sqrt{\Omega_m} H_0 r(z_{\text{dec}}) \quad (3.36)$$

where $z_{\text{dec}} \approx 1090$ is the redshift of decoupling. It can be approxi-

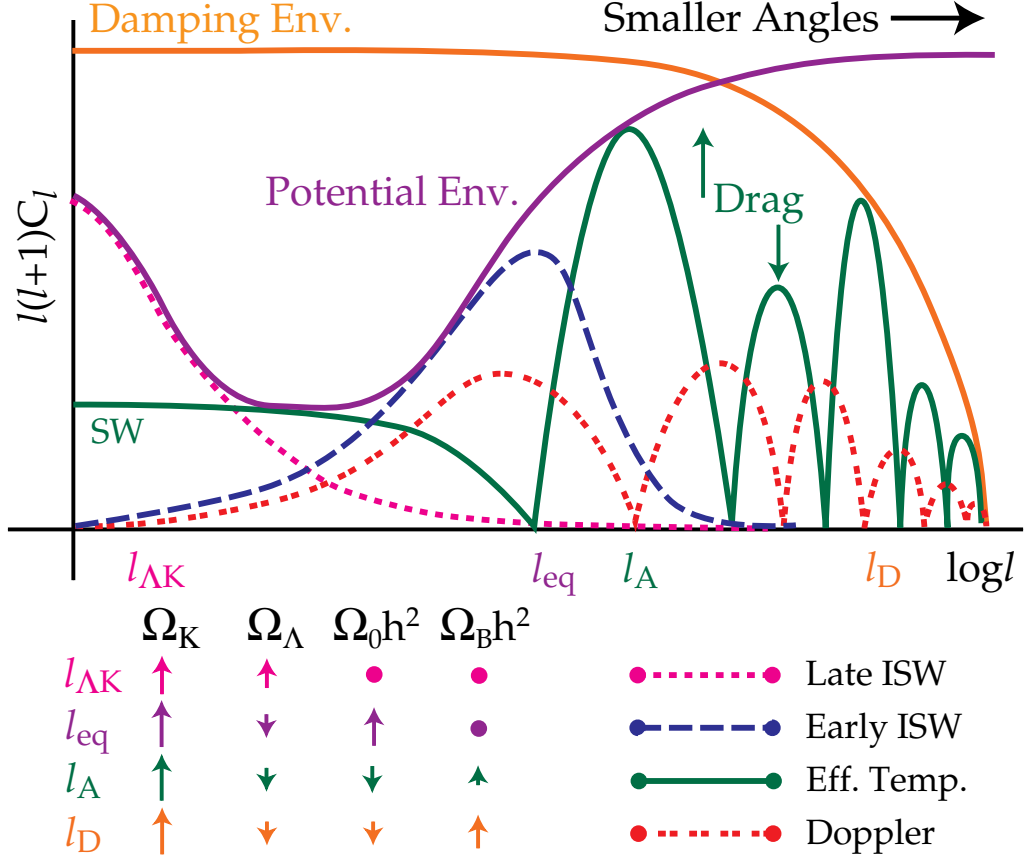


Figure 3.12: The contributions from the principal physical effects to the CMB TT angular power spectrum, for a scale-invariant, adiabatic perturbation model. At large scales, the Sachs–Wolfe (SW) and late-time Integrated Sachs–Wolfe (ISW) effect dominate. At smaller scales, intrinsic anisotropy (denoted ‘Eff. Temp.’ in the plot), and the Doppler effect, from baryon–photon acoustic oscillations close to the surface of last scattering dominate. At a window of intermediate scales, the early-time ISW dominates. The damping envelope shows the suppression of acoustic oscillations due to diffusion; the photons undergo Compton scattering, which has a finite mean-free-path set by the Compton wavelength – hence smaller-wavelength perturbations are damped. This damping continues through hydrogen ionization to the reionization era. The potential envelope shows the similar contribution from gravitational-potential effects alone. The peak structure is further modulated by the gravitational drag of baryons during recombination, affecting the acoustic oscillations, so that their heights differ (‘Eff. Temp.’ curve). The power spectrum encodes four characteristic length scales, $l_{\Lambda K}$, l_{eq} , l_A and l_D , which roughly correspond to the different physical effects described. These scales govern the fitting of cosmological parameters to the angular power spectrum, and an indication of the relative effects of single-parameter variations (increases) on the different scales is given. The parameter $\Omega_0 \equiv \Omega_m$. Reproduced from Hu (2008).

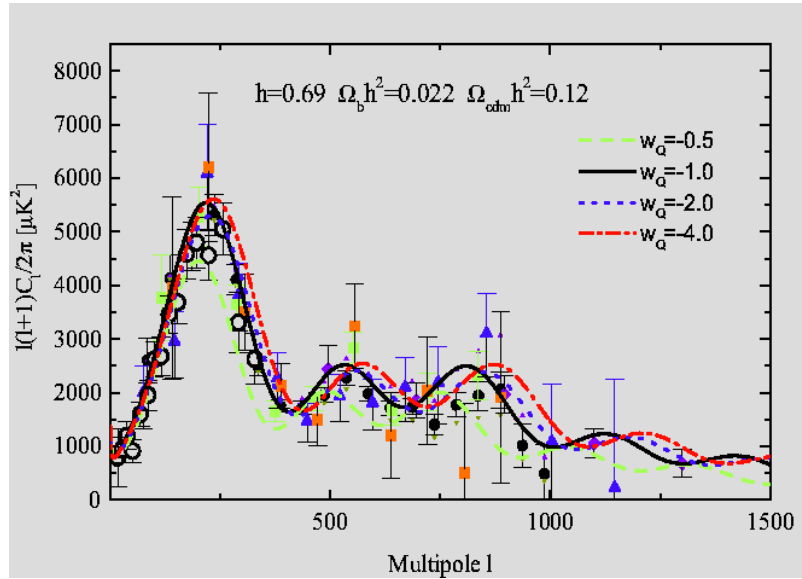


Figure 3.13: The CMB spectrum for a number of different values of w_{DE} (here called w_Q). The overall shift in l is clearly visible. Reproduced from [Melchiorri et al. \(2003b\)](#).

mated as ([Hu & Sugiyama, 1996](#))

$$z_{\text{dec}} = 1048 [1 + 0.00124(\Omega_b h^2)^{-0.738}] [1 + g_1(\Omega_m h^2)^{g_2}] , \quad (3.37)$$

where

$$g_1 = \frac{0.0783(\Omega_b h^2)^{-0.238}}{1 + 39.5(\Omega_b h^2)^{0.763}} , \quad (3.38)$$

$$g_2 = \frac{0.560}{1 + 21.1(\Omega_b h^2)^{1.81}} . \quad (3.39)$$

The expression for \mathcal{R} is proportional to the angular diameter distance $d_A(z_{\text{dec}})$, and the major effect induced by Ω_{DE} and w_{DE} is through its effect on this angular diameter distance to the surface of last scattering. The position of the first power spectrum peak is essentially a measure of this distance. Since the shift effect is proportional to l , that indicates we might be able to distinguish different w_{DE} by studying the small scale part of the spectrum (see [Fig. 3.13](#)). However, due to cosmological parameter degeneracies, curves for different values of w_{DE} can be made to coincide by varying other cosmological parameters.

Another distance measure is given by the *acoustic scale*

$$l_A \equiv \frac{\pi r(z_{\text{dec}})}{r_s(z_{\text{dec}})} , \quad (3.40)$$

where the sound horizon r_s is defined as in [Eq. \(3.27\)](#), but now evaluated at $z = z_{\text{dec}}$. This quantity can be thought of as encoding the spacing between peaks in the TT spectrum, in combination with the peak-shift parameter.

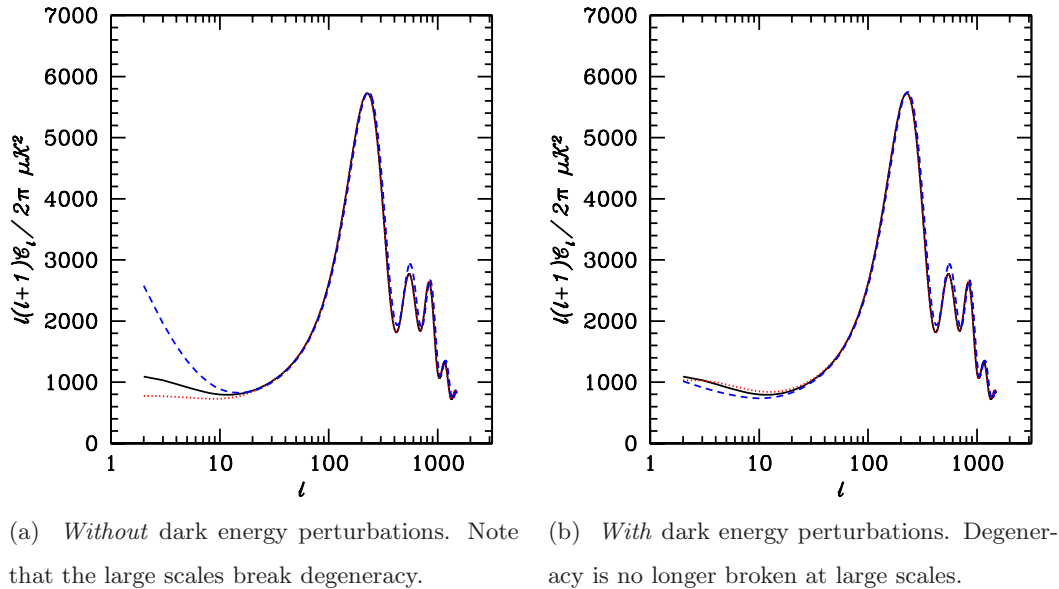


Figure 3.14: The CMB spectra for three different sets of parameters (including a constant w_{DE}) degenerate at small scales, with and without dark energy perturbations. Reproduced from [Weller & Lewis \(2003\)](#).

It has been shown that these distance measures capture most of the information in the CMB TT spectrum relevant for standard dark energy models (e.g. [Wang & Mukherjee, 2007](#); [Komatsu et al., 2008](#)). To test early-dark-energy models ([Wetterich, 2003a,b](#); [Caldwell et al., 2003](#); [Doran & Robbers, 2006](#)), it is also possible to go further without a fully-fledged CMB analysis, by modelling the peak spacings in more detail ([Doran & Lilley, 2002](#); [Corasaniti & Melchiorri, 2008](#)).

Turning to the large-scale part of the spectrum, dark energy will particularly have an effect on the Integrated Sachs–Wolfe effect. More precisely, dark energy will have perturbations in its energy–momentum tensor (unless it is a constant, $w_{\text{DE}} = -1$) which will affect the growth of perturbations and therefore the ISW effect (and also via the expansion itself). This must be taken into account when attempting to place constraints on dark energy models from large-scale CMB anisotropy measurements. The importance of this effect was studied by [Weller & Lewis \(2003\)](#). Assuming some constant equations of state $w_{\text{DE}} < -1/3$, they compared an unphysical analysis *without* dark energy perturbations to a proper analysis with perturbations. The unphysical analysis (Fig. 3.14a) shows a significant difference in large-scale anisotropies for different values of w_{DE} , but when perturbations are included the differences between different values of w_{DE} are very small (Fig. 3.14b). This can be a powerful probe of dark energy when correlated with large-scale structure surveys which map the gravitational potentials causing the ISW ef-

fect (Corasaniti et al., 2004; Pogosian et al., 2005).

In addition to the TT spectrum, important information is encoded in the TE , EE and BB spectra of the CMB, where E and B denote the E -mode and B -mode polarization components of the radiation. Particularly, they carry information about the reionization epoch, the adiabaticity of primordial perturbations, and perhaps the gravitational waves expected from inflation/Big Bang (Hu & White, 1997).

3.3.2 Number Counts (Clusters of Galaxies)

Perhaps the easiest way of studying the structure of the Universe is to simply count the number of objects of a particular type that we can observe, and then use this to draw conclusions about the statistical distribution of matter in the Universe. The most promising application of this type involves mapping of the distribution of galaxy clusters. Although we will focus on these, the following methodology is also applicable to other objects, such as quasars.

Supposing we consider objects described by a set of p observables $\mathbf{O} = \{O_1, O_2, \dots, O_p\}$, the differential number of such objects can be written

$$dN(z, \mathbf{O}) = n(z, \mathbf{O}) \frac{d^2V}{dzd\Omega} dz d^p\mathbf{O} d\Omega, \quad (3.41)$$

where $n(z, \mathbf{O})$ is the differential spatial-observable comoving number density, and

$$\frac{d^2V}{dzd\Omega} = H_0^{-1} \frac{r^2(z)}{E(z)} \quad (3.42)$$

is the differential comoving cosmic volume element per unit redshift and solid angle. Provided we have a way of theoretically predicting $n(z, \mathbf{O})$, we can use such data to test theory. Normally, the number counts are binned in some combination of redshift and \mathbf{O} . In each bin, the observed number is assumed Poisson distributed. Care has to be taken to consider possible correlations between observables.

Models of structure formation essentially predict the statistical distribution of objects of a particular mass, since this is what the size of the overdensity corresponds to. It is therefore natural to attempt to use this as the observable. However, since a dominant fraction of the matter in the Universe is ‘dark’, it is quite difficult to probe the total mass distribution of most objects. One therefore has to rely on proxy observables based on radiation emanating from some part of the object. As such, these type of probes are sensitive to uncertainty in selection and the relationship between proxy observable(s) and mass.

A common way of writing the number density in terms of mass and proxy observable is that the differential comoving number density of haloes in a mass interval dO about O at redshift z is

$$n(M, z) \frac{dM}{dO} dO = -F(\sigma) \frac{\rho_{m,0}}{M\sigma(M, z)} \frac{d\sigma(M, z)}{dM} \frac{dM}{dO} dO, \quad (3.43)$$

where $\sigma(M, z)$ is the dispersion of the density field at some comoving scale $R = (3M/4\pi\rho_{m,0})^{1/3}$ and redshift z , and $\rho_{m,0}$ is the matter density at the present time. Via $\sigma(M, z)$, from Eq. (3.21), we can probe the growth suppression factor and the primordial density perturbations. The expression clearly assumes that a relationship $M(O, z)$ is given. The function $F(\sigma)$ describes the distribution of gravitationally collapsed objects of a particular size, encoded by σ . It has to be computed numerically through N -body simulation for the gravitational theory of choice, e.g. General Relativity. The current standard approximation (within GR) is

$$F_J(\sigma) = 0.315 \exp[-|\ln \sigma^{-1} + 0.61|^{3.8}], \quad (3.44)$$

which has been shown by [Jenkins et al. \(2001\)](#) to be a good fit (accurate to better than 20 per cent) to the mass functions recovered from various large N -body simulations, in the regime $-1.2 \leq \ln \sigma^{-1} \leq 1.05$. Here, the halo mass is defined at a mean overdensity of 180 with respect to the background matter density, independently of the cosmological parameters assumed, or equivalently to a mean overdensity of $180\Omega_m(z)$ with respect to the critical density. This result has been confirmed and refined by [Evrard et al. \(2002\)](#); [Hu & Kravtsov \(2003\)](#); [Klypin et al. \(2003\)](#); [Linder & Jenkins \(2003\)](#); [Reed et al. \(2003\)](#); [Lokas et al. \(2004\)](#); [Warren et al. \(2006\)](#); [Reed et al. \(2007\)](#).

Galaxy clusters are the largest virialized objects to have formed so far in the Universe. Their linear size is therefore around $10h^{-1}$ Mpc (see Sect. 2.3), and they have a mass on the order of 10^{14} – $10^{15}M_\odot$. They consist of tens to thousands of galaxies, hot (10^7 – 10^8 K) electron gas which emits X-rays, and a large dark matter core. The abundance of galaxy clusters as a function of mass and redshift can give a powerful constraint on cosmological models. Specifically, data on the evolution of the number density of galaxy clusters with redshift has been used to obtain direct estimates for both σ_8 , the dispersion of the mass field smoothed on a scale of $8h^{-1}$ Mpc, and on Ω_m , the present mean mass density of the Universe ([Frenk et al., 1990](#); [Oukbir & Blanchard, 1992](#); [Viana & Liddle, 1996](#); [Oukbir & Blanchard, 1997](#); [Henry, 1997](#); [Bahcall et al., 1997](#); [Eke et al., 1998](#); [Reichart et al., 1999](#); [Donahue & Voit, 1999](#); [Viana & Liddle, 1999](#); [Blanchard et al., 2000](#); [Henry, 2000](#); [Borgani et al., 2001](#); [Refregier et al., 2002](#); [Henry, 2004](#); [Gladders et al.,](#)

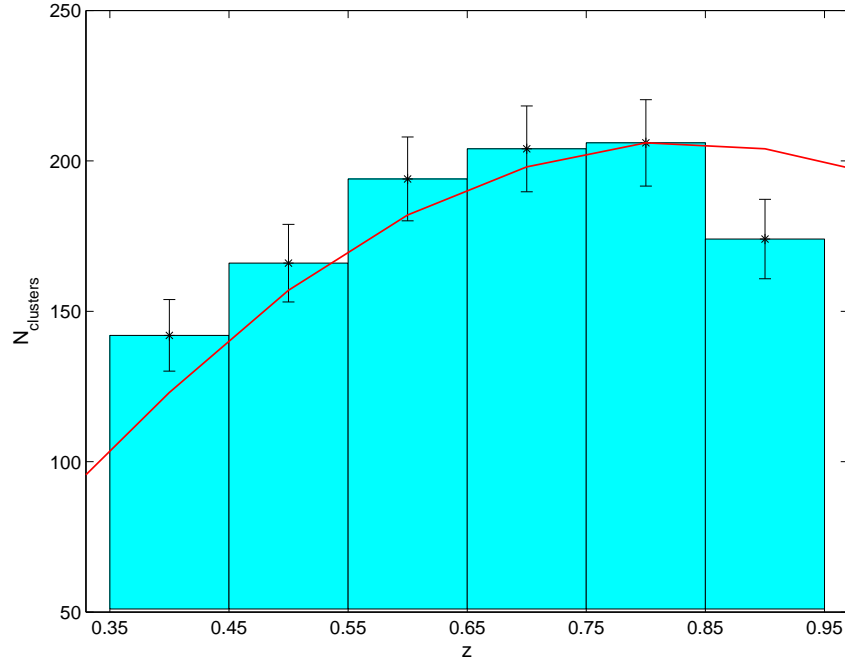
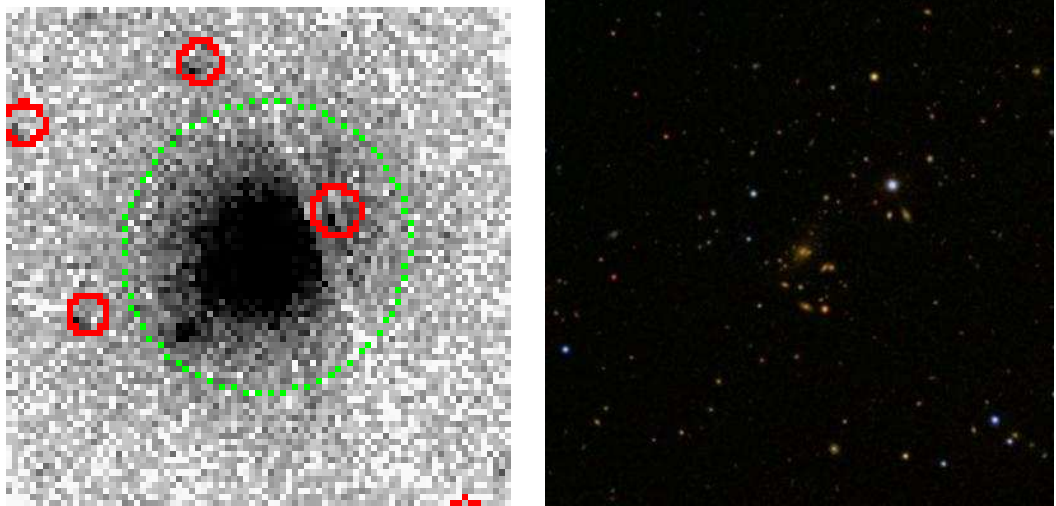


Figure 3.15: The redshift distribution of galaxy clusters found in the Red-Sequence Cluster Survey (RCS-1). Reproduced from [Gladders et al. \(2007\)](#).

[2007](#); [Roza et al., 2007a](#)). An example of the redshift distribution of galaxy clusters is shown in Fig. 3.15. Furthermore, cluster data could be used to constrain the present energy density of a dark energy component, Ω_{DE} , and its equation of state ([Wang & Steinhardt, 1998](#); [Haiman et al., 2001](#); [Huterer & Turner, 2001](#); [Levine et al., 2002](#); [Weller et al., 2002](#); [Battye & Weller, 2003](#); [Hu, 2003](#); [Majumdar & Mohr, 2003, 2004](#); [Wang et al., 2004a](#); [Lima & Hu, 2005](#); [Mantz et al., 2008](#)), or more simply the present vacuum energy density associated with a cosmological constant, $\Omega_{\Lambda} \equiv \Lambda/3H_0^2$ ([Holder et al., 2001](#)).

Others have suggested using galaxy clusters to constrain particle physics beyond the Standard Model of Particle Physics (e.g. [Wang et al., 2005](#); [Erlich et al., 2008](#)), or modified-gravity models where it has been shown that e.g. the Dvali–Gabadadze–Porrati (DGP) modified-gravity model should be testable in coming surveys ([Tang et al., 2006](#); [Schäfer & Koyama, 2008](#)). An alternative method to abundance evolution using X-ray galaxy clusters to constrain cosmology, is based on the gas mass fraction (e.g. [Allen et al., 2002](#); [Ettori et al., 2003](#); [Rapetti et al., 2005](#); [Allen et al., 2008](#); [Rapetti et al., 2008](#)).

Galaxy cluster measurements are complementary to other cosmological constraints derived from the Cosmic Microwave Background (CMB) and distant Type Ia Supernovae observations, and as explained in Sect. 3.1.4 thus help break degeneracies among the various cosmological parameters ([Bahcall et al., 1999](#); [Haiman et al., 2001](#); [Huterer & Turner, 2001](#); [Levine et al., 2002](#); [Battye & Weller, 2003](#); [Melchiorri et al., 2003a](#); [Wang et al.,](#)



(a) X-ray emission observed by *XMM-Newton*. The rings are source markers from the automated XCS analysis pipeline. A very bright central X-ray source is visible. (b) Optical emission observed by the Sloan Digital Sky Survey. An overdensity of galaxies in the centre can be clearly identified.

Figure 3.16: The galaxy cluster XMMXCS J092018.9+370618.0 in X-ray and optical.

2004a).

The cluster X-ray temperature is one of the best proxy observables in lieu of mass; it is a better estimator of the cluster mass than the cluster X-ray luminosity but more difficult to determine (e.g. Balogh et al., 2006; Zhang et al., 2006), and galaxy clusters are also most unambiguously identified in X-ray images. This makes X-ray-based galaxy cluster surveys those with the most accurately determined selection function. An example of a galaxy cluster detected through X-ray emission in the *XMM* Cluster Survey (XCS; Romer et al., 2001), is shown in Fig. 3.16, along with its optical image as well.

In Chapter 6, we forecast expected parameter constraints from the *XMM* Cluster Survey, using the methodology described above.

3.4 Data Analysis

3.4.1 Frequentists and Bayesians

Over the past decade or so, cosmology has entered the era of precision tests, which makes it increasingly important to have robust tools for testing, discarding and selecting favoured models. Traditionally, this has been done following a frequentist approach involving tests such as the reduced χ^2 and the associated P -test. This has been largely sufficient given the limited resolution of experiments and complexity of cosmological models tested. The

frequentist approach is however inherently biased as results implicitly depend on the intentions of the observer and even unobserved data (known as the ‘optional stopping problem’, see [Gregory, 2005](#)). The least one would like to ask of a robust method is to have all biases explicitly specified and the results otherwise only dependent on the observed data, and therefore some people argue that the frequentist methodology is unsatisfactory.

A consistent solution to these issues can be found in the Bayesian approach to parameter estimation and model selection. We describe these methods in the following Sections. Proponents of the two approaches have tended to take rather passionate stances in relation to each other, with the Bayesian methodology currently experiencing a revival. A common criticism of the Bayesian approach is that results depend on the priors you assign, which are subjective. Hence the results are subjective and in some sense depends on the observer, and are therefore not ‘scientific’. In this author’s opinion, one reason for the controversies stem from a difference in (or lack of) philosophy of science. A frequentist approach would appear to implicitly assume that an infinite/sufficiently large number of repetitions of a well-defined and distinct experiment for a typical observer is in principle possible. However, this carries assumptions about the nature of reality and our place in it. In the case where ‘infinite data’ are in principle available, we do not need to worry about prior assumptions (e.g. ‘optional stopping problem’), as the data will eventually dominate. In cosmology, situations where such assumptions do not hold up are commonplace, and frequentist methods are therefore unsatisfactory. We therefore argue that subjectivity is not a flaw of the Bayesian method, but rather a feature of Nature which the method forces us to take into account and make explicit. The interpretation of observations, indeed the concept of observation in the first place, is intrinsically dependent on our assumptions about Nature. As explained above, the frequentist approach involves similar assumptions implicitly. This is analogous to not specifying the selection function in an experiment (i.e. assuming statistical completeness).

From a more formal point of view, it has been shown that Bayesian statistics is the unique generalization of Boolean logic in the presence of uncertainty, which thus provides a strong argument in favour of it being the appropriate framework for statistical scientific reasoning ([Jaynes, 2003](#)).

For highly phenomenological models, it may be very difficult to assign reasonable priors. This only reflects the high state of ignorance such a model is a representation of.

An excellent introduction to Bayesian statistics in its own right, and as applied to cosmology, is given in [Trotta \(2008\)](#).

3.4.2 Bayesian Parameter Estimation

Assuming a prior probability distribution $\Pi(\Theta)$, the posterior probability of the parameters Θ , given the data used, is given according to Bayes' theorem (Bayes, 1763) by

$$P(\Theta|\text{data}) \equiv \frac{1}{\mathcal{Z}} \mathcal{L}(\text{data}|\Theta)\Pi(\Theta) \quad (3.45)$$

where \mathcal{L} is the probability of the data given the parameter values Θ , also known as the *likelihood* of the data. Specifying the likelihood requires having a model for the measurement errors. The likelihood is often represented in terms of the χ^2 function, which in reference to the case of Gaussian measurement errors,

$$\mathcal{L} \propto \exp \left[- \sum_{i=1}^N \frac{(y_i - y(x_i; \Theta))^2}{2\sigma_i^2} \right] = \exp [-\chi^2(\Theta; \text{data})/2] , \quad (3.46)$$

is given by $\chi^2 \equiv -2 \ln \mathcal{L}$. The quantity $\mathcal{Z} = \int \mathcal{L}(\text{data}|\Theta)\Pi(\Theta)d\Theta$ is a normalization constant, called the *Bayesian evidence*. It is irrelevant for parameter estimation, but highly relevant for model selection as discussed below.

We thus see that Bayesian parameter estimation requires the specification of a theoretical model for predicting the observed quantities ($y(x_i; \Theta)$), a prior probability distribution for the model parameters ($\Pi(\Theta)$), and a model for the measurement errors ($\mathcal{L}(\text{data}|y)$).

3.4.3 Bayesian Model Selection

Any model can be extended with new components, implying new parameters. Such a model will always fit the data at least as well as the original model does, however with parameters becoming less and less constrained as the number of parameters increases. In addition to a determination of the best-fitting parameters within a given model (parameter estimation), one therefore needs to compare the different models in order to determine which *model* is the preferred fit to the data. Model selection statistics address this issue (Jeffreys, 1961; Kass & Raftery, 1995; Mackay, 2003; Liddle, 2004; Liddle et al., 2006a; Mukherjee et al., 2006a; Trotta, 2007). These set up a tension between the number of model parameters and the goodness of fit. In the context of Bayesian inference the best such statistic is the *Bayesian evidence* (Jeffreys, 1961; Mackay, 2003),

$$\mathcal{Z} = \int \mathcal{L}(\text{data}|\Theta)\Pi(\Theta)d\Theta . \quad (3.47)$$

This is the average likelihood, weighted by the prior beliefs. It is a measure of the probability of the model, given the data, taking into account what the prior beliefs about

$\ln(B_{12})$	Evidence against Model 2
0 – 1	Worth only a bare mention
1 – 2.5	Positive evidence
2.5 – 5	Strong evidence
> 5	Decisive evidence

Table 3.1: The Jeffreys evidence scale.

parameter values are. It is only meaningful in terms of evidence *relative* to some other model, and therefore one normally considers the *Bayes factor*

$$B_{12} \equiv \frac{\mathcal{Z}_1}{\mathcal{Z}_2} = \frac{P(D|M_1)}{P(D|M_2)} = \frac{P(M_1|D) \Pi(M_2)}{P(M_2|D) \Pi(M_1)}. \quad (3.48)$$

The Bayes factor measures the relative probability of two models (M_1 and M_2), given the data and prior assumptions, for the case that the prior model probability $\Pi(M_1) = \Pi(M_2)$. More generally, it is simply the relative power of Model 1 (M_1) over Model 2 (M_2) in explaining the observed data D given the prior model probabilities $\Pi(M_1)$ and $\Pi(M_2)$. A standard reference scale for the strength of evidence given by Bayes factors is the Jeffreys scale (Jeffreys, 1961), shown in Table 3.1.

To calculate the full Bayesian evidence is typically a supercomputer class problem. Recent advances in computational routines (Mukherjee et al., 2006b; Feroz & Hobson, 2008) have however made evidence calculations increasingly tractable.

As an alternative to an exact numerical computation, different approximations can be used. A subset of such approximations are given by *information criteria*. Examples are the Akaike Information Criterion (AIC), the Deviance Information Criterion (DIC), and the Bayesian Information Criterion (BIC). See Liddle, 2007 for a review of information criteria. Arguably, the most popular criterion is the BIC. This is an approximation to the evidence in terms of the maximum likelihood, which is reasonable in the limit of unimodal, narrow, Gaussian distributions. The BIC is given by

$$\text{BIC} = -2 \ln \mathcal{L}_{\max} + D \ln N, \quad (3.49)$$

where \mathcal{L}_{\max} is the likelihood of the best-fitting parameters for that model, D the number of model parameters, and N the number of data points used in the fit. Models are ranked with the lowest value of the BIC indicating the preferred model. A difference of two for the BIC is regarded as positive evidence, and of six or more as strong evidence, against the model with the larger value (Jeffreys, 1961). The use of the BIC in cosmology has

been heavily criticized by [Efstathiou \(2008\)](#), arguing that it is unable to provide reliable model selection in most cases of interest/relevance.

3.4.4 The Monte Carlo Markov Chain Method

To estimate parameters we wish to find $P(\Theta|\text{data})$ explicitly as a function of Θ . This is in general non-trivial, and the standard approach is to explore the parameter space in some way and keep a histogram characterizing $P(\Theta|\text{data})$. We choose to explore the parameter space using a Monte Carlo Markov Chain (MCMC) approach ([Gilks et al., 1996](#); [Lewis & Bridle, 2002](#); [Verde et al., 2003](#); [Dunkley et al., 2005](#)). MCMC calculations are generally preferable over grid methods as they scale approximately linearly with the dimension of the problem, rather than exponentially.

The MCMC method provides a random sequence of samples, which are distributed according to the posterior probability distribution, $P(\Theta|\text{data})$. The sequence of samples is generated using the Metropolis–Hastings algorithm ([Gilks et al., 1996](#)), of which the following is the most common implementation:

- given a starting point Θ_i , choose a new point Θ_{i+1} according to a trial distribution $f(\Theta_{i+1}|\Theta_i)$
- accept the new point with probability $\min\{P(\Theta_{i+1}|\text{data})/P(\Theta_i|\text{data}), 1\}$
- if the new point is accepted, update the chain position, otherwise remain at the same location, then repeat

Provided that the trial distribution is symmetric, $f(\Theta_{i+1}|\Theta_i) = f(\Theta_i|\Theta_{i+1})$, the resulting Markov Chain will converge to the posterior probability distribution ([Gilks et al., 1996](#)). Most commonly this is realized through a Gaussian trial distribution. The choice of trial distribution is key to achieving an efficient computation, i.e. for the chain to converge to the posterior with a minimal number of evaluations of the probability function. There is a publicly available computer program for cosmological parameter estimation based on MCMC, called COSMOMC ([Lewis & Bridle, 2002](#)), which includes automatic optimization of the trial distribution. For the purposes of the work in this thesis, a custom MCMC code was developed. It constitutes an example of standard methods for MCMC optimization and convergence testing.

Our MCMC algorithm is the following:

1. The starting points for the Markov chains are chosen to be close to the expected high-likelihood region with some random spread, checking that they satisfy the priors.

2. Starting with an initial best guess for the covariance matrix of the underlying posterior distribution, we optimize the step sizes (covariance matrix) of the Gaussian trial distribution with the iteration rule (Gilks et al., 1996)

$$\mathbf{C}_i^T = (2.4^2/D)\mathbf{C}_{i-1}, \quad (3.50)$$

where \mathbf{C}_i^T is the i^{th} estimate of the covariance matrix of the trial distribution, D is the number of parameters and \mathbf{C}_{i-1} the covariance matrix of the $(i-1)^{\text{th}}$ chain produced (with \mathbf{C}_0 our initial best guess). We use chains of typically a few thousand elements for the optimization process, and continue updating the trial distribution until there is no significant increase in the sampling efficiency (assessed by comparing the eigenvalues of the covariance matrices). Between each iteration, the parameter space is rotated to the eigenspace of the new covariance matrix, to maximise the efficiency in exploring the shape of the likelihood distribution.

3. The full production run is started. A set of three or more chains is generated, and only these are used for the final analysis. We generate well separated starting points as before for each of the chains. The chains are tested for convergence and mixing using the Gelman–Rubin test (Gelman & Rubin, 1992; Gilks et al., 1996), which compares the variances within a chain to the variances between chains, which in the asymptotic limit should give a Gelman–Rubin ratio $R = 1$. We require $R < 1.05$ for each parameter. A consistently high and non-convergent Gelman–Rubin ratio is indicative of a very loosely constrained parameter.

In the above, all calculations of covariances and means are done by first dropping an initial burn-in section from the chain. We define the burn-in section following Tegmark et al. (2004) as the elements in the chain from the beginning up to the first element to have a likelihood value above the median likelihood value of the whole chain. Chains can be analyzed and visualized with e.g. GETDIST, provided with COSMOMC (Lewis & Bridle, 2002). We have employed a version of this program, slightly modified by us to suit our purposes.

An illustration of the MCMC process is shown in Fig. 3.17, capturing the convergence from prior to posterior as iterations proceed.

3.5 Current Status

We present in this Section the best current measurements of cosmological parameters from Type Ia supernovae, the cosmic microwave background, and large-scale structure. We will

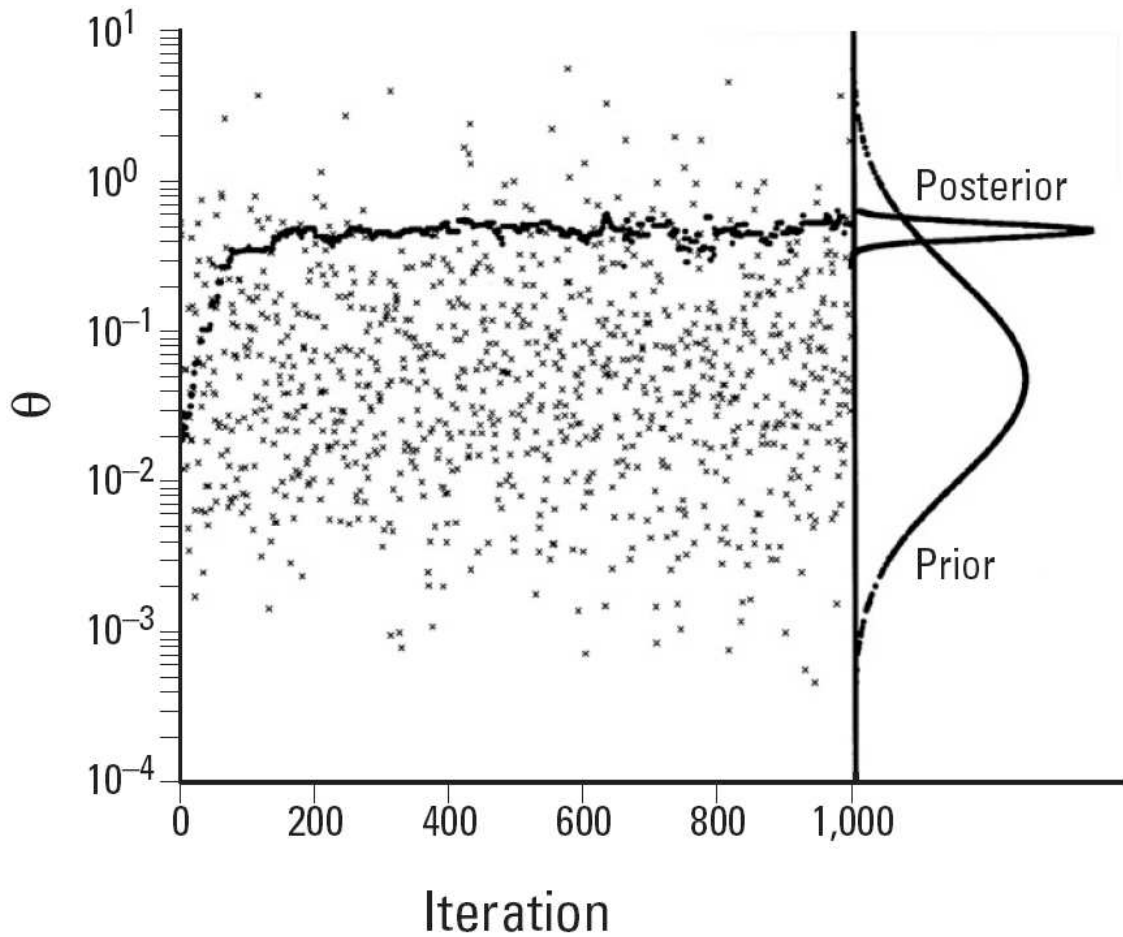


Figure 3.17: Monte Carlo Markov Chain in action. A Markov chain sample from the prior distribution (crosses), and the posterior distribution (circles) as a function of the number of iteration steps, for a generic model parameter θ and arbitrary data. The burn-in convergence to the posterior distribution can be clearly seen. The prior and posterior probability distributions resulting are shown on the right-hand vertical axis. Reproduced from [Bois \(2000\)](#).

consider four different models:

Flat Λ CDM The baseline model with a cosmological constant but no curvature.

Flat w CDM As above but where a constant equation of state of dark energy w_{DE} is also fitted to the data.

Non-flat Λ CDM Like flat Λ CDM, but where Ω_k is also allowed to be non-zero and fitted to the data.

Non-flat w CDM Like flat w CDM, but where Ω_k is also allowed to be non-zero and fitted to the data.

In all cases, adiabatic primordial scalar perturbations with a power-law spectrum are assumed.

3.5.1 Type Ia Supernovae

The union of essentially all so-far available SNIa data from various experiments have recently been self-consistently analyzed by the Supernova Cosmology Project team, forming the Union sample (Kowalski et al., 2008).

For the case of a flat universe with a cosmological constant, this data on its own constrains

$$\Omega_m = 0.287^{+0.029+0.039}_{-0.027-0.036}, \quad (3.51)$$

where the second uncertainty is systematic (Kowalski et al., 2008).

For the case of a non-flat universe or a free-to-vary dark energy equation of state $w_{\text{DE}} \neq -1$, supernova data on its own cannot constrain both Ω_m and Ω_Λ (or w_{DE}) well. The resulting two-dimensional parameter constraints are shown in Fig. 3.18.

3.5.2 Cosmic Microwave Background

The latest results from CMB measurements are shown in Table 3.2 (p. 57), for the two flat models we consider. Although some of these constraints are very narrow, dropping the flatness assumption leads to a significantly increased uncertainty, as can be seen in Fig. 3.19 (p. 56).

3.5.3 Large-Scale Structure

The most recent measurements based on the large-scale structure of the Universe are the 2dF+SDSS measurement of the shape and baryon acoustic oscillation peak of the

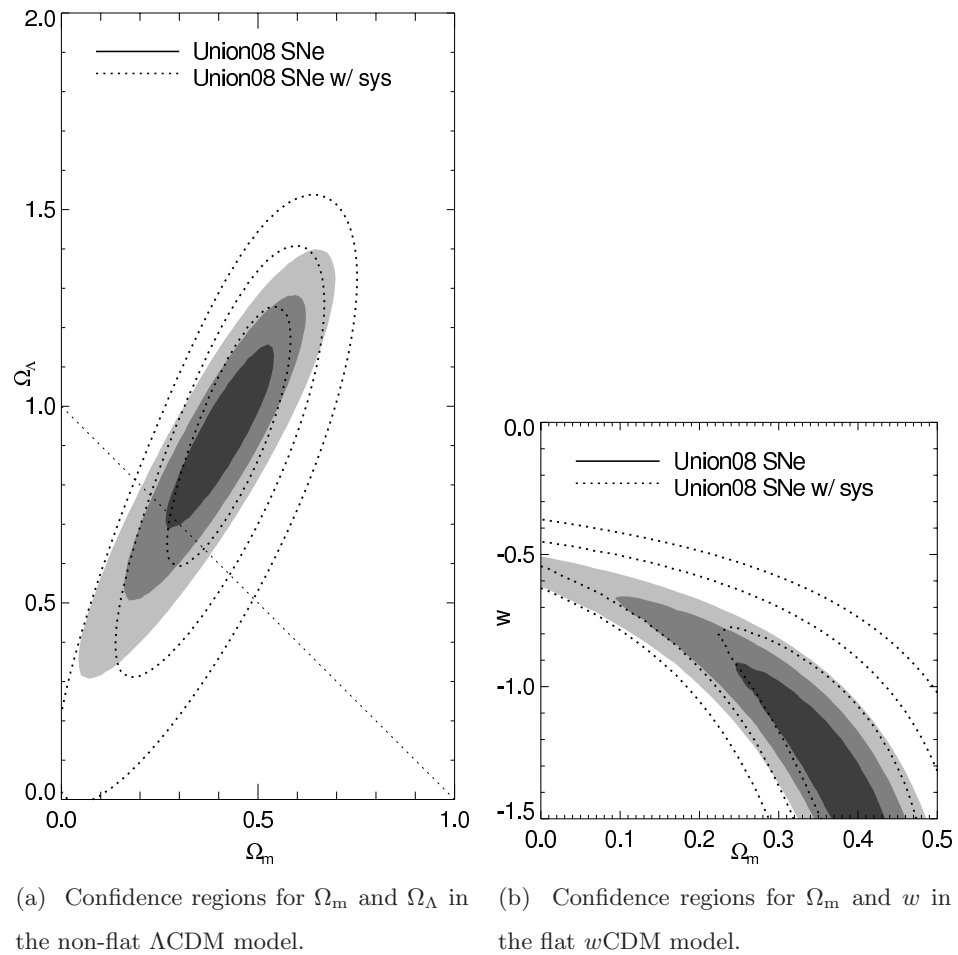


Figure 3.18: Most recent confidence regions for non-flat Λ CDM and flat w CDM models, based on essentially all currently available SNIa data. The contours represent 68%, 95% and 99% confidence levels. The dotted contours include systematic errors, whereas the shaded do not. Reproduced from [Kowalski et al. \(2008\)](#).

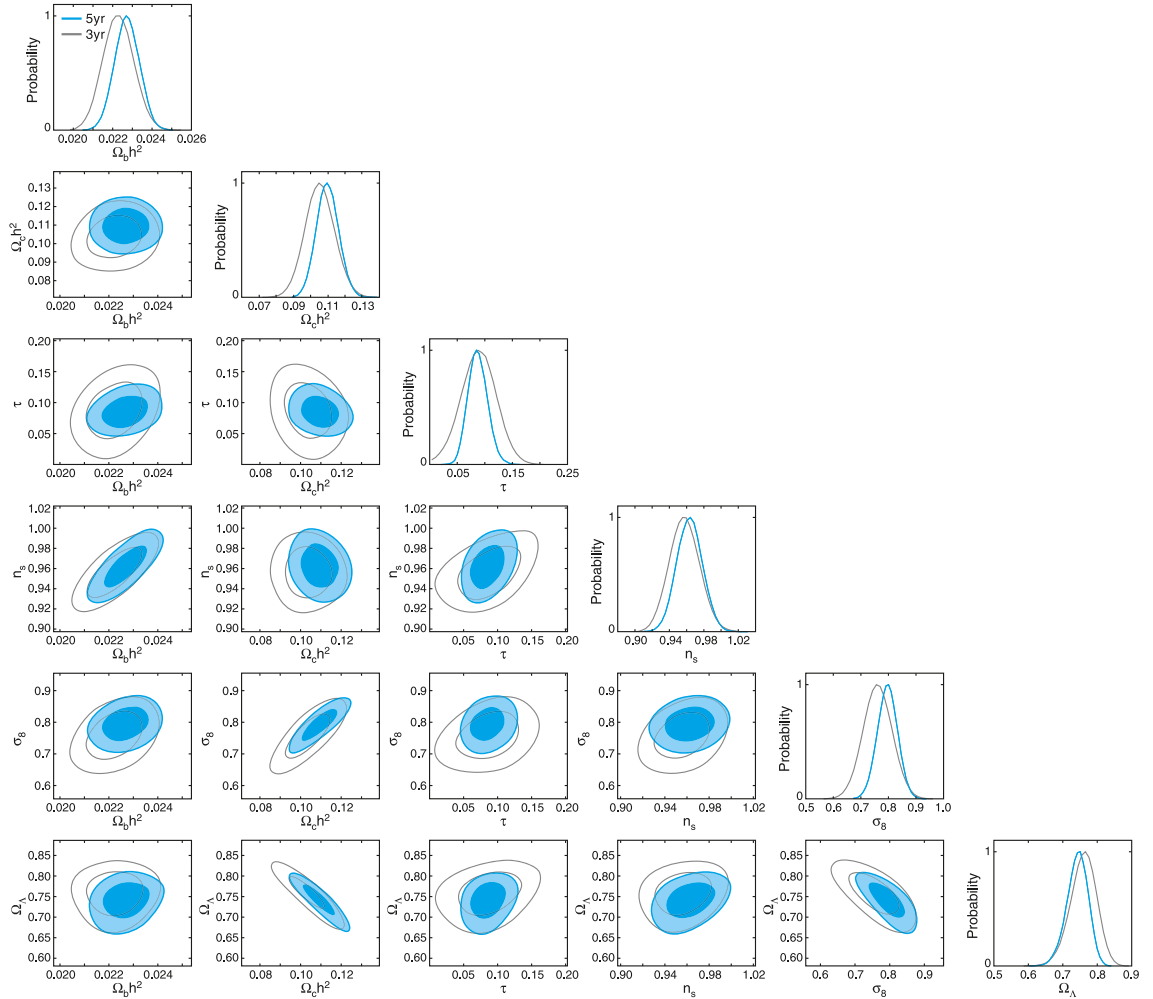


Figure 3.19: Current best parameter constraints from CMB data (*WMAP* 5-year), and comparison to *WMAP* 3-year results, for the non-flat Λ CDM model. The contours represent 68% and 95% confidence levels. The parameter $\Omega_c = \Omega_m - \Omega_b$. Reproduced from [Dunkley et al. \(2008\)](#).

Model	Flat Λ CDM	Flat w CDM
h	$0.719^{+0.026}_{-0.027}$	$0.74^{+0.15}_{-0.14}$
Ω_m	0.258 ± 0.030	$0.27^{+0.11}_{-0.10}$
Ω_b	0.0441 ± 0.0030	0.046 ± 0.018
w	-1	$-1.06^{+0.41}_{-0.42}$
n_s	$0.963^{+0.014}_{-0.015}$	0.963 ± 0.016
σ_8	0.796 ± 0.036	0.81 ± 0.14
τ	0.086 ± 0.017	$0.086^{+0.017}_{-0.016}$

Table 3.2: Current best measurements from the CMB alone, of the most common cosmological parameters (for flat models). Only the WMAP5 data (Komatsu et al., 2008) was used, however adding additional CMB data from Boomerang+CBI+VSA+ACBAR only negligibly affects the results.

matter power spectrum (Tegmark et al., 2004; Eisenstein et al., 2005; Cole et al., 2005; Percival et al., 2007), the *Chandra* catalogue of galaxy clusters, analyzed with the gas mass fraction method (Allen et al., 2008), and cluster abundance data in catalogues from the Red-Sequence Cluster Survey (RCS; Gladders et al., 2007) and the SDSS (Roza et al., 2007a). The cluster X-ray luminosity function has also been employed in Mantz et al. (2008), using BCS, REFLEX and MACS data.

The results from the 2dF+SDSS measurement on dark energy is shown in Fig. 3.20. One of the main strengths with BAO data so far is the near-orthogonality to those of other probes (see further in Sect. 3.5.4). For structure parameters, the SDSS finds $\Omega_m h = 0.213 \pm 0.023$ and $\sigma_8 = 0.89 \pm 0.02$ assuming $h = 0.72$ and $\Omega_b/\Omega_m = 0.17$ in a flat, scale-invariant Λ CDM model (Tegmark et al., 2004). The 2dF survey finds that $\Omega_m h = 0.168 \pm 0.016$ with the same assumptions, but instead constrains $\Omega_b/\Omega_m = 0.185 \pm 0.046$ (Cole et al., 2005). These estimates appear inconsistent, and it may be that this is due to inaccurate modelling of galaxy bias (Percival et al., 2007).

Allen et al. (2008) find that, with what they call ‘standard’ priors on Ω_b and h , the *Chandra* data gives constraints of $\Omega_m = 0.26 \pm 0.06$, $\Omega_\Lambda = 0.86 \pm 0.19$ for a non-flat Λ CDM model. For a flat w CDM model, the results are $\Omega_m = 0.28 \pm 0.06$, $w_{DE} = -1.14^{+0.27}_{-0.35}$. This includes marginalization over a number of nuisance parameters describing cluster physics. The two-dimensional probability distributions are shown in Fig. 3.21.

The RCS (Gladders et al., 2007) finds that $\Omega_m = 0.31^{+0.11}_{-0.10}$ and $\sigma_8 = 0.67^{+0.18}_{-0.13}$ for a flat Λ CDM model, including marginalization over nuisance parameters, also with restrictive

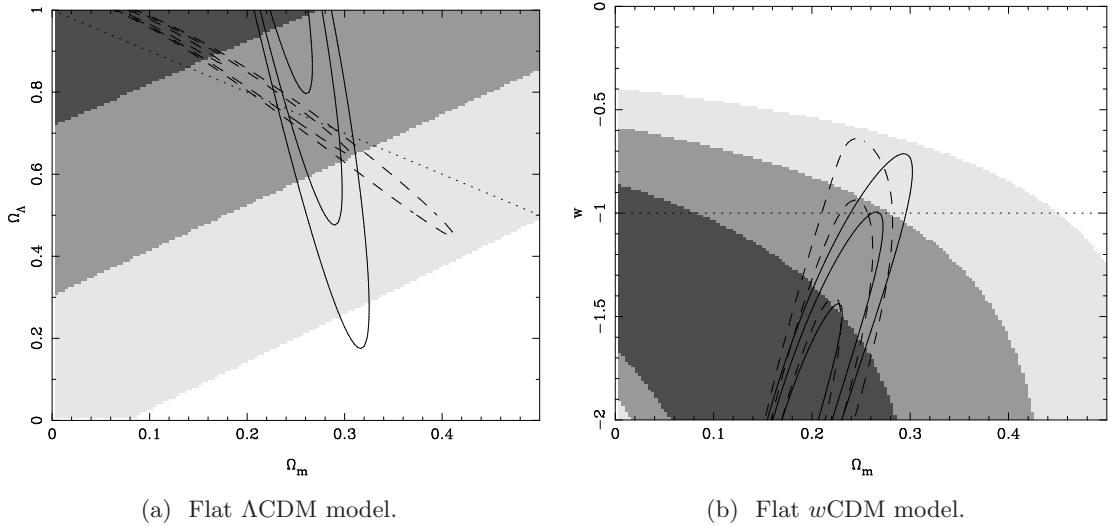


Figure 3.20: Current best parameter constraints from BAO data (2dF+SDSS). The contours represent 68%, 95% and 99% confidence levels. The shaded contours are based on measuring d_V^{2dF}/d_V^{SDSS} , whereas the solid contours use r_s^{BAO}/d_V from both catalogues. The dashed contours also include the *WMAP* 3-year peak shift measurement. Reproduced from [Percival et al. \(2007\)](#).

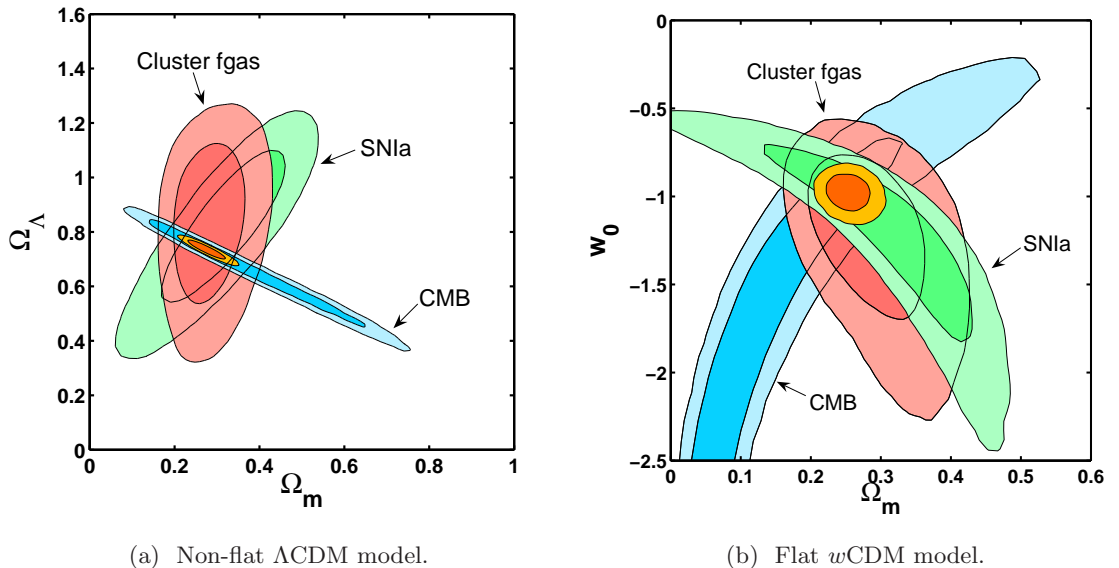


Figure 3.21: Parameter constraints from gas mass fraction analysis of *Chandra* data, denoted ‘Cluster fgas’ in the plots (red contours). Constraints from CMB and supernova data are also shown (blue and green), as well as the combination of those with the ‘Cluster fgas’ constraints (orange/yellow). The contours represent 68% and 95% confidence levels. Reproduced from [Allen et al. \(2008\)](#).

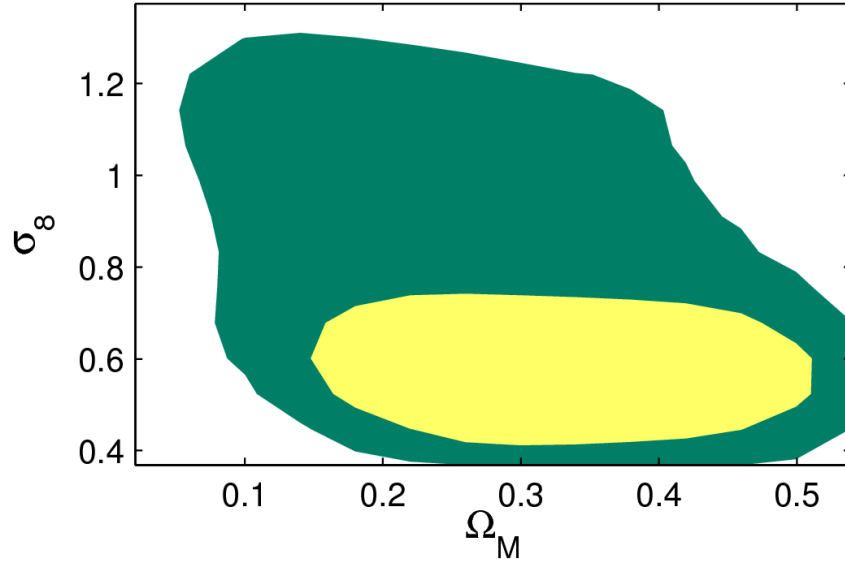


Figure 3.22: Parameter constraints on σ_8 and Ω_m in a flat Λ CDM model, from cluster abundance data in the Red-Sequence Cluster Survey (RCS). The contours represent 68% and 95% confidence levels. Reproduced from [Gladders et al. \(2007\)](#).

priors on h and Ω_b . The two-dimensional probability distribution is shown in Fig. 3.22.

From the SDSS, [Rozo et al. \(2007a\)](#) find $\sigma_8 = 0.92 \pm 0.10$ for the same model, but employ very restrictive CMB and supernova priors on Ω_m and h as well.

Employing the X-ray luminosity function, [Mantz et al. \(2008\)](#) find $\Omega_m = 0.28^{+0.11}_{-0.07}$, $\sigma_8 = 0.78^{+0.11}_{-0.13}$ for the flat Λ CDM model, and $\Omega_m = 0.24^{+0.15}_{-0.07}$, $\sigma_8 = 0.85^{+0.13}_{-0.20}$, $w_{DE} = -1.4^{+0.4}_{-0.7}$ for the flat w CDM model. Again, marginalization over a number of nuisance parameters is included.

Large-scale structure probes are of significant importance as degeneracy breakers, and have great potential to also provide high constraining power in their own right. A limiting factor so far is systematic and selection effects, and some hints of discrepancy between the above values for σ_8 and Ω_m , and those from the CMB, could be due to such reasons.

3.5.4 Joint Constraints

The best constraints on cosmological parameters are currently found from the combination of supernova, cosmic microwave background and baryon acoustic oscillation data. The basic results are presented in Table 3.3, which is based on the Union supernova sample ([Kowalski et al., 2008](#)); the ‘SNALL’ combination of the ‘gold’ [Riess et al. \(2004\)](#), SNLS [Astier et al. \(2006\)](#), and ESSENCE [Wood–Vasey et al. \(2007\)](#) supernova data; the ‘WMAP5’ WMAP 5-year CMB data ([Komatsu et al., 2008](#)); the ‘SDSSBAO’ SDSS-LRG

Model	Flat Λ CDM	Flat w CDM		Non-flat Λ CDM		Non-flat w CDM	
Data set	A	B	C	B	C	B	C
h	0.705 ± 0.013	0.697 ± 0.014	–	0.688 ± 0.020	–	$0.687^{+0.019}_{-0.020}$	–
Ω_m	0.274 ± 0.013	0.278 ± 0.015	0.274 ± 0.016	$0.282^{+0.015}_{-0.016}$	$0.285^{+0.020}_{-0.019}$	$0.281^{+0.016}_{-0.015}$	0.285 ± 0.020
Ω_b	0.0456 ± 0.0015	0.0467 ± 0.0018	–	0.0480 ± 0.0027	–	$0.481^{+0.0027}_{-0.0026}$	–
Ω_Λ	$1 - \Omega_m$	$1 - \Omega_m$	$1 - \Omega_m$	0.723 ± 0.015	0.724 ± 0.022	$0.724^{+0.015}_{-0.016}$	0.725 ± 0.022
w	-1	$-0.972^{+0.061}_{-0.060}$	$-0.969^{+0.059}_{-0.063}$	-1	-1	$-0.984^{+0.065}_{-0.064}$	$-1.001^{+0.069}_{-0.073}$
n_s	0.960 ± 0.013	0.962 ± 0.014	–	0.962 ± 0.013	–	0.962 ± 0.014	–
σ_8	0.812 ± 0.026	$0.799^{+0.044}_{-0.043}$	–	0.798 ± 0.034	–	$0.788^{+0.045}_{-0.044}$	–
τ	0.084 ± 0.016	0.085 ± 0.016	–	$0.087^{+0.016}_{-0.017}$	–	0.087 ± 0.016	–

Table 3.3: Current best measurements of the most common cosmological parameters. Data sets: A – UNION+WMAP5+BAO, B – SNALL+WMAP5+BAO, C – UNION+WMAP5+SDSSBAO (only \mathcal{R} and l_Λ from WMAP5, hence no constraint on h and Ω_b). See text for details. Systematic errors have not been included for supernova measurements, for ease of comparison with other results. WMAP5 results are insensitive to systematics, except for n_s and τ (Komatsu et al., 2008).

baryon acoustic oscillation measurement (Eisenstein et al., 2005); and the ‘BAO’ combined 2dF+SDSS baryon acoustic oscillation data (Percival et al., 2007). With the combination of these data, dramatic improvement over the single-probe constraints is obtained. To illustrate the impact of the combination of various data sets on the parameter constraints, we also include a selection of figures with two-dimensional parameter constraints, based on these data. As such, the intention is not to represent or discuss the properties of the different data sets in great detail. Results are shown for Ω_m and Ω_Λ in the non-flat Λ CDM model and Ω_m and w in the flat w CDM model (Fig. 3.23), Ω_k and w in the non-flat w CDM model (Fig. 3.24, p. 63), and σ_8 and w in the flat w CDM model (Fig. 3.25, p. 63).

In terms of model selection, the preferred model is the flat Λ CDM model, with adiabatic perturbations. The scalar power spectrum is close to scale invariant ($n_s = 1$), but the data also give a fairly strong detection of $n_s \neq 1$. This pushes the evidence in favour of a non-Harrison–Zel’dovich spectrum, but not decisively so (Parkinson et al., 2006; Trotta, 2007). Although the evidence appears to be clearly in favour of the existence of dark energy, and the concordance of the standard cosmological model, it may well be possible to fit the relevant data with relatively small modifications to the standard assumptions. In this context, it is worthwhile to remind oneself that we lack any fundamental understanding of the underlying phenomena, when interpreting observations (Sarkar, 2008).

3.6 Future Prospects

Despite the paradigm shift that the last twenty years of observations have meant, the future promises even greater leaps forward as vast amounts of new data become available: cosmology is becoming a precise, data-driven and increasingly non-linear field. Over the next decade or two, a host of new telescopes and satellites covering all wavelengths will come online and/or complete their work, such as

Radio The Low Frequency Array (LOFAR) and the Square Kilometre Array (SKA)

Microwave The Arcminute Microkelvin Imager (AMI), the South Pole Telescope (SPT) and *Planck*

Far infra-red *Herschel*

Infra-red–optical The Dark Energy Survey (DES), the *James Webb Space Telescope* (*JWST*) and the Large Synoptic Survey Telescope (LSST)

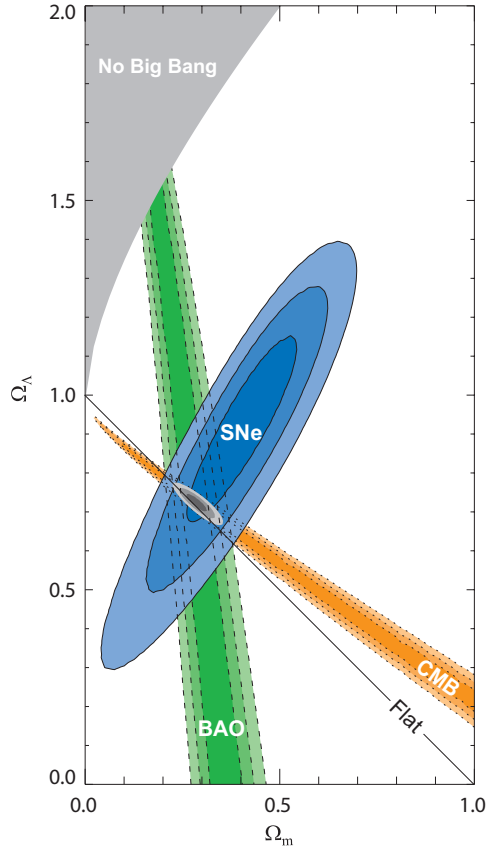
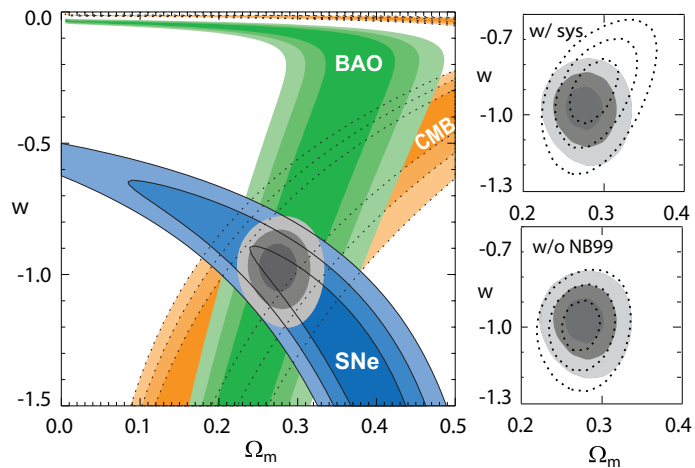
(a) Ω_m and Ω_Λ in the non-flat Λ CDM model.(b) Ω_m and w in the flat w CDM model. The upper right panel shows the effect of systematic errors (dotted), and the lower right panel the impact of the SCP Nearby 1999 data (see reference for details).

Figure 3.23: Current best parameter constraints for non-flat Λ CDM and flat w CDM models, based on Union supernova, WMAP5 cosmic microwave background and SDSSBAO baryon acoustic oscillation data (see text for details). The contours represent 68%, 95% and 99% confidence levels. Reproduced from [Kowalski et al. \(2008\)](#).

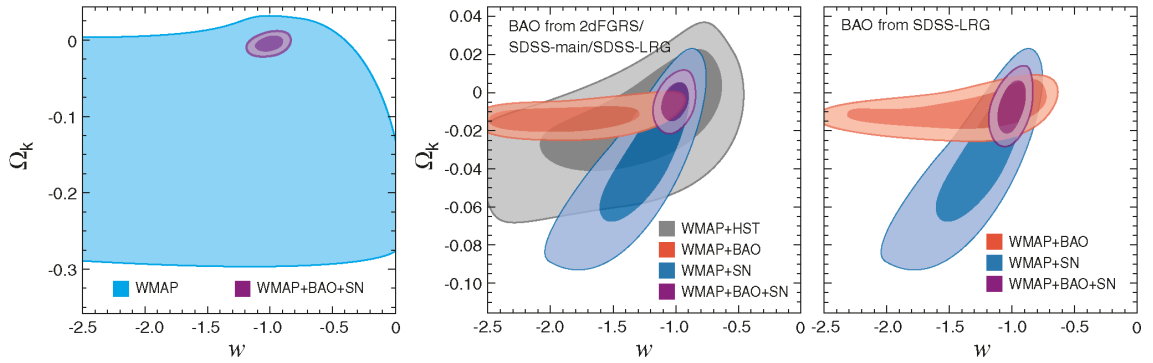


Figure 3.24: Current best parameter constraints for Ω_k and w in the non-flat w CDM model, based on Union supernova, WMAP5 cosmic microwave background, and BAO/S-DSSBAO baryon acoustic oscillation data (see text for details). The contours represent 68% and 95% confidence levels. Reproduced from [Komatsu et al. \(2008\)](#).

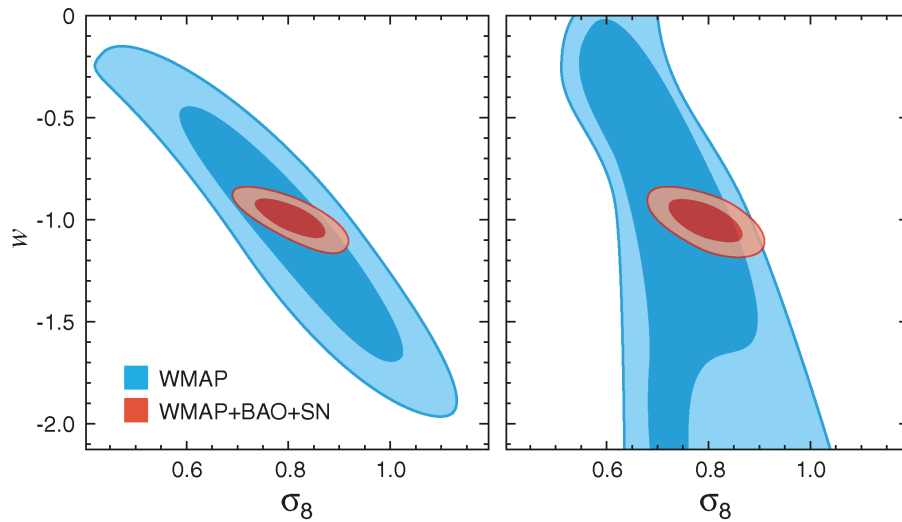


Figure 3.25: Current best parameter constraints for σ_8 and w in the flat w CDM model, based on Union supernova, WMAP5 cosmic microwave background, and BAO baryon acoustic oscillation data (see text for details). The contours represent 68% and 95% confidence levels. Reproduced from [Komatsu et al. \(2008\)](#).

Optical The Panoramic Survey Telescope & Rapid Response System (Pan-Starrs) and the *Dark Universe Explorer (DUNE)*

X-ray The *Extended Roentgen Survey with an Imaging Telescope Array (eROSITA)*, the *X-ray Evolving Universe Mission (XEUS)* and *Constellation-X*

Gamma-ray *Fermi Gamma-ray Space Telescope* (formerly *GLAST*)

as well as the NASA Joint Dark Energy Mission, and Inflation Probe. Observational access to the dark ages and beyond will extend with first steps in 21cm hydrogen-line surveys and maturing gravitational wave observatories, e.g. the Laser Interferometer Gravitational Wave Observatory (LIGO), the *Laser Interferometer Space Antenna (LISA)*, and the *Big Bang Observer (BBO)*. Likewise, simulations of structure formation and astrophysical processes in e.g. reionization, galaxies and clusters of galaxies will become ever more sophisticated with increasing computing power.

The major upcoming survey is the *Planck* mission to study the cosmic microwave background anisotropies, which (along with CMB polarization surveys) should teach us more about inflation, dark energy and reionization (e.g. [Bond et al., 1997](#); [Pahud et al., 2006, 2007](#)). With some luck, the Large Hadron Collider (LHC; [Mavromatos, 2007](#)) or *Fermi* ([Baltz et al., 2008](#)) will shed light on what the cold dark matter is made of, or perhaps even dark energy.

Future surveys will predominantly be based on four different techniques: baryon acoustic oscillations, galaxy clusters, supernovae, and weak lensing (not discussed in this thesis – see [Albrecht et al. \(2006\)](#) for a review of all these techniques). Additional important survey types will include Lyman- α forest data to constrain neutrino properties, and 21cm radiation tomography of the early Universe to constrain reionization and dark energy. In all cases, potential sources of systematics are of great importance to robust predictions and conclusions, and will be a significant focus in the years to come.

A significant driver for future surveys is the desire to constrain the equation of state of dark energy, including its possible time evolution. There is also the potential to uncover evidence for modified gravity, i.e. deviations from General Relativity, underlying the dark energy phenomenon. Due to the complementary nature of the probes, testing both cosmic expansion and perturbation growth, we can achieve significant progress in this direction. Within the next twenty years, we can expect to measure a constant w_{DE} to within 1% or less. We should also have measured the time evolution of w_{DE} to within, say, 10%. This number might be regarded as tentative, as it depends on how the time evolution is

parameterized. At some level though, if we measured $w_{\text{DE}} \neq -1$, it would be indicative of dynamical dark energy – so measuring the time evolution well is in such a case not crucial. Depending on what is the correct theory for dark energy and gravitation, we may also find evidence of deviations from General Relativity (Heavens, 2008).

In addition to the dark energy effort, observational probes of structure formation will become increasingly accurately modelled alongside the major planned cluster and weak-lensing surveys (in synergy with reionization-epoch studies), either leading to moderate revisions of the CDM paradigm, or a convergence to $\{\Gamma, \sigma_8, n_s\}$ parameter values obtained from the CMB anisotropy. With more precise data probing initial conditions, we may also find first strong detections of primordial non-Gaussianity (e.g. f_{NL}).

Chapter 4

Selected Theoretical Challenges

4.1 Dark Energy

4.1.1 Observational Concordance – Theoretical Discordance

As explained in Sect. 2.2, the concept of dark energy or a cosmological constant goes back to the period of Einstein’s original formulation of General Relativity, and has been in and out of fashion through the years. However, as described in the preceding Chapter, a number of recent observations, including Type Ia supernova luminosity distance data, cosmic microwave background anisotropies, and growth of large-scale structure, now indicate that the expansion of the Universe is accelerating (see Sect. 3.5). The source for this observed acceleration is generally called *dark energy*. The nature of dark energy in our Universe remains unknown, and is likely to be the subject of intense observational attention over the coming decade (Albrecht et al., 2006). We will present here the basic theoretical problems that dark energy poses. For further extensive reviews of dark energy, see Sahni & Starobinsky (2000); Carroll (2001); Sahni (2002); Padmanabhan (2003); Peebles & Ratra (2003); Sahni & Starobinsky (2006); Copeland (2007).

The weight of the still-emerging set of concordant observations on theory is now heavy. To account for the observations within the context of General Relativity, we require a term in the Einstein equation which effectively behaves as a negative-pressure perfect (unclustered) fluid, with equation of state close to -1 . The extra term in Einstein’s equation,

$$G_{\mu\nu} = T_{\mu\nu}, \quad (4.1)$$

can be viewed either as an additional energy–momentum contribution (i.e. in $T_{\mu\nu}$), or a gravitational term constituting a correction to General Relativity. There are thus essentially three approaches to solving the problem of dark energy: the most economical is the

cosmological constant, which would essentially be just another constant of nature. Another option is a dynamical source in the energy–momentum tensor, typically a canonical scalar field generically dubbed quintessence (see Sect. 5.1.1). Alternatively, the modification could be in the Einstein tensor, typically through braneworld scenarios and e.g. Gauss–Bonnet modified-gravity actions (Sahni, 2005; Nojiri et al., 2005). The last two possibilities clearly point toward either new physics beyond the Standard Model of Particle Physics, or a new gravitational theory. The possibility of a cosmological constant is neither gravity nor particle physics, and a cosmological constant as a new constant of nature would still beg the question of what it ‘is’; all currently-known constants of nature are coupling constants. A possible resolution would be that it follows as a coupling constant from a quantum theory of gravity. At some level, all these explanations have their motivation in similar fundamental physics, perhaps string theory: the cosmological constant seems closely related to a fundamental quantum gravity length scale (Padmanabhan, 2005a), dynamical scalar fields are highly abundant in supersymmetric theories (such as string theory), and corrections to the Einstein–Hilbert action are also generically predicted in string theory.

Besides implying the existence of a new term in the Einstein equation, current measurements also indicate that the value of Λ (or some alternative component) today is extremely specialized, i.e. that we are living in a special epoch. This is somewhat unsettling: how do we explain this without resorting to fine-tuning of initial conditions? This is explored further in the following two Sections.

Observationally, the situation from the point of view of theory can be regarded as moderately promising. One complication is that any modification to General Relativity is perfectly degenerate with some scalar-field model, if one considers only cosmological distance data. However, adding data sensitive to the growth of structure can break this degeneracy. This is the focus for much of cosmological observations over the next decade or so. Additionally, we can expect to learn more about particle physics beyond the Standard Model of Particle Physics with the Large Hadron Collider (LHC) at CERN just coming online. This is discussed further in Sect. 3.6.

Apart from these explanations based on new physics, a recent development is the revival of discussion around the possibility that the perceived acceleration might be wholly or partly due to a systematic error: observations deal with quantities smoothed on some scale, but this smoothing does not commute with the non-linear Einstein equations. Hence the smoothed quantities do not in principle follow the Einstein equations, so this assump-

tion that is usually made might introduce systematic errors. Whereas some researchers argue that the corrections are negligible¹, others claim that further calculations are needed (Buchert, 2008).

4.1.2 Coincidence Problem

A significant problem in cosmology is the so called *coincidence problem*: why is the fraction of energy density in dark energy today, Ω_Λ , so similar to the fraction of energy density in non-relativistic matter today, Ω_m ? There is, it seems, *a priori* nothing that requires this, and since for a cosmological constant $\Omega_\Lambda \sim \text{const.}$ whereas $\Omega_m \propto a^{-3}$, we would have to fine-tune the initial conditions on the order of 10^{-100} to ensure that they have similar values today.

However, if we lift the restriction that the energy density contributing to Ω_Λ comes from a cosmological constant and allow it to evolve in time there is the possibility that the energy density has just evolved towards its natural value today. The ‘seriousness’ of this problem ultimately depends on the theoretical model proposed. Some tracker models of quintessence (see Sect. 5.1.2) can resolve this problem.

4.1.3 Fine-Tuning Problem

Since all energy should couple to gravity directly, we would expect that the constant zero-point energy of fields in the Universe also contributes in Einstein’s equations. We should hence regard a cosmological constant as a sum of this vacuum energy and a *bare* cosmological constant (or in general a dark energy contribution). The vacuum state of a quantized scalar field has an energy density of roughly $\rho_{\text{vac}} \sim 10^{74} \text{ GeV}^4$, and comparing this to the observational value of $\rho_{\text{vac}} + \rho_{\Lambda\text{-bare}} \sim 10^{-47} \text{ GeV}^4$ we realize that the energy density in bare Λ must be extremely fine-tuned. We would rather expect that some symmetry would ensure $\rho_{\text{vac}} + \rho_{\Lambda\text{-bare}} = 0$ or that $\rho_{\Lambda\text{-bare}}$ corresponds to something on the order of the Planck energy, but this seems ruled out by observations. The *fine-tuning problem* is thus exactly this: how can we explain this apparently extremely fine-tuned value of a cosmological constant? Some quintessence models can possibly resolve this problem, although it seems difficult to explain the exact value apart from arguing that Λ has evolved for a long time towards its natural value zero.

¹e.g. J. Bardeen, talk entitled *Backreaction as an explanation for dark energy*, given at ‘The Very Early Universe 25 Years On’ workshop at the University of Cambridge, 17 December 2007.

4.2 Priors: Measures, Multiverses, and the Knowable

As we touched upon in the previous Section, explaining dark energy appears difficult without resorting to fine-tuning. More specifically, what we generally mean by fine-tuning is that the probability for the range of initial conditions consistent with observations is extremely small. This depends on what probabilistic weight the theory assigns to different initial conditions, through e.g. some symmetry principle, boundary conditions, or by way of its dynamics. This probability distribution is the *prior* distribution relevant for interpreting observations (see Sect. 3.4.2). As such, it can have significant impact on what conclusions are drawn based on experimental data.

For crude phenomenological models, the above prescriptions for calculating a prior distribution typically fail, since they imply some level of knowledge of the physical degrees of freedom in the problem. We then end up with very broad probability distributions. This is the situation for dark energy at present; the lack of sufficiently-predictive theories means that significant observational effort is necessary to make progress, and update our prior distribution with data robustly.

However, the problem of priors, or *measures*, is generic in cosmology. With the help of inflation, we may answer the question of why our Universe has the large-scale structure, etc. that we observe, and not some other; all possible inflation-epoch initial conditions will be realized in causally separated regions of the Universe, and our patch happens to have this particular setup. However, although suggestions exist (e.g. Gibbons et al., 1987; Page, 1987; Hawking & Page, 1988; Vilenkin, 1998; Kofman et al., 2002; Hollands & Wald, 2002; Hawking & Hertog, 2002; Aguirre et al., 2007; Garriga et al., 2006; Hartle et al., 2008; Gibbons & Turok, 2008; Page, 2008; De Simone et al., 2008), it is not known what the probability of inflation itself is, i.e. what the initial-conditions measure is in whichever theory underlies inflation. We can generalize this problem to a measure on the *multiverse*, which may include (explicitly or implicitly depending on fundamental theory) the probability distribution for e.g. physical constants and/or initial conditions (relevant for e.g. chaotic inflation and string theory). The multiverse will here be taken to be some ensemble of possible universes, without going into specific detail. Tegmark (2007) has conceptually divided the multiverse into several levels, the first one corresponding to other unobservable patches in the Universe, and the fourth and last to the ‘mathematical-equations’ level (‘why these equations?’). The development appears to point in the direction of Platonism, but perhaps also a new type of ‘Platonic realism’, seen e.g. in the Mathematical Universe Hypothesis (Tegmark, 2008) that the Universe *is* Mathematics.

This hypothetical ensemble of universes is one that we cannot observe; our inferences about it must therefore be based on the one realization that we do have. This means that we are able to empirically falsify only theories which are in disagreement with our Universe. As a result of this, we are forced into a Bayesian statistical framework: we are not able to ever update probability through observation (at least once observations begin to exhaust the information attainable by humans in the observable Universe²), and must therefore specify a degree-of-belief prior probability distribution on the multiverse. Any such prior can have no free parameters, as they would be unconstrainable and cut by Ockham’s razor. Finding such prior probability distributions is a major challenge in fundamental theory, with major potential for pitfalls. Where current work leads remains to be seen. Perhaps the best we can ever do is some form of Maximum Entropy priors on the multiverse, unless e.g. self-consistency or naturalness conditions restrict the priors, or resort to some version of the anthropic principle (Barrow & Tipler, 1986; Tegmark et al., 2006a).

Clearly, at this point we are venturing into metaphysics. This is usually a departing point for disagreements within physics, often involving heated arguments³. Husserlian horizons like those described in Sect. 1.1 contribute to prejudices about what the physical (and spiritual) world is and how it operates. The scientific method provides a powerful tool with the help of which such prejudices gradually can be downgraded, by repeated empirical observation, which has traditionally been the case. However, the realm of applicability of the scientific method is restricted by the possibility of repeated observation of a physical system, in principle unaffected by the observational apparatus itself. For the case of the multiverse measure problem, it is not self-evident that resolution along these lines will be possible. We might be sensing limits to Popperian science (the end of science has been declared many times, but this is not the claim here!). To quote G. W. Gibbons, the situation ‘challenges our basic notions of science as a rational activity’⁴.

It thus appears that following the route of science, we are eventually led back to

²This ‘fundamental’ uncertainty is commonly referred to as *cosmic variance*.

³A recent example of the prevalence of personal preference in physics can be found in the early days of General Relativity. Among others, Einstein, Weyl, and Eddington were heavily involved in considering the epistemological and philosophical implications of the new theory, for instance the ‘geometrical unification’ idea (Ryckman, Fall 2008). Bohr, Pauli and Schrödinger were also endeavouring with philosophical challenges within quantum theory (e.g. complementarity, Hilgevoord & Uffink, Fall 2008), a debate that goes on today with the ‘Many-Worlds’ a recent popular interpretation (Vaidman, Fall 2008).

⁴Talk entitled *Priors*, given at ‘The Very Early Universe 25 Years On’ workshop at the University of Cambridge, 20 December 2007.

metaphysics of one sort or another. In this realm, the scientific method cannot uniquely save us from our mental and physical horizons. A formalization of logical reasoning which can take into account this uncertainty is therefore required, to be able to meaningfully engage in deductive reasoning and discourse. A new principle to balance our emotional response to lack of information (see Sect. 1.1). The Bayesian statistical framework is the natural candidate to form a basis for such a formal system, since it is the unique extension of Boolean logic in the presence of uncertainty (see Sect. 3.4.1). One might perhaps speculate further about ‘why this logic?’, but we shall not enter into that philosophical debate here, although note that e.g. *fuzzy logic* (Wilkinson, 1963; Zadeh et al., 1996) is by some considered a viable alternative.

Chapter 5

Reconstruction of Quintessence

5.1 Introduction

5.1.1 Quintessence

While a pure cosmological constant remains the simplest interpretation of present data, a leading alternative possibility is the *quintessence* paradigm (after the heavenly fifth element in Plato’s and Aristotle’s natural philosophy, [Plato, 2000](#); [Aristotle, 1965](#)), whereby the observed acceleration is driven by the potential energy of a single canonically-normalized scalar field ([Wetterich, 1988](#); [Ratra & Peebles, 1988](#)). It is usually assumed to have minimal coupling to gravity and no, or very weak, coupling to other fields ([Carroll, 1998](#)). This is as yet a largely *phenomenological* approach to solving the problem of what constitutes dark energy. There is however an abundance of scalar fields in e.g. supersymmetric particle models and string theory, from which forms of the self-interaction potential could be inferred. One would therefore hope that at some point in the future, quintessence could be derived from such a model.

By analogy to common particle physics concepts, we assume that the scalar field has a Lagrangian density

$$L_\phi = \frac{1}{2}g^{\mu\nu}\phi_{,\mu}\phi_{,\nu} - V(\phi) \tag{5.1}$$

i.e. a canonical sum of kinetic and potential energy (this is the only Lorentz invariant such quantity with no higher than first derivatives in the field, see e.g. [Peskin & Schroeder](#),

1995). The Einstein–Hilbert action then becomes

$$\begin{aligned}
S &= \frac{1}{2} \int R \sqrt{-g} \, d^4x + \\
&\quad \frac{1}{2} \int \left(\frac{1}{2} g^{\mu\nu} \phi_{,\mu} \phi_{,\nu} - V(\phi) \right) \sqrt{-g} \, d^4x + \\
&\quad \frac{1}{2} \int (L_m + L_r) \sqrt{-g} \, d^4x,
\end{aligned} \tag{5.2}$$

where L_m and L_r are Lagrangian densities for non-relativistic and relativistic matter respectively, and g the determinant of the metric. The variation of this action with respect to the metric yields the Einstein equations. In particular, the second and third terms yield the energy–momentum tensor. By this identification, we find that the energy–momentum tensor for the scalar field ϕ is

$$T_{\mu\nu}^\phi = \phi_{,\mu} \phi_{,\nu} - \frac{1}{2} g_{\mu\nu} \phi_{,\gamma} \phi^{,\gamma} + g_{\mu\nu} V(\phi). \tag{5.3}$$

Identifying the comoving frame of the scalar field with the cosmic frame we find that

$$T_{00}^\phi = \frac{1}{2} \dot{\phi}^2 + \frac{1}{2a^2} (\nabla\phi)^2 + V(\phi), \tag{5.4}$$

$$T_{ii}^\phi = 3a^2 \left(\frac{1}{2} \dot{\phi}^2 + V(\phi) \right) - \frac{1}{2} (\nabla\phi)^2, \tag{5.5}$$

$$T_{0i}^\phi = \dot{\phi} \phi_{,i}. \tag{5.6}$$

Comparing to the energy–momentum tensor for a perfect fluid in the cosmic frame, Eq. (2.8) on p. 13, we see that

$$\rho_\phi = \frac{1}{2} \dot{\phi}^2 + V(\phi) + \frac{1}{2a^2} (\nabla\phi)^2, \tag{5.7}$$

$$p_\phi = \frac{1}{2} \dot{\phi}^2 - V(\phi) - \frac{1}{6a^2} (\nabla\phi)^2, \tag{5.8}$$

and also have the constraint

$$\dot{\phi} \phi_{,i} = 0, \tag{5.9}$$

encoding that we are considering the background evolution, i.e. the homogeneous part. Since we are considering an evolving scalar field, we must assume that $\dot{\phi} \neq 0$ in general and hence $\phi_{,i} \equiv 0$, as it should be by homogeneity. We thus finally arrive at

$$\rho_\phi = \frac{1}{2} \dot{\phi}^2 + V(\phi), \tag{5.10}$$

$$p_\phi = \frac{1}{2} \dot{\phi}^2 - V(\phi). \tag{5.11}$$

We also define the pressure–energy density ratio

$$w_\phi \equiv \frac{p_\phi}{\rho_\phi} = \frac{\dot{\phi}^2 - 2V(\phi)}{\dot{\phi}^2 + 2V(\phi)}, \tag{5.12}$$

which is of course the *equation of state*. The use of the term is not entirely consistent here: we cannot assume a one-to-one equation of state between p and ρ , since V and $\dot{\phi}$ in general could vary arbitrarily. Note that, from the definition, $-1 \leq w_\phi \leq 1$.

The variation of the action, Eq. (5.2), with respect to ϕ and similar dynamical variables for L_m and L_r yields equations of motion for the different fields. For ϕ , this leads to the equation of motion

$$\ddot{\phi} + 3H\dot{\phi} + V'(\phi) = 0, \quad (5.13)$$

which we also find by inserting Eqs.(5.7–5.8) in Eq. (2.12), p. 14. The Friedmann equation, Eq. (2.9) on p. 13, is now

$$H^2 = \frac{1}{3} \left(\frac{1}{2} \dot{\phi}^2 + V(\phi) + \rho_m + \rho_r \right), \quad (5.14)$$

where ρ_m, ρ_r are the energy densities of non-relativistic and relativistic matter respectively.

To see that this field can mimic a cosmological constant, for which $p = -\rho$, we consider the case where the scalar field ϕ is slowly rolling, encoded by

$$\dot{\phi}^2 \ll V. \quad (5.15)$$

We see that the field ϕ then acts approximately as a cosmological constant since

$$p_\phi \approx -\rho_\phi, \quad (5.16)$$

by Eq. (5.12).

5.1.2 Tracker Potentials

Cosmological tracker potentials/solutions have been studied in detail by numerous authors (Wetterich, 1988; Ratra & Peebles, 1988; Ferreira & Joyce, 1997; Copeland et al., 1998; Ferreira & Joyce, 1998; Liddle & Scherrer, 1999; Zlatev et al., 1999; Zlatev & Steinhardt, 1999; Steinhardt et al., 1999; Brax & Martin, 1999a; de Ritis et al., 2000; Barreiro et al., 2000; Ureña-López & Matos, 2000; Johri, 2001; Bean et al., 2001; Rubano & Barrow, 2001; Johri, 2002; Baccigalupi et al., 2002; Wang & Feng, 2003; Bludman, 2004; Tsujikawa, 2006; Amendola et al., 2006; Das et al., 2006; Linder, 2006). These potentials are such that the late-time evolution of the field can be essentially independent of initial conditions, thus providing a possible solution to the coincidence problem (see Sect. 4.1.2). This behaviour is achieved through a type of dynamical attractor solution, and the conditions for it to be possible given a particular potential have been given and studied in detail by Steinhardt et al. (1999).

Defining $\Gamma \equiv V''V/(V')^2$, where prime denotes a derivative with respect to the field, the two sufficient conditions for a potential to possess a tracker solution are

$$\Gamma > 1 - \frac{1 - w_b}{6 + 2w_b}, \quad (5.17)$$

$$\left| \Gamma^{-1} \frac{d\Gamma}{d \ln a} \right| = \left| \frac{d\phi}{d \ln a} \left(\frac{V'}{V} + \frac{V'''}{V''} - 2 \frac{V''}{V'} \right) \right| \ll 1, \quad (5.18)$$

where w_b is the equation of state of the background component, e.g. $w_b = 0$ during matter domination. The first of these conditions ensures convergence to the tracker solution (i.e. perturbations away from it are suppressed, see e.g. [Liddle & Scherrer, 1999](#); [Steinhardt et al., 1999](#)). If $\Gamma < 1 - (1 - w_b)/(6 + 2w_b)$ the field freezes quickly, and we end up having to fine-tune initial conditions, which is what we are trying to avoid ([Steinhardt et al., 1999](#)). The second condition ensures an adiabatic evolution of the field that is necessary for the first condition to be applicable (and is arguably what one would expect of a function that is to maintain a dynamical attractor independent of initial conditions).

If these conditions are fulfilled, the field will eventually approach the tracker solution by today for most reasonable initial values $\rho_{\phi,i}$: in the range

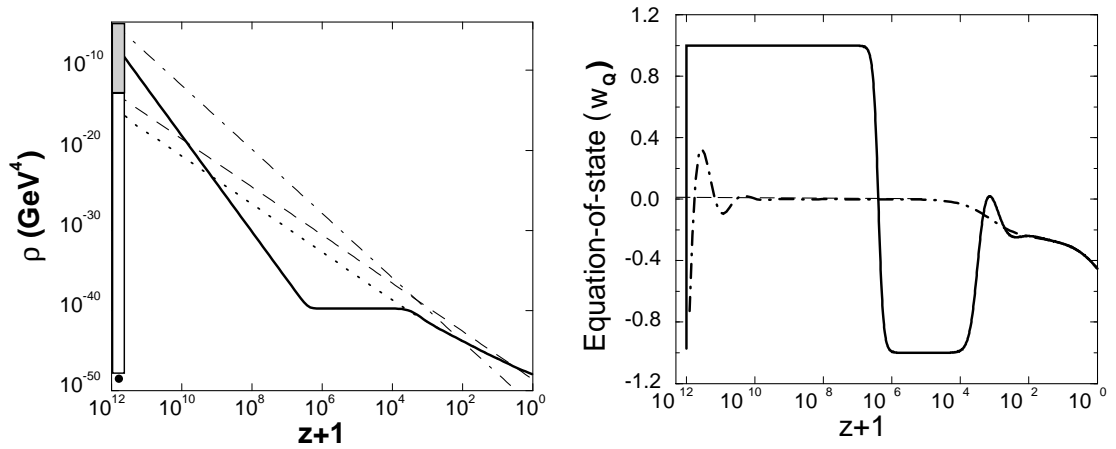
$$\rho_{c,0} < \rho_{\phi,i} < \rho_{b,i}, \quad (5.19)$$

where $\rho_{c,0}$ is the present time critical energy density and $\rho_{b,i}$ is the initial background energy density, solutions will have approached the tracker solution by the present time. This range of initial conditions spans nearly 100 orders of magnitude, and includes ‘equipartition after inflation’, $\Omega_{\phi,i} \sim 10^{-3}$. The initial conditions will either ‘overshoot’ or ‘undershoot’ the tracker-solution value for ρ_ϕ . In the first case, the field rolls down the potential rapidly, eventually freezing, but then later joins the tracker solution and starts rolling again. In the case of ‘undershoot’, the field stays frozen, and like in the ‘overshoot’ case then joins the tracker solution and starts rolling. The evolution of the field energy density will then track the evolution of the background, typically matter, but eventually overtakes it. An example of the behaviour of the energy density of a tracker quintessence field is shown in [Fig. 5.1a](#).

In the tracker solution, the equation of state will then evolve according to

$$w_\phi \approx w_{\text{tracker}} = \frac{w_b - 2(\Gamma - 1)}{1 + 2(\Gamma - 1)}, \quad (5.20)$$

possibly breaking away from the tracker solution if either of the conditions later become violated. An illustration of the behaviour of the equation of state can be seen in [Fig. 5.1b](#).



(a) The energy density ρ_ϕ of the quintessence field, here called simply ρ . The grey range of values corresponds to higher initial conditions for ρ at high redshift compared to the tracker solution value, whereas the white range corresponds to initial conditions slightly lower than the tracker solution value. The black dot corresponds to the initial condition where the ‘missing’ energy consists of vacuum energy. Overall, this range of allowed initial conditions spans more than 100 orders of magnitude. The thick solid line corresponds to a case with the potential $V(\phi) \propto \phi^{-6}$. In this ‘overshooting’ case, the energy density first drops below the tracker solution (dotted line) as the field rolls down the potential. It then freezes, and starts rolling only later when it ‘catches up’ with the tracker solution. It then tracks the matter background (dashed line), eventually overtaking it. The dash-dotted and dashed lines are the radiation and matter energy densities respectively.

(b) The equation of state w_ϕ of the quintessence field, here called w_Q . The oscillating curves correspond to higher (solid) and slightly lower (dash-dotted) initial conditions at high redshift compared to the tracker solution value. The initial velocity at high redshift is assumed to be zero. The solid line corresponds to the same potential and initial conditions as the solid line in Fig. 5.1a. The amplitude of oscillations in $w(z)$ around the tracker solution (thin-dashed curve originating at $w_Q = 0$) decays exponentially with decreasing $\ln(1+z)$, and the evolution thus approaches the tracker solution regardless of the different initial conditions. Although not directly corresponding to our models, the figure illustrates qualitatively the tracker property.

Figure 5.1: Examples of the dynamical behaviour of tracker quintessence. Although not directly corresponding to our models, the figures illustrate qualitatively the tracker property. Reproduced from [Steinhardt et al. \(1999\)](#).

For most reasonable models of tracker type it is approximately true that $w_\phi \geq -0.8$ (Steinhardt et al., 1999). Therefore, they should be observationally distinguishable from a cosmological constant. Interestingly, a large number of quintessence potentials popular in the literature do *not* satisfy the conditions for tracking behaviour (Steinhardt et al., 1999).

5.1.3 Reconstructing $V(\phi)$

The scheme of reconstructing cosmological scalar field potentials is essentially due to Huterer & Turner (1999); Starobinsky (1998) with many subsequent works (Nakamura & Chiba, 1999; Saini et al., 2000; Gerke & Efstathiou, 2002; Daly & Djorgovski, 2003, 2004, 2005, 2007; Wetterich, 2004; Simon et al., 2005; Sahlén et al., 2005; Guo et al., 2005; Tsujikawa, 2005; Zhang, 2006; Guo et al., 2007). The purpose is to use observational data to directly reconstruct the shape of the potential $V(\phi)$, which can be done knowing $\{\Omega_m, H(z)\}$.

Here, we work under the assumption that quintessence is a valid description of observational data (an assumption to be tested separately), and seek to impose optimal constraints on the model via exact numerical computation. More specifically, the quintessence potential $V(\phi)$ was reconstructed directly in terms of an expansion in the field using an MCMC approach. By assuming a particular physical model for dark energy, this method is distinct from parameterized equation-of-state methods for reconstructing dark energy.

Although there is a general motivation in supersymmetric theories for the introduction of a scalar field to provide the dark energy, there is no strong theoretical motivation for a particular form of the quintessence potential. Hence for the purposes of a general reconstruction a sufficiently general expansion of the potential has to be considered.

In Sahlén et al. (2005), we carried out a direct reconstruction of the quintessence potential based on the Type Ia supernova (SNIa) luminosity–redshift measurements made/collated by Riess et al. (2004). The current treatment updates and extends that work in three ways:

1. We include additional data coming from cosmic microwave background (CMB) anisotropies (Spergel et al., 2007; Komatsu et al., 2008) and baryon acoustic oscillations (Eisenstein et al., 2005; Percival et al., 2007), as well as using newer supernova data from the SuperNova Legacy Survey (SNLS; Astier et al., 2006), and the Union data set (Kowalski et al., 2008). We also apply a Big Bang Nucleosynthesis (BBN)

constraint on the dark energy density. We do not use constraints from the growth rate of structure, which are not yet competitive with the data we do use.

2. Where previously we approximated the quintessence potential via a Taylor series, we now additionally explore use of Padé approximant expansions in order to test robustness under choice of expansion.
3. By studying the dynamical properties of models permitted by the data, we assess whether current observations favour or disfavour the hypothesis that the quintessence field is of tracker form, hence potentially addressing the coincidence problem.

The treatment is based on [Sahlén et al. \(2007\)](#), but has been updated with the new ‘extended’ data combination (Union+WMAP5+2dF+SDSS+BBN) that will be presented below. ‘New data’ will in the following typically mean new relative to [Sahlén et al. \(2005\)](#).

[Huterer & Peiris \(2007\)](#) also reconstruct quintessence potentials from a similar compilation of current data. Although phrased in the language of flow equations, their approach, like ours here and in [Sahlén et al. \(2005\)](#), amounts to fitting the coefficients of a Taylor expansion of the potential. They do not consider Padé approximants. Their approach implies different priors for the parameters than the ones used here, and they treat the scalar field velocity a little differently. Our results appear in good agreement, in particular our determination that present data mildly favour tracker models over non-tracker models concurring with their conclusion that freezing models are mildly preferred to thawing ones (in the terminology of [Caldwell & Linder, 2005](#)).

5.2 Formalism

5.2.1 Cosmological Model

For the range of redshifts that we consider (determined by the range in the data), the radiation density will be relevant, and so we include it, along with non-relativistic matter and dark energy in the form of quintessence. The Friedmann equation, Eq. (2.9) on p. 13, thus reads

$$H^2(z) = H_0^2 [\Omega_r(1+z)^4 + \Omega_m(1+z)^3 + \Omega_k(1+z)^2] + \frac{1}{3}\rho_\phi, \quad (5.21)$$

with $\rho_\phi = \dot{\phi}^2/2 + V(\phi)$ the quintessence density. The current fractional quintessence density Ω_ϕ is determined by the boundary condition below. The radiation density is given by Eq. (2.25) on p. 15, with $N_{\text{eff}} = 3.04$ effective neutrino species, where we use a photon

density $\Omega_\gamma = 2.469 \times 10^{-5} h^{-2}$ (for a temperature $T_{\text{CMB}} = 2.725$ K, e.g. [Komatsu et al., 2008](#)). This prescription for Ω_γ is also used for calculating acoustic horizons, Eq. (3.27) on p. 35, relevant for some observables.

We expand the quintessence potential $V(\phi)$ in a series about the present value of the field that is taken (without loss of generality) to be zero. Together with the Klein–Gordon equation

$$\ddot{\phi} + 3H\dot{\phi} = -\frac{dV}{d\phi}, \quad (5.22)$$

from Eq. (5.13), this fully specifies the dynamics of the expansion. Since $\Omega_r + \Omega_m + \Omega_\phi + \Omega_k = 1$, we have the present boundary condition

$$\dot{\phi}_0 = \pm \sqrt{2[(1 - \Omega_r - \Omega_m - \Omega_k)\rho_{c,0} - V(\phi_0)]}, \quad (5.23)$$

where subscript ‘0’ indicates present value, and ρ_c is the critical density. In practice, we use this conversely, choosing $\dot{\phi}_0$ and letting that specify Ω_k . Additionally assuming a flat universe, Ω_m is determined by the boundary condition.

We usually assume a flat universe (motivated by CMB measurements and the inflationary paradigm), but also consider the non-flat case when explicitly stated. The additional priors we assume for our cosmology are

$$\Omega_m \geq 0, \quad (5.24)$$

$$\Omega_{\text{kin}}(z \geq 1) < 0.5, \quad (5.25)$$

where $\Omega_{\text{kin}} = \dot{\phi}^2/6H^2$ is the fraction of critical energy density in field kinetic energy density. The last condition is a means of encoding that the field should not interfere too much with structure formation (as we do not use data sensitive to that), and is discussed further in [Sahlén et al. \(2005\)](#). The choice of this prior is somewhat arbitrary, but necessary so that unphysical models with too much quintessence that interfere with structure formation at $z \gtrsim 1$ are at least marginally excluded. We use Ω_{kin} to encode this condition, as it can be expected to be relatively monotonic with redshift, and thus provide a ‘stable’ criterion. The constraint on Ω_{kin} is in practice applied up to last scattering, $z = 1089$. When we use supernova data only, the upper limit is $z = 2$, as in [Sahlén et al. \(2005\)](#).

5.2.2 Potential Parameterizations

To explore the space of potentials, we need to assume some functional form for the potential. We choose two classes of expansions, a Taylor series, and a Padé series, to parameterize the potential function $V(\phi)$. In the absence of a theoretical bias for the functional

form of the potential, these expansions seem suitably general and simple to provide a reasonably fair sampling of the space of potential functions.

Taylor Series

We use a Taylor series to model the potential $V(\phi)$ as

$$V(\phi) = V_0 + V_1\phi + V_2\phi^2 + \dots \quad (5.26)$$

where ϕ is in units of the reduced Planck mass M_{P} with ϕ presently zero. We will refer to a constant potential with non-zero kinetic energy allowed as a *skater* model, after [Linder \(2005\)](#).

We put the following flat priors on the parameters:

$$V_0 \geq 0, \quad |V_1| \leq 2, \quad |V_2| \leq 5. \quad (5.27)$$

These priors are irrelevant for parameter estimation, as they are significantly broader than the high-likelihood region (this also applies to the corresponding priors for Padé series below). However, to assess how favoured tracker behaviour is, we do need to put some limits, so that we can sample a finite region of the prior parameter space (see further in [Sect. 5.4.3](#)).

Padé Series

In addition to the Taylor series expansion, we also use Padé approximant expansions in order to test the robustness of results to the method used. Padé approximants are rational functions of the form

$$R_{M/N}(\phi) = \frac{\sum_{i=0}^M a_i \phi^i}{1 + \sum_{j=1}^N b_j \phi^j}, \quad (5.28)$$

that can be used to approximate functions. These approximants typically have better-behaved asymptotics, i.e. stay closer to the approximated function, than Taylor expansions because of their rational structure. An extensive exposé on Padé approximants can be found in [Baker & Graves-Morris \(1981\)](#). For our study, we assume

$$V(\phi) = R_{M/N}(\phi), \quad (5.29)$$

where again ϕ is in units of M_{P} with ϕ presently zero. Specifically, we use Padé series $R_{0/1}$, $R_{1/1}$ and $R_{0/2}$, as these form an exhaustive set of lowest order and next-to-lowest order non-trivial expansions with two or three parameters. As will be evident from our results, higher orders are unmotivated given the known difficulty for data to constrain

more than two dark energy/quintessence evolution parameters (Maor & Brustein, 2003; Linder & Huterer, 2005; Sahlén et al., 2005).

Padé series have poles, but, as will be discussed in Sect. 5.5, data constrains models so that the presence of poles is not felt.

To enable comparison between our results for the two different parameterization classes, the priors for the Padé series case are set by evaluating the MacLaurin expansion of the Padé series, identifying the order coefficients, and using the Taylor-series priors for those, i.e.

$$a_0 = V_0, \quad (5.30)$$

$$a_1 - a_0 b_1 = V_1, \quad (5.31)$$

$$b_1(a_0 b_1 - a_1) - a_0 b_2 = V_2. \quad (5.32)$$

This does not limit us to a finite region, so we additionally require $|b_1| \leq 2$.

5.3 Observables

The observables we consider are essentially geometric in nature, namely Type Ia supernovae luminosity–redshift data, the CMB peak-shift and angular-scale parameters, and the geometric probe of the baryon acoustic oscillation scale. We also include a Big Bang Nucleosynthesis (BBN) prior on the amount of dark energy.

We have not included growth-of-structure observations, which are not yet competitive with the measures we do use (see e.g. Wang et al. 2004b for a directly-comparable example).

5.3.1 SNIa Luminosity–Redshift Relation

Type Ia supernova observations and observables are introduced in Sect. 3.2.1. We use the 115 measurements of $m(z)$ measured/compiled by the SNLS team (Astier et al., 2006), covering the redshift range $z = 0.015$ – 1.01 . The observed magnitudes (indexed by i) are given by

$$m_i = m_{B,i}^* + \alpha(s_i - 1) - \beta c_i \quad (5.33)$$

where m_B^* is the rest-frame B-band magnitude at maximum B-band luminosity, and s and c are the shape and colour parameters. These are derived from the light-curve fits and are reported by the SNLS team. The shape parameter s corresponds to the width of the light curve (or equivalently, the decline rate), and the colour parameter c to the

overall normalization. The parameters α and β are free parameters and should be varied in cosmological fits. However, as they are independent of cosmology (Fouchez, 2006), we fix them to the SNLS best-fit values

$$\alpha = 1.52 \pm 0.14, \quad (5.34)$$

$$\beta = 1.57 \pm 0.15, \quad (5.35)$$

without introducing any bias, and include their uncertainty in the magnitude uncertainties we use. In principle, these two parameters are correlated to some degree, but we neglect this correlation.

We also use the 307 supernovae in the Union compilation (Kowalski et al., 2008) from the Supernova Cosmology Project (SCP), which constitutes a consistent and uniform sample of essentially all supernova data so far, including the SNLS data used above. It covers the redshift range $z = 0.015$ – 1.55 . The Union sample Hubble diagram is shown in Fig. 3.6, p. 33. We employ the magnitude and error estimates provided by the SCP, but do not include the systematic errors that they quote. Because the observable quantity reported in Kowalski et al. (2008) is different from that in Astier et al. (2006), the parameter $\eta = M_{\text{Union}}^* - \mathcal{M}$ will be used to parameterize the supernova-magnitude nuisance parameter for the Union data set, unlike \mathcal{M} for SNLS. Here, M_{Union}^* is the estimate of intrinsic supernova magnitude for the Union data set. The parameter \mathcal{M} is defined through Eq. (3.25) on p. 33.

For comparison to the paper Sahlén et al. (2005), where the parameter η is also used, likewise $\mathcal{M} = M_{\text{Riess}}^* - \eta$, with M_{Riess}^* the estimate of intrinsic supernova magnitude for the Riess et al. (2004) data set.

5.3.2 CMB Peak-Shift and Acoustic-Scale Parameters

The CMB anisotropy observables are introduced in Sect. 3.3.1. We use the recent WMAP3 data (Spergel et al., 2007) as analyzed by Wang & Mukherjee (2006), who found

$$\mathcal{R}(z_{\text{dec}} = 1089) = 1.70 \pm 0.03 \quad (5.36)$$

for the peak-shift parameter, Eq. (3.36) on p. 40.

With the release of 5-year data results, the *WMAP* team provided a refined set of observables which capture most of the CMB constraining power on dark energy (Komatsu et al., 2008), the distance priors, including their covariance matrix. The likeli-

hood for these observables can be calculated as

$$\chi_{\text{WMAP5}}^2 = \sum_{i,j} \Delta_i^{\text{WMAP5}} C_{ij}^{-1} \Delta_j^{\text{WMAP5}}, \quad (5.37)$$

where i and j run over $l_A(z_{\text{dec}})$, $\mathcal{R}(z_{\text{dec}})$ and z_{dec} – see Sect. 3.3.1 for definitions and the prescriptions we use. The deviations

$$\Delta^{\text{WMAP5}} = (l_A(z_{\text{dec}}) - l_A^{\text{WMAP5}}, \mathcal{R}(z_{\text{dec}}) - \mathcal{R}^{\text{WMAP5}}, z_{\text{dec}} - z_{\text{dec}}^{\text{WMAP5}}), \quad (5.38)$$

where the ‘WMAP5’ superscript denotes the Maximum Likelihood estimates of these quantities from WMAP5 data, i.e.

$$l_A^{\text{WMAP5}}(z_{\text{dec}}) = 302.10, \quad (5.39)$$

$$\mathcal{R}^{\text{WMAP5}}(z_{\text{dec}}) = 1.710, \quad (5.40)$$

$$z_{\text{dec}}^{\text{WMAP5}} = 1090.04. \quad (5.41)$$

The inverse covariance matrix is given by

$$C^{-1} = \begin{pmatrix} 1.800 & 27.968 & -1.103 \\ 27.968 & 5667.577 & -92.263 \\ -1.103 & -92.263 & 2.923 \end{pmatrix}, \quad (5.42)$$

with the order of parameters as listed above.

5.3.3 Baryon Acoustic Peak

The baryon acoustic oscillation observables are introduced in Sect. 3.2.2. We use the measurement (fairly insensitive to dark energy model) from the SDSS luminous red galaxy power spectrum (Eisenstein et al., 2005)

$$A(z_{\text{BAO}} = 0.35) = 0.469 \left(\frac{n_s}{0.98} \right)^{-0.35} \pm 0.017, \quad (5.43)$$

which, assuming the WMAP3 mean value $n_s = 0.95$ (Spergel et al., 2007), yields $A(z = 0.35) = 0.474 \pm 0.017$. The quantity $A(z)$ is defined in Eq. (3.32) on p. 35.

In addition, we also consider the joint 2dF+SDSS measurement of the ratio $r_s^{\text{BAO}}/d_V(z)$ of the acoustic horizon scale at the drag epoch, Eq. (3.27) on p. 35, and the acoustic scale in the galaxy distribution, Eq. (3.31), at two redshifts $z = 0.2$ (2dF) and $z = 0.35$ (SDSS). The likelihood for these observables can be calculated as (Percival et al., 2007)

$$\chi_{2\text{dFSDSS}}^2 = \sum_{i,j} \Delta_i^{2\text{dFSDSS}} V_{ij}^{-1} \Delta_j^{2\text{dFSDSS}}, \quad (5.44)$$

where i and j run over $r_s/d_V(0.2)$ and $r_s/d_V(0.35)$ – see Sect. 3.2.2 for definitions and the prescriptions we use. The deviations

$$\Delta^{2\text{dFSDSS}} = \left(\left[\frac{r_s}{d_V(0.2)} \right] - \left[\frac{r_s}{d_V(0.20)} \right]^{2\text{dF}}, \left[\frac{r_s}{d_V(0.35)} \right] - \left[\frac{r_s}{d_V(0.35)} \right]^{\text{SDSS}} \right), \quad (5.45)$$

where the ‘2dF’ and ‘SDSS’ superscripts denote the Maximum Likelihood estimates of these quantities from 2dF and SDSS data, i.e.

$$\left[\frac{r_s}{d_V(0.20)} \right]^{2\text{dF}} = 0.1980, \quad (5.46)$$

$$\left[\frac{r_s}{d_V(0.35)} \right]^{\text{SDSS}} = 0.1094. \quad (5.47)$$

The inverse covariance matrix is given by

$$V^{-1} = \begin{pmatrix} 35059 & -24031 \\ -24031 & 108300 \end{pmatrix}, \quad (5.48)$$

with the order of parameters as listed above. We note that there is some uncertainty as to the consistency of this combined data set (Percival et al., 2007; Komatsu et al., 2008).

5.3.4 Big Bang Nucleosynthesis

To constrain possible early dark energy, we shall also use a Big Bang Nucleosynthesis (BBN) prior, given by (Wright, 2007)

$$S^{\text{BBN}} \equiv \frac{E(z_{\text{BBN}})}{\sqrt{E^2(z_{\text{BBN}}) - \rho_\phi(z_{\text{BBN}})/\rho_{c,0}}} = 0.942 \pm 0.030, \quad (5.49)$$

with a Gaussian distribution at $z_{\text{BBN}} = 10^9$. Here, $E(z) \equiv H(z)/H_0$.

5.4 Data Analysis

5.4.1 Parameter Estimation

The posterior probability of the parameters Θ , given the data and a prior probability distribution $\Pi(\Theta)$, is (see Sect. 3.4.2)

$$P(\Theta|\text{data}) = \frac{1}{\mathcal{Z}} e^{-[\chi_{\text{SN Ia}}^2(\Theta) + \chi_{\text{CMB}}^2(\Theta) + \chi_{\text{BAO}}^2(\Theta) + \chi_{\text{BBN}}^2(\Theta)]/2} \Pi(\Theta). \quad (5.50)$$

We consider two combinations of data sets, ‘basic’ and ‘extended’, with ‘basic’ being defined by

$$\chi_{\text{SNIa}}^2(\Theta) = \sum_{i=1}^{N_{\text{SNLS}}} \frac{[m_i^{\text{SNLS}} - m(z_i; \Theta)]^2}{\sigma_i^2}, \quad (5.51)$$

$$\chi_{\text{CMB}}^2(\Theta) = \frac{[\mathcal{R}_{\text{obs}}^{\text{WMAP3}} - \mathcal{R}(z_{\text{dec}} = 1089; \Theta)]^2}{\sigma_{\mathcal{R}, \text{WMAP3}}^2}, \quad (5.52)$$

$$\chi_{\text{BAO}}^2(\Theta) = \frac{[A_{\text{obs}} - A(z_{\text{BAO}}; \Theta)]^2}{\sigma_A^2}, \quad (5.53)$$

$$\chi_{\text{BBN}}^2(\Theta) = 0. \quad (5.54)$$

Here, we sum over all N_{SNLS} data points for the SNLS supernova data. Overall, we here have 115(SNIa)+1(CMB)+1(BAO) data points. Note that no BBN constraint is included.

The ‘extended’ data combination is defined by

$$\chi_{\text{SNIa}}^2(\Theta) = \sum_{i=1}^{N_{\text{Union}}} \frac{[m_i^{\text{Union}} - m(z_i; \Theta)]^2}{\sigma_i^2}, \quad (5.55)$$

$$\chi_{\text{CMB}}^2(\Theta) = \chi_{\text{WMAP5}}^2, \quad \text{Eq. (5.37)}, \quad (5.56)$$

$$\chi_{\text{BAO}}^2(\Theta) = \chi_{\text{2dFSDSS}}^2, \quad \text{Eq. (5.44)}, \quad (5.57)$$

$$\chi_{\text{BBN}}^2(\Theta) = \frac{[S_{\text{obs}}^{\text{BBN}} - S^{\text{BBN}}(z_{\text{BBN}}; \Theta)]^2}{\sigma_{\text{SBBN}}^2}. \quad (5.58)$$

Again we sum over all N_{Union} data points for the Union supernova data. This combination contains 307(SNIa)+3(CMB)+2(BAO)+1(BBN) data points.

For the ‘basic’ data combination, the parameter space we study is

$$\Theta = (\mathcal{M}, \dot{\phi}_0, \text{potential parameters}), \quad (5.59)$$

and for the ‘extended’ data combination,

$$\Theta = (\eta, \dot{\phi}_0, \Omega_b h^2, h, \text{potential parameters}). \quad (5.60)$$

For the non-flat case, Ω_m will be added to these. The parameter estimation is carried out using a Bayesian MCMC approach, as outlined in Sects. 3.4.2 & 3.4.4. We marginalize over $\Omega_b h^2$ and h for all presented results.

5.4.2 Model Selection

To test the necessity of quintessence for explaining the observed data, we perform model selection in complement to the parameter estimation, as introduced in Sect. 3.4.3. Because of the difficulty in calculating the Bayesian evidence and the non-availability of an efficient generic code at the time the work was carried out, we estimate the Bayesian evidence

using an information criterion, more specifically the Bayesian Information Criterion (BIC), Eq. (3.49) on p. 50. The BIC has also been deployed for dark energy model selection in Bassett et al. (2004); Szydlowski & Godłowski (2006); Szydlowski et al. (2006). Recall from Sect. 3.4.3 that a difference of two for the BIC is regarded as positive evidence, and of six or more as strong evidence, against the model with the larger value.

It is worth mentioning that although we specifically consider a quintessence scenario, a model selection result favouring more than one potential parameter would indicate a dynamical dark energy component more generally, since for every choice of $\{H(z), \rho_m(z)\}$ there exists a corresponding quintessence potential and field initial conditions, by virtue of Picard’s existence theorem for ODE’s (demonstrated explicitly in e.g. Padmanabhan, 2005b). Hence, scalar field scenarios are generally degenerate with e.g. modifications of gravity if one considers only the expansion history of the Universe. However cross-correlating with perturbation growth history can break this degeneracy (e.g. Corasaniti et al., 2004; Ishak et al., 2006; Bertschinger & Zukin, 2008).

5.4.3 Tracker Viability

Identifying Tracker Solutions

To classify general scalar field evolutions as coming from a tracker potential capable of solving the coincidence problem or not, we need to test for both tracker conditions and whether the field evolves according to the tracker solution. As these conditions are approximate in nature, we must specify some $\epsilon \geq 0, \delta \geq 0$ such that if

$$\Gamma > 1 - \frac{1 - w_b}{6 + 2w_b}, \quad (5.61)$$

$$\left| \Gamma^{-1} \frac{d\Gamma}{d \ln a} \right| < \epsilon, \quad (5.62)$$

$$|w_\phi - w_{\text{tracker}}| < \delta, \quad (5.63)$$

$$w_\phi < w_b, \quad (5.64)$$

are all fulfilled for some range in redshift over which we require the field to be in the tracker solution, the potential is classified as a tracker potential. Here, w_b is the background equation of state. To provide a satisfactory solution to the coincidence problem, the field should have $w_\phi < w_b$ while in the tracker solution. This condition is automatically satisfied if the tracker conditions are fulfilled with $\Gamma > 1$ and the field is in the tracker solution. However, in our analysis there is some room for fields with $w_\phi \geq w_b$, since the field is allowed to deviate slightly from the tracker solution, and we also consider $\Gamma > 1 - (1 - w_b)/(6 + 2w_b)$ as tracking rather than $\Gamma > 1$ that is typically used. Cases

satisfying the former Γ -criterion but not the latter are generally disfavoured because they would correspond to $w_\phi > w_b$ in the tracker solution and hence not be very successful for solving the coincidence problem. In our set-up this is not necessarily true, and this is the reason for not choosing the more commonly-used latter criterion. Instead, we ensure a solution to the coincidence problem by enforcing $w_\phi < w_b$. In particular, we require $\Gamma > 5/6$ and $w_\phi < 0$ since we are concerned with the matter-dominated epoch.

Note that we are not connecting our analysis directly with any specific particle physics model and its initial conditions at early times, and assessing whether the present-time observables are highly insensitive to variations in those initial conditions. We are only addressing the question whether the (essentially late-time) evolution of quintessence is more consistent with such a class of tracker potentials, or with a class that does not have such behaviour. As the shape of the potential at high redshifts is almost unconstrained by data (see also e.g. [Daly & Djorgovski 2003, 2004, 2005, 2007](#)), we adopt the viewpoint that a suitable *true* tracker potential with insensitivity to initial conditions can always be made to coincide with our lower-redshift behaviour.

As we need a non-zero second derivative of the potential with respect to the field for Γ to fulfil the tracker conditions, we restrict ourselves to the quadratic potential and the Padé series for the tracker viability analysis.

Tracker or Non-Tracker?

To assess whether models which exhibit tracker-solution behaviour are favoured by data over models which do not, we need some quantity to measure this preference. A well-defined and well-motivated quantity is provided within the framework of Bayesian model selection (see Sect. [3.4.3](#)), where the Bayes factor B_{12} , Eq. [\(3.48\)](#) on p. [50](#), can be used to perform this type of comparison.

For the purposes of assessing the viability of tracker solutions for explaining the observed data, we define the following models:

$$M_1 = \{V \text{ is a tracker potential}\}, \quad (5.65)$$

$$M_2 = \{V \text{ is not a tracker potential}\}. \quad (5.66)$$

As these two models are disjoint subsets of the model space, the Bayes factor can be estimated from Monte Carlo Markov chains: letting f_{post} be the fraction of chain elements from the posterior distribution satisfying the tracker criteria, and f_{pri} the corresponding

fraction for the prior distribution, the Bayes factor, Eq. (3.48) on p. 50, is given by

$$B_{12} \approx \frac{f_{\text{post}}(1 - f_{\text{pri}})}{f_{\text{pri}}(1 - f_{\text{post}})}, \quad (5.67)$$

since the fractions of tracker and non-tracker chain elements must sum to one for both prior and posterior. In the limit of equal fractions in prior and posterior, $B_{12} = 1$, whereas in the limit of complete suppression of tracker models in the posterior (so that $f_{\text{post}} = 0$) we have $B_{12} = 0$ in which case Model 2 is infinitely favoured over Model 1. We use the Jeffreys scale, Table 3.1 (p. 50), to rank models. We compute the uncertainties in the Bayes factor following a procedure described in Appendix A.1.

The method presented above treats tracker behaviour as a Boolean one-parameter property. It is thus insensitive to intrinsic biases of the combined potential parameterization and parameter priors in fulfilling the different tracker criteria, as well as how close to the tracker criterion limits models typically fall. It would be possible to go further and estimate the distributions of parameters measuring each of the three tracker criteria. We outline a possible procedure for this in Appendix A.2, but present data do not appear to justify such a sophisticated approach and we do not pursue this further here.

5.5 Results

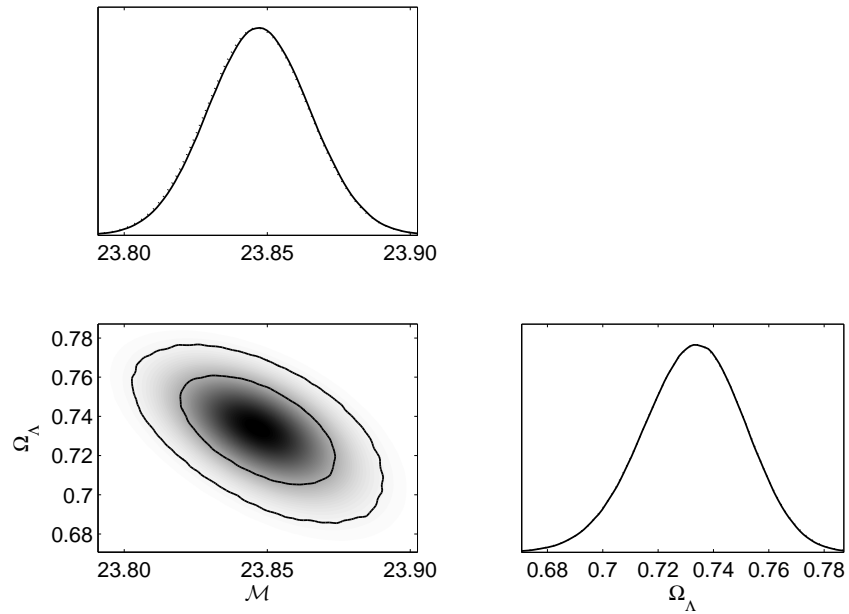
5.5.1 Parameter Estimation

We present the probability distributions for the fitted models in Figs. 5.2–5.7. Marginalized parameter constraints and best-fit values are given in Tables 5.1–5.4. Plots of some dynamical properties of the best-fit models can be found in Figs. 5.8 & 5.9. The results are discussed further below, and model comparison carried out in the following subsection.

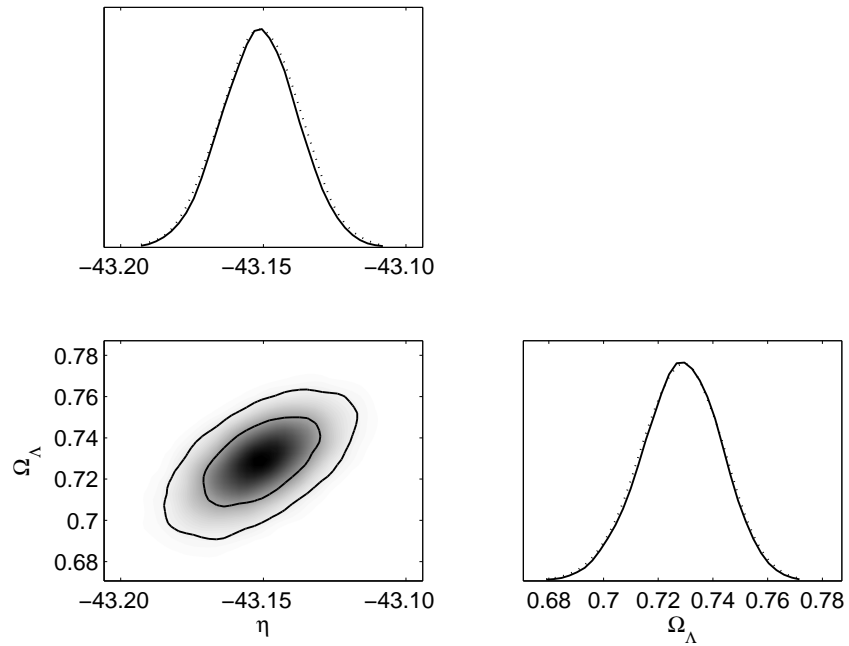
Cosmological Constant

The probability distributions for the cosmological constant case are shown in Fig. 5.2. Looking at Fig. 5.2a, with the ‘basic’ data combination, and the parameter constraints in Table 5.1 (p. 90), these are improved by roughly a factor of two compared to our previous analysis (Sahlén et al., 2005). They differ slightly from the results of Liddle et al. (2006b) using the same data set, albeit within uncertainties. This is most likely due to their different treatment of SNLS SNIa errors.

Using the ‘extended’ data combination, Fig. 5.2b, does not have a very strong additional impact on the size of constraints in this model. However, from Fig. 5.3 (p. 91) it is apparent that there is additional constraining power in the data, since allowing a non-flat



(a) 'Basic' data combination.



(b) 'Extended' data combination.

Figure 5.2: One and two-dimensional likelihood distributions for a flat cosmological constant model (Λ). Solid lines are marginalized 1D likelihoods and dotted lines mean 1D likelihoods. Solid 2D contours represent 68% and 95% regions of the marginalized distribution, and shading reflects the mean distribution. The same scaling has been adopted in both plots.

‘Basic’, Flat	Cosmological constant (Λ)	Skater	Linear	Quadratic ^a
\mathcal{M}	$23.85^{+0.02}_{-0.02}$	$23.86^{+0.01}_{-0.03}$	$23.86^{+0.02}_{-0.02}$	23.86
$\dot{\phi}_0/H_0 M_{\text{P}}$	–	5.4×10^{-5} (5.5×10^{-2}) $ \dot{\phi}_0 /H_0 M_{\text{P}} < 3.7 \times 10^{-2}$ (95% CL)	-2.7×10^{-3} (-6.5×10^{-2}) $ \dot{\phi}_0 /H_0 M_{\text{P}} < 0.61$ (95% CL)	–0.15
$V_0/\rho_{\text{c},0}$	$0.73^{+0.02}_{-0.02}$	$0.72^{+0.03}_{-0.01}$	$0.72^{+0.02}_{-0.03}$	0.73
$V_1/\rho_{\text{c},0}$	–	–	3.6×10^{-3} (8.7×10^{-3}) $ V_1 /\rho_{\text{c},0} < 0.76$ (95% CL)	0.58
$V_2/\rho_{\text{c},0}$	–	–	–	2.1
$-2 \ln \mathcal{L}_{\text{max}}$	113.6	113.4	113.4	112.9
BIC	123.1	127.7	132.4	136.7
BIC – BIC $_{\Lambda}$	0	4.6	9.3	13.6

^a Since at least one parameter is unconstrained by the data for this model, we only give the best-fit parameter values found in our Markov chains.

Table 5.1: Marginalized median and best-fit model parameters and BIC values for the cosmological constant ($\Omega_{\Lambda} = V_0/\rho_{\text{c},0}$) and Taylor-series parameterizations in a flat universe, with the ‘basic’ data combination. Best-fit values are given in parentheses when differing from the median. Note that the likelihood distribution is symmetric under simultaneous change of sign of $\dot{\phi}_0$ and odd-order potential expansion coefficients.

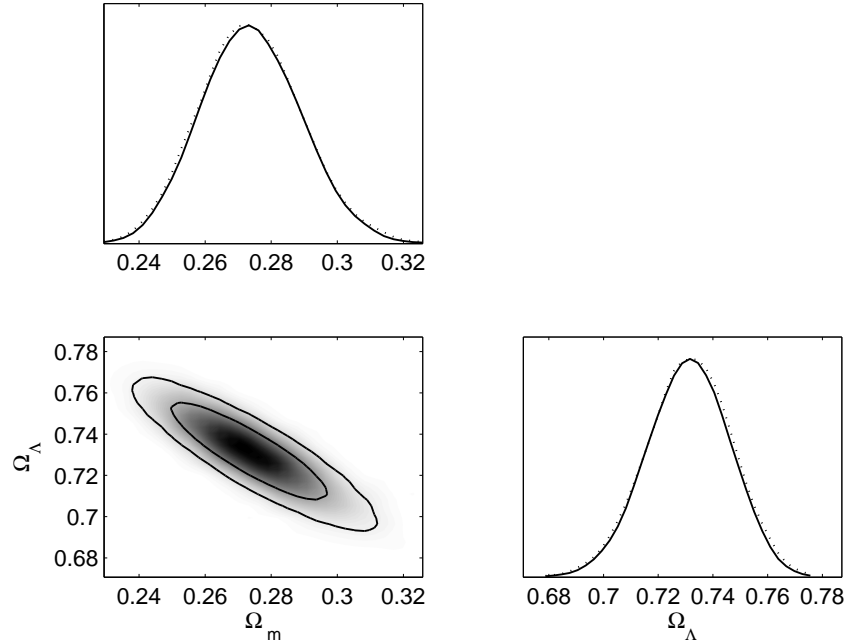


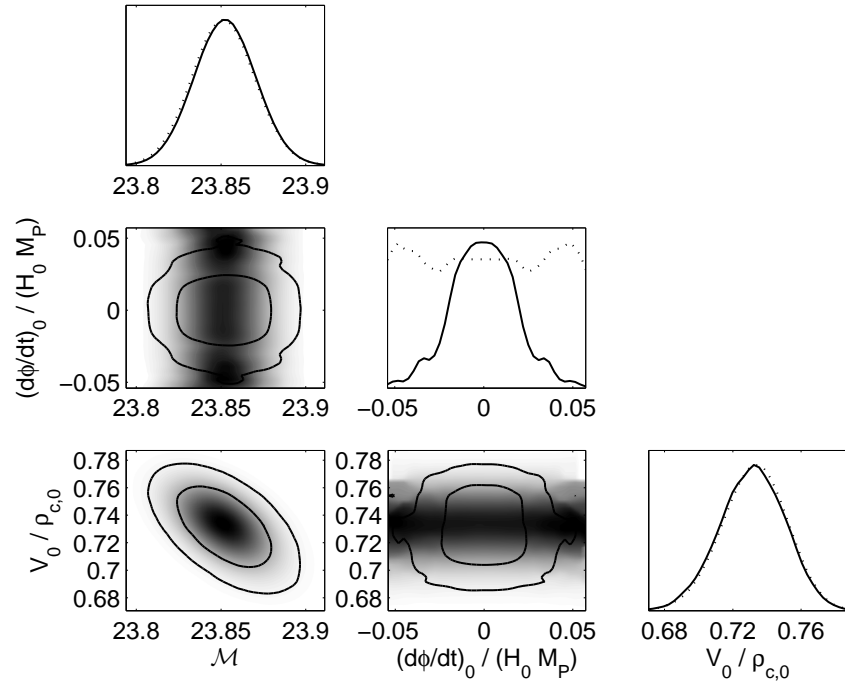
Figure 5.3: As Fig. 5.2, for a non-flat cosmological constant model and with the ‘extended’ data combination.

universe only negligibly affects the size of constraints. The data combination places a strong constraint on the spatial curvature.

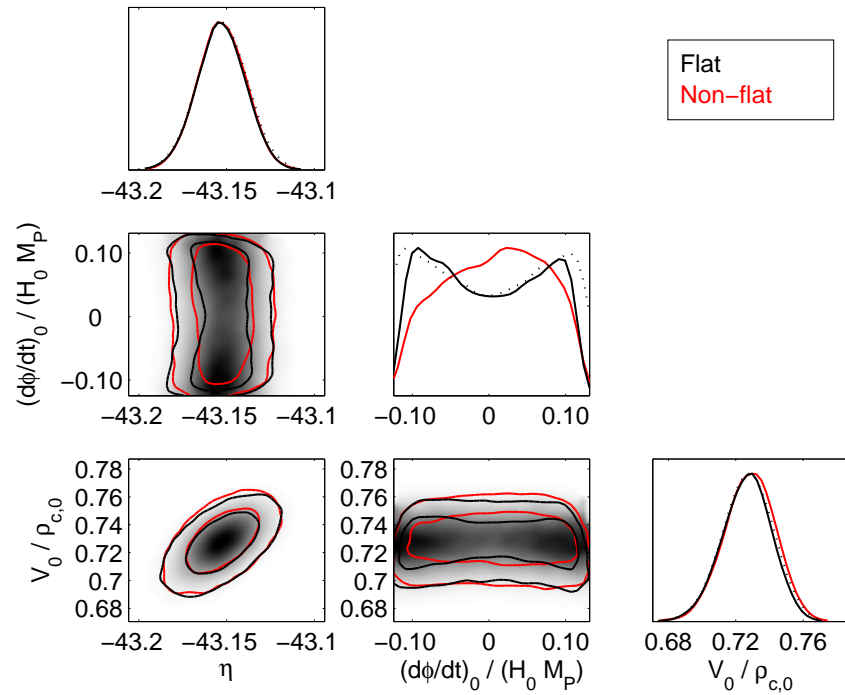
Skater

The likelihood distributions are shown in Fig. 5.4. The constraints for the ‘basic’ data combination are shown in Fig. 5.4a, and in Fig. 5.4b for the ‘extended’ data combination. Fig. 5.5 (p. 93) shows the results for SNLS alone. Note the symmetry in $\dot{\phi}_0$, due to the dependence only on $\dot{\phi}_0^2$. This symmetry suggests that $\dot{\phi}_0^2$ might be a more natural parameter than $\dot{\phi}_0$, something which may also be argued from the point of view of a Hamiltonian system (e.g. Gibbons & Turok, 2008). Such considerations are however more relevant for a system specified with high-energy initial conditions after inflation. The degeneracy between V_0 and $\dot{\phi}_0$ present in our previous analysis (where $|\dot{\phi}_0|$ was positively correlated with V_0 , Sahlén et al., 2005) is no longer apparent with the full ‘basic’ or ‘extended’ data combinations, while still being visible if we use SNLS supernovae alone. This degeneracy stems from the fact that with supernovae we are really only sensitive to an effective quintessence equation of state (Maor et al., 2001a,b, 2002), which the data require to be close to -1 . Thus, increasing the kinetic energy of the field must be compensated by an increase in potential energy to maintain the same effective equation of state.

Additionally, the mild preference in the Riess et al. (2004) ‘gold’ data for a non-zero $\dot{\phi}_0$



(a) 'Basic' data combination.



(b) 'Extended' data combination.

Figure 5.4: As Fig. 5.2 for a 'skater' model, a constant potential with kinetic energy. Note the different scales for $\dot{\phi}_0$ in the two plots.

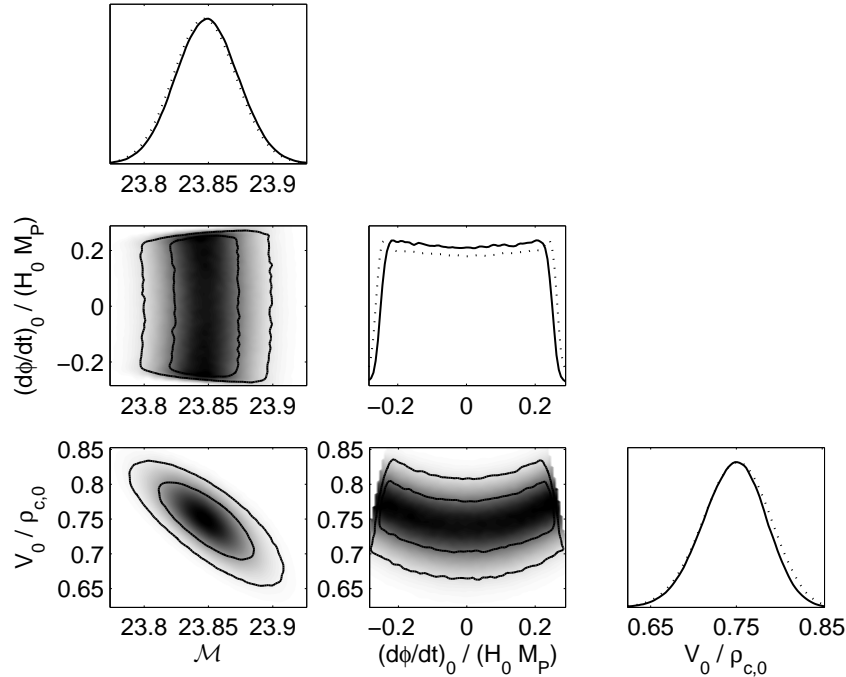


Figure 5.5: As Fig. 5.2a for a constant potential with kinetic energy. **SNLS data only.** Note that here the prior $\Omega_{\text{kin}}(z \geq 1) < 0.5$ is applied only up to $z = 2$.

is not present in the SNLS sample, despite the $\dot{\phi}_0$ - V_0 degeneracy being present. Instead, the likelihood distribution is essentially flat in $\dot{\phi}_0$. This could be a reflection of the better quality/homogeneity of the SNLS sample over [Riess et al.](#) (another possibility is the difference in redshift coverage). In the previous analysis, these two effects conspired to give a different best-fit value of V_0 in the skater scenario ($V_0 = 0.74$) compared to the cosmological constant (where $V_0 = \Omega_\Lambda = 0.69$). That we here do not feel the degeneracy is to some degree linked to our prior limiting $\Omega_{\text{kin}}(z \geq 1) < 0.5$ now being applied to much higher redshifts, restricting the range of allowed $\dot{\phi}_0$. However the new data do reduce the degeneracy significantly on their own (we checked by doing the analysis without the prior on Ω_{kin}). Also, using only the SNLS data with $\Omega_{\text{kin}}(1 \leq z \leq 2) < 0.5$ (Fig. 5.5), the flatness of the distribution in $\dot{\phi}_0$ ensures that the best-fit value of V_0 in that case is only marginally different from that for the full analysis, even though the degeneracy is stronger. These observations illustrate the need for good-quality data sensitive to perturbation growth history (e.g. weak lensing) to break the $\dot{\phi}_0$ - V_0 degeneracy.

Looking at Fig. 5.4b (p. 92), we can see that there is no significant gain from using the additional data in the ‘extended’ data combination. In fact, the best-fit value for V_0 conspires to make the constraints on $\dot{\phi}_0$ larger than with the ‘basic’ data combination, since our prior on Ω_{kin} becomes less restrictive. In contrast to the ‘basic’ data combination, we

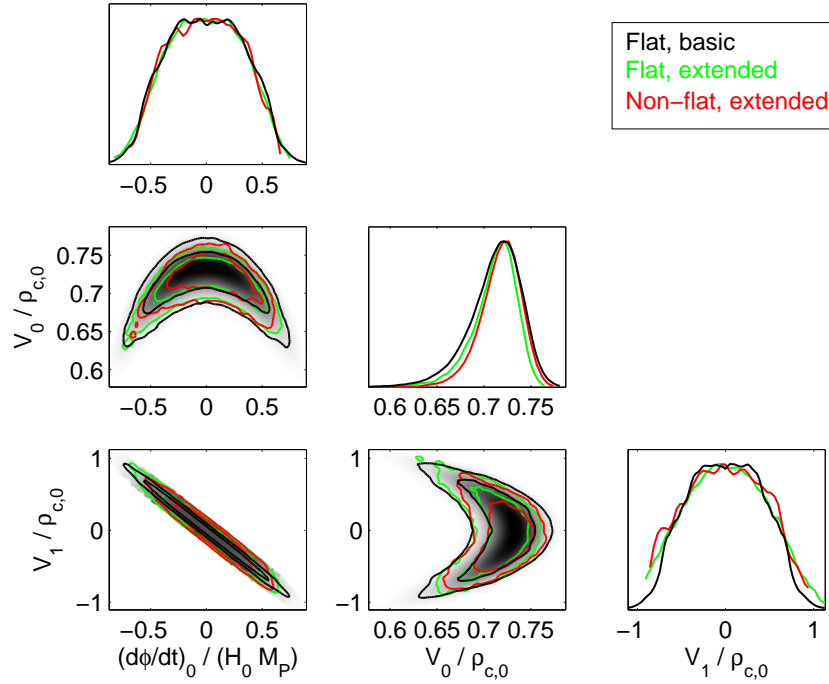


Figure 5.6: As Fig. 5.2 for a linear potential. The slight variations in lines/contours should not be taken as significant.

do find a preference for a non-zero value of $\dot{\phi}_0$. However, this is relieved once the spatial curvature is allowed to be non-zero.

Linear Potential

The likelihood distributions for the ‘basic’ and ‘extended’ data combinations are shown in Fig. 5.6. There is a bimodality, not very readily discerned from the plot, in the $\dot{\phi}_0$ – V_1 distribution, reflecting that models are identical under simultaneous change of sign of $\dot{\phi}_0$ and odd-order expansion coefficients. Hence, it is symmetric with respect to a line through the origin aligned with the degeneracy direction. The first change from previous constraints (Sahlén et al., 2005) is that the V_0 – $\dot{\phi}_0$ degeneracy is now clearly visible in the case of the linear potential (there were only hints of it in the previous analysis). That is to say, the data quality is getting closer to hitting the degeneracy. In addition, we have a degeneracy between V_1 and $\dot{\phi}_0$, coming from the possibility to achieve a particular velocity of the field in the past by either changing the present velocity $\dot{\phi}_0$ or the slope V_1 . As in the case of a ‘skater’ model, adding the ‘extended’ data combination has essentially no significance for the constraints obtained.

Although not excluding the possibility, the ‘basic’ data combination does not favour a potential where the field is rolling uphill (corresponding to the upper right-hand and

lower left-hand quadrants of the $\dot{\phi}_0 - V_1$ distribution), in a flat universe. This appears to be due to the new SNLS data, which do not show a particular preference for a non-zero present field velocity, thus not pushing us into these quadrants. It could be that the preference for an uphill rolling field found in our previous analysis (Sahlén et al., 2005) was an artifact of the Riess et al. data. The observational consequences of such an uphill rolling field could be interpreted as $w < -1$ if an ‘unsuitable’ parameterization is used to fit the data (Maor et al., 2002; Csáki et al., 2006). It could thus be that the strong $w < -1$ preference found in the Riess et al. data (see e.g. Nesseris & Perivolaropoulos, 2005) is due to some systematic effect in the data, causing a preference for an uphill rolling field and also corresponding to a preference for $w < -1$ in fits of $w(z)$. This agrees with the findings of Nesseris & Perivolaropoulos (2005), who for three different parameterizations of w find that the best-fit $w(z)$ consistently does not cross the phantom divide line $w = -1$ with the SNLS data set, but does with the Riess et al. ‘gold’ set. The analyses by Barger et al. (2006); Xia et al. (2006); Jassal et al. (2006) lend support to this conclusion as well, as does a recent analysis by Nesseris & Perivolaropoulos (2007), who however find that other cosmological data do gently favour phantom divide line crossing provided $0.2 \lesssim \Omega_m \lesssim 0.25$.

The ‘extended’ data combination does show a preference for uphill-rolling fields, just as for non-zero field velocity in the ‘skater’ model (see Table 5.2), all in a flat universe. But again, as for the ‘skater model’, once we allow a non-flat universe, this preference disappears (see Table 5.3, p. 97) instead favouring a downhill-rolling field. An obvious difference between the two data combinations is the redshift range of supernovae. The Union data set contains supernovae with much higher redshifts (up to $z = 1.55$) than does the SNLS (highest redshift $z = 1.01$). Considering the effects we observe, it could be that a small amount of spatial curvature is becoming sufficiently relevant for some high-redshift supernovae, to cause this behaviour.

These considerations highlight the importance of interpreting analyses with care, as we are not probing $w(z)$ directly (Maor et al., 2001a,b, 2002). This has been elaborated upon by several authors in terms of eigenmodes, either as principal components or weight functions (see Sect. 3.1.4).

Padé $R_{0/1}$ Potential

The likelihood distributions for the ‘basic’ data combination are shown in Fig. 5.7 (p. 98). As the $R_{0/1}$ potential is close to the linear case for small ϕ , we can use this to compare results. That is, when $\dot{\phi}_0$ or b_1 (which mainly determine the field velocity) are close to

‘Extended’ Flat	Cosmological constant (Λ)	Skater	Linear	Quadratic ^a
η	-43.15 ± 0.01	-43.15 ± 0.01	-43.16 ± 0.02	-43.16
$\dot{\phi}_0/H_0 M_P$	–	-4.1×10^{-3} (0.11) $ \dot{\phi}_0 /H_0 M_P < 0.11$ (95% CL)	1.8×10^{-2} (-8.3×10^{-2}) $ \dot{\phi}_0 /H_0 M_P < 0.59$ (95% CL)	-0.26
$V_0/\rho_{c,0}$	$0.73^{+0.01}_{-0.02}$	$0.73^{+0.01}_{-0.02}$	$0.72^{+0.03}_{-0.02}$ (0.73)	0.72
$V_1/\rho_{c,0}$	–	–	2.0×10^{-2} (-3.5×10^{-2}) $ V_1 /\rho_{c,0} < 0.77$ (95% CL)	0.54
$V_2/\rho_{c,0}$	–	–	–	3.2
$-2 \ln \mathcal{L}_{\max}$	322.1	321.4	321.4	321.0
BIC	345.1	350.2	355.9	361.3
BIC – BIC $_{\Lambda}$	0	5.1	10.8	16.2

^a See Note a of Table 5.1 (p. 90).

Table 5.2: As Table 5.1 for a flat universe, with the ‘extended’ data combination.

‘Extended’ Non-flat	Cosmological constant (Λ)	Skater	Linear	Quadratic ^a
Ω_m	0.27 ± 0.02	$0.27^{+0.02}_{-0.01}$	$0.27^{+0.02}_{-0.02}$	0.27
$\dot{\phi}_0/H_0M_P$	–	1.1×10^{-2} (0.11) $ \dot{\phi}_0 /H_0M_P < 0.11$ (95% CL)	8.2×10^{-2} (–0.18) $ \dot{\phi}_0 /H_0M_P < 0.52$ (95% CL)	–0.28
$V_0/\rho_{c,0}$	0.73 ± 0.02	$0.73^{+0.01}_{-0.02}$	$0.72^{+0.02}_{-0.02}$	0.71
$V_1/\rho_{c,0}$	–	–	-8.8×10^{-2} (0.32) $ V_1 /\rho_{c,0} < 0.67$ (95% CL)	0.75
$V_2/\rho_{c,0}$	–	–	–	3.3
$-2 \ln \mathcal{L}_{\max}$	321.6	321.5	321.5	321.0
BIC	350.3	356.0	361.7	367.0
BIC – BIC $_{\Lambda}$	0	5.7	11.4	16.7

^a See Note a of Table 5.1 (p. 90).

Table 5.3: As Table 5.1 for a universe with spatial curvature allowed, with the ‘extended’ data combination. We have omitted the parameter η here as it is of no interest to our discussion.

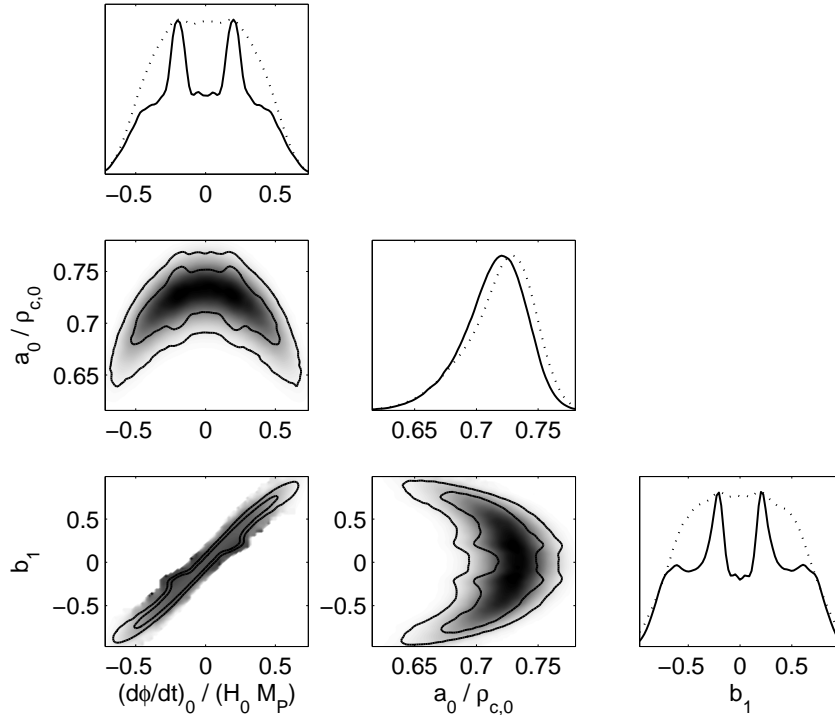


Figure 5.7: As Fig. 5.2 for a Padé series with $M = 0, N = 1$ ($R_{0/1}$).

zero we should expect results to compare well with the linear potential which, comparing Fig. 5.7 with Fig. 5.6 (p. 94), we see that they do. Thus, the discussion above for the linear potential applies to this case as well. However, as we move away from $\dot{\phi}_0 = 0$ and $b_1 = 0$, we see that b_1 is limited to somewhat smaller values than for the linear case (using the relation $V_1 \approx -a_0 b_1$), while the constraints on $\dot{\phi}_0$ are almost identical. This indicates that data prefer not to move very far away from a linear potential. The other main feature of the likelihood distributions are bumps found in the $\dot{\phi}_0$ - b_1 distributions. These are a feature of the likelihood distribution, but the exact size depends on our prior enforcing $\Omega_{\text{kin}}(z \geq 1) < 0.5$ up to high redshifts. The 1D parameter constraints for the $R_{0/1}$ potential are shown in Table 5.4.

Padé series, by construction, have poles. One might be concerned about how this affects our results if the field reaches a pole, but the data is sufficiently constraining that the poles are effectively never felt. We tested this by doing the analysis with a prior excluding all models where a pole is reached before $z = 5$, and saw no change in the results.

Due to the strong similarity between the $R_{0/1}$ potential and the linear potential, we do not consider it worthwhile to examine it further with the ‘extended’ data combination or for the non-flat case.

‘Basic’, Flat	Padé $R_{0/1}$	Padé $R_{0/2}$ ^a	Padé $R_{1/1}$ ^a
\mathcal{M}	$23.86^{+0.02}_{-0.02}$	23.86	23.86
$\dot{\phi}_0/H_0M_{\text{P}}$	1.2×10^{-3} (0.20) $ \dot{\phi}_0 /H_0M_{\text{P}} < 0.57$ (95% CL)	-3.9×10^{-2}	-9.8×10^{-2}
$a_0/\rho_{\text{c},0}$	$0.72^{+0.02}_{-0.03}$	0.73	0.73
$a_1/\rho_{\text{c},0}$	–	–	–0.18
b_1	2.1×10^{-3} (0.18) $ b_1 < 0.82$ (95% CL)	–0.41	–0.29
b_2	–	–1.2	–
$-2 \ln \mathcal{L}_{\text{max}}$	113.3	112.9	113.3
BIC	132.3	136.7	137.1
BIC – BIC $_{\Lambda}$	9.2	13.6	14.0

^a See Note a of Table 5.1 (p. 90).

Table 5.4: Marginalized median and best-fit model parameters and BIC values for the Padé series parameterizations in a flat universe, with the ‘basic’ data combination. Best-fit values are given in parentheses when differing from the median.

Higher-Order Potentials

In the three next-higher-order cases (quadratic, $R_{1/1}$, and $R_{0/2}$), we find that the additional parameter is unconstrained by the data, and we learn nothing useful about parameters from these models. Their principal interest lies in model comparison, discussed next, where the best-fit found can still be used to assess how the models compare in explaining the data.

5.5.2 Model Comparison

The BIC values obtained for all models are shown in the preceding Tables 5.1–5.4. Note that although some parameterizations have unconstrained parameters, their BIC value can be evaluated with Eq. (3.49) on p. 50 from the best fit found in our Monte Carlo Markov chains. It is clear that the cosmological constant, showing a BIC difference of at least 4.6 compared to the other models, is positively favoured by both the ‘basic’ and ‘extended’ data combination. This is a strengthening compared to our previous analysis where this value was 4.0. In fact, the best-fit χ^2 changes only marginally between models, thus providing strong evidence against linear/Padé $R_{0/1}$ and higher-order potentials whose extra parameters add no value. An interesting feature of the new data set is that it much more strongly disfavours a quadratic potential over the other Taylor expansions than just the Riess et al. data. Likewise, the lowest-order Padé expansion is favoured by the same amount compared to the higher-order Padé expansions.

The best-fit cosmologies for the ‘basic’ data combination (Figs. 5.8 & 5.9) now show more convergence in their dynamical properties, although still exhibiting increasing variation with redshift. In particular, we find that where previously the evolution of Ω_ϕ for the best-fit quadratic potential was such that Ω_ϕ stayed between 0.75 and 0.96 (for $0 \leq z \leq 2$), the evolution is now very reasonable (see Fig. 5.9, p. 102). The strong evolution previously seen in w_ϕ is now more limited, reflecting the order-of-magnitude smaller best-fit values for $\dot{\phi}_0$ and V_1 (though the overall compression of the uncertainties is much less than this). However, the ranges of Ω_ϕ and w_ϕ that are allowed may seem large compared to those from other CMB and BBN constraints on dark energy. The reason is that the ‘basic’ data combination only employs the WMAP3 peak-shift parameter (hence not the full CMB information), and no BBN constraint. For the ‘extended’ data combination, which includes a more complete set of CMB observables and a BBN constraint, we find qualitatively the same cosmological dynamics but a somewhat narrower range in Ω_ϕ and w_ϕ (not reproduced here).

All best-fit models fall into the ‘freezing’ category of Caldwell & Linder (2005). For

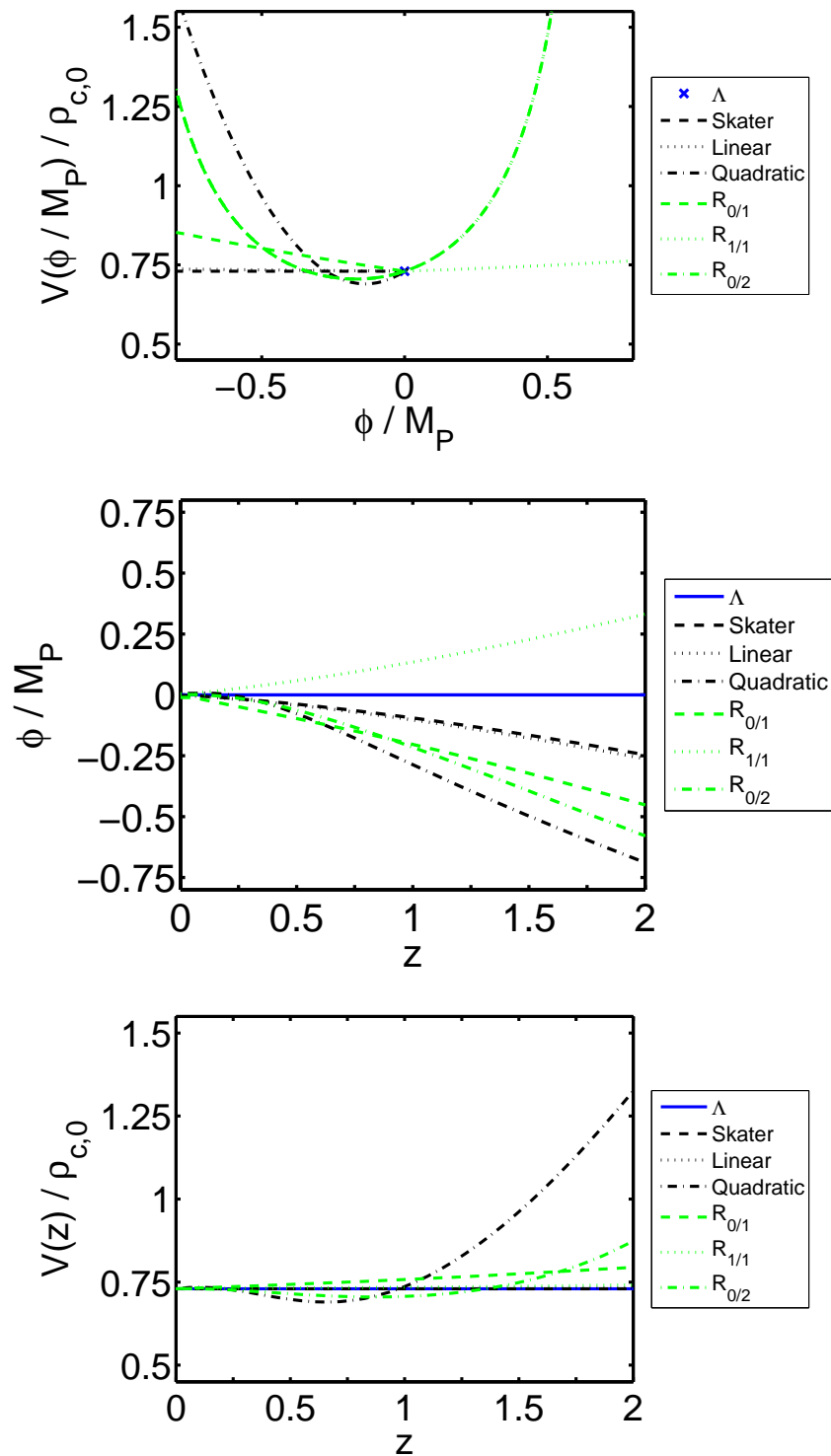


Figure 5.8: Best-fit potentials as a function of the field, and the field and potentials as a function of redshift, for the ‘basic’ data combination.

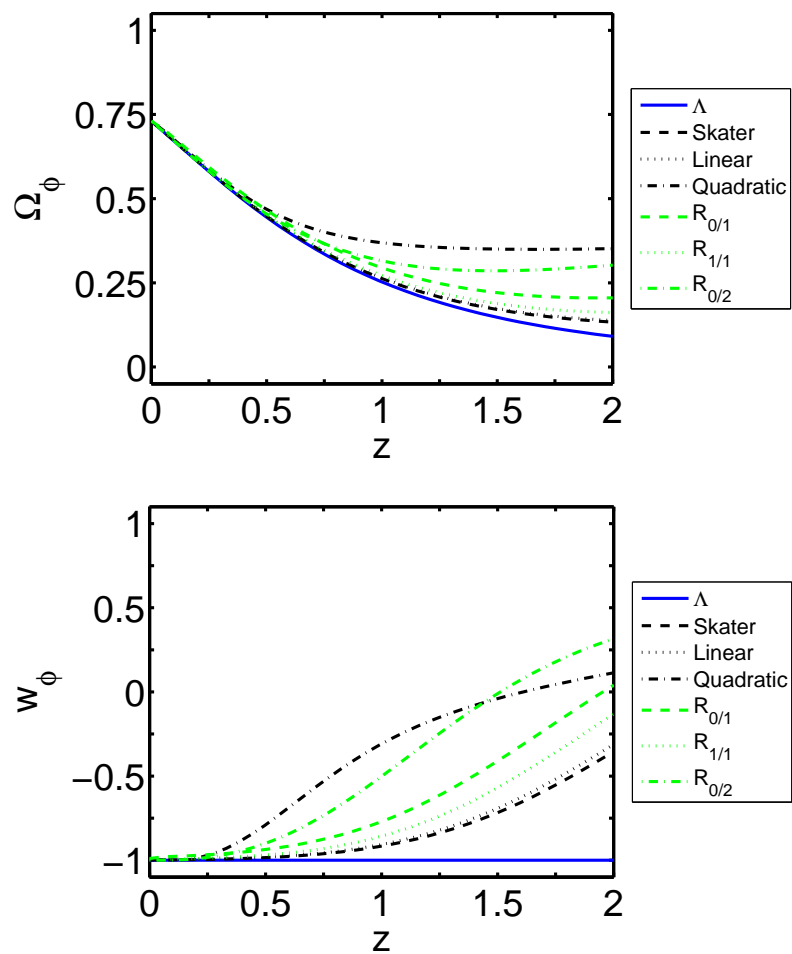


Figure 5.9: Best-fit Ω_ϕ and w_ϕ as a function of redshift, for the ‘basic’ data combination.

the skater model this behaviour is built-in, but it is somewhat intriguing in terms of naturalness that the best-fit linear potential can exhibit freezing while at the same time rolling downhill (see Figs. 5.8 & 5.9). The potentials with curvature incorporate this best-fit behaviour by making the field reach the potential minimum in the recent past (around $z = 0.5$ to $z = 1$), thus providing a braking force to precipitate the accelerated expansion of the universe. This situation would appear somewhat more natural from a dynamical point of view, and it could be that the best-fit linear potential is trying to approximate this, though data is unable to sufficiently constrain the models with curvature in the potential. On the other hand, model selection using the BIC also strongly disfavours these models. The conclusion must be that complementary or better-quality data is needed to resolve this possible contradiction.

If the linear-potential results stand up, they will put the well-motivated models of quintessence based on pseudo-Nambu–Goldstone bosons (pNGBs, [Hill et al., 1989](#); [Frieman et al., 1992](#); [Fukugita & Yanagida, 1994](#); [Frieman et al., 1995](#); [Kaloper & Sorbo, 2006](#)) and similar models under pressure, as these rely on a thawing field that is becoming dynamical and cosmologically dominant in the present epoch. However a field just passing the potential minimum fits well with the pNGB picture, as well as other tracker-type potentials that show a cross-over behaviour, such as the SUGRA ([Binétruy, 1999](#); [Brax & Martin, 1999b](#); [Brax et al., 2001](#)) and Albrecht–Skordis ([Albrecht & Skordis, 2000](#); [Skordis & Albrecht, 2002](#)) potentials where the field is starting to feel a curvature in the potential at late times. Such models exhibit early quintessence ([Wetterich, 2003a,b](#); [Caldwell et al., 2003](#); [Doran & Robbers, 2006](#)), and can thus be constrained using Big Bang Nucleosynthesis and CMB observations ([Bean et al., 2001](#)), as we have also employed here. It will be interesting to see what future data, including those sensitive to perturbation growth and supernovae, can tell.

These observations are in line with studies by e.g. [Bludman \(2004\)](#) and [Linder \(2006\)](#), who both conclude that quintessence generically cannot be described by slow-roll, and that tracking must break down and move towards slow-roll in the recent past (begging the question why this is happening precisely now).

5.5.3 Tracker Viability

In carrying out the tracker viability analysis, we consider four implementations in all by combining two choices of conditions. The first is to demand either that the field remains in the tracker regime until the present, or that it is allowed to break out of tracking after

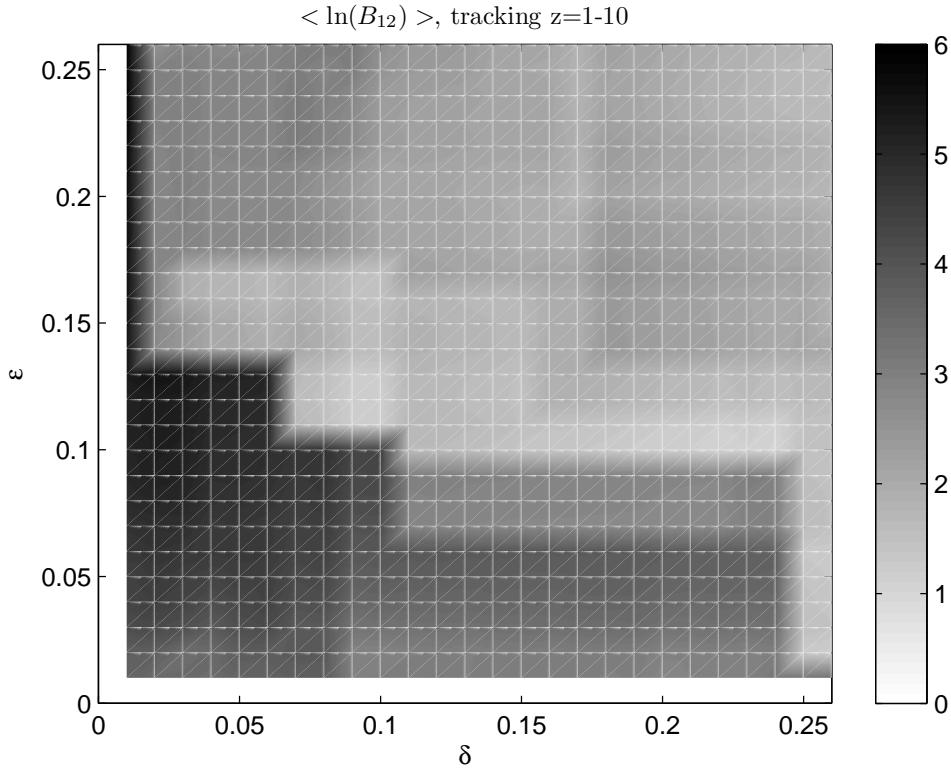


Figure 5.10: Model average of $\ln(B_{12})$ for tracking required between redshift 1 and 10, as a function of ϵ and δ , using the ‘basic’ data set.

a redshift of $z = 1$. The second is to consider two different upper limits for the redshift range where the field is required to be in the tracker regime, namely $z = 2$ and $z = 10$; the former more or less represents where the data actually lie, while the latter extrapolates the potential to higher redshifts.

We find that all four cases give qualitatively the same outcome, and so focus on just one choice, where tracking is imposed between $z = 10$ and $z = 1$. We only carry out the analysis for the ‘basic’ data combination, as we found the dynamical behaviour favoured by the ‘extended’ data combination exceedingly similar to the preferences of the ‘basic’ data combination.

The model average of $\ln B_{12}$, denoted $\langle \ln B_{12} \rangle$, for this scenario is shown in Fig. 5.10, for different combinations of ϵ and δ . For combinations of sufficiently-small ϵ and δ , no models satisfying our tracker conditions are found in the prior and/or posterior (with those ϵ and δ limits different for the different parameterizations). We exclude these cases from our model average, as they effectively correspond to an infinite uncertainty in the derived value for $\ln B_{12}$. A very small fraction of the models feel the presence of a pole at a redshift lower than the upper tracker-regime redshift, and are also excluded. We also point out that

for Padé $R_{0/1}$, $\Gamma = 2$. Thus, the first two tracker conditions are automatically fulfilled, corresponding to a delta-function prior on C_1 and C_2 in the language of Appendix A.2. One might consider this a strong bias, and hence we exclude this parameterization from our Bayes factor model average, and thus use the quadratic, $R_{1/1}$ and $R_{0/2}$ potentials to arrive at our conclusions.

It is clear from Fig. 5.10 that the average indication is in favour of tracker behaviour over non-tracker behaviour. The smallest value of the Bayes factor in the figure is 0.98. Limiting our attention to the region where $\epsilon \leq 0.1, \delta \leq 0.1$, and hence the tracker conditions are best obeyed, the smallest value is 2.9. This general trend is seen in all four cases we analyze, with the strongest preference for tracking in the case presented. However, the model uncertainties in $\langle \ln B_{12} \rangle$ are comparable to $\langle \ln B_{12} \rangle$ (particularly for small ϵ and δ) and a firm conclusion thus cannot be drawn. (As a side note, the Poisson uncertainties are relatively small and contribute at most on the order of 10% to the total uncertainties.)

The possible preference for tracker fields is in contrast with the commonly-discussed expectation $w_\phi^{\text{eff}} \gtrsim -0.8$ for trackers, based on general inverse-power-law series potentials Steinhardt et al. (1999). Here, $w_\phi^{\text{eff}} = \int_{a_{\text{obs}}}^1 w_\phi(a) \Omega_\phi(a) da / \int_{a_{\text{obs}}}^1 \Omega_\phi(a) da$. While this seems to indicate that tracker potentials are disfavoured by current data, our results suggest that the data may act somewhat more strongly against non-tracker models than against tracker ones.

5.6 Conclusions

We have updated parameter constraints on the quintessence potential along with cosmological parameters using recent SNLS supernova luminosity–redshift data, the WMAP3 CMB peak-shift parameter measurement, and the SDSS measurement of baryon oscillations (the ‘basic’ data combination). We have also tested an ‘extended’ data combination consisting of the Union supernova data set, the WMAP5 CMB peak-shift and angular-scale parameters, the 2dF+SDSS measurement of the baryon acoustic scale, and a Big Bang Nucleosynthesis prior on the dark energy density. The preferred field dynamics appear robust under the different parameterizations and data combinations used.

We find that, compared to our previous work (Sahlén et al., 2005), parameter constraints are improved by roughly a factor of two. We also find that linear-potential models where the field rolls uphill, although not excluded, do not provide the best fit to the ‘basic’ data combination. The previous mild preference for these models could have been an artifact of the Riess et al. ‘gold’ SNIa data. This observation agrees with the conclu-

sions of other authors that the SNLS data do not particularly favour an equation of state crossing the phantom divide line, whereas the [Riess et al.](#) data do. Although higher-order potentials are not constrained by the data, those best-fit potentials exhibit ‘cross-over’ behaviour, feeling a curvature in the potential in the recent past. This qualitatively agrees with some well-motivated tracking quintessence models.

Employing the ‘extended’ data combination, we find that parameter constraints are consistent with the ‘basic’ data combination, but improve only negligibly on the ‘basic’ constraints. The ‘extended’ data favour an uphill-rolling field, although such preference disappears once we allow the spatial curvature to be non-zero. We speculate that the high-redshift supernovae in the Union sample could be sensitive to a small curvature component in the Universe, which could manifest itself like this. By contrast, the SNLS supernovae in the ‘basic’ data combination are at lower redshifts.

From the point of view of model selection, the cosmological constant is now even more strongly favoured than in [Sahlén et al. \(2005\)](#), compared to the dynamical models we consider (see also [Saini et al., 2004](#); [Liddle et al., 2006b](#)). The models with curvature in the potential are also strongly disfavoured as compared to the constant and linear potentials, which appear dynamically less natural in the context of the complete evolution expected from high redshift.

We employ a model selection framework to investigate whether potentials that exhibit tracker behaviour at intermediate/late times are favoured by data over those potentials that do not. We conclude that although our results show some indication that tracker behaviour is favoured, the model uncertainty on the result is too large to draw any firm conclusion. We note that if the dynamics of our higher-order best-fit potentials and the preference for a tracking potential both stand up in the light of new data, the coincidence problem in the context of quintessence may simply appear in a new guise — why is the field starting to slow-roll now?

It will be interesting to see how future perturbation growth data will help break degeneracies, and, combined with supernova and CMB data, constrain quintessence models and potentially change the model selection picture as well.

Chapter 6

Forecast Constraints from Galaxy Clusters in the XCS

6.1 Introduction

As explained in Sect. 3.3.2, the abundance of galaxy clusters is a powerful probe of cosmological parameters, in particular the mean matter density Ω_m and the matter field dispersion σ_8 . Several surveys have been proposed with the explicit aim of significantly increasing the number of known distant clusters of galaxies. These proposals rely on a variety of detection methods across a wide range of wavelengths: the Sunyaev–Zel’dovich (SZ) effect in the millimeter (see Carlstrom et al. 2002 for a review, and Juin et al. 2005 for a list of proposed surveys); galaxy overdensities in the visible/infrared (e.g. Gladders & Yee, 2005; Hsieh et al., 2005; Rozo et al., 2007b); bremsstrahlung emission by the intracluster medium (ICM) in the X-rays (e.g. Jahoda & the *DUET* collaboration, 2003; Haiman et al., 2005; Pierre et al., 2008). Galaxy cluster identification using weak lensing techniques is another possibility (e.g. Wittman et al., 2006), but is still in its infancy. Many of these proposals, in particular those regarding the detection of distant clusters through their X-ray emission, imply the building of new observing facilities such as *eROSITA* (Predehl et al., 2006), that will likely take many years to yield results. The cluster X-ray temperature is one of the best proxy observables in lieu of mass; it is a better estimator of the cluster mass than the cluster X-ray luminosity but more difficult to determine (e.g. Balogh et al., 2006; Zhang et al., 2006), and galaxy clusters are also most unambiguously identified in X-ray images. This makes X-ray-based galaxy cluster surveys those with the most accurately determined selection function. For all these reasons, the XCS Consortium has undertaken to construct a galaxy cluster catalogue, called

XCS: XMM Cluster Survey, based on the serendipitous identification of galaxy clusters in public *XMM-Newton* (*XMM*) data (Romer et al., 2001).

The aim of this work is to forecast the expected galaxy cluster samples from the XCS and, based on those, its ability to constrain cosmology and cluster scaling relations using only self-calibration. Specifically, we consider the expected constraints on Ω_m , σ_8 and the luminosity–temperature relation for a flat universe. Our results represent the statistical power expected to be present in the full *XMM* archive. This work builds upon previous efforts in several ways, and to a large extent constitutes the first coherent treatment of effects and methods previously only considered separately. Specifically, we combine all the following characteristics:

1. we use a Monte Carlo Markov Chain (MCMC) approach and can thus characterize all degeneracies exactly (in contrast to Fisher matrix analyses),
2. we include scatter in scaling relations in the parameter estimation (enabled by MCMC),
3. we include a detailed, simulated selection function (essentially that of the *XMM* archive), not a simple hard flux/photon-count/mass limit,
4. we include realistic photometric redshift errors, including degradation and catastrophic errors,
5. we include temperature measurement errors, partly based on detailed simulations of *XMM* observations, and propagate the redshift errors to the temperature, and,
6. we investigate quantitatively the effect on cosmological constraints from systematic errors in cluster scaling relation and measurement error characterization.

Our work builds on the galaxy cluster survey exploitation methods developed and studied primarily in Haiman et al. (2001); Holder et al. (2001); Levine et al. (2002); Hu & Kravtsov (2003); Hu (2003); Battye & Weller (2003); Majumdar & Mohr (2003, 2004); Lima & Hu (2004); Wang et al. (2004a); Lima & Hu (2005). Forecasted cosmological constraints from *XMM* data have also been considered for the *XMM-LSS* survey in Refregier et al. (2002), but they did not take into account scaling-relation scatter or measurement errors, and used the Press–Schechter mass function. The most relevant precursors to this work are Haiman et al. (2001) and Majumdar & Mohr (2004), who consider cosmological constraints expected from the *Dark Universe Exploration Telescope* (*DUET*; Jahoda & the *DUET* collaboration, 2003) – a 10000 deg² X-ray survey with flux

limit $\sim 5 \times 10^{-14}$ erg s $^{-1}$ cm $^{-2}$ in the 0.5-2 keV band. We extend the methodology of both papers through each of the six points above, either by more detailed modelling or by obtaining more robust results through the use of MCMC. Other relevant works are [Huterer et al. \(2004, 2006\)](#) and [Lima & Hu \(2007\)](#), who discuss photometric redshifts. We particularly complement these analyses through our detailed treatment/inclusion of measurement errors and selection effects. The recent work by [Rapetti et al. \(2008\)](#) takes an approach similar to ours in that they employ MCMC, include scaling-relation scatter and consider measurement errors, but focuses on combining future X-ray gas mass fraction measurements with SZ cluster and CMB power spectrum data.

The structure of this Chapter is as follows. We begin by reviewing the progress to date of the XCS and present the survey selection function (Sect. 6.2). Next, we present the models and methodology we use to derive constraints on cosmological parameters from the simulated XCS sample (Sects. 6.3 & 6.4). We then go on to the expected cluster distributions and, our estimates for the constraints on σ_8 , Ω_m , and cluster scaling relation parameters that we expect to obtain from the XCS using self-calibration, including the effect of temperature measurement errors and relying on photometric methods to obtain XCS galaxy cluster redshifts (Sect. 6.5). We discuss and summarize our findings in Sect. 6.6. Additional material setting out modelling details is provided in Appendix B.

6.2 The *XMM* Cluster Survey (XCS)

6.2.1 Background and Current Status

XMM-Newton is the most sensitive X-ray spectral imaging telescope deployed to date. It is typically used in pointing mode, whereby it observes a single central target for a long period of time (the typical exposure time being ~ 20 kilo-seconds). The field of view of the *XMM* cameras is roughly half a degree across, so that a considerable area around the central target is observed ‘for free’ during these long pointings. Already many thousands of these pointings are available in the public *XMM* archive. The XCS is exploiting this archive by carrying out a systematic search for serendipitous detections of clusters of galaxies in the outskirts of *XMM* pointings ([Romer et al., 2001](#)). Once a cluster candidate has been selected from the archival imaging data, it is then followed up using optical imaging and/or optical spectroscopy, to confirm the identification of the X-ray source and to measure redshifts (see Sect. 6.3.4). For those XCS clusters that were detected with sufficient counts, an X-ray spectroscopy analysis is carried out, again using the archival

Survey	⁵⁰⁰ XCS
Sky coverage	500 deg ² (serendipitous)
Redshift coverage	0.1 – 1.0
X-ray temperature coverage	2 – 8 keV
Min. photon count	500
X-ray flux limit	By selection function ^a

^a The flux limit is $\sim 3.5 \times 10^{-13}$ erg s⁻¹ cm⁻² in the [0.1, 2.4] keV band, if defined as a probability of detection greater than or equal to 50%. See also Sect. 6.5.2 and Fig. 6.9.

Table 6.1: Survey specifications.

data, in order to measure the temperature of the hot intracluster medium (ICM). These temperatures can then be used to study cluster scaling relations and/or to estimate the mass of the cluster (see Sects. 6.3.2 & 6.3.3).

The XCS project is ongoing, but already more than 2000 *XMM* pointings have been analysed, yielding a cluster candidate catalogue numbering almost 2000 entries. So far, the XCS covers a combined area of 170 square degrees suitable for cluster searching; i.e. this 170 deg² area excludes overlapping and repeat exposures, regions of low Galactic latitude, the Magellanic clouds, and pointings with very extended central targets. With many thousand more *XMM* pointings waiting to be analysed by the XCS, and a mission lifetime extending to 2013, a conservative estimate for the final XCS area for cluster searching is 500 square degrees. We use 500 deg² herein for XCS cosmology forecasting (see Table 6.1), assume a redshift range of $0.1 \leq z \leq 1$, and temperatures of $2 \text{ keV} \leq T \leq 8 \text{ keV}$. We further limit our representative survey to clusters with photon counts > 500 (⁵⁰⁰XCS hereafter), so that we can be sure to estimate X-ray temperatures with reasonable accuracy (see Sect. 6.3.5). The lower redshift limit is associated with cluster extents becoming too large, and the cosmic volume also becoming small. The maximum redshift is chosen so that the luminosity–temperature relation can still be reliably modelled/estimated (see Sect. 6.3.3). The temperature range is chosen such that we can expect i) a small contamination from galaxy groups (which typically have temperatures $T < 2 \text{ keV}$), yet include as many of the numerous low-temperature clusters as possible, and ii) that clusters above the high-temperature limit are sufficiently rare that none can be expected. The final cluster catalogue (without the cut-offs defined above for ⁵⁰⁰XCS) will contain several thousand

clusters out to a redshift of $z \approx 2$. The highest-redshift cluster discovered by the XCS so far is XMMXCS J2215.9-1738 at $z = 1.457$ (Stanford et al., 2006; Hilton et al., 2007).

In addition to producing one of the largest samples of X-ray clusters ever compiled, the XCS will also be a valuable resource for cosmology studies (see Sect. 6.4). This is because the catalogue will be accompanied by a complete description of the selection function. In this work we make use of an initial XCS selection function that assumes simple models for the distribution of the ICM, and flat cosmologies (see below). Future cosmology analyses will take advantage of more sophisticated selection functions that are based on hydrodynamical simulations of clusters (Kay et al., 2007).

6.2.2 The XCS Selection Function

In order to properly model the selection function of a survey like the XCS, it is important to account for all of the observational variations present in real data. We can achieve this by placing a sample of fake surface-brightness profiles into real *XMM* Observation Data Files (ODFs). This ensures that our simulated images re-create real-life issues such as clusters lying on chip gaps and point-source contamination. The fake surface-brightness profiles are created as follows. We use an isothermal β model with $\beta = 2/3$, core radius $r_c = 160$ kpc, and plasma metallicity $Z = 0.3Z_\odot$. For a given cosmology we simulate 700 sets of cluster parameters:

- 10 redshifts (linearly spaced 0.1–1.0)
- 10 luminosities (logarithmically spaced $0.178\text{--}31.623 \times 10^{44}$ erg s $^{-1}$)
- 7 temperatures (linearly spaced 2–8 keV)

For selection function determination, we drew on a list of 1764 ODFs that have already been processed by the XCS and have been deemed to be suitable for cluster searching (see above). Before each selection function run, a smaller list of 100 ODFs is selected at random from the full set of 1764. These 100 ODFs are then copied from the main XCS archive to local processing nodes for temporary storage, to speed up the analysis. Tests have shown that with 100 ODFs it is still possible to reproduce the variance in exposure time, target type, point source density, etc., inherent to the XCS. In the following we define a ‘selection function run’ as the analysis over the 700 sets of cluster parameters and 100 ODFs – a total of 70000 combinations.

For each of the 700 different combinations of cluster parameters, the process proceeds as follows. First, to account for the fact that the XCS searches the entire field of view

for serendipitous cluster detections, the centre of the fake surface-brightness profile is randomly positioned into a blank *XMM*-style ODF, with a uniform probability across the field of view. The profile is then convolved with the appropriate PSF model. For this purpose we use the two-dimensional medium-accuracy model¹. At this stage, an ODF is chosen at random from the list of 100 stored locally, into which the fake source will later be added. The profile is then assigned an absorbed count rate using a series of arrays calculated using XSPEC (Arnaud, 1996). The arrays tabulate conversions from unabsorbed bolometric luminosity to absorbed count-rate as a function of temperature, redshift, hydrogen column density, and *XMM* camera/filter combination. The fake count-rate image is then multiplied by the exposure map of the chosen ODF to account for vignetting, masking and chip gaps. Finally, the fake cluster image is added to the original ODF at the chosen position, and the ODF is run through our source detection/classification pipeline to determine if the fake cluster passes our automated cluster-candidate selection process. For more details on the detection/classification pipeline, refer to Davidson et al. (in preparation). The process is repeated a total of one hundred times, so that we can build up an average XCS detectability for that parameter combination. Once the full set of 700 combinations has been tested 100 times each, the run is complete. We then change the cosmology inputs and start the entire sequence again. The process is very CPU intensive; each selection function run (of 700×100 combinations) takes several weeks to run on a single node. For the forecasting work presented herein, we carried out seven selection function runs over the flat Λ CDM cosmologies with $\Omega_m = 0.22, 0.26, 0.28, 0.30, 0.32, 0.34$ and 0.38 . We limit ourselves to flat cosmologies as we use a flatness prior in the forecasting of cosmological constraints.

The resulting selection function is shown in Fig. 6.1 for the two luminosity–temperature relations (see Sect. 6.3.3) we consider. Note that the selection function in regions where we have not calculated it explicitly is extrapolated from the region where we have done so. Hence, its features in those extrapolated regions should only be considered a rough indication of its behaviour, particularly in the high-redshift, high-temperature region. This region is only relevant for including measurement errors, and since such high-temperature clusters are exceedingly rare, the uncertainty in this part of the selection function has no significant impact on our results².

¹http://xmm.vilspa.esa.es/external/xmm_sw_cal/calib/

²We have verified this with further numerical calculations.

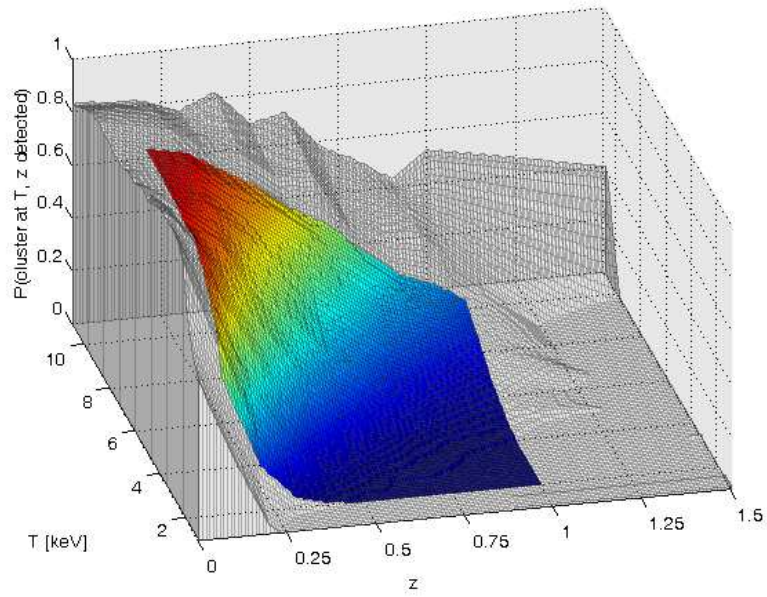
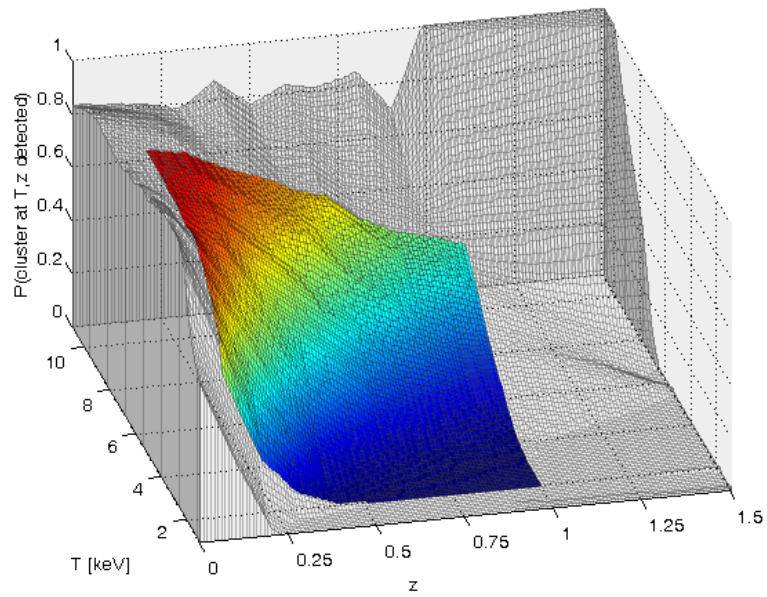
(a) Constant L - T relation(b) Self-similar L - T relation

Figure 6.1: Selection function for our fiducial cosmology and different L - T evolution. Values in the shaded region are extrapolated from those in the coloured region ($0.1 \leq z \leq 1.0$, $2 \text{ keV} \leq T \leq 8 \text{ keV}$), for which the selection function has been calculated explicitly.

6.3 From X-ray Observables to Mass

6.3.1 Modelling Summary

Making predictions for X-ray cluster observations requires the modelling of scaling relations to relate temperature to mass, and temperature to luminosity. In addition, the observables will have uncertainties associated with them, which need to be taken into account. The following subsections detail our modelling assumptions, but we summarize them here for reference and orientation.

We first assume that we know a priori exactly how the cluster X-ray temperature relates to luminosity at the present time, and how this relation evolves with redshift. We then study how the constraints on cosmological parameters degrade if such an assumption is dropped. We consider four extra free parameters: two parameters to characterize the present-day, power-law, relation between cluster X-ray temperature and luminosity, another to describe its redshift evolution as a power of $(1 + z)$, and lastly one for the logarithmic dispersion in the (assumed) Gaussian distribution of the intrinsic (redshift-independent) scatter in the relation between cluster X-ray temperature and luminosity.

In addition, we evaluate the full impact on the XCS's ability to impose constraints on cosmological parameters that arises from assuming a dispersion in the Gaussian photometric redshift distribution of either 5 or 10 percent about the true redshift, both with and without the presence of unaccounted-for catastrophic errors in the photometric redshift estimation procedure. Further, we will also determine the impact of a systematic mis-estimation of the assumed true dispersion in the photometric redshifts about the true redshift. Our aim is to test the impact of realistic assumptions regarding the distribution of photometric redshifts around the true redshift, and then determine by how much such impact increases by considering a worst-case scenario.

Similarly, we consider the impact of realistic X-ray temperature errors obtained from simulations based on the relevant *XMM* fields, as well as significantly larger errors corresponding to a worst-case scenario. Lastly, we consider the impact of incorrect assumptions about the cluster scaling relations on cosmological constraints.

Summary tables with our main cluster scaling relation and measurement error assumptions are given in Sect. 6.5. Detailed information on the mathematical treatment is given in Appendix B.

6.3.2 The X-ray Temperature to Mass Relation

We need to assume a relation between cluster X-ray temperature and mass to be able to predict cluster distributions. The reason is that presently the effect of cosmological parameters on the galaxy cluster population can only be accurately predicted as a function of cluster mass (e.g. [Reiprich & Böhringer, 2002](#)). The X-ray temperature is one of the best proxy observables, as explained in Sect. 6.1.

Evolution

We assume the self-similar prediction (e.g. [Kaiser, 1986](#); [Bryan & Norman, 1998](#); [Voit, 2005a](#)),

$$T \propto M_v^{2/3} [\Delta_v(z) E^2(z)]^{1/3}, \quad (6.1)$$

for the redshift dependence of the relation between cluster X-ray temperature and virial mass to hold for any combination of cosmological parameters, given that it is consistent with the most recent analyses of observational data ([Ettori et al. 2004a,b](#); [Arnaud et al. 2005](#); [Kotov & Vikhlinin 2005, 2006](#); [Vikhlinin et al. 2006](#); [Zhang et al. 2006](#)). Here M_v is the cluster virial mass, while $\Delta_v(z)$ is the mean overdensity within the cluster virial radius with respect to the critical density. If the only relevant energy densities in the Universe are those associated with non-relativistic matter and a cosmological constant, then from Eq. (2.23) on p. 15,

$$E^2(z) = \Omega_m(1+z)^3 + (1 - \Omega_m), \quad (6.2)$$

where we have also restricted ourselves to a flat universe, $\Omega_k = 0$, as we will in our analysis – see Sect. 6.4.2. Deviations from a self-similar mass–temperature relation will be considered in Sect. 6.5.5, as also explained in Sect. 6.3.3.

Normalization

The constant of proportionality is set by demanding that for our fiducial cosmological model (with $\sigma_8 = 0.8$, see Sect. 6.4.2)

$$M_{500} = 3 \times 10^{14} h^{-1} M_\odot \quad (6.3)$$

at $z = 0.05$ for an X-ray temperature of 5 keV, where M_{500} is the mass within a sphere centered on the cluster within which its mean density falls to 500 times the critical density at the cluster redshift. In this way, our fiducial cosmological model reproduces the local abundance of galaxy clusters as given by the HIFLUGCS catalogue ([Reiprich & Böhringer 2002](#); [Pierpaoli et al. 2001](#); [Viana et al. 2003](#)). Note that such a normalization of the

cluster X-ray temperature to mass relation happens to be very close to that directly derived from X-ray data by [Arnaud et al. \(2005\)](#) and [Vikhlinin et al. \(2006\)](#).

The conversion between M_{500} and the halo mass, $M_{180\Omega_m(z)}$, will be carried out by using the formulae derived by [Hu & Kravtsov \(2003\)](#) under the assumption that the halo density profile is of the NFW type ([Navarro et al., 1995, 1996, 1997](#)), and we will take the concentration parameter to be 5. This has been shown to provide a good description of the typical density profile in galaxy clusters (see [Arnaud 2005](#) or [Voit 2005b](#) and references therein; [Vikhlinin et al. 2006](#)).

The normalization of the M - T relation is subject to a number of uncertainties, the most important of which are the possible violation of hydrostatic equilibrium ([Rasia et al. 2004; Nagai et al. 2007](#)) and the possible difference between the spectroscopic X-ray temperature and the temperature of the electron gas ([Mazzotta et al., 2004; Rasia et al., 2005; Vikhlinin, 2006](#)). The precise level of these effects remains to be firmly established, but could be of the order 50% in the normalization mass (e.g. [Vikhlinin, 2006; Nagai et al., 2007](#)). The scatter, as well as slope, could also be under-estimated due to these effects ([Vikhlinin, 2006; Nagai et al., 2007](#)). We make some estimates of all these systematic effects on cosmological constraints in Sect. 6.5.5.

Scatter

We assume that the intrinsic scatter in the relation between cluster X-ray temperature and mass has a Gaussian distribution (truncated at 3σ and re-normalized) with a redshift-independent dispersion of 0.10 about the logarithm of the temperature. This is motivated by both cluster X-ray data analysis (e.g. [Arnaud et al., 2005; Vikhlinin et al., 2006; Zhang et al., 2006](#)) and results from N -body hydrodynamic simulations (e.g. [Viana et al. 2003; Borgani et al. 2004; Balogh et al. 2006; Kravtsov et al. 2006](#)). As explained in the preceding Section, we consider systematic deviations in the scatter in Sect. 6.5.5.

6.3.3 The X-ray Luminosity to Temperature Relation

In order to understand how the XCS selection function depends on cluster mass, we need to know how cluster X-ray luminosity and temperature relate to cluster mass (see Sect. 6.2.2). In practice, we will use the relation between luminosity and temperature instead of that between luminosity and mass, in effect relating these two quantities via the temperature. This makes sense because the estimation of cluster mass from X-ray data is always based on the X-ray temperature, via the assumption of hydrostatic equilibrium, and not on

the luminosity. Thus, while we always need, at least implicitly, to know how the cluster luminosity relates to temperature to derive the relation between the luminosity and mass from X-ray data, the reverse is not true.

As for the mass–temperature relation, assuming self-similarity leads to a specific prediction (Kaiser, 1986),

$$L(z, T) = L(0.05, T) \left[\frac{\Delta_v(z) E^2(z)}{\Delta_v(0.05) E^2(0.05)} \right]^{1/2}, \quad (6.4)$$

under which clusters with the same X-ray temperature are predicted to be more X-ray luminous if they have a higher redshift. We have chosen here to normalize the relation with respect to the local ($z = 0.05$) relation. Based on this expression, we write the L – T relation in the general form

$$\log_{10} \left(\frac{L_X}{10^{44} h^{-2} \text{ erg s}^{-1}} \right) = \alpha + \beta \log_{10} \left(\frac{kT}{1 \text{ keV}} \right) + \gamma_s \log_{10} [\Delta_v(z) E^2(z)] + \gamma_z \log_{10} (1 + z) + N(0, \sigma_{\log L_X}), \quad (6.5)$$

and discuss below the assumptions made for the different parameters.

Evolution (γ_s, γ_z)

We consider two possible fiducial scenarios, which bracket most observational results and theoretical expectations: either

- no evolution ($\gamma_s = \gamma_z = 0$) *or*
- self-similar evolution ($\gamma_s = 1/2, \gamma_z = 0$)

for the fiducial combination of cosmological parameters. The parameters γ_s and γ_z are defined above in Eq. (6.5). Presently, there is some uncertainty surrounding the redshift evolution of the relation between cluster X-ray luminosity and temperature. Essentially, what we know is how that relation behaves for redshifts below 0.3 (e.g. Ikebe et al. 2002; Novicki et al. 2002; Ota et al. 2006; Zhang et al. 2006). For higher redshifts, the data is still sparse, and the evidence contradictory, from claims that the relation between cluster X-ray luminosity and temperature barely evolves at all with redshift (Holden et al., 2002; Ettori et al., 2004a,b; Ota et al., 2006; Branchesi et al., 2007), to claims that its evolution is close to the self-similar prediction (Novicki et al., 2002; Vikhlinin et al., 2002; Lumb et al., 2004; Kotov & Vikhlinin, 2005; Maughan et al., 2006; Zhang et al., 2006; Hicks et al., 2008). Some authors argue that self-similarity remains viable at all redshifts, and that at least some of the observed discrepancies could be due to selection

effects, as the Malmquist bias from scaling-relation scatter (also discussed below) could distort the deduced evolution if the sample selection is not sufficiently understood (e.g. Branchesi et al., 2007; Maughan, 2007; Pacaud et al., 2007; Nord et al., 2008). On the other hand, Hilton et al. (2007) argue for deviation from the self-similar prediction based on a set of high-redshift clusters combined with the recently discovered XCS cluster XMMXCS J2215.9-1738 at $z = 1.457$.

When the XCS catalogue becomes available, the relation between cluster X-ray luminosity and temperature, as a function of redshift, will be estimated jointly with the cosmological parameters, but for now we will have to rely on the limited information available.

Normalization & Slope (α, β)

We assume the local ($z = 0.05$) relation between the cluster X-ray luminosity in the *ROSAT* [0.1, 2.4] keV band and temperature to be

$$\log_{10} \left(\frac{L_X}{h^{-2} \text{ erg s}^{-1}} \right) = 42.1 + 2.5 \log_{10} \left(\frac{kT}{1 \text{ keV}} \right), \quad (6.6)$$

as was derived in Viana et al. (2003) for a combination of cosmological parameters similar to those assumed for our fiducial cosmological model. The X-ray data used in Viana et al. (2003) was that of galaxy clusters present in the HIFLUGCS catalogue (Reiprich & Böhringer, 2002), and therefore the conversion between L_X and X-ray bolometric luminosity is performed through a fit (derived by us) based on the values both quantities take for the galaxy clusters in HIFLUGCS,

$$L_{\text{bol}} = \frac{L_X}{0.25 + 0.7 \exp(-0.23kT/1 \text{ keV})}. \quad (6.7)$$

As in Ikebe et al. (2002), the relation between the cluster X-ray luminosity and temperature derived in Viana et al. (2003) takes into account the fact that any flux-limited sample of galaxy clusters will be composed of objects which are on average more X-ray luminous than the mean luminosity of all existing galaxy clusters with the same redshift and X-ray temperature. This Malmquist type of bias increases with decreasing temperature, and thus ignoring it leads not only to an overestimation of the normalization of the relation between luminosity and temperature, but also to an underestimation of its slope.

Scatter ($\sigma_{\log L_X}$)

We assume that the intrinsic scatter in the relation between cluster X-ray luminosity (in the 0.1 to 2.4 keV band) and temperature has a redshift-independent Gaussian distribution

(truncated at 3σ and re-normalized) about the logarithm of the X-ray luminosity, with 1σ dispersion $\sigma_{\log L_X} = 0.30$ (Ikebe et al., 2002; Viana et al., 2003). This is also close to what was found by Kay et al. (2007) in the CLEF simulation. Although Kay et al. also observe an evolution of the scatter with redshift, there is no strong observational evidence for or against such an evolution at present, and therefore we do not include it in our analysis.

The existence of intrinsic scatter in the relation between cluster luminosity and mass will effectively increase the observed number of galaxy clusters above any X-ray luminosity (or flux) threshold, relative to the case without scatter. This results from the steepness of the cluster mass function, due to which significantly more clusters have their X-ray luminosity scattered up than down across any given luminosity threshold. Therefore, intrinsic scatter between X-ray luminosity and mass can have a considerable impact on the predicted number of XCS clusters and on the estimation of the constraints the XCS will impose on cosmological parameters. This scatter can be considered as the combination of the scatter in the luminosity to temperature and temperature to mass relations, with clear observational evidence that the former dominates over the latter (Stanek et al., 2006; Zhang et al., 2006).

As higher redshifts are considered, it is expected that an increasing number of galaxy clusters will have undergone recent major mergers, not only leading to increased scatter in the cluster scaling relations but also making its distribution highly non-Gaussian, with long tails developing towards both high X-ray luminosity and, to a lesser degree, temperature, at fixed mass (Randall et al., 2002). This has the potential to substantially affect the estimation of the constraints the XCS will be able to impose on cosmological parameters. There is a lack of high-redshift observational data in this regard and we are also not confident that we will detect, for the purposes of understanding this behaviour, many useful clusters at $z > 1$. We therefore chose to consider in the estimation procedure only those clusters in the mock XCS catalogues which have a redshift $z \leq 1$.

6.3.4 Photometric Redshifts

The Role of Photometric Redshifts

Redshifts are required for XCS clusters, both to place them correctly in the evolutionary sequence and to allow the measurement of X-ray temperatures from *XMM* spectra. With regard to the latter point, pure thermal bremsstrahlung spectra are essentially featureless (barring a high-energy cut-off), making them degenerate in temperature and redshift. Therefore, in the absence of independent redshift information, all one can measure from a

typical XCS cluster spectrum would be a so-called apparent X-ray temperature, i.e. one scaled by $(1+z)$, see Appendix B.1.2. As shown by Liddle et al. (2001), these apparent temperatures are not sufficient to allow one to measure cosmological parameters from cluster catalogues. As a result, optically-determined redshifts will be required for almost all clusters in the XCS catalogue (the exception being a tiny number that are detected with sufficient signal to noise to allow X-ray emission features, such as the Iron K complex at ~ 7 keV, to be resolved over the thermal continuum).

As is now typical for cluster surveys (e.g. Gladders & Yee, 2005), the XCS is relying heavily on the photometric redshift technique for its optical follow-up. This is because photometric redshifts are much more efficient, in terms of telescope time requirements, than spectroscopic redshifts. However, they have the disadvantage, over spectroscopic redshifts, that the redshift errors are larger and sometimes poorly understood. The XCS is using both public-domain photometry (e.g. from SDSS and 2MASS) and proprietary data from the NOAO–XCS Survey (NXS, Miller et al., 2006) to both optically confirm (as clusters) XCS candidates and to measure photometric redshifts. To date, more than 400 XCS candidates have been optically confirmed in this way.

Errors on photometric redshifts must be accounted for when determining cosmological parameters from cluster surveys, and so we have included prescriptions for such errors in the forecasting work presented herein. Our prescriptions include both purely statistical errors and so-called catastrophic systematic errors. As shown by previous work (Huterer et al., 2004, 2006; Lima & Hu, 2007), purely statistical errors have a negligible impact on cosmological parameter constraints. By contrast, if catastrophic errors are not accounted for properly in the fitting, they could have a significant impact on cosmological parameter constraints. We note that previous work has concentrated only on the impact of redshift errors on the evolutionary sequence, whereas we have also included the impact of photometric errors on X-ray temperature determinations.

Distribution

Following Huterer et al. (2004) we assume that the statistical error in the photometric redshifts of individual galaxy clusters has a Gaussian distribution about the true redshift, z_t . In an attempt to reproduce the expected degradation with redshift of the absolute accuracy of cluster photometric redshift estimation methods, and in contrast to Huterer et al. (2004) but in the same way as Lima & Hu (2007), we will assume the dispersion to be proportional to $(1+z_t)$, normalized at $z_t = 0$ to either $\sigma_0 = 0.05$ or $\sigma_0 = 0.10$ (Gladders & Yee,

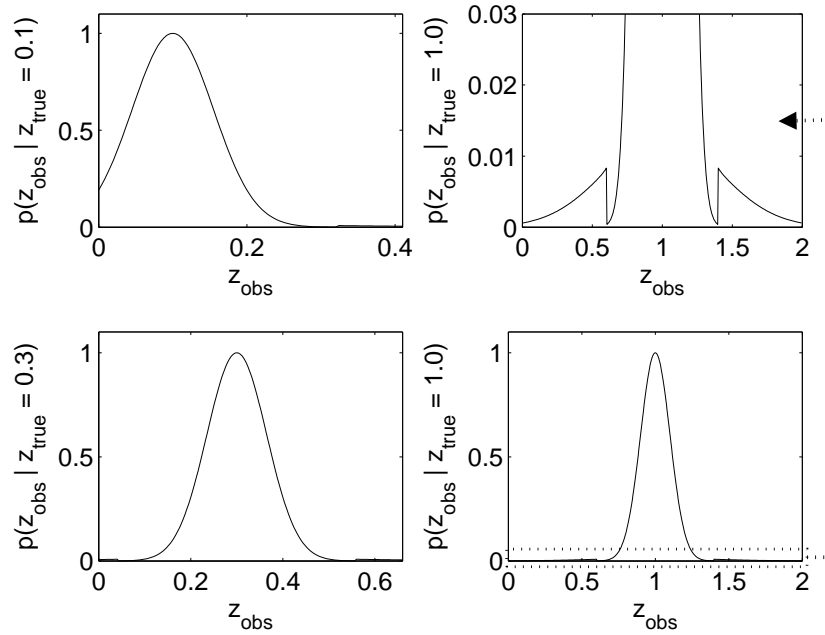


Figure 6.2: Realistic redshift error distributions at various redshifts. The upper right panel shows a magnification of the bottom-right distribution, highlighting the catastrophic-error part of the distribution.

2000; Gladders, 2004; Gladders & Yee, 2005; Gladders et al., 2007). Unaccounted-for systematic errors in the photometric redshift estimation procedure are much harder to model, because they can take a variety of guises. We will consider here one such type of error: catastrophic errors in the photometric redshift estimation procedure. The existence of unaccounted-for catastrophic errors will be modelled by assigning a random photometric redshift error to either a fraction $f_{\text{cat}} = 0.05$ or $f_{\text{cat}} = 0.10$ of the galaxy clusters, drawn from a Gaussian distribution that has four times the dispersion of the standard distribution, with the requirement that the photometric redshift error has to be at least 1σ away from the true redshift. The functional form of the redshift error distribution is given in Appendix B.1.

We label the case $\{\sigma_0 = 0.05, f_{\text{cat}} = 0.05\}$ ‘realistic’ and the case $\{\sigma_0 = 0.10, f_{\text{cat}} = 0.10\}$ ‘worst-case’ redshift errors. Examples of realistic redshift error distributions are shown in Fig. 6.2.

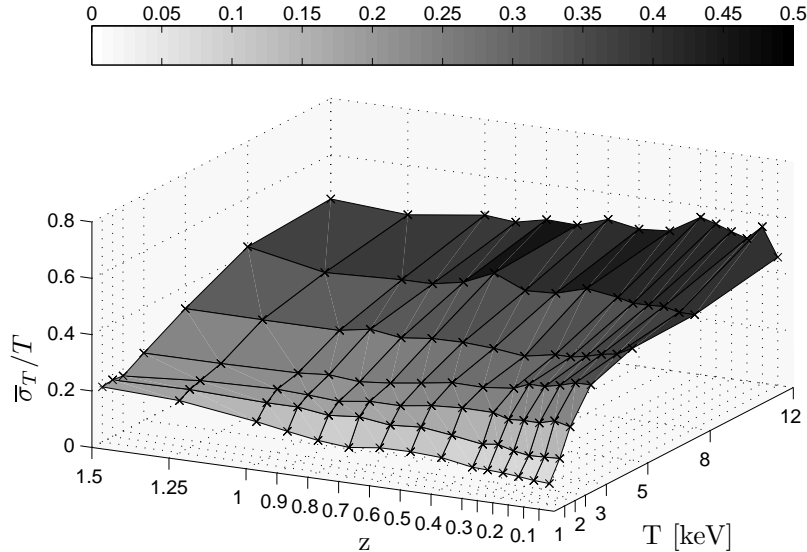


Figure 6.3: Mean fractional temperature errors from the simulations performed, for 500 photons, and as marginalized over expected absorption columns for the XCS.

6.3.5 X-ray Temperature

Estimating the Measurement Errors

Initial estimates (Liddle et al., 2001) showed that X-ray temperatures measured for XCS clusters are expected to have an associated measurement uncertainty of less than 20 percent at 1σ . However, these estimates were based on a photon count of 1000 and assume a single hydrogen column density over the *XMM* fields, and are therefore not directly applicable to our 500 XCS sample. Hence, in order to estimate the temperature errors that will be present in the XCS statistical sample more accurately, we have conducted Monte Carlo simulations using the XSPEC spectral fitting package (Arnaud, 1996). We created 1000 sets of fake spectra for the *XMM-Newton* EPIC PN and MOS instruments, from a MEKAL plasma model (Mewe et al., 1986) multiplied by a WABS photo-electric absorption model (Morrison & McCammon, 1983). Responses for a mean off-axis angle were used and a mean background was added. The model was then fitted to each of the spectra to derive a temperature. A plasma metallicity of $0.3Z_{\odot}$ was used throughout, in accordance with the assumptions in our selection function calculations (see Sect. 6.2.2), and we assume a photon count of 500. This procedure was repeated for a range of input temperatures, redshifts and absorption columns. We then marginalize over the hydrogen absorption columns using the expected hydrogen column distribution for our *XMM* fields.

The mean fractional temperature errors from our simulations are shown in Fig. 6.3.

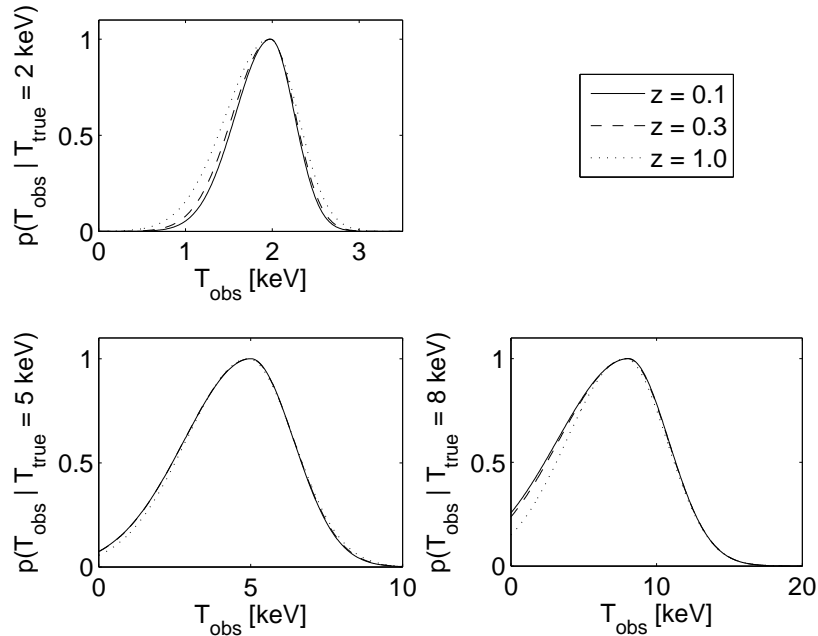


Figure 6.4: Realistic temperature error distributions at various redshifts and temperatures, based on our *XMM-Newton* simulations, for a photon count of 500.

The largest influence on the temperature errors comes from the input temperature itself. Since metal lines in the spectrum provide much better constraints on the temperature than the shape of the bremsstrahlung continuum, and the fraction of line emission in the spectrum declines with increasing temperature, the errors are larger for hotter clusters. The effect of redshift on the errors is much smaller and itself temperature-dependent. For low-temperature systems at high redshifts, part of the X-ray spectrum is shifted out of the bottom of the *XMM* passband, increasing the errors. For high-temperature systems, the effect of increasing redshift is to shift the source spectrum to lower energies for which the *XMM* effective area is larger, thus decreasing the errors.

Distribution

The distribution of temperatures obtained in our simulations was fitted by an asymmetric Gaussian function to parameterize the temperature error distribution, with the fractional error given by a two-dimensional quadratic expression in temperature and redshift. We marginalize over the distribution of absorption columns found in XCS fields to obtain mean parameters for our asymmetric Gaussian error distribution. The exact functional form of the fitted error distribution is given in Eq. (B.8), p. 196 in Appendix B.1.

We will label the case with σ_T according to our simulation results as ‘realistic’ and

the case with three times this dispersion as ‘worst-case’ temperature errors. Examples of realistic temperature error distributions are shown in Fig. 6.4 (p. 123). Note that, as we are assuming that all detected clusters have a photon count of exactly 500, our error distributions represent a worst-case scenario in this regard.

6.4 From Mass to Cosmology and Constraints

6.4.1 The Mass Function

Having connected our direct X-ray observables to cluster mass using the methodology in the preceding Section, we can then combine these relations with the mass function (below) to find the cluster distribution as a function of temperature and redshift. As explained in Sect. 3.3.2, the differential comoving number density of haloes in a mass interval dM about M at redshift z can be written as

$$n(M, z) dM = -F(\sigma) \frac{\rho_{m,0}}{M\sigma(M, z)} \frac{d\sigma(M, z)}{dM} dM, \quad (6.8)$$

where $F(\sigma)$ is the mass function, $\sigma(M, z)$ is the dispersion of the density field at some comoving scale $R = (3M/4\pi\rho_{m,0})^{1/3}$ and redshift z , and $\rho_{m,0}$ is the matter density at the present time.

Parameterization

We will use the Jenkins mass function, Eq. (3.44) on p. 45, to parameterize the mass function $F(\sigma)$. As explained in Sect. 3.3.2, this is a good fit to N -body-simulation mass functions. We therefore use this fit to estimate the expected number density of haloes for any given combination of cosmological parameters. This also makes the like-for-like comparison with other cluster constraints straightforward, as most rely on the Jenkins mass function. The dispersion σ is calculated using the fit in Eqs. (3.22) & (3.23), p. 26.

6.4.2 Cosmology

We have already seen that cosmology enters into the prediction of cluster numbers as a function of temperature and redshift through the selection function, the cluster scaling relations, and the mass dispersion. Additionally, the cosmic volume dV/dz , Eq. (3.42) on p. 44, will also enter as we need to multiply the differential distribution by this quantity (discussed in the following Section).

Parameter	Value	Prior
Ω_m	0.3	[0.1, 1]
Ω_Λ	0.7	$1 - \Omega_m$
σ_8	0.8	[0.3, 1.3]
Ω_b	0.044	0.044
h	0.75	0.75
n_s	1	1

Table 6.2: Cosmology assumptions used. Fiducial values are given first, followed by priors assumed in parameter estimation.

Parameters

We work within the Cold Dark Matter (CDM) paradigm, with adiabatic, Gaussian primordial scalar density perturbations. We assume that $\Omega_m = 0.3, \Omega_\Lambda = 0.7, \sigma_8 = 0.8, \Omega_b = 0.044$ and $h = 0.75$. Although the Hubble constant h will affect the probability of detecting clusters through its effect on the observed luminosity, we fix it here for simplicity and since we are mainly interested in the other cosmological parameters listed above. We also expect that the effect of h on Γ (see below) will be of more significance. As we do not expect the XCS to have particularly competitive constraining power on Ω_k , we restrict our analysis to the case of a flat universe, $\Omega_k = 0$, in accordance with observations of e.g. the cosmic microwave background (Komatsu et al., 2008). We take the present-day shape of the matter power spectrum to be well approximated by a CDM model with scale-invariant primordial density perturbations whose transfer function shape parameter is $\Gamma \approx \Omega_m h \times \exp[-\Omega_b(1 + \sqrt{2h}/\Omega_m)] = 0.18$. This is the mean value obtained from different analyses of SDSS data (Szalay et al., 2003; Pope et al., 2004; Tegmark et al., 2004; Eisenstein et al., 2005; Blake et al., 2007; Padmanabhan et al., 2007) and also perfectly compatible with the 5-year *WMAP* data (Komatsu et al., 2008). We have checked that assuming Γ is either 0.16 or 0.20 does not change our results. (In a real data analysis, using the shape parameter is too simplistic, but for forecasting purposes it is sufficient.) A summary of our cosmological parameter assumptions is given in Table 6.2.

6.4.3 Combining Observables and Cosmology

As we have seen, our cluster distribution calculations involve many different steps and components. Importantly, they rely on both simulation and observational data, as well

as direct theoretical input. A schematic overview of the relevant inputs, processes and outputs is shown in a flowchart form in Fig. 6.5. Collecting all components (see also Sect. 3.3.2), the number of clusters in $dTdz$ around (T, z) is given by

$$n(M(T, z), z) \frac{dM}{dT} f_{\text{sky}}(L(T, z), T, z) \frac{dV}{dz} dT dz \quad (6.9)$$

where f_{sky} combines survey area and selection function. This expression ignores scatter in the scaling relations and measurement errors. A complete treatment is given in Appendix B.1. The remaining component for arriving at parameter constraints is the likelihood, which is described next.

6.4.4 Likelihood

Turning our attention to using the cluster distribution prediction for cosmological constraints and forecasting, we need an expression for the likelihood of an observed catalogue of galaxy clusters. The likelihood \mathcal{L} for a given observed catalogue is simply the product of the Poisson probabilities of observing N_i XCS clusters in the bin with widths $\Delta T, \Delta z$ centered at each of the (T_i, z_i) positions,

$$\mathcal{L} = \prod_i \left[\frac{\lambda_i^{N_i}}{N_i!} e^{-\lambda_i} \right] \quad (6.10)$$

where

$$\lambda_i = N(T_i - \Delta T/2, T_i + \Delta T/2, z_i - \Delta z/2, z_i + \Delta z/2) \quad (6.11)$$

is the expected number of XCS clusters in bin i , taking into account sky coverage, survey selection function, and any uncertainties in scaling relations or measurements (see equations in Appendix B.1). We do not take into account the fact that the positions of galaxy clusters are spatially correlated, because the mean distance between XCS clusters is typically much larger than the observationally determined correlation length in the range $10 - 20 h^{-1} \text{ Mpc}$ (see e.g. Nichol et al. 1992; Romer et al. 1994; Collins et al. 2000; Gonzalez et al. 2002; Brodwin et al. 2007), as a result of the *XMM* pointings being scattered all over the sky. Even if the XCS area was contiguous, given the very large depth of the XCS, the impact of cluster spatial correlations on the estimation of cosmological parameters with the XCS galaxy cluster abundance data would be small (White, 2002; Hu & Kravtsov, 2003; Holder, 2006; Hu & Cohn, 2006). Such information can however be very useful for the purposes of self-calibrating the $M-T$ relation, and is a powerful component in contiguous surveys (e.g. Lima & Hu, 2004, 2005; Majumdar & Mohr, 2004; Wang et al., 2004a).

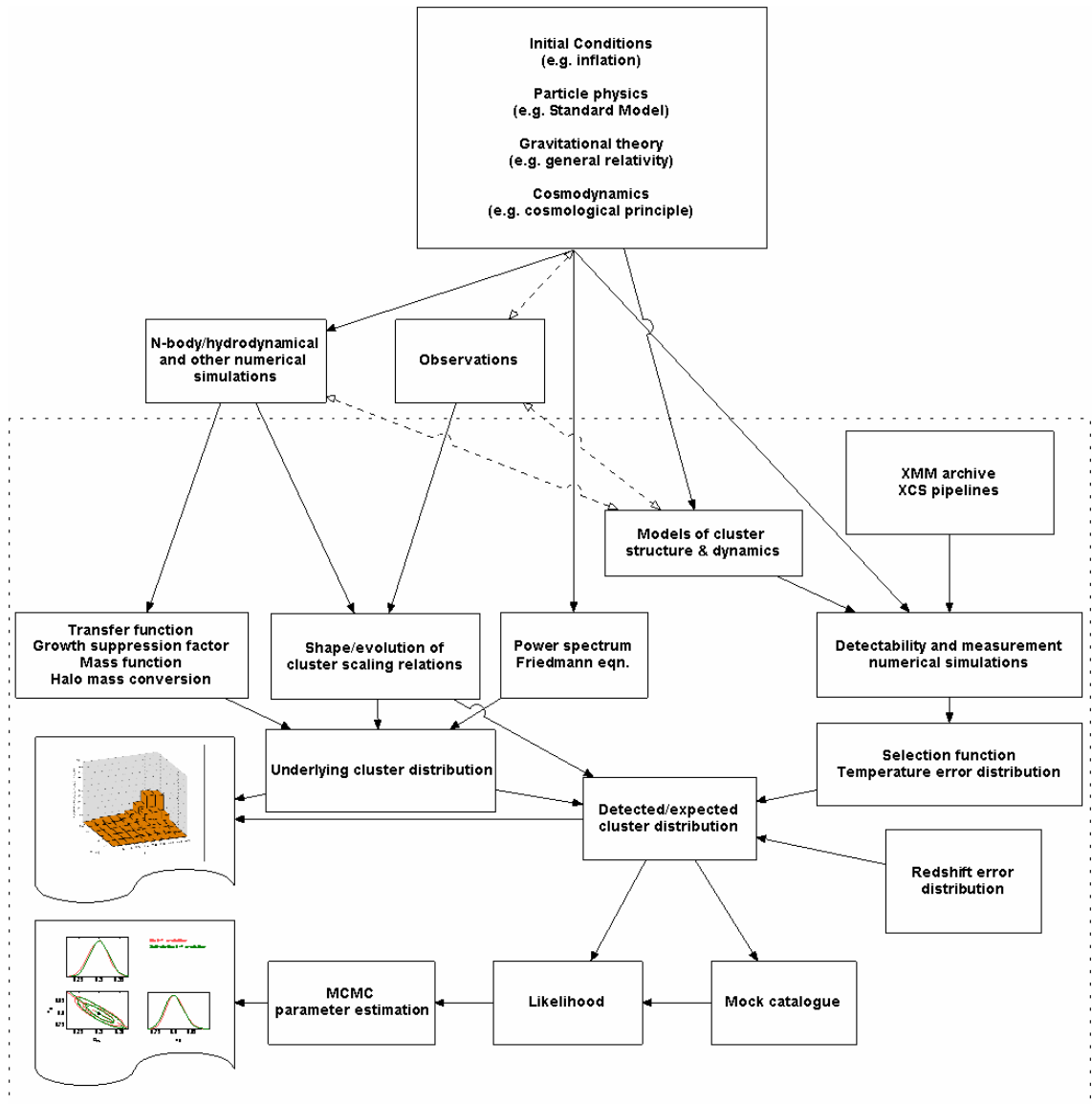


Figure 6.5: Flowchart for cluster predictions and forecast parameter estimation. The dash-enclosed area indicates the processes that enter in our calculations. Bi-directional dashed arrows are used to indicate the main circular relations, where information from one part is used to inform another, which then informs the first, and so on.

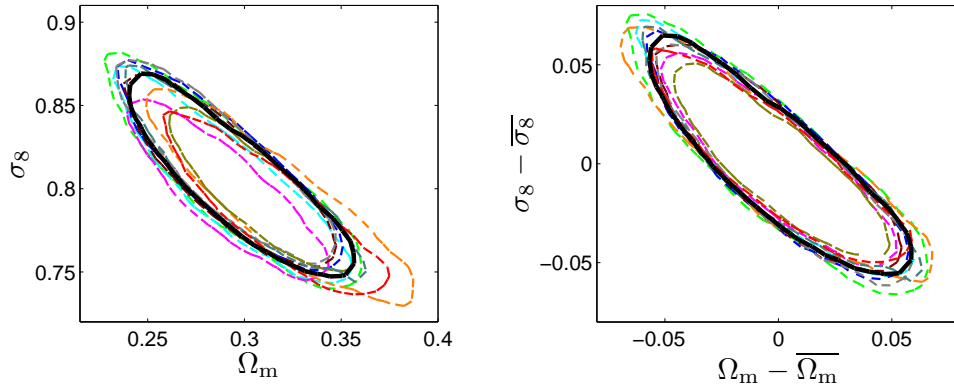


Figure 6.6: Parameter constraints (95% confidence level) for a set of 10 random realizations of the catalogue Poisson distribution (dashed coloured lines) compared to the average-catalogue parameter constraint (solid black line). In the right-hand panel, each contour has been re-centered around its distribution mean. A constant L – T relation and no L – T or M – T scatter was assumed.

As we are seeking to obtain expected/typical constraints, in a sense a Maximum Likelihood (ML) point estimate, we use $N_i = \lambda_i^*$, where the asterisk denotes fiducial-model values. Using this ‘average-catalogue’ construction, we obtain an excellent estimate of the size and shape of the expected likelihood contours, but avoid the offset in the best fit away from the fiducial parameter values that is associated with, e.g., the most likely Poisson realization. Any random realization of a Poisson sample will exhibit such an offset. Examples can be seen in the right-hand panel of Fig. 6.6, where the results for the average-catalogue method is compared to those for random catalogue realizations. We wish to avoid offsets of this type as we are mainly interested in the shape and size of contours, or wish to separate possible biases from such an offset. This methodology is explained and motivated in detail in Appendix B.2. As stated above, Fig. 6.6 compares constraints derived using this method to constraints derived from a Poisson sample of mock catalogues. The results confirm that constraints derived using our methodology provide an excellent estimate of the expected constraints. Note that in future real data analyses this methodology cannot be used, and there will in general be some offset.

The exploration of the likelihood function in parameter space was carried out using a custom code based on standard Monte Carlo Markov Chain techniques (see Sect. 3.4.4). The calculation of the integrals involved in the likelihood (see description in Appendix B) was done with the state-of-the-art numerical integration packages CUBPACK (Cools & Haegemans, 2003) and CUBA (Hahn, 2005).

Quantity	Labels/assumptions	
Redshift z	Realistic $\sigma(z)/(1+z) = 0.05$ 5% catastrophic (syst.)	Worst – case $\sigma(z)/(1+z) = 0.10$ 10% catastrophic (syst.)
X-ray temperature T	Realistic XSPEC-simulated XMM–Newton errors	Worst – case $\sigma(T) = 3 \times \sigma(T)_{\text{Realistic}}$

Table 6.3: Summary of measurement error assumptions and their labelling. See Sects. 6.3.4 & 6.3.5 and Appendix B for details.

6.5 Results

6.5.1 Labelling

X-ray temperature and redshift errors will be indicated as ‘realistic’ or ‘worst-case’ according to Table 6.3; see Sects. 6.3.4 and 6.3.5 as well as Appendix B. The colouring scheme in Table 6.4 will be used to indicate the fiducial cluster scaling relation model; see Sects. 6.3.2 and 6.3.3 as well as Appendix B.

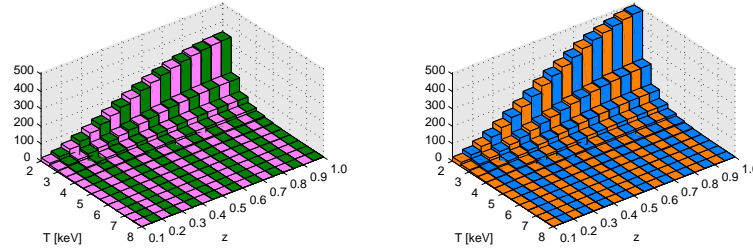
6.5.2 Expected Cluster Distributions

Without Measurement Errors

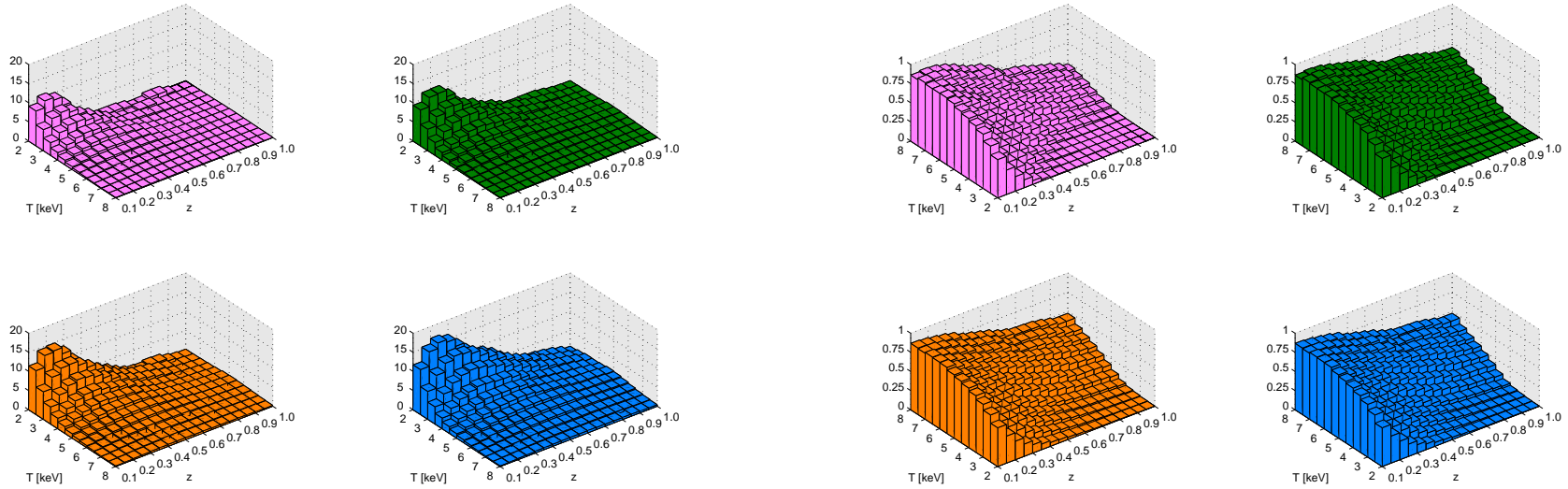
The expected 2D (T, z) distributions of clusters for our four standard models are shown in Fig. 6.7 on p. 131; Fig. 6.7a (underlying distributions), Fig. 6.7b (expected detections) and Fig. 6.7c (detection efficiency), where the selection function has been used to go from Fig. 6.7a to Fig. 6.7b. The expected redshift distributions and total cluster number counts are shown similarly in Fig. 6.8 (p. 132). Note that as the L – T relation changes, so does the expected number of detected clusters, since we are more likely to detect a cluster the more luminous it is (and for a given temperature, the cluster luminosity increases with redshift for self-similar L – T evolution). The underlying distribution however is of course not dependent on the L – T relation. We find that ^{500}XCS can be expected to find somewhere in the range of 250–700 clusters for its projected area of 500 deg² and $0.1 \leq z \leq 1.0$, $2 \text{ keV} \leq T \leq 8 \text{ keV}$. This corresponds to around 20 percent of the 1500–3300 total number of clusters we would expect to detect with no photon count cut-off (effectively a ~ 50 -photon cut-off). This full set of XCS clusters will constitute a significant sample (relative to previous studies), representing around a quarter to a third of the actual 7000–10000 clusters present in the observed fields. Going to higher redshifts, we roughly estimate that

Parameter	Description	No $L-T$ / $M-T$ scatter Constant $L-T$	No $L-T$ / $M-T$ scatter Self-similar $L-T$	$L-T$ / $M-T$ scatter Constant $L-T$	$L-T$ / $M-T$ scatter Self-similar $L-T$
Colouring		Pink	Green	Orange	Blue
$L-T$:		-1.90	-1.92	-1.90	-1.92
α	Normalization	[-1.90]	[-1.92]	flat, unrestricted	flat, unrestricted
β	Slope	2.5 [2.5]	2.5 [2.5]	2.5 flat, unrestricted	2.5 flat, unrestricted
γ_s	Self-similarity exp.	0 [0]	1/2 [1/2]	0 [0]	1/2 [1/2]
γ_z	Redshift exp.	0 [0]	0 [0]	0 [-1, 1.5]	0 [-1, 1.5]
$\sigma_{\log L_X}$	Scatter	0 [0]	0 [0]	0.3 [0.2, 0.4]	0.3 [0.2, 0.4]
m_L	Max. scatter in units of $\sigma_{\log L_X}$	-	-	3 [3]	3 [3]
$M-T$:		self-similar, normalized to HIFLUGCS			
evolution					
$\sigma_{\log T}$	Scatter	0 [0]	0 [0]	0.1 [0.1]	0.1 [0.1]
m_T	Max. scatter in units of $\sigma_{\log T}$	-	-	3 [3]	3 [3]

Table 6.4: Cluster scaling relation assumptions and their labelling. Fiducial values are given first, followed by priors assumed in parameter estimation below (usually in brackets). Note that the colour coding at the top of the table is used to indicate these fiducial models throughout. See Sects. 6.3.2 & 6.3.3 and Appendix B for details.



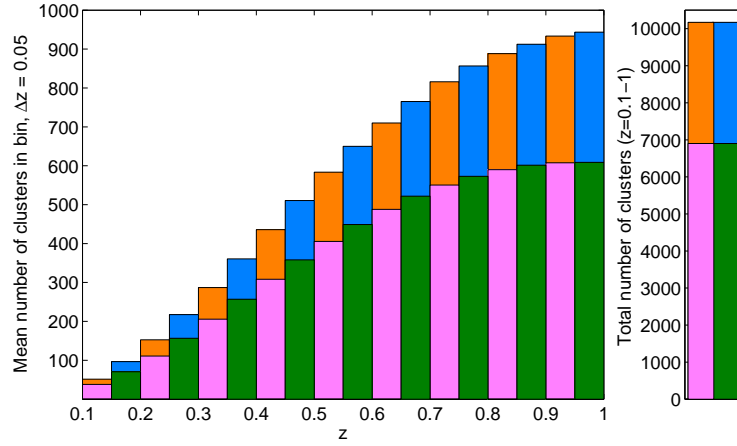
(a) Underlying cluster distribution. Note that only the $M-T$ relation is relevant for the underlying distribution, and we therefore colour according to both $L-T$ assumptions with the same $M-T$ relation. The numbers fall for higher redshifts, by coincidence peaking at $z \sim 1$. Note that the T -axis is reversed for clarity here, compared to below.



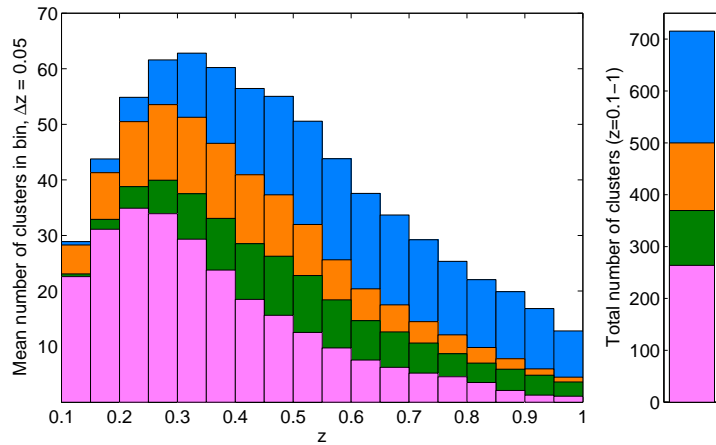
(b) Expected detections using selection function.

(c) Detected fraction per bin.

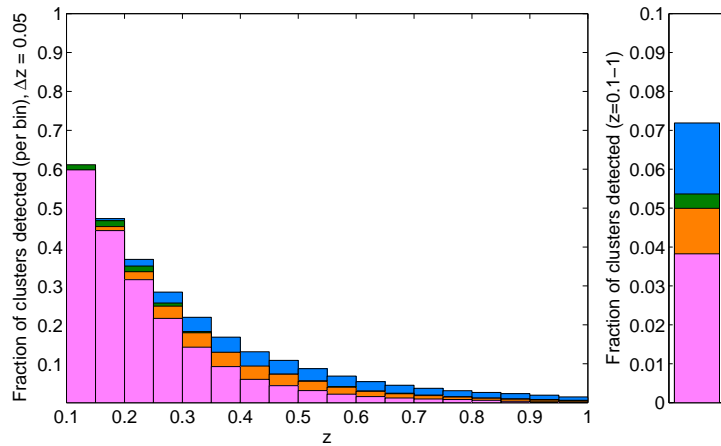
Figure 6.7: Expected cluster number count distributions for ^{500}XCS , for no $L-T$ nor $M-T$ scatter and no $L-T$ evolution (pink), no $L-T$ nor $M-T$ scatter and self-similar $L-T$ evolution (green), $L-T$ and $M-T$ scatter and no $L-T$ evolution (orange), and $L-T$ and $M-T$ scatter and self-similar $L-T$ evolution (blue). Bin sizes are $\Delta z = 0.05$ and $\Delta T = 0.5 \text{ keV}$.



(a) Underlying cluster distribution. Note that only the $M-T$ relation is relevant for the underlying distribution, and we therefore colour according to both $L-T$ assumptions with the same $M-T$ relation. The numbers fall for higher redshifts, by coincidence peaking at $z \sim 1$.



(b) Expected detections using selection function.



(c) Detected fraction of clusters per bin.

Figure 6.8: Expected cluster distributions for the ^{500}XCS , for our four different cluster scaling relation cases.

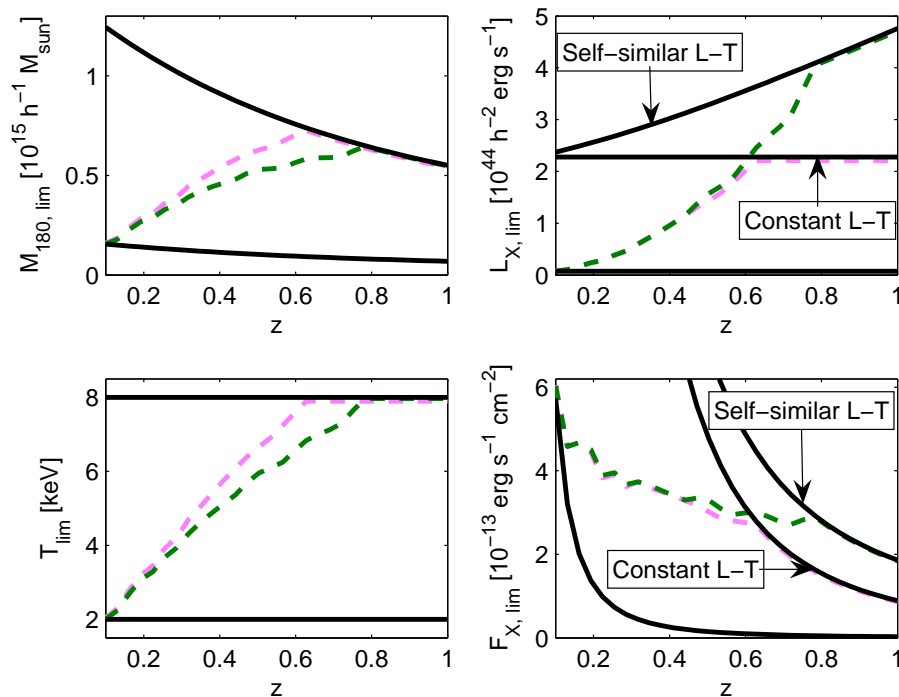


Figure 6.9: Expected observational limits for the ^{500}XCS (defined as $P(\text{detection}) \geq 0.5$), for the simplest case of no scatter in the cluster scaling relations and a constant (pink dashed line) or self-similar (green dashed line) L - T relation. Solid lines correspond to the hard temperature cut $2 \text{ keV} \leq T \leq 8 \text{ keV}$.

a minimum of 250 clusters will be found at $z > 1$, of which at least 10 should have > 500 photons.

An overview of the expected observational limits of the ^{500}XCS for mass, X-ray temperature, X-ray luminosity and X-ray flux (in the $[0.1, 2.4]$ keV band), is given in Fig. 6.9. We have there defined the detection limit, through the selection function, as $P(\text{detection}) \geq 0.5$. These limits are thus the values above which we expect to detect, with a photon count of 500 or above, at least half of the clusters. It is worth noting that the change in detection probability is slow as a function of X-ray temperature, and hence the concept of e.g. a single flux limit (which would correspond to a sharp transition between one and zero in the probability) is not suitable for defining the XCS sample. The underlying reason for this is that the *XMM* archive images occupy a range of different exposure times, hence individual flux limits. Caution is therefore advised when comparing Fig. 6.9 to similar plots based on a single flux or mass limit. For comparison, using $P(\text{detection}) \geq 0.05$ to define the detection limit leads to a flux limit of $\sim 5 \times 10^{-14} \text{ erg s}^{-1} \text{ cm}^{-2}$, considerably lower than that shown in Fig. 6.9.

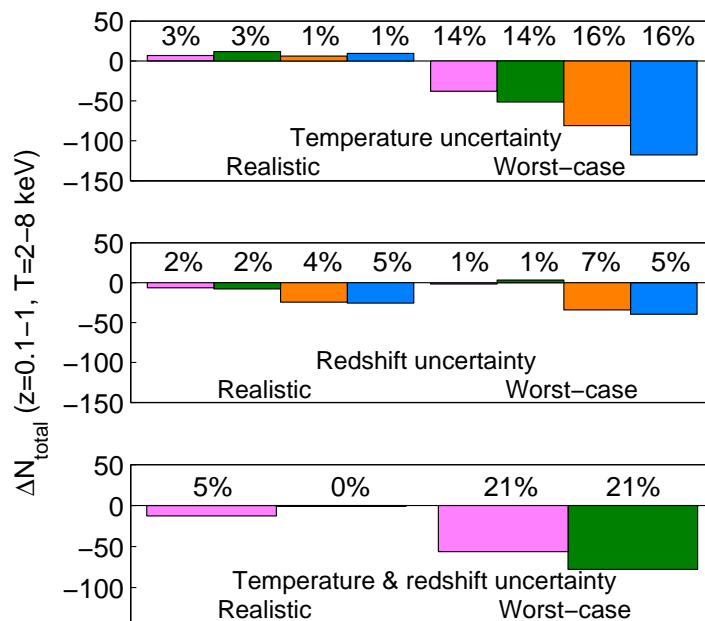


Figure 6.10: Changes in total number of clusters due to our different error assumptions, compared to no-errors distributions in Fig. 6.8b (p. 132).

With Measurement Errors

Introducing measurement errors for redshift and X-ray temperature will introduce scattering of clusters across the redshift and temperature cut-offs. As the cluster distribution is not symmetric with respect to these cut-offs, there may be a net increase/decrease in the expected number of clusters as a result (a type of Malmquist bias). Furthermore, the measurement error distributions may also be asymmetric, as is our temperature error distribution. Note that the relevant ‘underlying’ cluster distributions for these purposes are the expected detections, shown in Fig. 6.7b (p. 131).

The change in the expected total number of clusters as a result of different measurement error assumptions are shown in Fig. 6.10. We find that the effect of measurement errors on the number count is significantly less than the effect of intrinsic scaling-relation scatter (cf. Fig. 6.8b, p. 132). This is not surprising since the scaling-relation scatter is based on the true underlying cluster distribution in Fig. 6.7a (p. 131), a much steeper function than the expected detections in Fig. 6.7b.

We also see that only in the case of worst-case temperature errors is the Malmquist bias significant, and as we shall see later only in this case do the measurement errors give a significant bias in cosmological constraints, if unaccounted for. For realistic temperature

errors, a net increase in clusters is seen, as the skewness of the temperature error distribution toward low temperatures (Fig. 6.4, p. 123) is compensated by the somewhat larger number of low-temperature clusters scattering up in temperature at the low-temperature end. For worst-case temperature errors the temperature is very poorly constrained, and this compensatory effect is not sufficient to counteract the net decrease in number of clusters. Redshift errors tend to cause a loss of clusters at the low-redshift end, as the smaller cosmic volume at lower redshifts means more clusters scatter down in redshift than scatter up. However, the redshift errors also affect the temperature determination, so that low-temperature clusters scattering up could give a net increase. For realistic redshift errors the size of this induced error in temperature is 5 percent, which is too small to have a significant impact. For worst-case redshift errors, we see that for the case with no scaling-relation scatter, the induced temperature error of 10 percent reduces the loss of clusters compared to that for realistic redshift errors. For the case with scaling-relation scatter, this effect is not significant, presumably due to the much sharper drop in cluster numbers at low redshifts seen for these models (Fig. 6.8b, p. 132), leading to the direct redshift error dominating.

The fractional change in the number of clusters is very similar for the case with scaling-relation scatter as without such scatter. Hence, for the case with scatter, the statistical effect will tend to be larger since the difference to the N_{ideal} clusters with no measurement errors relative to the Poisson error bars,

$$\frac{\delta N_{\text{ideal}}}{\sigma((1 + \delta)N_{\text{ideal}})} = \frac{\delta}{\sqrt{(1 + \delta)}} \sqrt{N_{\text{ideal}}}, \quad (6.12)$$

grows with the number of clusters (and scatter increases the number). Here, δ is the fractional change in the number of clusters. Based on this, we estimate that for all the models we consider, an upper limit on the fractional change in cluster count for a less than 1σ (2σ) bias in constraints is around 4 (8) percent, which compares favourably with the results for realistic errors in Fig. 6.10. (This comparison could be made more rigorous using the Kolmogorov–Smirnov test as in Haiman et al. (2001), but this treatment is sufficient for our purposes.) Due to computational limitations we have not calculated the change in number count for the case with scaling-relation scatter and both types of measurement errors, but based on the results obtained would expect them to be very similar (in fractional terms) to the results for the no-scatter case.

6.5.3 Constraints: Without Measurement Errors

Known Scaling Relations, No Scatter

For both choices of L – T relation (constant and self-similar), the expected constraints are shown in Fig. 6.11a. We expect ^{500}XCS to measure $\Omega_m = 0.3 \pm 0.02$, $\sigma_8 = 0.8 \pm 0.02$ in each case. The σ_8 – Ω_m degeneracy differs somewhat between the two L – T cases, for a constant L – T approximately given by

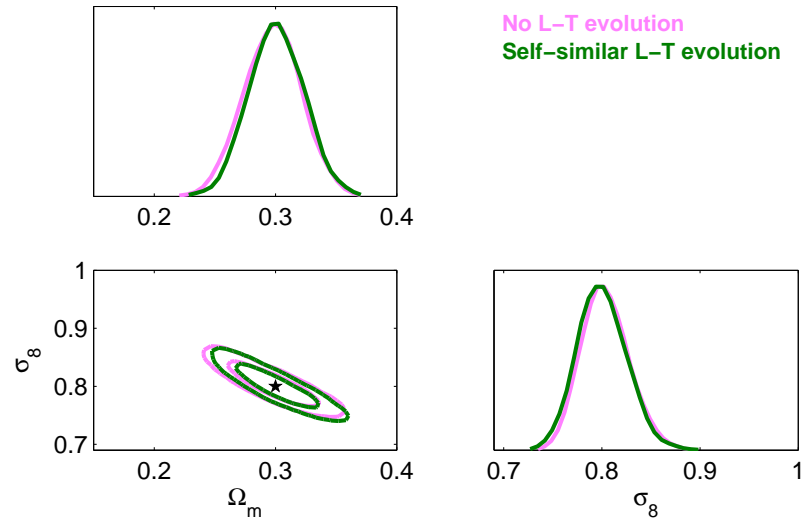
$$\sigma_8 = 0.8 \left(\frac{\Omega_m}{0.3} \right)^{-0.36}, \quad (6.13)$$

and for a self-similar L – T by

$$\sigma_8 = 0.8 \left(\frac{\Omega_m}{0.3} \right)^{-0.40}. \quad (6.14)$$

These degeneracies are somewhat different from previous studies, e.g. $\sigma_8 \propto \Omega_m^{-0.47}$ in Viana & Liddle (1999). That study however used only the total number of clusters above a certain temperature threshold to arrive at constraints. The orientation also depends on redshift depth (Levine et al., 2002). These constraints are better than what has been forecast for XMM –LSS (Refregier et al., 2002), but the comparison is not entirely like-for-like as they employ the Press–Schechter mass function and assume a rather different fiducial σ_8 and Γ . The constraints are also fairly competitive with what can be expected from other surveys using e.g. the South Pole Telescope (SPT), *Planck* or *DUET* (Majumdar & Mohr, 2004; Geisbüsch & Hobson, 2007), but in making this comparison one should note that we employ much more restrictive priors; the set of free parameters is not exactly the same.

The constraints in Fig. 6.11a are for a photon-count threshold of 500. Lowering the photon-count threshold so that more clusters are included in the sample should clearly affect the size of constraints. We find that using all detections (corresponding to an effective photon-count threshold of typically ~ 50 photons) improves 1D constraints by about 40 percent (Fig. 6.12, p. 138). This corresponds to an increase in the number of clusters used of around 1200–1700 (400–500 percent). For clusters with few photon counts the temperature errors will become very large (Liddle et al., 2001). Contamination from e.g. galaxy groups will also rise sharply with decreasing photon-count threshold, partly because clusters with low photon count will tend to have a low temperature. Hence, these estimates provide only upper limits on the possible constraint improvement. Taking error and contamination effects into account, it is likely that there would be only a weak improvement by including those XCS clusters expected to have a photon count below 500. However, follow-up observations with e.g. *XMM* or *XEUS* could improve the photon



(a) Known scaling relations, no scatter

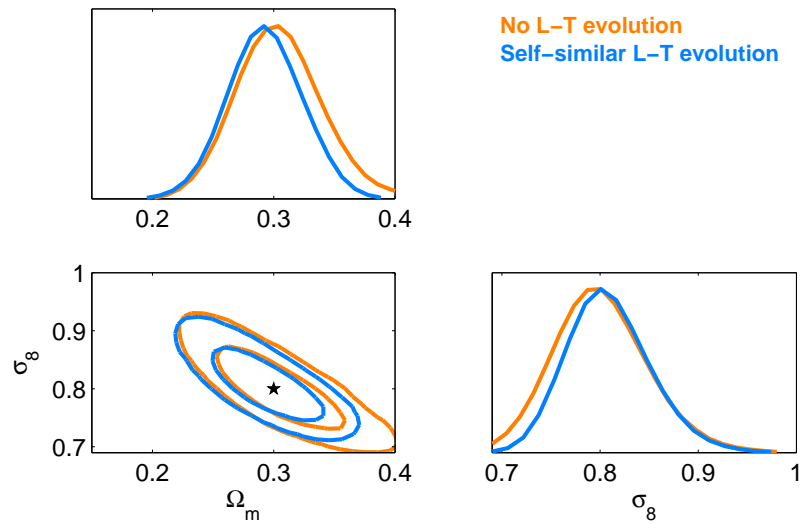
(b) Self-calibration of L - T relation, with scatter

Figure 6.11: Expected 68% and 95% parameter constraints for ^{500}XCS , without measurement errors. Stars denote the fiducial model assumed.

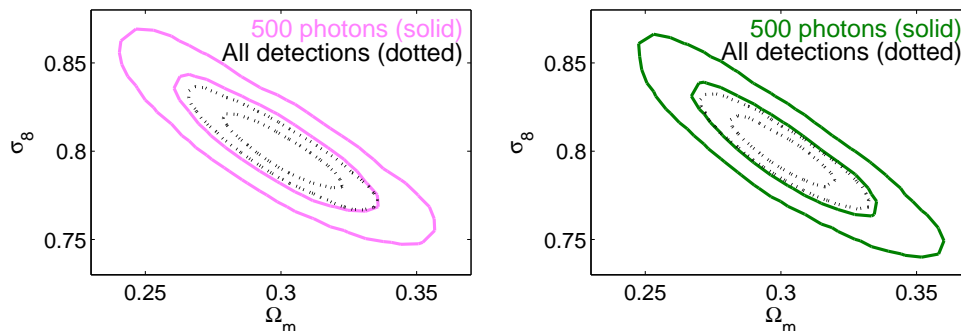


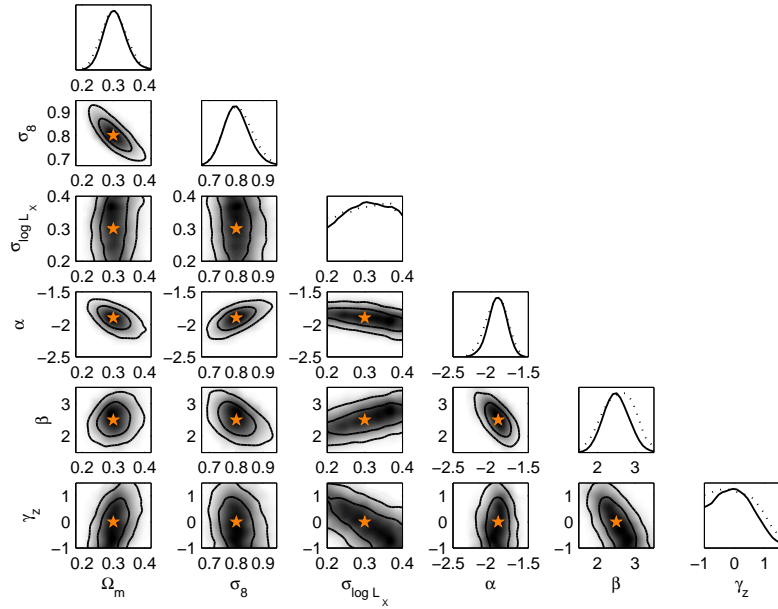
Figure 6.12: Comparison of ^{500}XCS to the case where all detections are used. A constant (left) or self-similar (right) L - T relation, and no L - T or M - T scatter was assumed. Contours correspond to 68% and 95% confidence levels.

statistics of those clusters enough to make their inclusion in the analysis worthwhile. We discuss this in more detail in Sect. 6.6.

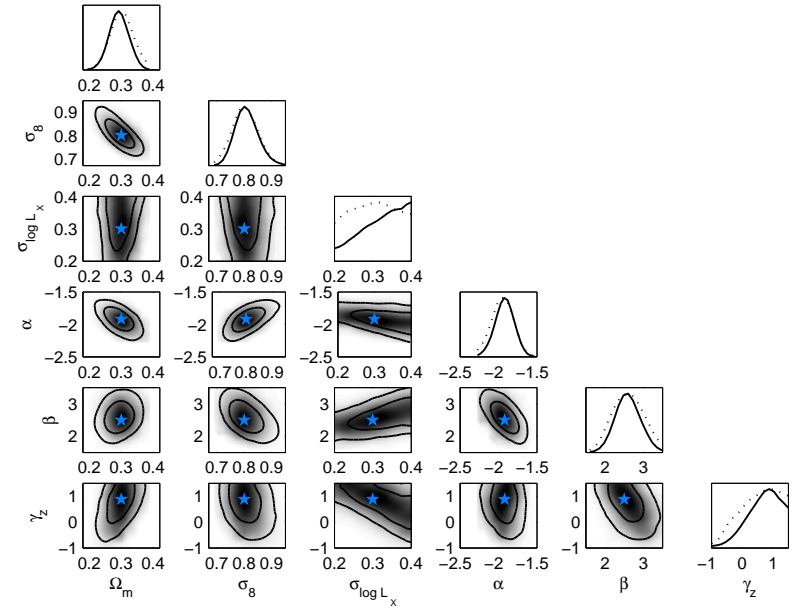
Self-calibration of L - T Relation, With Scatter

Self-calibration is the process by which e.g. the L - T relation can be constrained jointly with cosmological parameters using only the (T, z) cluster number counts (Hu, 2003; Lima & Hu, 2004; Majumdar & Mohr, 2004; Lima & Hu, 2005).

We find that jointly fitting for the cosmological parameters and the L - T relation, ^{500}XCS will measure $\Omega_m = 0.3 \pm 0.03, \sigma_8 = 0.8 \pm 0.05$ under our assumptions. The marginalized Ω_m - σ_8 likelihood distributions are shown in Fig. 6.11b (p. 137), and the full set of likelihood distributions in Fig. 6.13 (note that Fig. 6.11b is just the top triangles of these plots). The 1D parameter constraints are listed in Table 6.5 (p. 140). The constraints for the case of self-similar L - T evolution appear narrower than for a constant L - T . This is due to the redshift-evolution prior, explained below, significantly cutting the distribution. We thus believe the constant L - T case to be most representative of the constraints we can expect. As expected, the constraints on Ω_m and σ_8 degrade when marginalizing over the four L - T parameters (compared to Fig. 6.11a), but still remain relatively small. In comparison to the South Pole Telescope, *Planck*, and *DUET* (Majumdar & Mohr, 2004; Geisbüsich & Hobson, 2007), our constraints are still competitive (we lack comparable results for *XMM*-LSS, but expect to do better given our larger survey area and depth). However, if we were to consider self-calibration of the M - T relation as well (rather than using an external description, as described in Sect. 6.3.2), those surveys would have more power than the XCS (using only archival *XMM* data) through the use of the cluster power



(a) Constant L - T relation



(b) Self-similar L - T relation. (As can be surmised from some of the 1D distributions, the marginalized and mean likelihoods approach each other very slowly in the MCMC due to the prior cutting the distribution, however the statistical properties of the distribution have converged appropriately.)

Figure 6.13: Expected 68% and 95% parameter constraints for ^{500}XCS , with scaling-relation scatter and no measurement errors, and fitting jointly with L - T relation (self-calibration) for which reasonable priors on scatter and redshift evolution have been adopted. Solid lines correspond to marginalized likelihood, dotted lines and shading to mean likelihood. Stars denote the fiducial model assumed.

L - T evolution		Known scaling relations, no scatter	Self-calibration of L - T , with scatter
Constant	Ω_m	0.30 ± 0.02	0.30 ± 0.03
	σ_8	0.80 ± 0.02	0.80 ± 0.05
	$\sigma_{\log L_X}$	–	[0.2, 0.4]
	α	–	-1.91 ± 0.12
	β	–	2.50 ± 0.33
	γ_z	–	[-1, 1.5]
Self-similar	Ω_m	0.30 ± 0.02	0.30 ± 0.03
	σ_8	0.80 ± 0.02	0.80 ± 0.04
	$\sigma_{\log L_X}$	–	[0.2, 0.4]
	α	–	-1.92 ± 0.12
	β	–	2.55 ± 0.31
	γ_z	–	[-1, 1.5]

Table 6.5: Expected 1σ parameter constraints for ^{500}XCS when marginalized over all other parameters, without measurement errors. Note that, with our assumptions, the constraints on $\sigma_{\log L_X}$ and γ_z are given by the prior ranges, which in the light of only such data as here would thus be too narrow.

spectrum (Majumdar & Mohr, 2004; Lima & Hu, 2004). In fact, we do not expect XCS to have any significant constraining power if the M – T relation is self-calibrated as well. We show examples of the effects of M – T systematics in Sect. 6.5.5. It has been shown (e.g. Majumdar & Mohr, 2004) that small follow-up samples can dramatically improve the situation. Therefore, weak-lensing/SZ follow-up and/or a contiguous e.g. *XMM* survey would be highly advantageous (see also Bergé et al., 2008; Pierre et al., 2008). Comparing to Fig. 6.11a, although we lose constraining power due to an increase in the number of parameters, since we are including scaling-relation scatter the number of clusters increases significantly which mitigates the degradation. Note that, as shown in Table 6.4 (p. 130), we fit the data to a power-law L – T relation $\sim (1+z)^{\gamma_z}$. Although the functional form for a self-similar L – T used to generate data is different in principle, we have checked that a power law can approximate its redshift evolution very well.

Using (T, z) number-count self-calibration, based only on archival *XMM* data (Fig. 6.13, p. 139), we can constrain the L – T normalization α to ± 0.12 (or ± 6 percent) and the L – T slope β to $\sim \pm 0.3$ (or ± 13 percent). The self-calibration procedure is not able to jointly constrain the scatter $\sigma_{\log L_X}$ and redshift evolution γ_z significantly. We have therefore imposed flat priors on these parameters, $0.2 \leq \sigma_{\log L_X} \leq 0.4$ and $-1 \leq \gamma_z \leq 1.5$ to limit the distribution within reasonable bounds of a size reflecting the minimum accuracy to which we would hope to measure these parameters from our direct L – T data, i.e. also taking into account the measured X-ray flux (see also Table 6.4, p. 130).

Thus, the self-calibration power to constrain the L – T relation is present in the data, but as can be seen in Fig. 6.13 (p. 139) there are strong degeneracies between parameters. The main degeneracy is that between γ_z and $\sigma_{\log L_X}$; increasing $\sigma_{\log L_X}$ can easily be offset by reducing γ_z , which also is easy to understand physically as they both effectively scale the cluster luminosities up or down, and corresponds to the observation by several authors (e.g. Branchesi et al., 2007; Maughan, 2007; Nord et al., 2008; Pacaud et al., 2007) that L – T scatter can mimic L – T evolution (also discussed in Sect. 6.3.3). The redshift evolution γ_z is also degenerate with the L – T slope β , which is thus itself degenerate with $\sigma_{\log L_X}$. Interestingly though, the cosmological parameters show little degeneracy with $\sigma_{\log L_X}$. It is the result of these degeneracies that all four L – T parameters cannot be jointly constrained. Bayesian Complexity (Kunz et al., 2006) suggests that at most five parameters (including Ω_m and σ_8) can be fully constrained, which is also what we find in practice. As one might expect, we will therefore have to rely on our direct L – T measurement to constrain the L – T scatter and evolution (as proposed by Verde et al. 2002; Hu 2003; Battye & Weller

2003; Wang et al. 2004a; Lima & Hu 2005).

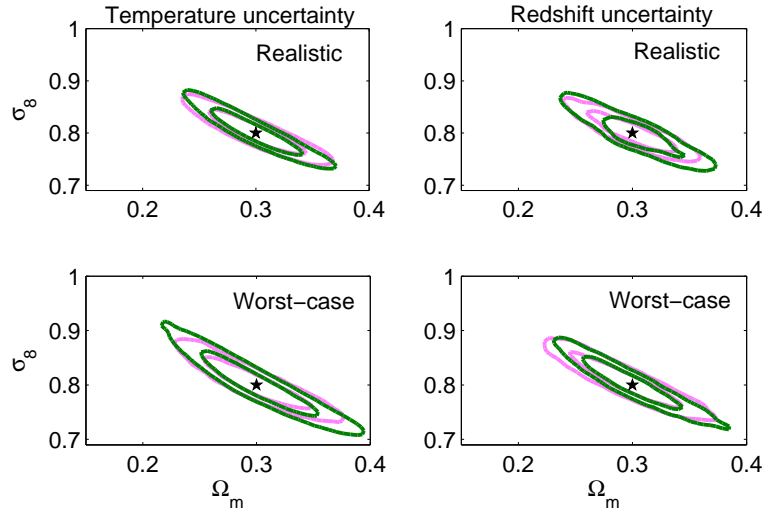
The fact that our relatively generous priors on the L – T scatter and evolution still restricts the distribution, affecting the size of cosmological constraints, also serves to illustrate a slightly different point of view: turning the problem around, and using complementary cosmological data to constrain e.g. Ω_m and σ_8 , thereby possibly also improving constraints on astrophysical parameters (as noted by e.g. Levine et al., 2002; Hu & Kravtsov, 2003; Hu, 2003).

6.5.4 Constraints: With Measurement Errors

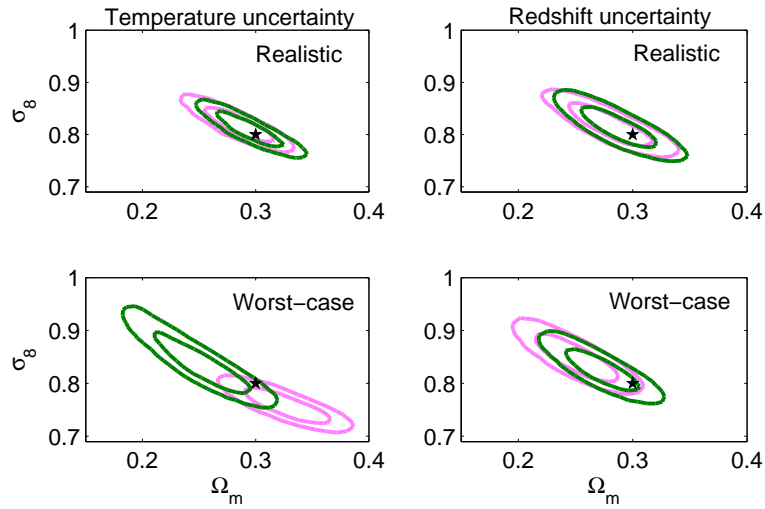
Known Scaling Relations, No Scatter

The effect on derived cosmological constraints from measurement errors in X-ray temperature and redshift is small. Taking into account knowledge of the error distributions in the data analysis, we find that the size of uncertainties increases somewhat compared to the no-errors case (see Fig. 6.14a and Table 6.6 [p. 144], cf. Fig. 6.11a [p. 137] and column 1 in Table 6.5 [p. 140]). Interestingly, even with temperature or redshift errors of an unrealistically large magnitude, the effect on the constraints is small. As such, we expect the broadening of constraints due to measurement errors to be a minor effect compared to the effects of possible systematic errors. These findings are in agreement with what has already been found by e.g. Huterer et al. (2004, 2006); Lima & Hu (2007).

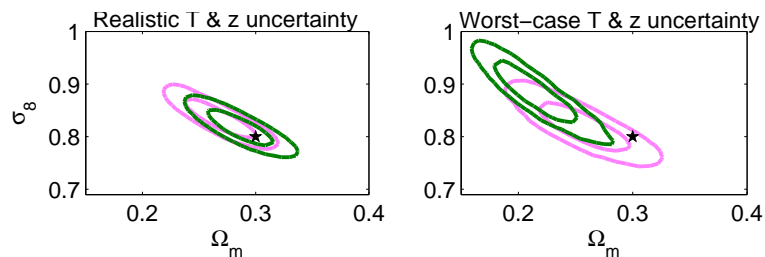
The effect of ignoring temperature and redshift errors in the fitting procedure can to some extent model one such systematic; poor knowledge of the measurement error distributions. As can be seen in Fig. 6.14b, we find that when ignoring measurement errors in the fitting, for all combinations of single measurement errors (i.e. only z or T at a time), the difference in cosmological constraints compared to the fiducial model is within 2σ (and most are within 1σ). For combined z and T measurement errors, the same is still true for realistic errors, but for a self-similar L – T and worst-case errors the bias is larger than 2σ (see Fig. 6.14c). These results agree well with the expectations presented in Sect. 6.5.2, and thus suggest that a good estimate of the bias in cosmological constraints due to Malmquist-bias effects can be obtained by comparing the net Malmquist bias to the Poisson error of the total cluster number count (at least to roughly discriminate $> 2\sigma$ bias from $< 2\sigma$ bias). This is not that surprising as the shape of the cluster distribution does not differ much between such models, and thus the total number count carries most of the information (also noted in Haiman et al., 2001). The 1D constraints corresponding to Figs. 6.14b & 6.14c are listed in Table 6.7 (p. 145).



(a) Accounted-for single measurement errors



(b) Unaccounted-for single measurement errors



(c) Unaccounted-for combined measurement errors

Figure 6.14: Expected 68% and 95% parameter constraints for ^{500}XCS , for known scaling relations, no scatter, and with measurement errors. Stars denote the fiducial model assumed.

$L-T$ evolution		Realistic T errors	Worst-case T errors	Realistic z errors	Worst-case z errors
Constant	Ω_m	0.30 ± 0.03	0.30 ± 0.03	0.30 ± 0.02	0.30 ± 0.03
	σ_8	0.80 ± 0.03	0.80 ± 0.03	0.80 ± 0.02	0.80 ± 0.03
Self-similar	Ω_m	0.30 ± 0.03	0.30 ± 0.03	0.30 ± 0.03	0.30 ± 0.03
	σ_8	0.80 ± 0.03	0.80 ± 0.04	0.80 ± 0.03	0.80 ± 0.03

Table 6.6: Expected 1σ parameter constraints for ^{500}XCS when marginalized over the other parameter, for known scaling relations, no scatter, and with accounted-for measurement errors.

L - T evolution		Realistic T errors	Worst-case T errors	Realistic z errors	Worst-case z errors	Realistic T & z errors	Worst-case T & z errors
Constant	Ω_m	0.28 ± 0.02	0.33 ± 0.02	0.28 ± 0.02	0.25 ± 0.02	0.27 ± 0.02	0.26 ± 0.03
	σ_8	0.82 ± 0.02	0.76 ± 0.02	0.82 ± 0.03	0.85 ± 0.03	0.83 ± 0.02	0.82 ± 0.03
Self-similar	Ω_m	0.29 ± 0.02	0.25 ± 0.03	0.29 ± 0.02	0.27 ± 0.02	0.29 ± 0.02	0.22 ± 0.02
	σ_8	0.81 ± 0.02	0.84 ± 0.04	0.81 ± 0.03	0.83 ± 0.03	0.82 ± 0.02	0.88 ± 0.04

Table 6.7: Expected 1σ parameter constraints for ^{500}XCS when marginalized over the other parameter, for known scaling relations, no scatter, and with unaccounted-for measurement errors.

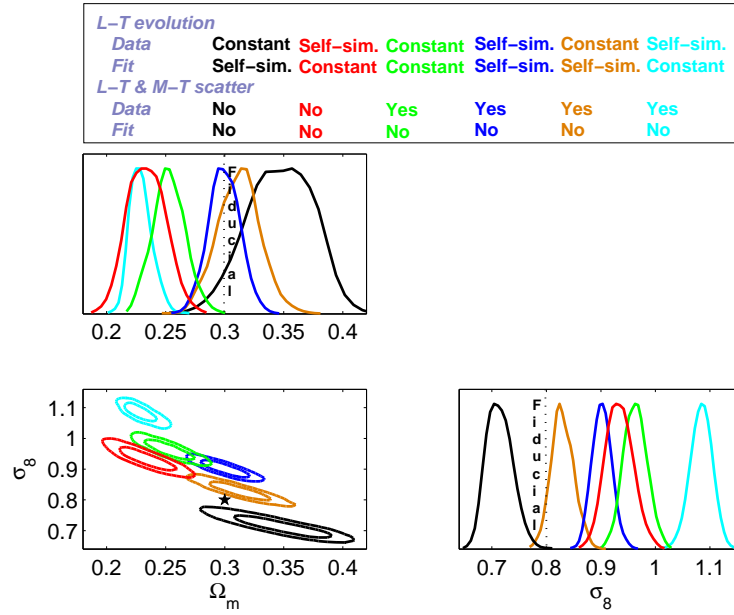
Self-calibration of L – T Relation, With Scatter

Because of computational limitations we have not explicitly calculated cosmological constraints for self-calibration with measurement errors. We have however checked that when scatter is included in the data, the effect of temperature and redshift errors on the expected cluster distribution is very similar to the case where no scatter is included, see Fig. 6.10 (p. 134), and the discussion in the preceding Section and Sect. 6.5.2. We thus expect that the effect from measurement errors on constraints where scatter is included, with or without self-calibration, can be expected to be small or negligible – both in terms of bias if the errors are ignored, or broadening of error contours when errors are taken into account. We therefore believe that the self-calibration results for the case without measurement errors (Figs. 6.11b [p. 137] & 6.13 [p. 139], Table 6.5 [p. 140]) should provide a good rough approximation of the expected self-calibration constraints with measurement errors. Note that this situation is bound to change once direct L – T data is added to the procedure, as the temperature errors will then have a significant impact on the accuracy to which the evolution of the L – T relation can be determined, hence setting the size of the constraints on $\sigma_{\log L_X}$ and γ_z . One can therefore *not* conclude that temperature errors are largely unimportant for the cosmological constraints we will ultimately produce from the data, but an upper limit on the size is set by this work (see e.g. Verde et al., 2002; Hu, 2003; Battye & Weller, 2003). Comparing to the results of e.g. Lima & Hu (2004, 2005); Majumdar & Mohr (2004); Wang et al. (2004a), we find that the degradation of constraints due to self-calibration of the L – T relation appears smaller than the corresponding effect due to self-calibration of e.g. the M – T relation as in those works (but consistent, roughly a factor 1.5–2.5 compared to a factor 2–10). A like-for-like comparison is however not possible, due to different sets of free parameters, redshift ranges and survey areas. The effect of M – T relation uncertainty is considered further in the following Section.

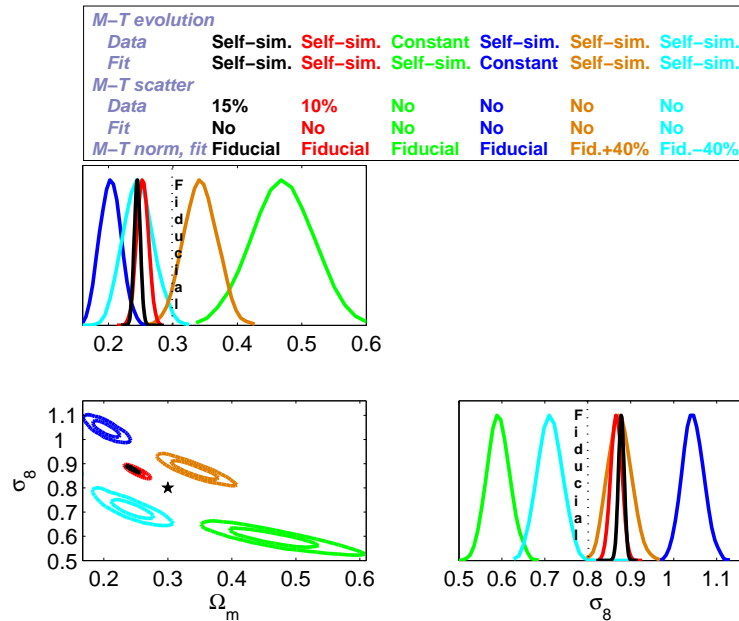
6.5.5 Constraints: Systematic Biases

It is clear from the above Sections that measurement errors in the guises we consider are not expected to be a major source of bias or degradation of constraints vis-à-vis the underlying cluster distribution. However, if incorrect assumptions as to the characteristics of the M – T and L – T relations are used when fitting the data, significant bias may occur, as seen in Fig. 6.15.

Looking first at Fig. 6.15a, the figure shows how both the size and best-fitting values of



(a) Luminosity–temperature assumptions. Mass–temperature scatter assumption is also varied.



(b) Mass–temperature assumptions. A self-similar $L-T$ relation with scatter has been assumed.

Figure 6.15: Expected 68% and 95% parameter constraints from the ^{500}XCS , for various cluster scaling-relation assumptions inconsistent with the fiducial model used for generating the data. The different data and fitting assumptions are colour coordinated with the contours (within each plot, but not between plots), and listed in the panels above the two plots. The model parameters are the same as previously, and listed in Table 6.4 (p. 130). The corresponding cluster distributions in redshift and temperature can be found in Fig. 6.7b (p. 131).

cosmological constraints are affected when ignoring scatter in the scaling relations, using an inappropriate L - T relation, or both. The first case (from left in the panel above the plot) shows how using a self-similar L - T to fit data coming from a constant L - T leads to an overestimation of Ω_m . Comparing the second, third and fourth cases, we can see that L - T evolution and scaling-relation scatter all have a similar effect when unaccounted for, all leading to an overestimation of σ_8 (and consequently underestimation of Ω_m). As they both have a similar effect, the self-similar evolution in the fifth case can mimic some of the unaccounted-for scatter, leading to a lesser overestimation than for the previous cases. On the other hand, the sixth and last case combines the two effects thus leading to a dramatic overestimation of σ_8 . As such, this last case represents a worst-case scenario for this type of bias.

The other figure, Fig. 6.15b (p. 147), shows how constraint size and best-fitting values vary with systematic errors in the M - T relation only. The first two cases (from left in the panel above the plot) illustrates significantly underestimating a scatter of 10 or 15 percent (deviations similar to what might be expected according to Vikhlinin 2006). This leads to an overestimation of σ_8 , and relatively narrow constraints, since scatter significantly increases the number of detected clusters. The largest impact seen in this figure comes from poor knowledge of the redshift evolution of the M - T relation, seen in the second pair of contours. We consider a self-similar M - T analyzed as constant in redshift, and a constant M - T analyzed as self-similar. In both cases the deviation from the fiducial model is very significant, with the size of constraints also affected, due to the fiducial-model assumptions having a significant impact on the number of detected clusters. The third, and last, pair of contours show the effect of over- or underestimating the normalization mass by 40% (this value agrees with what might be expected according to e.g. Vikhlinin 2006). Overestimation of the mass leads to an overestimation of σ_8 , since the higher the assumed mass for a given temperature, the fewer the number of clusters at that temperature. Underestimation of the mass consequently also leads to an underestimation of σ_8 .

In most cases, the constraints are more than 3σ away from the fiducial model. Referring back to the discussion on Poisson errors in Sect. 6.5.2 and applying that to the relevant cluster distributions (see Fig. 6.8b, p. 132), this result is not surprising. We find that in terms of total number count Poisson error bars, the discrepancy between data and fitting assumptions are at least $\sim 6\sigma$. These limitations will apply to any galaxy cluster survey employing cluster scaling relations to arrive at results, certainly all X-ray surveys, with

the exact susceptibility to bias given by the combination of true cluster distribution and survey selection function. This stresses the importance of knowledge of the behaviour of the scaling relations in the form of self-calibration and/or separate follow-up information. For this, accurate knowledge of the selection function is necessary, so that scaling-relation scatter and evolution can be correctly distinguished (as pointed out in e.g. [Pacaud et al., 2007](#)).

6.6 Conclusions

6.6.1 The XCS Forecast

The *XMM* Cluster Survey (XCS) will cover 500 deg² and is expected to produce one of the largest catalogues of galaxy clusters so far, with $\sim 1500\text{--}3300$ clusters having $0.1 \leq z \leq 1$, $2 \text{ keV} \leq T \leq 8 \text{ keV}$. Around 20 percent of these will belong to the ⁵⁰⁰XCS sample that have sufficient photons (> 500) for their X-ray temperature to be reliably estimated. In a rough approximation, we expect to find an additional 250 or more clusters at $z > 1$, of which at least 10 should have > 500 photons. We have proven the potential of the XCS with the recent discovery of the most distant galaxy cluster known, XMMXCS J2215.9-1738 at $z = 1.457$ ([Stanford et al., 2006](#); [Hilton et al., 2007](#)). Cluster redshifts are obtained from both public-domain photometry and the NOAO–XCS Survey (NXS) ([Miller et al., 2006](#)). To date, more than 400 XCS candidates have been optically confirmed.

We have shown the power in determining both cosmological and astrophysical parameters expected from the *XMM* archive, using only self-calibration from the (T, z) distribution and taking detailed selection function, cluster distribution and measurement error modelling into account in a Monte Carlo Markov Chain (MCMC) setting. Inclusion of the selection function requires the specification of the luminosity–temperature relation, and thus enables us to also self-calibrate this relation. We also introduce and motivate a new ‘smoothed Maximum Likelihood estimate’ of the expected constraints, which can be regarded as intermediate between a Fisher matrix analysis and a full mock catalogue ensemble averaging in MCMC.

We expect the ⁵⁰⁰XCS to measure

$$\begin{aligned} \sigma(\Omega_m) &< 0.03 \quad (10\%), & \sigma(\alpha) &< 0.12 \quad (6\%), \\ \sigma(\sigma_8) &< 0.05 \quad (6\%), & \sigma(\beta) &< 0.33 \quad (13\%), \end{aligned}$$

for a flat Λ CDM universe, the uncertainty on Ω_m also being that on Ω_Λ . The cosmological constraints are similar to those already obtained using gas mass fraction measurements

(e.g. Allen et al., 2002, 2008). They are better than those that can be expected from *XMM*–LSS (Refregier et al., 2002), because XCS covers more area than *XMM*–LSS (predicted maximum area of 64 deg², but so far results for only 5 deg² have been published) and has a higher average exposure time. Our constraints are also somewhat competitive compared to expected constraints from e.g. the SPT, *Planck*, and *DUET* (Majumdar & Mohr, 2004; Geisbüsch & Hobson, 2007), except if self-calibration of the mass–temperature relation is also considered. The scatter and redshift evolution of the luminosity–temperature relation cannot be jointly constrained to a significant degree by the self-calibration data alone; additional data – archival *XMM* and/or follow-up – is needed to distinguish e.g. no evolution from self-similar evolution if the scatter is left as a free parameter. Like e.g. Levine et al. (2002); Hu & Kravtsov (2003); Hu (2003), we note that there is also potential to use this conversely, to let complementary cosmological data help constrain astrophysical parameters.

6.6.2 Measurement Errors

We include for the first time realistic temperature measurement errors, based on detailed XSPEC simulations of the *XMM* fields, and propagate redshift errors to the temperature determination. The presence of realistic or worst-case measurement errors in X-ray temperature and redshift will have only a small impact on the accuracy to which cosmological parameters can be expected to be measured, of order 0.01 in 1D confidence limits. Furthermore, we find that imperfect knowledge of the variances of measurement errors, or the presence of catastrophic photometric redshifts, should not produce significant bias in the cosmological constraints. We conclude that, under these assumptions, even ignoring the expected realistic measurement errors in the data analysis will provide a reasonable estimate of the true constraints. For the case where direct L – T data is included in the analysis, the impact of measurement errors (including susceptibility to systematics) will be larger (Verde et al., 2002; Hu, 2003; Battye & Weller, 2003). The size of constraints forecast here provide an upper limit for that scenario.

It is already known (Huterer et al., 2004, 2006; Lima & Hu, 2007) that irreducible systematic errors in redshift estimation is a potential problem for cluster surveys, but we leave for future work the specific requirements for the XCS.

We do not yet take into account the variation of photon count with temperature/luminosity, and how that affects the size of temperature errors. Including this effect, instead of employing a lower threshold only, may well improve the size of our constraints. However

the maximum improvement for self-calibration is small. For inclusion of direct L – T data the importance will be larger.

6.6.3 Cluster Scaling Relations

The choice of L – T relation itself has no significant impact on the size of cosmological constraints. In our considerations, we do not yet take into account the separate L – T measurement to be performed by the XCS. In the final data analysis, the L – T measurements will be jointly fitted with the cluster distribution. Hence, our expected constraints represent a worst-case scenario of no direct data on the L – T relation. We plan to revisit the issue of the XCS L – T measurement in the future. As an example, estimates for the *DUET* survey (Majumdar & Mohr, 2004) show that follow-up information on the M – T relation can improve constraints by more than a factor of three.

We quantitatively show that making incorrect assumptions (within current theoretical/observational accuracy) about the cluster scaling relations can typically result in at least a 2σ – 3σ bias in cosmological constraints, a result which can be considered generic for all X-ray and SZ cluster surveys, and those optical surveys relying on cluster scaling relations. Thus, parameterizing the scaling relations appropriately and using self-calibration and/or follow-up information is crucial to arrive at robust results. This places high demands on precise characterization of the survey selection function to accurately distinguish scaling-relation evolution and scatter. That is not a problem for X-ray cluster surveys (as they generally have the best-understood selection functions), and shows the importance of the XCS measurement of the L – T relation for cosmological applications. The *XMM*–LSS collaboration have already pointed this out, and obtained some first results (Pacaud et al., 2007). A potential pitfall however is the possible redshift evolution of the L – T scatter, as observed in the CLEF simulation (Kay et al., 2007). This has not so far been considered in the literature, but is a possible source of bias that should be better understood. The future *XEUS* mission (Bleeker & Mendez, 2002) will be of great importance for precision measurements of all details of the L – T relation. The XCS will provide thousands of clusters for *XEUS* to target.

An important source of uncertainty is the mass–temperature relation. We have shown quantitatively that, as for the luminosity–temperature relation, imperfect knowledge can easily lead to significant bias. Joint estimation of the mass–temperature relation will lead to broader constraints, and we do not expect the XCS to be able to constrain both the L – T and M – T relations simultaneously. Generally, it has been found that an accuracy of less

than 10 percent in the M – T relation will be needed, and that self-calibration (particularly if making use of the power spectrum, which XCS can not do) and/or small follow-up samples can achieve that (Holder et al., 2001; Haiman et al., 2001; Levine et al., 2002; Majumdar & Mohr, 2003, 2004; Wang et al., 2004a; Lima & Hu, 2004, 2005). A recent development is the claim that the X-ray luminosity is a better mass proxy than previously thought (Maughan, 2007). This remains somewhat controversial, but could be worthwhile to consider. Its potentially low scatter and the prospect of including low-temperature clusters, for which the temperature cannot be accurately measured, makes this interesting. We leave the XCS-specific details for future work.

It has also been noted by, amongst others, Younger et al. (2006) and Ascasibar & Diego (2008), that the choice of parameterization for the cluster scaling relations can have a significant impact on the size of cosmological constraints, and they argue that a physically-motivated form is beneficial. As also noted by Lima & Hu (2007), efforts in correlating physical properties of clusters, such as that of Shaw et al. (2006), could therefore be of great importance for the size of cosmological constraints, not just biases or astrophysics. However, as the observed dependence on parameterization appears to largely come from an Ω_m – Ω_Λ degeneracy, and in this work we assume that $\Omega_\Lambda = 1 - \Omega_m$, we do not expect this to be of importance for our results here.

6.6.4 Other Systematic Errors

A variety of uncertainties enter our calculations. Mostly, these uncertainties are possible sources of systematic error, and apart from the cases of measurement errors and scaling relations discussed above we do not attempt to quantify this. Our aim here is primarily to forecast the inherent cosmological and L – T constraining power, in the approximation that these systematics are sufficiently under control. Several other authors have already studied these, and other, systematics in some detail, e.g. Haiman et al. (2001); Holder et al. (2001); Levine et al. (2002); Battye & Weller (2003); Lima & Hu (2004, 2005).

In a future data analysis, it will be important to consider what effects the uncertainty in the mass function has, something which has often been ignored (Wang et al., 2004a). The current uncertainty is estimated to be around 10 percent (Haiman et al., 2005), which is in line with the upper-limit requirement estimated by Holder et al. (2001). Warren et al. (2006) estimate that their mass function is sufficiently well-determined not to have any significant impact on the results from combined South Pole Telescope (SPT) and Dark Energy Survey (DES) data. That would imply that the accuracy is sufficient

for our purposes as well. We should also calculate the mass dispersion $\sigma(M)$ in a more robust fashion. The details in mass conversion (e.g. concentration parameter) have some uncertainty as well, but we expect this to be entirely negligible.

The cluster model assumptions made in our calculation of the selection function could have an impact on cluster detectability and thus cosmological constraints. For this reason, we are currently studying the selection function when the detection pipeline is applied to simulated clusters from the CLEF simulation (Kay et al., 2007), to understand the impact of various cluster properties.

6.6.5 Sensitivity to Fiducial Model and Priors

Another source of uncertainty in our forecasting of constraints is the fiducial models assumed. Naïvely, we would expect the area of the 2D Ω_m - σ_8 contours to be approximately conserved for moderate deviations from our fiducial model (defined as those Ω_m - σ_8 combination which fall within our, say, 2σ contours). The contour orientation, however, would be shifted along the Ω_m - σ_8 degeneracy. Therefore, decreasing the fiducial Ω_m is likely to decrease the 1D uncertainty on Ω_m and increase that on σ_8 to a first approximation (and vice versa). Having said this, the curvature of the degeneracy is not very strong over the relevant parameter range, and it would therefore be surprising if the size of constraints changed by any significant amount.

Dropping our assumption of spatial flatness, we do not expect strong constraining power on Ω_Λ , based on results such as Allen et al. (2002). One should note though that the utilization of X-ray galaxy clusters over a large range of redshifts has additional constraining power compared to Allen et al. (2002), as those results are based only on the gas mass fraction in nearby clusters; most of the constraining power on Ω_Λ comes from $z > 0.5$ (Holder et al., 2001; Levine et al., 2002). The constraints on Ω_m and σ_8 should broaden as a consequence of dropping the flatness assumption. Such an increase could arguably be alleviated by employing appropriate parameterizations for the cluster scaling relations, as discussed above in Sect. 6.6.3. This, as well as the constraining power on modified-gravity models, is a topic for further investigation.

The assumption of fixed values for the priors of some cosmological parameters, e.g. the scalar spectral index and the Hubble constant, is not realistic given the uncertainty that still exists regarding their true values. Relaxing those priors would increase the size of constraints, though probably not in a significant manner.

6.6.6 Survey Specifications

We expect to find a relatively small number of clusters at $z > 1$ with > 500 photons (of order 10–70). As such, we would naïvely not expect them to provide significant additional constraining power on cosmological parameters for a given L – T relation and a flat universe. However the $z > 1$ clusters may well prove important for constraining the L – T relation, and for constraints in a non-flat universe.

Lowering the photon-count threshold would at best improve constraints by ~ 40 percent, as discussed in the following Section, but would lead to contamination problems. Lowering the temperature threshold does not seem feasible, due to the same contamination problems.

6.6.7 Future Surveys and Outlook

Re-imaging of the XCS sample with *XMM* and/or *XEUS* could improve temperature errors sufficiently, so that at least some of the remaining ~ 80 percent of the XCS clusters not in the ^{500}XCS could be used for constraints (this corresponds to no photon-count cut-off in our calculations – effectively a ~ 50 -photon cut-off). We find that an upper limit on the improvement in constraints is by 1σ (2D) or ~ 40 percent (1D), which thus also represents the best one could possibly do with the current *XMM* archive *using* (T, z) *self-calibration only*. Once we add direct L – T data to the procedure, the lever arm from re-imaging will be more significant. The *XMM*–LSS collaboration argue (Pacaud et al., 2007) that the most efficient way to constrain the L – T evolution is to increase the sample size, rather than improve temperature errors, and propose a future 200 deg² *XMM* survey with this rationale (Pierre et al., 2008). A complementary approach to additional observations would be to also use the luminosity–mass relation as mass proxy for those clusters for which the temperature determination is difficult (Maughan, 2007), or attempt to use the relatively new quantity Y_X advocated by e.g. Kravtsov et al. (2006).

It would be worthwhile to investigate future *XEUS*, *XMM* and *eROSITA* survey strategies to reach the improvement limit above and to go beyond it, which should also make an extended redshift coverage more viable. The *XMM* and *eROSITA* surveys would be contiguous, and thus enable the use of the cluster power spectrum. Such information is not available to the XCS, as it is a serendipitous survey. It is well-known that using power-spectrum information can have a dramatic impact on the size of constraints, particularly helping with self-calibration of the mass–temperature relation (e.g. Majumdar & Mohr, 2004; Lima & Hu, 2004). Follow-up observations of cluster masses, using weak lensing

and/or SZ for only a small subset of clusters, can also have significant impact on the constraining power on the mass–temperature relation (Majumdar & Mohr, 2004; Bergé et al., 2008; Pierre et al., 2008). In general one will be faced with a trade-off between survey area and depth, taking into account power-spectrum self-calibration of the M – T relation (and potential weak-lensing and/or SZ follow-up), abundance self-calibration of the L – T relation, and direct measurement of the L – T relation. The weighting chosen will depend on the weight one assigns to measuring cosmological vs. cluster-physics parameters. It would be interesting to apply our comprehensive framework to assess this.

The development of good physical models of cluster structure and evolution promises to be useful both for arriving at narrow and robust cosmological constraints, and for understanding cluster physics. The characterization of cluster scaling relations and survey selection functions in terms of such properties could, utilized in cluster survey self-calibration and in combination with e.g. cosmic microwave background and supernova data, provide significant constraints on cluster physics. A benefit of models based on well-understood physics is that priors could be defined in a less ambiguous manner than is usual for cosmology. Therefore, Bayesian model selection could prove very useful for determining which physical effects are important in clusters, without any controversy over priors. The prescription of physically meaningful priors on cluster physics could help provide priors/constraints on other phenomenological cosmology parameters, for which the choice of priors is usually controversial, through the self-calibration mechanism. One might therefore eventually make additional use of this ‘noise’ as ‘signal’ for cosmological physics.

The future for galaxy clusters as a precision and complementary cosmological tool looks increasingly promising, with a range of surveys planned or underway, and numerous simulations undertaken to understand the mass function and cluster physics. The XCS will produce one of the largest ever catalogues of galaxy clusters, providing valuable information on cosmology and cluster physics through the luminosity–temperature relation, beating a path for the many planned surveys. The interface between well-understood cluster physics and cosmology, cross-calibration, and complementary cosmological data will surely be important for constraining dark energy, the primordial power spectrum, and cluster physics over the next decade and beyond.

Chapter 7

Summary and Outlook

Humans appear to have always been fascinated by the heavens, our Universe. This seems to originate in our very fundamental needs for existence, and as a result, different mythical cosmologies have flourished over the years, and arguably still do. Physical cosmology emerged during the 20th century, through the discovery of General Relativity and the Standard Model of Particle Physics, and building on Newtonian physics.

The last two decades have heralded a new ‘golden age’ of cosmology: major advances in our understanding of the Universe have been achieved, thanks to state-of-the-art experimental technology combined with theories ripe for testing. The coming two decades promise yet more advances, through a host of new experimental projects. Cosmology is becoming precise, increasingly non-linear, and data-driven.

This places great importance on data analysis methodology. Understanding systematic errors, and employing a robust statistical framework, will be key to success. We have argued here that the Bayesian statistical methodology is the appropriate tool for including uncertainty, interpreting data, estimating parameters and choosing between models.

We applied the Bayesian framework and examined such issues in two topical studies; one testing a well-motivated dark energy candidate, quintessence, with current data (Chapter 5), and one focusing on future cosmic-structure measurements using X-ray galaxy clusters (Chapter 6), one of the most important future observational probes identified by the Dark Energy Task Force ([Albrecht et al., 2006](#)).

Although we currently know little about what dark matter is, and even less about dark energy, we can reasonably expect to have *some* answers in the next decade or two. Maybe one day this mysterious dark energy will not seem so unnatural. We will also learn more about inflation (or possible alternatives). The details of the CDM model will be tested. The dark ages and reionization will be explored. Gravitational waves may be observed.

The Universe as we know it will change.

With this expected avalanche of data, and the pushing further, another problem looms on the horizon. Within modern physics and cosmology, there appear to be limits to the applicability of the scientific method. This, combined with the profound emotional implications of the subject itself, suggests that the answers to some future questions in the field could be highly sensitive to the aesthetic/psychological sensibilities of individual researchers. The multiverse scenario poses an important future challenge, to clearly distinguish metaphysics from physics. An almost Nietzschean transformation may at some level be required, to disentangle personal prejudices (even though the ‘aesthetic intuition’ of researchers can be of great importance for developing theories). This, too, begs new theoretical and statistical methods, and possibly new interdisciplinary approaches. Perhaps a paradigm shift à la Kuhn? The search for harmony continues.

κοσμοίμην

I wish to arrange myself

Bibliography

2dFGRS (2008). The 2dFGRS Image Gallery. Web site.

URL <http://www2.aao.gov.au/2dFGRS/> 36

Aguirre, A., Gratton, S., & Johnson, M. C. (2007). Hurdles for Recent Measures in Eternal Inflation. *Phys. Rev. D*, 75, 123501. 69

Albrecht, A., & Skordis, C. (2000). Phenomenology of a Realistic Accelerating Universe Using Only Planck-Scale Physics. *Phys. Rev. Lett.*, 84, 2076–2079. 103

Albrecht, A., et al. (2006). Report of the Dark Energy Task Force. *E-print (arXiv:astro-ph/0609591)*. 10, 64, 66, 156

Allen, S. W., Rapetti, D. A., Schmidt, R. W., Ebeling, H., Morris, R. G., & Fabian, A. C. (2008). Improved constraints on dark energy from *Chandra* X-ray observations of the largest relaxed galaxy clusters. *Mon. Not. R. Astron. Soc.*, 383, 879–896. 46, 57, 58, 150

Allen, S. W., Schmidt, R. W., & Fabian, A. C. (2002). Cosmological constraints from the X-ray gas mass fraction in relaxed lensing clusters observed with *Chandra*. *Mon. Not. R. Astron. Soc.*, 334, L11–L15. 46, 150, 153

Alpher, R. A., Bethe, H., & Gamow, G. (1948). The Origin of Chemical Elements. *Phys. Rev.*, 73, 803–804. 36

Alpher, R. A., & Herman, R. C. (1948). On the Relative Abundance of the Elements. *Phys. Rev.*, 74, 1737–1742. 36

Amendola, L., Quartin, M., Tsujikawa, S., & Waga, I. (2006). Challenges for scaling cosmologies. *Phys. Rev. D*, 74(2), 023525–+. 74

Aristotle (1965). *Du ciel (De Caelo)*. Collection Budé. Les Belles Lettres. 72

Arnaud, K. A. (1996). XSPEC: The First Ten Years. In G. Jacoby, & J. Barnes (Eds.) *Astronomical Data Analysis Software and Systems V*, vol. 101 of *ASP Conference Series*, (p. 17). 112, 122

- Arnaud, M. (2005). X-ray observations of Clusters of Galaxies. In F. Melchiorri, & Y. Rephaeli (Eds.) *Proc. Enrico Fermi International School of Physics Course CLIX (arXiv:astro-ph/0508159)*. [116](#)
- Arnaud, M., Pointecouteau, E., & Pratt, G. W. (2005). The structural and scaling properties of nearby galaxy clusters – II. The M – T relation. *Astron. Astrophys.*, *441*, 893–903. [115](#), [116](#)
- Ascasibar, Y., & Diego, J. M. (2008). A phenomenological model of galaxy clusters. *Mon. Not. R. Astron. Soc.*, *383*, 369–374. [152](#)
- Astier, P., et al. (2006). The Supernova Legacy Survey: measurement of Ω_M , Ω_Λ and w from the first year data set. *Astron. Astrophys.*, *447*, 31–48. [31](#), [59](#), [77](#), [81](#), [82](#)
- Aurelius, M. (1909). *Plato, Epictetus, Marcus Aurelius*, vol. 2 of *The Harvard Classics*. P.F. Collier & Son. [2](#)
- Baccigalupi, C., Balbi, A., Matarrese, S., Perrotta, F., & Vittorio, N. (2002). Constraints on flat cosmologies with tracking quintessence from cosmic microwave background observations. *Phys. Rev. D*, *65*(6), 063520–+. [74](#)
- Bahcall, N. A., Fan, X., & Cen, R. (1997). Constraining Ω with Cluster Evolution. *Astrophys. J.*, *485*, L53+. [45](#)
- Bahcall, N. A., Ostriker, J. P., Perlmutter, S., & Steinhardt, P. J. (1999). The cosmic triangle: Revealing the state of the universe. *Science*, *284*, 1481–1488. [46](#)
- Baker, G. A., & Graves-Morris, P. R. (1981). *Padé Approximants*, vol. 1 & 2. Addison–Wesley. [80](#)
- Balogh, M. L., et al. (2006). An analytic investigation of the scatter in the integrated x-ray properties of galaxy groups and clusters. *Mon. Not. R. Astron. Soc.*, *366*, 624–634. [47](#), [107](#), [116](#)
- Baltz, E. A., et al. (2008). Pre-launch estimates for *GLAST* sensitivity to Dark Matter annihilation signals. *J. Cosmol. Astropart. Phys.*, *0807*, 013. [64](#)
- Bardeen, J. M. (1980). Gauge-invariant cosmological perturbations. *Phys. Rev. D*, *22*, 1882–1905. [16](#)
- Bardeen, J. M., Bond, J. R., Kaiser, N., & Szalay, A. S. (1986). The statistics of peaks of Gaussian random fields. *Astrophys. J.*, *304*, 15–61. [18](#), [19](#)
- Bardeen, J. M., Steinhardt, P. J., & Turner, M. S. (1983). Spontaneous creation of almost scale-free density perturbations in an inflationary universe. *Phys. Rev. D*, *28*, 679–693.

- Barger, V., Guarnaccia, E., & Marfatia, D. (2006). Classification of dark energy models in the (w_0, w_a) plane. *Phys. Lett. B*, *635*, 61–65. [95](#)
- Barreiro, T., Copeland, E. J., & Nunes, N. J. (2000). Quintessence arising from exponential potentials. *Phys. Rev. D*, *61*(12), 127301–+. [74](#)
- Barris, B. J., et al. (2004). Twenty-Three High-Redshift Supernovae from the Institute for Astronomy Deep Survey: Doubling the Supernova Sample at $z > 0.7$. *Astrophys. J.*, *602*, 571–594. [31](#)
- Barrow, J. D., & Tipler, F. J. (1986). *The anthropic cosmological principle*. Atmospheric Chemistry & Physics. [70](#)
- Bartolo, N., Matarrese, S., & Riotto, A. (2005). Primordial non-Gaussianity from different cosmological scenarios. *Nucl. Phys. B Proc. Suppl.*, *148*, 56–63. [27](#)
- Bassett, B. A., Corasaniti, P. S., & Kunz, M. (2004). The Essence of Quintessence and the Cost of Compression. *Astrophys. J.*, *617*, L1–L4. [86](#)
- Battye, R. A., & Weller, J. (2003). Constraining cosmological parameters using Sunyaev–Zel’dovich cluster surveys. *Phys. Rev. D*, *68*, 083506. [46](#), [108](#), [141](#), [146](#), [150](#), [152](#)
- Bayes, T. (1763). An essay towards solving a problem in the doctrine of chances. *Phil. Trans. R. Soc. London*, *53*, 370–418. [49](#)
- Bean, R., Hansen, S. H., & Melchiorri, A. (2001). Early-universe constraints on dark energy. *Phys. Rev. D*, *64*(10), 103508–+. [74](#), [103](#)
- Bennett, C. L., et al. (1994). Cosmic temperature fluctuations from two years of *COBE* differential microwave radiometers observations. *Astrophys. J.*, *436*, 423–442. [38](#)
- Bennett, C. L., et al. (1996). Four-Year *COBE* DMR Cosmic Microwave Background Observations: Maps and Basic Results. *Astrophys. J.*, *464*, L1+. [38](#)
- Bergé, J., et al. (2008). Combined analysis of weak lensing and X-ray blind surveys. *Mon. Not. R. Astron. Soc.*, (pp. 218–+). [141](#), [155](#)
- Bergman, B. (1931). *Trots allt*. Albert Bonniers Förlag. [1](#)
- Bergström, L., & Goobar, A. (2004). *Cosmology and Particle Astrophysics*. Springer–Praxis. [11](#)
- Berig (2008). Image:Gs 19, Ockelbo (yggdrasil).jpg. Web site.
URL [http://commons.wikimedia.org/wiki/Image:Gs_19,_Ockelbo_\(yggdrasil\).jpg](http://commons.wikimedia.org/wiki/Image:Gs_19,_Ockelbo_(yggdrasil).jpg)

- Bernardeau, F., Colombi, S., Gaztañaga, E., & Scoccimarro, R. (2002). Large-scale structure of the Universe and cosmological perturbation theory. *Phys. Rep.*, *367*, 1–3. [20](#)
- Bernstein, J. (1988). *Kinetic theory in the expanding universe*. Cambridge University Press. [18](#)
- Bertschinger, E. (1998). Simulations of Structure Formation in the Universe. *Ann. Rev. Astron. Astrophys.*, *36*, 599–654. [20](#)
- Bertschinger, E., & Zukin, P. (2008). Distinguishing modified gravity from dark energy. *Phys. Rev. D*, *78*(2), 024015–+. [29](#), [86](#)
- Binétruy, P. (1999). Models of dynamical supersymmetry breaking and quintessence. *Phys. Rev. D*, *60*(6), 063502–+. [103](#)
- Blake, C., Collister, A., Bridle, S., & Lahav, O. (2007). Cosmological baryonic and matter densities from 600000 SDSS luminous red galaxies with photometric redshifts. *Mon. Not. R. Astron. Soc.*, *374*, 1527–1548. [125](#)
- Blake, C., & Glazebrook, K. (2003). Probing Dark Energy Using Baryonic Oscillations in the Galaxy Power Spectrum as a Cosmological Ruler. *Astrophys. J.*, *594*, 665–673. [35](#)
- Blanchard, A., Sadat, R., Bartlett, J. G., & Le Dour, M. (2000). A new local temperature distribution function for X-ray clusters: cosmological applications. *Astron. Astrophys.*, *362*, 809–824. [45](#)
- Bleeker, J., & Mendez, M. (2002). The *XEUS* Mission. *Preprint (arXiv:astro-ph/0207283)*. [151](#)
- Blomberg, H. (2006). Image:Hällristning, Fossum, den 29 juni 2006, bild 3.JPG. Web site. URL <http://tinyurl.com/tanumrockcarvings> [4](#)
- Bludman, S. (2004). Tracking quintessence would require two cosmic coincidences. *Phys. Rev. D*, *69*(12), 122002–+. [74](#), [103](#)
- Bois, F. Y. (2000). Statistical Analysis of Clewell et al. PBPK Model of Trichloroethylene Kinetics. *Environmental Health Perspectives Supplements*, *108*(S2), 307–316. [53](#)
- Bond, J. R., & Efstathiou, G. (1984). Cosmic background radiation anisotropies in universes dominated by nonbaryonic dark matter. *Astrophys. J.*, *285*, L45–L48. [18](#), [35](#)
- Bond, J. R., Efstathiou, G., & Tegmark, M. (1997). Forecasting cosmic parameter errors from microwave background anisotropy experiments. *Mon. Not. R. Astron. Soc.*, *291*, L33–L41. [40](#), [64](#)

- Bond, J. R., & Szalay, A. S. (1983). The collisionless damping of density fluctuations in an expanding universe. *Astrophys. J.*, *274*, 443–468. [18](#)
- Borgani, S., et al. (2001). Measuring Ω_m with the *ROSAT* Deep Cluster Survey. *Astrophys. J.*, *561*, 13–21. [45](#)
- Borgani, S., et al. (2004). X-ray properties of galaxy clusters and groups from a cosmological hydrodynamical simulation. *Mon. Not. R. Astron. Soc.*, *348*, 1078–1096. [116](#)
- Branch, D., & Tammann, G. A. (1992). Type IA supernovae as standard candles. *Ann. Rev. Astron. Astrophys.*, *30*, 359–389. [30](#)
- Branchesi, M., Gioia, I. M., Fanti, C., & Fanti, R. (2007). High redshift X-ray galaxy clusters. II. The L_X – T relationship revisited. *Astron. Astrophys.*, *472*, 739–748. [117](#), [118](#), [141](#)
- Brax, P., & Martin, J. (1999a). Cosmological Implications of the Supergravity Tracking Potential. *Preprint (arXiv:astro-ph/9912005)*. [74](#)
- Brax, P., & Martin, J. (1999b). Quintessence and supergravity. *Phys. Lett. B*, *468*, 40–45. [103](#)
- Brax, P., Martin, J., & Riazuelo, A. (2001). Quintessence with two energy scales. *Phys. Rev. D*, *64*(8), 083505–+. [103](#)
- Brodwin, M., et al. (2007). Galaxy Cluster Correlation Function to $z \sim 1.5$ in the IRAC Shallow Cluster Survey. *Astrophys. J.*, *671*, L93–L96. [126](#)
- Bryan, G. L., & Norman, M. L. (1998). Statistical Properties of X-Ray Clusters: Analytic and Numerical Comparisons. *Astrophys. J.*, *495*, 80–+. [115](#)
- Buchert, T. (2008). Dark Energy from structure: a status report. *Gen. Relativ. Gravit.*, *40*, 467–527. [68](#)
- Caldwell, R. R., Doran, M., Müller, C. M., Schäfer, G., & Wetterich, C. (2003). Early Quintessence in Light of the *Wilkinson Microwave Anisotropy Probe*. *Astrophys. J.*, *591*, L75–L78. [43](#), [103](#)
- Caldwell, R. R., & Linder, E. V. (2005). Limits of Quintessence. *Phys. Rev. Lett.*, *95*(14), 141301–+. [78](#), [100](#)
- Carlstrom, J. E., Holder, G. P., & Reese, E. D. (2002). Cosmology with the Sunyaev–Zel’dovich Effect. *Ann. Rev. Astron. Astrophys.*, *40*, 643–680. [107](#)
- Carroll, S. M. (1998). Quintessence and the Rest of the World: Suppressing Long-Range Interactions. *Phys. Rev. Lett.*, *81*, 3067–3070. [72](#)

- Carroll, S. M. (2001). The Cosmological Constant. *Liv. Rev. Rel.*, 4, 1–+. [66](#)
- Carroll, S. M., Press, W. H., & Turner, E. L. (1992). The cosmological constant. *Ann. Rev. Astron. Astrophys.*, 30, 499–542. [18](#)
- Cole, S., et al. (2005). The 2dF Galaxy Redshift Survey: power-spectrum analysis of the final data set and cosmological implications. *Mon. Not. R. Astron. Soc.*, 362, 505–534. [35](#), [57](#)
- Coles, P., & Lucchin, F. (2002). *Cosmology: The Origin and Evolution of Cosmic Structure*. Wiley–VCH, 2 ed. [16](#)
- Colgate, S. A. (1979). Supernovae as a standard candle for cosmology. *Astrophys. J.*, 232, 404–408. [30](#)
- Collins, C. A., et al. (2000). The *ROSAT*–ESO Flux-Limited X-ray (REFLEX) galaxy cluster survey – II. The spatial correlation function. *Mon. Not. R. Astron. Soc.*, 319, 939–948. [126](#)
- Cools, R., & Haegemans, A. (2003). Algorithm 824: *CUBPACK*: a package for automatic cubature; framework description. *ACM Transactions on Mathematical Software*, 29(3), 287–296. [vi](#), [128](#)
- Copeland, E. J. (2007). Dynamics of Dark Energy. In *Particles, Strings, and Cosmology – PASCOS 2007*, vol. 957 of *American Institute of Physics Conference Series*, (pp. 21–29). [66](#)
- Copeland, E. J., Liddle, A. R., & Wands, D. (1998). Exponential potentials and cosmological scaling solutions. *Phys. Rev. D*, 57, 4686–4690. [74](#)
- Corasaniti, P. S., Kunz, M., Parkinson, D., Copeland, E. J., & Bassett, B. A. (2004). Foundations of observing dark energy dynamics with the *Wilkinson Microwave Anisotropy Probe*. *Phys. Rev. D*, 70(8), 083006–+. [44](#), [86](#)
- Corasaniti, P. S., & Melchiorri, A. (2008). Testing cosmology with cosmic sound waves. *Phys. Rev. D*, 77(10), 103507–+. [43](#)
- Crittenden, R. G., & Pogosian, L. (2005). Investigating dark energy experiments with principal components. *Preprint (arXiv:astro-ph/0510293)*. [28](#)
- Csáki, C., Kaloper, N., & Terning, J. (2006). The accelerated acceleration of the universe. *J. Cosmol. Astropart. Phys.*, 6, 22–+. [95](#)
- Daly, R. A., & Djorgovski, S. G. (2003). A Model-Independent Determination of the Expansion and Acceleration Rates of the Universe as a Function of Redshift and Con-

- straints on Dark Energy. *Astrophys. J.*, 597, 9–20. [77](#), [87](#)
- Daly, R. A., & Djorgovski, S. G. (2004). Direct Determination of the Kinematics of the Universe and Properties of the Dark Energy as Functions of Redshift. *Astrophys. J.*, 612, 652–659. [77](#), [87](#)
- Daly, R. A., & Djorgovski, S. G. (2005). Constraints on the Physical Parameters of the Dark Energy Using a Model-Independent Approach. *Preprint (arXiv:astro-ph/0512576)*. [77](#), [87](#)
- Daly, R. A., & Djorgovski, S. G. (2007). A Nearly Model-Independent Characterization of Dark Energy Properties as a Function of Redshift. *Nucl. Phys. B Proc. Suppl.*, 173, 19–23. [77](#), [87](#)
- Das, R., Kephart, T. W., & Scherrer, R. J. (2006). Tracking quintessence and k-essence in a general cosmological background. *Phys. Rev. D*, 74(10), 103515–+. [74](#)
- Dave, R., Caldwell, R. R., & Steinhardt, P. J. (2002). Sensitivity of the cosmic microwave background anisotropy to initial conditions in quintessence cosmology. *Phys. Rev. D*, 66(2), 023516–+. [17](#)
- Davis, T. M., et al. (2007). Scrutinizing Exotic Cosmological Models Using ESSENCE Supernova Data Combined with Other Cosmological Probes. *Astrophys. J.*, 666, 716–725. [31](#)
- de Bernardis, P., et al. (2000). A flat Universe from high-resolution maps of the cosmic microwave background radiation. *Nature (London)*, 404, 955–959. [38](#)
- de Ritis, R., Marino, A. A., Rubano, C., & Scudellaro, P. (2000). Tracker fields from nonminimally coupled theory. *Phys. Rev. D*, 62(4), 043506–+. [74](#)
- De Simone, A., Guth, A. H., Linde, A., Noorbala, M., Salem, M. P., & Vilenkin, A. (2008). Boltzmann brains and the scale-factor cutoff measure of the multiverse. *Preprint (arXiv:0808.3778)*. [69](#)
- Dicke, R. H., Peebles, P. J. E., Roll, P. G., & Wilkinson, D. T. (1965). Cosmic Black-Body Radiation. *Astrophys. J.*, 142, 414–419. [38](#)
- Dickinson, C., et al. (2004). High-sensitivity measurements of the cosmic microwave background power spectrum with the extended Very Small Array. *Mon. Not. R. Astron. Soc.*, 353, 732–746. [38](#)
- Dodelson, S. (2003). *Modern cosmology*. Academic Press. [11](#), [38](#)
- Donahue, M., & Voit, G. M. (1999). Ω_m from the Temperature-Redshift Distribution of

- EMSS Clusters of Galaxies. *Astrophys. J.*, 523, L137–L140. 45
- Doran, M., & Lilley, M. (2002). The location of cosmic microwave background peaks in a universe with dark energy. *Mon. Not. R. Astron. Soc.*, 330, 965–970. 43
- Doran, M., & Robbers, G. (2006). Early dark energy cosmologies. *J. Cosmol. Astropart. Phys.*, 6, 26–+. 43, 103
- Dunkley, J., Bucher, M., Ferreira, P. G., Moodley, K., & Skordis, C. (2005). Fast and reliable Markov chain Monte Carlo technique for cosmological parameter estimation. *Mon. Not. R. Astron. Soc.*, 356, 925–936. 51
- Dunkley, J., et al. (2008). Five-Year *Wilkinson Microwave Anisotropy Probe* (*WMAP*) Observations: Likelihoods and Parameters from the *WMAP* data. Preprint (*arXiv:0803.0586*). 56
- Efstathiou, G. (2008). Limitations of Bayesian Evidence applied to cosmology. *Mon. Not. R. Astron. Soc.*, 388, 1314–1320. 51
- Efstathiou, G., & Bond, J. R. (1986). Isocurvature cold dark matter fluctuations. *Mon. Not. R. Astron. Soc.*, 218, 103–121. 18
- Efstathiou, G., & Bond, J. R. (1999). Cosmic confusion: degeneracies among cosmological parameters derived from measurements of microwave background anisotropies. *Mon. Not. R. Astron. Soc.*, 304, 75–97. 40
- Efstathiou, G., Bond, J. R., & White, S. D. M. (1992). *COBE* background radiation anisotropies and large-scale structure in the universe. *Mon. Not. R. Astron. Soc.*, 258, 1P–6P. 19
- Einstein, A. (1916). Die Grundlage der allgemeinen Relativitätstheorie. *Ann. Phys. (Leipzig)*, 354, 769–822. 11, 12
- Einstein, A. (1917). Kosmologische Betrachtungen zur allgemeinen Relativitätstheorie. *Sitzungsberichte der Königlich Preussischen Akademie der Wissenschaften*, (pp. 142–152). 11, 12
- Einstein, A., & de Sitter, W. (1932). On the Relation between the Expansion and the Mean Density of the Universe. *Proc. Natl. Acad. Sci. USA*, 18, 213–214. 12
- Eisenstein, D. (2008). What is the acoustic peak? Web site.
URL http://cmb.as.arizona.edu/~eisenste/acousticpeak/acoustic_physics.html
- 34
- Eisenstein, D. J., & Hu, W. (1998). Baryonic Features in the Matter Transfer Function.

- Astrophys. J.*, 496, 605–+. 18, 35
- Eisenstein, D. J., & Hu, W. (1999). Power Spectra for Cold Dark Matter and Its Variants. *Astrophys. J.*, 511, 5–15. 18
- Eisenstein, D. J., et al. (2005). Detection of the Baryon Acoustic Peak in the Large-Scale Correlation Function of SDSS Luminous Red Galaxies. *Astrophys. J.*, 633, 560–574. 35, 37, 57, 61, 77, 83, 125
- Eke, V. R., Cole, S., Frenk, C. S., & Patrick Henry, J. (1998). Measuring Ω_0 using cluster evolution. *Mon. Not. R. Astron. Soc.*, 298, 1145–1158. 45
- Elias, J. H., Matthews, K., Neugebauer, G., & Persson, S. E. (1985). Type I supernovae in the infrared and their use as distance indicators. *Astrophys. J.*, 296, 379–389. 30
- Erlich, J., Glover, B., & Weiner, N. (2008). Sensitivity and insensitivity of galaxy cluster surveys to new physics. *J. Cosmol. Astropart. Phys.*, 3, 6–+. 46
- Etherington, I. M. H. (1933). On the Definition of Distance in General Relativity. *Philos. Mag.*, 15, 761–+. 23
- Ettori, S., Tozzi, P., & Rosati, P. (2003). Constraining the cosmological parameters with the gas mass fraction in local and $z > 0.7$ galaxy clusters. *Astron. Astrophys.*, 398, 879–890. 46
- Ettori, S., et al. (2004a). Evolution at $z \geq 0.5$ of the X-ray properties of simulated galaxy clusters: comparison with observational constraints. *Mon. Not. R. Astron. Soc.*, 354, 111–122. 115, 117
- Ettori, S., et al. (2004b). Scaling laws in X-ray galaxy clusters at redshift between 0.4 and 1.3. *Astron. Astrophys.*, 417, 13–27. 115, 117
- Evrard, A. E., et al. (2002). Galaxy clusters in hubble volume simulations: Cosmological constraints from sky survey populations. *Astrophys. J.*, 573, 7–36. 45
- FAMSI (2008). Codex Selden/Codex Añute. Web site.
URL <http://www.famsi.org/research/pohl/jpcodices/selden/> 5
- Feroz, F., & Hobson, M. P. (2008). Multimodal nested sampling: an efficient and robust alternative to Markov Chain Monte Carlo methods for astronomical data analyses. *Mon. Not. R. Astron. Soc.*, 384, 449–463. 50
- Ferreira, P. G., & Joyce, M. (1997). Structure Formation with a Self-Tuning Scalar Field. *Phys. Rev. Lett.*, 79, 4740–4743. 74
- Ferreira, P. G., & Joyce, M. (1998). Cosmology with a primordial scaling field. *Phys. Rev.*

- D*, 58(2), 023503–+. [74](#)
- Fouchez, D. (2006). Private communication. [82](#)
- Frenk, C. S., White, S. D. M., Efstathiou, G., & Davis, M. (1990). Galaxy clusters and the amplitude of primordial fluctuations. *Astrophys. J.*, 351, 10–21. [45](#)
- Friedmann, A. (1922). Über die Krümmung des Raumes. *Z. Phys. A*, 10, 377–386. [12](#)
- Friedmann, A. (1924). Über die Möglichkeit einer Welt mit konstanter negativer Krümmung des Raumes. *Z. Phys. A*, 21, 326–332. [12](#)
- Frieman, J. A., Hill, C. T., Stebbins, A., & Waga, I. (1995). Cosmology with Ultralight Pseudo Nambu–Goldstone Bosons. *Phys. Rev. Lett.*, 75, 2077–2080. [103](#)
- Frieman, J. A., Hill, C. T., & Watkins, R. (1992). Late-time cosmological phase transitions: Particle-physics models and cosmic evolution. *Phys. Rev. D*, 46, 1226–1238. [103](#)
- Fukugita, M., & Yanagida, T. (1994). Model for the cosmological constant. YITP-K-1098. [103](#)
- Garnavich, P. M., et al. (1998). Supernova Limits on the Cosmic Equation of State. *Astrophys. J.*, 509, 74–79. [31](#)
- Garriga, J., Schwartz–Perlov, D., Vilenkin, A., & Winitzki, S. (2006). Probabilities in the inflationary multiverse. *J. Cosmol. Astropart. Phys.*, 1, 17–+. [69](#)
- Geisbüsch, J., & Hobson, M. P. (2007). Cosmology with the Planck cluster sample. *Mon. Not. R. Astron. Soc.*, 382, 158–176. [136](#), [138](#), [150](#)
- Gelman, A., & Rubin, D. B. (1992). Inference from iterative simulation using multiple sequences. *Statistical Science*, 7(4), 457–472. [52](#)
- Gerke, B. F., & Efstathiou, G. (2002). Probing quintessence: reconstruction and parameter estimation from supernovae. *Mon. Not. R. Astron. Soc.*, 335, 33–43. [77](#)
- Gibbons, G. W., Hawking, S. W., & Stewart, J. M. (1987). A natural measure on the set of all universes. *Nucl. Phys. B*, 281, 736–751. [69](#)
- Gibbons, G. W., & Turok, N. (2008). Measure problem in cosmology. *Phys. Rev. D*, 77(6), 063516–+. [69](#), [91](#)
- Gilks, W. R., Richardson, S., & Spiegelhalter, D. J. (Eds.) (1996). *Markov Chain Monte Carlo in Practice*. Chapman & Hall. [51](#), [52](#)
- Gladders, M. D. (2004). The red sequence technique and high-redshift galaxy clusters. In J. S. Mulchaey, A. Dressler, & A. Oemler (Eds.) *Clusters of Galaxies: Probes of Cosmo-*

- logical Structure and Galaxy Evolution*, vol. 3 of *Carnegie Observatories Astrophysics Series*, (pp. 89–107). Cambridge University Press. [121](#)
- Gladders, M. D., & Yee, H. K. C. (2000). A New Method For Galaxy Cluster Detection. I. The Algorithm. *Astron. J.*, *120*, 2148–2162. [120](#)
- Gladders, M. D., & Yee, H. K. C. (2005). The Red-Sequence Cluster Survey. I. The Survey and Cluster Catalogs for Patches RCS 0926+37 and RCS 1327+29. *Astrophys. J. Suppl. Ser.*, *157*, 1–29. [107](#), [120](#), [121](#)
- Gladders, M. D., Yee, H. K. C., Majumdar, S., Barrientos, L. F., Hoekstra, H., Hall, P. B., & Infante, L. (2007). Cosmological Constraints from the Red-Sequence Cluster Survey. *Astrophys. J.*, *655*, 128–134. [45](#), [46](#), [57](#), [59](#), [121](#)
- Gonzalez, A. H., Zaritsky, D., & Wechsler, R. H. (2002). The Las Campanas Distant Cluster Survey Correlation Function. *Astrophys. J.*, *571*, 129–135. [126](#)
- Goobar, A., & Perlmutter, S. (1995). Feasibility of Measuring the Cosmological Constant Lambda and Mass Density Omega Using Type IA Supernovae. *Astrophys. J.*, *450*, 14–+. [30](#)
- Gregory, P. C. (2005). *Bayesian Logical Data Analysis for the Physical Sciences: A Comparative Approach with ‘Mathematica’ Support*. Cambridge University Press. [48](#)
- Guo, Z.-K., Ohta, N., & Zhang, Y.-Z. (2005). Parametrization of quintessence and its potential. *Phys. Rev. D*, *72*(2), 023504–+. [77](#)
- Guo, Z.-K., Ohta, N., & Zhang, Y.-Z. (2007). Parametrizations of the Dark Energy Density and Scalar Potentials. *Mod. Phys. Lett. A*, *22*, 883–890. [77](#)
- Guth, A. H. (1981). Inflationary universe: A possible solution to the horizon and flatness problems. *Phys. Rev. D*, *23*, 347–356. [19](#)
- Hahn, T. (2005). CUBA – a library for multidimensional numerical integration. *Comput. Phys. Commun.*, *168*, 78–95. [128](#)
- Haiman, Z., Mohr, J. J., & Holder, G. P. (2001). Constraints on Cosmological Parameters from Future Galaxy Cluster Surveys. *Astrophys. J.*, *553*, 545–561. [46](#), [108](#), [135](#), [142](#), [152](#)
- Haiman, Z., et al. (2005). An X-ray Galaxy Cluster Survey for Investigations of Dark Energy. *E-print (arXiv:astro-ph/0507013)*. [107](#), [152](#)
- Halverson, N. W., et al. (2002). Degree Angular Scale Interferometer First Results: A Measurement of the Cosmic Microwave Background Angular Power Spectrum. *Astro-*

- phys. J.*, 568, 38–45. 38
- Hamilton, A. J. S. (2005). Power Spectrum Estimation I. Basics. *Preprint (arXiv:astro-ph/0503603)*. 25
- Hamuy, M., et al. (1993). The 1990 Calán/Tololo Supernova Search. *Astron. J.*, 106, 2392–2407. 31
- Hanany, S., et al. (2000). MAXIMA-1: A Measurement of the Cosmic Microwave Background Anisotropy on Angular Scales of 10° – 5° . *Astrophys. J.*, 545, L5–L9. 38
- Hartle, J. B., Hawking, S. W., & Hertog, T. (2008). No-Boundary Measure of the Universe. *Phys. Rev. Lett.*, 100(20), 201301–+. 69
- Hawking, S. W., & Hertog, T. (2002). Why does inflation start at the top of the hill? *Phys. Rev. D*, 66(12), 123509–+. 69
- Hawking, S. W., & Page, D. N. (1988). How probable is inflation? *Nucl. Phys. B*, 298, 789–809. 69
- Heath, D. J. (1977). The growth of density perturbations in zero pressure Friedmann–Lemaître universes. *Mon. Not. R. Astron. Soc.*, 179, 351–358. 18
- Heavens, A. (2008). The cosmological model: an overview and an outlook. *J. Phys. Conf. Ser.*, 120(2), 022001–+. 65
- Henry, J. P. (1997). A Measurement of the Density Parameter Derived from the Evolution of Cluster X-Ray Temperatures. *Astrophys. J.*, 489, L1+. 45
- Henry, J. P. (2000). Measuring Cosmological Parameters from the Evolution of Cluster X-Ray Temperatures. *Astrophys. J.*, 534, 565–580. 45
- Henry, J. P. (2004). X-Ray Temperatures for the Extended Medium-Sensitivity Survey High-Redshift Cluster Sample: Constraints on Cosmology and the Dark Energy Equation of State. *Astrophys. J.*, 609, 603–616. 45
- Hicks, A. K., et al. (2008). *Chandra* X-Ray Observations of the $0.6 < z < 1.1$ Red-Sequence Cluster Survey Sample. *Astrophys. J.*, 680, 1022–1041. 117
- Hilgevoord, J., & Uffink, J. (Fall 2008). The Uncertainty Principle. In E. N. Zalta (Ed.) *The Stanford Encyclopedia of Philosophy*.
URL <http://plato.stanford.edu/archives/fall2008/entries/qt-uncertainty/>
70
- Hill, C. T., Schramm, D. N., & Fry, J. N. (1989). Cosmological structure formation from soft topological defects. *Comments Nucl. Part. Phys.*, 19(1), 25–39. 103

- Hillebrandt, W., & Niemeyer, J. C. (2000). Type IA Supernova Explosion Models. *Ann. Rev. Astron. Astrophys.*, *38*, 191–230. [31](#)
- Hilton, M., et al. (2007). The XMM Cluster Survey: The Dynamical State of XMMXCS J2215.9-1738 at $z = 1.457$. *Astrophys. J.*, *670*, 1000–1009. [111](#), [118](#), [149](#)
- Holden, B. P., Stanford, S. A., Squires, G. K., Rosati, P., Tozzi, P., Eisenhardt, P., & Spinrad, H. (2002). Moderate-Temperature Clusters of Galaxies from the RDCS and the High-Redshift Luminosity–Temperature Relation. *Astron. J.*, *124*, 33–45. [117](#)
- Holder, G. (2006). Likelihood Functions for Galaxy Cluster Surveys. *Preprint (arXiv:astro-ph/0602251)*. [126](#)
- Holder, G., Haiman, Z., & Mohr, J. J. (2001). Constraints on Ω_m , Ω_Λ , and σ_8 from Galaxy Cluster Redshift Distributions. *Astrophys. J.*, *560*, L111–L114. [46](#), [108](#), [152](#), [153](#)
- Hollands, S., & Wald, R. M. (2002). Essay: An Alternative to Inflation. *Gen. Relativ. Gravit.*, *34*, 2043–2055. [69](#)
- Holtzman, J. A. (1989). Microwave background anisotropies and large-scale structure in universes with cold dark matter, baryons, radiation, and massive and massless neutrinos. *Astrophys. J. Suppl. Ser.*, *71*, 1–24. [18](#), [35](#)
- Hsieh, B. C., Yee, H. K. C., Lin, H., & Gladders, M. D. (2005). A Photometric Redshift Galaxy Catalog from the Red-Sequence Cluster Survey. *Astrophys. J. Suppl. Ser.*, *158*, 161–177. [107](#)
- Hu, W. (2003). Self-consistency and calibration of cluster number count surveys for dark energy. *Phys. Rev. D*, *67*(8), 081304–+. [46](#), [108](#), [138](#), [141](#), [142](#), [146](#), [150](#)
- Hu, W. (2008). A Tour of CMB Physics. Web site.
URL <http://background.uchicago.edu/~whu/physics/tour.html> [41](#)
- Hu, W., & Cohn, J. D. (2006). Likelihood methods for cluster dark energy surveys. *Phys. Rev. D*, *73*(6), 067301–+. [126](#)
- Hu, W., & Dodelson, S. (2002). Cosmic Microwave Background Anisotropies. *Ann. Rev. Astron. Astrophys.*, *40*, 171–216. [38](#)
- Hu, W., & Kravtsov, A. V. (2003). Sample Variance Considerations for Cluster Surveys. *Astrophys. J.*, *584*, 702–715. [45](#), [108](#), [116](#), [126](#), [142](#), [150](#)
- Hu, W., & Sugiyama, N. (1995). Anisotropies in the cosmic microwave background: an analytic approach. *Astrophys. J.*, *444*, 489–506. [18](#)
- Hu, W., & Sugiyama, N. (1996). Small-Scale Cosmological Perturbations: an Analytic

- Approach. *Astrophys. J.*, 471, 542–+. [35](#), [42](#)
- Hu, W., & White, M. (1997). A CMB polarization primer. *New Astron.*, 2, 323–344. [44](#)
- Hubble, E. (1929). A Relation between Distance and Radial Velocity among Extra-Galactic Nebulae. *Proc. Natl. Acad. Sci. USA*, 15, 168–173. [12](#), [31](#)
- Hume, D. (1935). *Dialogues concerning Natural Religion*. Oxford University Press. [3](#)
- Huterer, D., & Cooray, A. (2005). Uncorrelated estimates of dark energy evolution. *Phys. Rev. D*, 71(2), 023506–+. [28](#)
- Huterer, D., Kim, A., Krauss, L. M., & Broderick, T. (2004). Redshift Accuracy Requirements for Future Supernova and Number Count Surveys. *Astrophys. J.*, 615, 595–602. [109](#), [120](#), [142](#), [150](#)
- Huterer, D., & Peiris, H. V. (2007). Dynamical behavior of generic quintessence potentials: Constraints on key dark energy observables. *Phys. Rev. D*, 75(8), 083503–+. [78](#)
- Huterer, D., & Starkman, G. (2003). Parametrization of Dark-Energy Properties: A Principal-Component Approach. *Phys. Rev. Lett.*, 90(3), 031301–+. [28](#)
- Huterer, D., Takada, M., Bernstein, G., & Jain, B. (2006). Systematic errors in future weak-lensing surveys: requirements and prospects for self-calibration. *Mon. Not. R. Astron. Soc.*, 366, 101–114. [109](#), [120](#), [142](#), [150](#)
- Huterer, D., & Turner, M. S. (1999). Prospects for probing the dark energy via supernova distance measurements. *Phys. Rev. D*, 60(8), 081301–+. [77](#)
- Huterer, D., & Turner, M. S. (2001). Probing dark energy: Methods and strategies. *Phys. Rev. D*, 64(12), 123527–+. [46](#)
- Ikebe, Y., Reiprich, T. H., Böhringer, H., Tanaka, Y., & Kitayama, T. (2002). A new measurement of the X-ray temperature function of clusters of galaxies. *Astron. Astrophys.*, 383, 773–790. [117](#), [118](#), [119](#)
- Ishak, M., Upadhye, A., & Spergel, D. N. (2006). Probing cosmic acceleration beyond the equation of state: Distinguishing between dark energy and modified gravity models. *Phys. Rev. D*, 74(4), 043513–+. [29](#), [86](#)
- Jahoda, K., & the *DUET* collaboration (2003). *DUET – The Dark Universe Exploration Telescope*. *Astron. Nachr.*, 324, 132–135. [107](#), [108](#)
- Jamsthaler, H. (1625). *Viatorium spagyricum*. Frankfurt. [xiii](#)
- Jassal, H. K., Bagla, J. S., & Padmanabhan, T. (2006). The vanishing phantom menace.

- Preprint (arXiv:astro-ph/0601389)*. [95](#)
- Jaynes, E. T. (2003). *Probability Theory: The Logic of Science*. Cambridge University Press. [48](#)
- Jeffreys, H. (1961). *Theory of Probability*. Oxford University Press. [49](#), [50](#)
- Jenkins, A., et al. (2001). The mass function of dark matter haloes. *Mon. Not. R. Astron. Soc.*, *321*, 372–384. [45](#)
- Jeong, E., & Smoot, G. F. (2007). Probing Non-Gaussianity In The Cosmic Microwave Background Anisotropies: One Point Distribution Function. *Preprint (arXiv:0710.2371)*. [27](#)
- Johri, V. B. (2001). Genesis of cosmological tracker fields. *Phys. Rev. D*, *63*(10), 103504–+. [74](#)
- Johri, V. B. (2002). Search for tracker potentials in quintessence theory. *Class. Quantum Grav.*, *19*, 5959–5968. [74](#)
- Jones, W. C., et al. (2006). A Measurement of the Angular Power Spectrum of the CMB Temperature Anisotropy from the 2003 Flight of BOOMERANG. *Astrophys. J.*, *647*, 823–832. [38](#)
- Juin, J. B., Yvon, D., Refregier, A., & Yèche, C. (2005). Cosmology with wide-field SZ cluster surveys: Selection and Systematic Effects. *Preprint (arXiv:astro-ph/0512378)*. [107](#)
- Jung, C. G. (2003). *Four Archetypes: Mother, Rebirth, Spirit, Trickster*. Routledge. [3](#)
- Kaiser, N. (1986). Evolution and clustering of rich clusters. *Mon. Not. R. Astron. Soc.*, *222*, 323–345. [115](#), [117](#)
- Kaloper, N., & Sorbo, L. (2006). Of pNGB quiNtessence. *J. Cosmol. Astropart. Phys.*, *4*, 7–+. [103](#)
- Kass, R. E., & Raftery, A. E. (1995). Bayes factors. *Journal of the American Statistical Association*, *90*, 773–795. [49](#)
- Kay, S. T., da Silva, A. C., Aghanim, N., Blanchard, A., Liddle, A. R., Puget, J.-L., Sadat, R., & Thomas, P. A. (2007). The evolution of clusters in the CLEF cosmological simulation: X-ray structural and scaling properties. *Mon. Not. R. Astron. Soc.*, *377*, 317–334. [111](#), [119](#), [151](#), [153](#)
- King, L. W. (2002). *The Seven Tablets of Creation: The Babylonian and Assyrian Legends Concerning the Creation of the World and of Mankind*. Adamant Media. [2](#)

- Klypin, A., Macciò, A. V., Mainini, R., & Bonometto, S. A. (2003). Halo Properties in Models with Dynamical Dark Energy. *Astrophys. J.*, *599*, 31–37. [45](#)
- Knop, R. A., et al. (2003). New Constraints on Ω_M , Ω_Λ , and w from an Independent Set of 11 High-Redshift Supernovae Observed with the Hubble Space Telescope. *Astrophys. J.*, *598*, 102–137. [31](#)
- Kofman, L., Linde, A., & Mukhanov, V. (2002). Inflationary Theory and Alternative Cosmology. *J. High Energy Phys.*, *10*, 57–+. [69](#)
- Komatsu, E., et al. (2008). Five-Year *Wilkinson Microwave Anisotropy Probe (WMAP)* Observations: Cosmological Interpretation. *Preprint (arXiv:0803.0547)*. [38](#), [39](#), [40](#), [43](#), [57](#), [59](#), [60](#), [63](#), [77](#), [79](#), [82](#), [84](#), [125](#)
- Kotov, O., & Vikhlinin, A. (2005). *XMM-Newton* Observations of Evolution of Cluster X-Ray Scaling Relations at $z = 0.4$ – 0.7 . *Astrophys. J.*, *633*, 781–790. [115](#), [117](#)
- Kotov, O., & Vikhlinin, A. (2006). *Chandra* Sample of Galaxy Clusters at $z = 0.4$ – 0.55 : Evolution in the Mass–Temperature Relation. *Astrophys. J.*, *641*, 752–755. [115](#)
- Kovac, J. M., Leitch, E. M., Pryke, C., Carlstrom, J. E., Halverson, N. W., & Holzappel, W. L. (2002). Detection of polarization in the cosmic microwave background using DASI. *Nature (London)*, *420*, 772–787. [38](#)
- Kowal, C. T. (1968). Absolute magnitudes of supernovae. *Astron. J.*, *73*, 1021–1024. [30](#)
- Kowalski, M., et al. (2008). Improved Cosmological Constraints from New, Old and Combined Supernova Datasets. *Preprint (arXiv:0804.4142)*. [31](#), [32](#), [33](#), [36](#), [54](#), [55](#), [59](#), [62](#), [77](#), [82](#)
- Kravtsov, A. V., Vikhlinin, A., & Nagai, D. (2006). A New Robust Low-Scatter X-Ray Mass Indicator for Clusters of Galaxies. *Astrophys. J.*, *650*, 128–136. [116](#), [154](#)
- Kulikovskij, P. G. (1944). *Astron. Zh. [Sov. Astron.]*, *21*, 211. [30](#)
- Kunz, M., Trotta, R., & Parkinson, D. (2006). Measuring the effective complexity of cosmological models. *Phys. Rev. D*, *74*, 023503. [141](#)
- Kuo, C. L., et al. (2004). High-Resolution Observations of the Cosmic Microwave Background Power Spectrum with ACBAR. *Astrophys. J.*, *600*, 32–51. [38](#)
- Kuo, C. L., et al. (2007). Improved Measurements of the CMB Power Spectrum with ACBAR. *Astrophys. J.*, *664*, 687–701. [38](#)
- Lahav, O., Lilje, P. B., Primack, J. R., & Rees, M. J. (1991). Dynamical effects of the cosmological constant. *Mon. Not. R. Astron. Soc.*, *251*, 128–136. [18](#)

- Leibundgut, B. (2008). Supernovae and cosmology. *Gen. Relativ. Gravit.*, *40*, 221–248. [31](#)
- Leitch, E. M., Kovac, J. M., Halverson, N. W., Carlstrom, J. E., Pryke, C., & Smith, M. W. E. (2005). Degree Angular Scale Interferometer 3 Year Cosmic Microwave Background Polarization Results. *Astrophys. J.*, *624*, 10–20. [38](#)
- Lemaître, G. (1927). Un Univers homogène de masse constante et de rayon croissant rendant compte de la vitesse radiale des nébuleuses extragalactiques. *Annales de la Société scientifique de Bruxelles A*, *47*, 49–56. [12](#)
- Lemaître, G. (1931). The Beginning of the World from the Point of View of Quantum Theory. *Nature (London)*, *127*, 706–+. [12](#), [36](#)
- Levine, E. S., Schulz, A. E., & White, M. (2002). Future Galaxy Cluster Surveys: The Effect of Theory Uncertainty on Constraining Cosmological Parameters. *Astrophys. J.*, *577*, 569–578. [46](#), [108](#), [136](#), [142](#), [150](#), [152](#), [153](#)
- Lewis, A., & Bridle, S. (2002). Cosmological parameters from CMB and other data: A Monte Carlo approach. *Phys. Rev. D*, *66*(10), 103511–+. [vi](#), [51](#), [52](#), [193](#)
- Liddle, A. (2003). *An Introduction to Modern Cosmology*. Wiley–VCH, 2 ed. [11](#)
- Liddle, A. R. (2004). How many cosmological parameters? *Mon. Not. R. Astron. Soc.*, *351*, L49–L53. [49](#)
- Liddle, A. R. (2007). Information criteria for astrophysical model selection. *Mon. Not. R. Astron. Soc.*, *377*, L74–L78. [50](#)
- Liddle, A. R., & Lyth, D. H. (2000). *Cosmological Inflation and Large-Scale Structure*. Cambridge University Press. [11](#), [16](#), [18](#), [19](#), [25](#)
- Liddle, A. R., Mukherjee, P., & Parkinson, D. (2006a). Cosmological model selection. *Astron. Geophys.*, *47*, 4.30–4.33. [49](#)
- Liddle, A. R., Mukherjee, P., Parkinson, D., & Wang, Y. (2006b). Present and future evidence for evolving dark energy. *Phys. Rev. D*, *74*(12), 123506–+. [88](#), [106](#)
- Liddle, A. R., & Scherrer, R. J. (1999). Classification of scalar field potentials with cosmological scaling solutions. *Phys. Rev. D*, *59*(2), 023509–+. [74](#), [75](#)
- Liddle, A. R., Viana, P. T. P., Romer, A. K., & Mann, R. G. (2001). Apparent and actual galaxy cluster temperatures. *Mon. Not. R. Astron. Soc.*, *325*, 875–880. [120](#), [122](#), [136](#)
- Lightman, A. P., & Schechter, P. L. (1990). The Omega dependence of peculiar velocities induced by spherical density perturbations. *Astrophys. J. Suppl. Ser.*, *74*, 831–+. [18](#)

- Lima, M., & Hu, W. (2004). Self-Calibration of Cluster Dark Energy Studies: Counts in Cells. *Phys. Rev. D*, *70*, 043504. [108](#), [126](#), [138](#), [141](#), [146](#), [152](#), [154](#)
- Lima, M., & Hu, W. (2005). Self-calibration of cluster dark energy studies: Observable-mass distribution. *Phys. Rev. D*, *72*(4), 043006–+. [46](#), [108](#), [126](#), [138](#), [142](#), [146](#), [152](#)
- Lima, M., & Hu, W. (2007). Photometric redshift requirements for self-calibration of cluster dark energy studies. *Phys. Rev. D*, *76*(12), 123013–+. [109](#), [120](#), [142](#), [150](#), [152](#)
- Linde, A. D. (1982). A new inflationary Universe scenario: a possible solution of the horizon, flatness, homogeneity, isotropy and primordial monopole problems. *Phys. Lett. B*, *108*, 389–393. [19](#)
- Linder, E. V. (1988). Light propagation in generalized Friedmann universes. *Astron. Astrophys.*, *206*, 190–198. [23](#)
- Linder, E. V. (2005). Curved space or curved vacuum? *Astropart. Phys.*, *24*, 391–399. [80](#)
- Linder, E. V. (2006). Paths of quintessence. *Phys. Rev. D*, *73*(6), 063010–+. [74](#), [103](#)
- Linder, E. V., & Huterer, D. (2005). How many dark energy parameters? *Phys. Rev. D*, *72*(4), 043509–+. [81](#)
- Linder, E. V., & Jenkins, A. (2003). Cosmic structure growth and dark energy. *Mon. Not. R. Astron. Soc.*, *346*, 573–583. [17](#), [45](#)
- Lokas, E. L., Bode, P., & Hoffman, Y. (2004). Cluster mass functions in the quintessential universe. *Mon. Not. R. Astron. Soc.*, *349*, 595–602. [45](#)
- Lumb, D. H., et al. (2004). The *XMM-NEWTON* Ω project. I. The X-ray luminosity–temperature relation at $z > 0.4$. *Astron. Astrophys.*, *420*, 853–872. [117](#)
- Lundmark, K. (1956). On metagalactic distance-indicators. *Vistas in Astronomy*, *2*, 1607–1619. [30](#)
- Ma, C.-P., Caldwell, R. R., Bode, P., & Wang, L. (1999). The Mass Power Spectrum in Quintessence Cosmological Models. *Astrophys. J.*, *521*, L1–L4. [17](#), [18](#), [26](#)
- Mackay, D. J. C. (2003). *Information Theory, Inference and Learning Algorithms*. Cambridge University Press. [49](#)
- Majumdar, S., & Mohr, J. J. (2003). Importance of Cluster Structural Evolution in Using X-Ray and Sunyaev-Zel’dovich Effect Galaxy Cluster Surveys to Study Dark Energy. *Astrophys. J.*, *585*, 603–610. [46](#), [108](#), [152](#)
- Majumdar, S., & Mohr, J. J. (2004). Self-Calibration in Cluster Studies of Dark Energy:

- Combining the Cluster Redshift Distribution, the Power Spectrum, and Mass Measurements. *Astrophys. J.*, *613*, 41–50. [46](#), [108](#), [126](#), [136](#), [138](#), [141](#), [146](#), [150](#), [151](#), [152](#), [154](#), [155](#)
- Mantz, A., Allen, S. W., Ebeling, H., & Rapetti, D. (2008). New constraints on dark energy from the observed growth of the most X-ray luminous galaxy clusters. *Mon. Not. R. Astron. Soc.*, *387*, 1179–1192. [46](#), [57](#), [59](#)
- Maor, I., & Brustein, R. (2003). Distinguishing among scalar field models of dark energy. *Phys. Rev. D*, *67*(10), 103508–+. [81](#)
- Maor, I., Brustein, R., McMahon, J., & Steinhardt, P. J. (2002). Measuring the equation of state of the universe: Pitfalls and prospects. *Phys. Rev. D*, *65*(12), 123003–+. [29](#), [91](#), [95](#)
- Maor, I., Brustein, R., & Steinhardt, P. J. (2001a). Limitations in Using Luminosity Distance to Determine the Equation of State of the Universe. *Phys. Rev. Lett.*, *86*, 6–9. [29](#), [91](#), [95](#)
- Maor, I., Brustein, R., & Steinhardt, P. J. (2001b). Erratum: Limitations in Using Luminosity Distance to Determine the Equation of State of the Universe [Phys. Rev. Lett. 86, 6 (2001)]. *Phys. Rev. Lett.*, *87*(4), 049901–+. [29](#), [91](#), [95](#)
- Mason, B. S., et al. (2003). The Anisotropy of the Microwave Background to $l = 3500$: Deep Field Observations with the Cosmic Background Imager. *Astrophys. J.*, *591*, 540–555. [38](#)
- Maspero, G. (1906). *History Of Egypt, Chaldæa, Syria, Babylonia, and Assyria*, vol. 3 of 12 of *History of Egypt, Chaldæa, Syria, Babylonia and Assyria in the light of recent discovery*. The Grolier Society / Gutenberg Project. [6](#)
- Maughan, B. J. (2007). The L_X – Y_X Relation: Using Galaxy Cluster X-Ray Luminosity as a Robust, Low-Scatter Mass Proxy. *Astrophys. J.*, *668*, 772–780. [118](#), [141](#), [152](#), [154](#)
- Maughan, B. J., Jones, L. R., Ebeling, H., & Scharf, C. (2006). The evolution of the cluster X-ray scaling relations in the Wide Angle *ROSAT* Pointed Survey sample at $0.6 < z < 1.0$. *Mon. Not. R. Astron. Soc.*, *365*, 509–529. [117](#)
- Mavromatos, N. E. (2007). LHC Physics and Cosmology. *E-print (arXiv:0708.0134)*. [64](#)
- Mazzotta, P., Rasia, E., Moscardini, L., & Tormen, G. (2004). Comparing the temperatures of galaxy clusters from hydrodynamical N -body simulations to *Chandra* and *XMM-Newton* observations. *Mon. Not. R. Astron. Soc.*, *354*, 10–24. [116](#)

- Melchiorri, A., Bode, P., Bahcall, N. A., & Silk, J. (2003a). Cosmological Constraints from a Combined Analysis of the Cluster Mass Function and Microwave Background Anisotropies. *Astrophys. J.*, 586, L1–L3. 46
- Melchiorri, A., Mersini, L., Ödman, C. J., & Trodden, M. (2003b). The state of the dark energy equation of state. *Phys. Rev. D*, 68(4), 043509–+. 40, 42
- MetropolitanMuseum (2008). Ancient Near Eastern Art – Reliefs from the Northwest Palace. Web site.
URL http://www.metmuseum.org/explore/anesite/html/el_ane_relief4.htm 5
- Mewe, R., Lemen, J. R., & van den Oord, G. H. J. (1986). Calculated X-radiation from optically thin plasmas. VI – Improved calculations for continuum emission and approximation formulae for nonrelativistic average Gaunt factors. *Astron. Astrophys.*, 65, 511. 122
- Miller, A. D., et al. (1999). A Measurement of the Angular Power Spectrum of the Cosmic Microwave Background from $l = 100$ to 400. *Astrophys. J.*, 524, L1–L4. 38
- Miller, A. D., et al. (2002). The QMAP and MAT/TOCO Experiments for Measuring Anisotropy in the Cosmic Microwave Background. *Astrophys. J. Suppl. Ser.*, 140, 115–141. 38
- Miller, C. J., Romer, A. K., Stanford, S. A., Hilton, M., Hosmer, M., & Merhtens, N. (2006). The NOAO–XCS Survey Program. vol. 38 of *Bull. Am. Astron. Soc.*, (pp. 998–+). 120, 149
- Montroy, T. E., et al. (2006). A Measurement of the CMB $\langle EE \rangle$ Spectrum from the 2003 Flight of BOOMERANG. *Astrophys. J.*, 647, 813–822. 38
- Morrison, R., & McCammon, D. (1983). Interstellar photoelectric absorption cross sections, 0.03–10 keV. *Astrophys. J.*, 270, 119. 122
- Mukhanov, V. (2005). *Physical foundations of cosmology*. Cambridge University Press. 11, 38
- Mukherjee, P., Parkinson, D., Corasaniti, P. S., Liddle, A. R., & Kunz, M. (2006a). Model selection as a science driver for dark energy surveys. *Mon. Not. R. Astron. Soc.*, 369, 1725–1734. 49
- Mukherjee, P., Parkinson, D., & Liddle, A. R. (2006b). A Nested Sampling Algorithm for Cosmological Model Selection. *Astrophys. J.*, 638, L51–L54. 50
- Nagai, D., Kravtsov, A. V., & Vikhlinin, A. (2007). Effects of Galaxy Formation on

- Thermodynamics of the Intracluster Medium. *Astrophys. J.*, *668*, 1–14. [116](#)
- Nakamura, T., & Chiba, T. (1999). Determining the equation of state of the expanding Universe: inverse problem in cosmology. *Mon. Not. R. Astron. Soc.*, *306*, 696–700. [77](#)
- NASA/ESA (2008). Hubble Space Telescope Image of Supernova 1994D in Galaxy NGC 4526. Web site.
URL <http://www.spacetelescope.org/images/html/opo9919i.html> [30](#)
- Naselsky, P. D., Novikov, D. I., & Novikov, I. D. (2006). *The Physics of the Cosmic Microwave Background*. Cambridge University Press. [38](#)
- Navarro, J. F., Frenk, C. S., & White, S. D. M. (1995). Simulations of X-ray clusters. *Mon. Not. R. Astron. Soc.*, *275*, 720–740. [116](#)
- Navarro, J. F., Frenk, C. S., & White, S. D. M. (1996). The Structure of Cold Dark Matter Halos. *Astrophys. J.*, *462*, 563–+. [116](#)
- Navarro, J. F., Frenk, C. S., & White, S. D. M. (1997). A Universal Density Profile from Hierarchical Clustering. *Astrophys. J.*, *490*, 493–+. [116](#)
- Nesseris, S., & Perivolaropoulos, L. (2005). Comparison of the legacy and gold type Ia supernovae dataset constraints on dark energy models. *Phys. Rev. D*, *72*(12), 123519–+. [95](#)
- Nesseris, S., & Perivolaropoulos, L. (2007). Crossing the phantom divide: theoretical implications and observational status. *J. Cosmol. Astropart. Phys.*, *1*, 18–+. [95](#)
- Netterfield, C. B., et al. (2002). A Measurement by BOOMERANG of Multiple Peaks in the Angular Power Spectrum of the Cosmic Microwave Background. *Astrophys. J.*, *571*, 604–614. [38](#)
- Nichol, R. C., Collins, C. A., Guzzo, L., & Lumsden, S. L. (1992). The Edinburgh–Durham Southern Galaxy Catalogue. V – The cluster correlation function. *Mon. Not. R. Astron. Soc.*, *255*, 21P–24P. [126](#)
- Nojiri, S., Odintsov, S. D., & Sasaki, M. (2005). Gauss–Bonnet dark energy. *Phys. Rev. D*, *71*(12), 123509–+. [67](#)
- Nord, B., Stanek, R., Rasia, E., & Evrard, A. E. (2008). Effects of selection and covariance on X-ray scaling relations of galaxy clusters. *Mon. Not. R. Astron. Soc.*, *383*, L10–L14. [118](#), [141](#)
- Novicki, M. C., Sornig, M., & Henry, J. P. (2002). The Evolution of the Galaxy Cluster Luminosity–Temperature Relation. *Astron. J.*, *124*, 2413–2424. [117](#)

- Ota, N., Kitayama, T., Masai, K., & Mitsuda, K. (2006). L_X - T Relation and Related Properties of Galaxy Clusters. *Astrophys. J.*, *640*, 673–690. [117](#)
- Oukbir, J., & Blanchard, A. (1992). X-ray clusters in open universes. *Astron. Astrophys.*, *262*, L21–L24. [45](#)
- Oukbir, J., & Blanchard, A. (1997). X-ray clusters: towards a new determination of the density parameter of the universe. *Astron. Astrophys.*, *317*, 1–13. [45](#)
- Pacaud, F., et al. (2007). The *XMM*-LSS survey: the Class 1 cluster sample over the initial 5 deg^2 and its cosmological modelling. *Mon. Not. R. Astron. Soc.*, *382*, 1289–1308. [118](#), [141](#), [149](#), [151](#), [154](#)
- Padmanabhan, N., et al. (2007). The clustering of luminous red galaxies in the Sloan Digital Sky Survey imaging data. *Mon. Not. R. Astron. Soc.*, *378*, 852–872. [125](#)
- Padmanabhan, T. (2003). Cosmological constant – the weight of the vacuum. *Phys. Rep.*, *380*, 235–320. [66](#)
- Padmanabhan, T. (2005a). A New Perspective on Gravity and Dynamics of Space-Time. *Int. J. Mod. Phys. D*, *14*, 2263–2269. [67](#)
- Padmanabhan, T. (2005b). Dark Energy: the Cosmological Challenge of the Millennium. *Current Science*, *88*, 1057–+. [86](#)
- Page, D. N. (1987). Probability of R^2 inflation. *Phys. Rev. D*, *36*, 1607–1624. [69](#)
- Page, D. N. (2008). Cosmological Measures without Volume Weighting. *Preprint (arXiv:0808.0351)*. [69](#)
- Pahud, C., Liddle, A. R., Mukherjee, P., & Parkinson, D. (2006). Model selection forecasts for the spectral index from the *Planck* satellite. *Phys. Rev. D*, *73*(12), 123524–+. [64](#)
- Pahud, C., Liddle, A. R., Mukherjee, P., & Parkinson, D. (2007). When can the *Planck* satellite measure spectral index running? *Mon. Not. R. Astron. Soc.*, *381*, 489–493. [64](#)
- Parkinson, D., Mukherjee, P., & Liddle, A. R. (2006). Bayesian model selection analysis of WMAP3. *Phys. Rev. D*, *73*(12), 123523–+. [61](#)
- Peacock, J. A. (1999). *Cosmological Physics*. Cambridge University Press. [16](#)
- Peacock, J. A., & Dodds, S. J. (1994). Reconstructing the Linear Power Spectrum of Cosmological Mass Fluctuations. *Mon. Not. R. Astron. Soc.*, *267*, 1020–+. [19](#)
- Pearson, T. J., et al. (2003). The Anisotropy of the Microwave Background to $l = 3500$: Mosaic Observations with the Cosmic Background Imager. *Astrophys. J.*, *591*, 556–574.

- Peebles, P. J., & Ratra, B. (2003). The cosmological constant and dark energy. *Rev. Mod. Phys.*, *75*, 559–606. [66](#)
- Peebles, P. J. E. (1993). *Principles of physical cosmology*. Princeton University Press. [11](#)
- Peebles, P. J. E., & Yu, J. T. (1970). Primeval Adiabatic Perturbation in an Expanding Universe. *Astrophys. J.*, *162*, 815–+. [35](#)
- Penzias, A. A., & Wilson, R. W. (1965). A Measurement of Excess Antenna Temperature at 4080 Mc/s. *Astrophys. J.*, *142*, 419–421. [38](#)
- Percival, W. J., Cole, S., Eisenstein, D. J., Nichol, R. C., Peacock, J. A., Pope, A. C., & Szalay, A. S. (2007). Measuring the Baryon Acoustic Oscillation scale using the Sloan Digital Sky Survey and 2dF Galaxy Redshift Survey. *Mon. Not. R. Astron. Soc.*, *381*, 1053–1066. [35](#), [36](#), [57](#), [58](#), [61](#), [77](#), [83](#), [84](#)
- Percival, W. J., et al. (2007). The shape of the SDSS DR5 galaxy power spectrum. *Astrophys. J.*, *657*, 645–663. [57](#)
- Perlmutter, S., & Schmidt, B. P. (2003). Measuring Cosmology with Supernovae. In K. Weiler (Ed.) *Supernovae and Gamma-Ray Bursters*, vol. 598 of *Lecture Notes in Physics*, (pp. 195–217). Springer Verlag. [31](#)
- Perlmutter, S., et al. (1998). Discovery of a supernova explosion at half the age of the universe. *Nature (London)*, *391*, 51–+. [31](#)
- Perlmutter, S., et al. (1999). Measurements of Omega and Lambda from 42 High-Redshift Supernovae. *Astrophys. J.*, *517*, 565–586. [31](#)
- Peskin, M. E., & Schroeder, D. V. (1995). *An Introduction to Quantum Field Theory*. Frontiers in Physics Series. Westview Press. [72](#)
- Phillips, M. M. (1993). The absolute magnitudes of Type IA supernovae. *Astrophys. J.*, *413*, L105–L108. [30](#)
- Piacentini, F., et al. (2006). A Measurement of the Polarization–Temperature Angular Cross-Power Spectrum of the Cosmic Microwave Background from the 2003 Flight of BOOMERANG. *Astrophys. J.*, *647*, 833–839. [38](#)
- Pierpaoli, E., Scott, D., & White, M. (2001). Power-spectrum normalization from the local abundance of rich clusters of galaxies. *Mon. Not. R. Astron. Soc.*, *325*, 77–88. [115](#)
- Pierre, M., Pacaud, F., & Melin, J. B. (2008). The XMM–LSS cluster sample and its cosmological applications: Prospects for the XMM next decade. *Astron. Nachr.*, *329*,

143–+. [107](#), [141](#), [154](#), [155](#)

Plato (2000). *Plato: Timaeus*. Hackett Publishing Co. [72](#)

Pogosian, L., Corasaniti, P. S., Stephan–Otto, C., Crittenden, R., & Nichol, R. (2005). Tracking dark energy with the integrated Sachs–Wolfe effect: Short and long-term predictions. *Phys. Rev. D*, *72*(10), 103519–+. [44](#)

Pope, A. C., et al. (2004). Cosmological Parameters from Eigenmode Analysis of Sloan Digital Sky Survey Galaxy Redshifts. *Astrophys. J.*, *607*, 655–660. [125](#)

Predehl, P., et al. (2006). *eROSITA*. In M. J. L. Turner, & G. Hasinger (Eds.) *Space Telescopes and Instrumentation II: Ultraviolet to Gamma Ray.*, vol. 6266 of *Proceedings of the SPIE*. [107](#)

Prinz, J. J. (2004). *Gut Reactions: A Perceptual Theory of Emotion*. Philosophy of Mind Series. Oxford University Press. [2](#)

Pskovskii, Y. P. (1962). The Frequency of Supernovae in Different Subtypes of Galaxies. *Sov. Astron.*, *5*, 498–+. [30](#)

Pskovskii, Y. P. (1967). The Photometric Properties of Supernovae. *Sov. Astron.*, *11*, 63–+. [30](#)

Randall, S. W., Sarazin, C. L., & Ricker, P. M. (2002). The Effect of Merger Boosts on the Luminosity, Temperature, and Inferred Mass Functions of Clusters of Galaxies. *Astrophys. J.*, *577*, 579–594. [119](#)

Rapetti, D., Allen, S. W., & Mantz, A. (2008). The prospects for constraining dark energy with future X-ray cluster gas mass fraction measurements. *Mon. Not. R. Astron. Soc.*, (pp. 740–+). [46](#), [109](#)

Rapetti, D., Allen, S. W., & Weller, J. (2005). Constraining dark energy with X-ray galaxy clusters, supernovae and the cosmic microwave background. *Mon. Not. R. Astron. Soc.*, *360*, 555–564. [46](#)

Rasia, E., Mazzotta, P., Borgani, S., Moscardini, L., Dolag, K., Tormen, G., Diaferio, A., & Murante, G. (2005). Mismatch between X-Ray and Emission-weighted Temperatures in Galaxy Clusters: Cosmological Implications. *Astrophys. J.*, *618*, L1–L4. [116](#)

Rasia, E., Tormen, G., & Moscardini, L. (2004). A dynamical model for the distribution of dark matter and gas in galaxy clusters. *Mon. Not. R. Astron. Soc.*, *351*, 237–252. [116](#)

Ratra, B., & Peebles, P. J. E. (1988). Cosmological Consequences of a Rolling Homoge-

- neous Scalar Field. *Phys. Rev. D*, *37*, 3406. [72](#), [74](#)
- Readhead, A. C. S., et al. (2004). Extended Mosaic Observations with the Cosmic Background Imager. *Astrophys. J.*, *609*, 498–512. [38](#)
- Reed, D., Gardner, J., Quinn, T., Stadel, J., Fardal, M., Lake, G., & Governato, F. (2003). Evolution of the mass function of dark matter haloes. *Mon. Not. R. Astron. Soc.*, *346*, 565–572. [45](#)
- Reed, D. S., Bower, R., Frenk, C. S., Jenkins, A., & Theuns, T. (2007). The halo mass function from the dark ages through the present day. *Mon. Not. R. Astron. Soc.*, *374*, 2–15. [45](#)
- Refregier, A., Valtchanov, I., & Pierre, M. (2002). Cosmology with galaxy clusters in the *XMM* large-scale structure survey. *Astron. Astrophys.*, *390*, 1–12. [45](#), [108](#), [136](#), [150](#)
- Reichardt, C. L., et al. (2008). High resolution CMB power spectrum from the complete ACBAR data set. *Preprint (arXiv:0801.1491)*. [38](#)
- Reichart, D. E., Nichol, R. C., Castander, F. J., Burke, D. J., Romer, A. K., Holden, B. P., Collins, C. A., & Ulmer, M. P. (1999). A Deficit of High-Redshift, High-Luminosity X-Ray Clusters: Evidence for a High Value of Ω_m ? *Astrophys. J.*, *518*, 521–532. [45](#)
- Reiprich, T. H., & Böhringer, H. (2002). The Mass Function of an X-Ray Flux-limited Sample of Galaxy Clusters. *Astrophys. J.*, *567*, 716–740. [115](#), [118](#)
- Riess, A. G., et al. (1998). Observational Evidence from Supernovae for an Accelerating Universe and a Cosmological Constant. *Astron. J.*, *116*, 1009–1038. [31](#)
- Riess, A. G., et al. (2004). Type Ia Supernova Discoveries at $z > 1$ from the Hubble Space Telescope: Evidence for Past Deceleration and Constraints on Dark Energy Evolution. *Astrophys. J.*, *607*, 665–687. [31](#), [59](#), [77](#), [82](#), [91](#), [93](#), [95](#), [100](#), [105](#), [106](#)
- Riess, A. G., et al. (2007). New Hubble Space Telescope Discoveries of Type Ia Supernovae at $z \geq 1$: Narrowing Constraints on the Early Behavior of Dark Energy. *Astrophys. J.*, *659*, 98–121. [31](#)
- Robertson, H. P. (1935). Kinematics and World-Structure. *Astrophys. J.*, *82*, 284–+. [12](#)
- Robertson, H. P. (1936a). Kinematics and World-Structure II. *Astrophys. J.*, *83*, 187–+. [12](#)
- Robertson, H. P. (1936b). Kinematics and World-Structure III. *Astrophys. J.*, *83*, 257–+. [12](#)
- Romer, A. K., Collins, C. A., Böhringer, H., Cruddace, R. G., Ebeling, H., MacGillivray,

- H. G., & Voges, W. (1994). The large-scale distribution of X-ray clusters of galaxies. *Nature (London)*, 372, 75–+. 126
- Romer, A. K., Viana, P. T. P., Liddle, A. R., & Mann, R. G. (2001). A Serendipitous Galaxy Cluster Survey with *XMM*: Expected Catalog Properties and Scientific Applications. *Astrophys. J.*, 547, 594–608. 47, 108, 109
- Rozo, E., Wechsler, R. H., Koester, B. P., Evrard, A. E., & McKay, T. A. (2007b). Optically-Selected Cluster Catalogs as a Precision Cosmology Tool. *Preprint (arXiv:astro-ph/0703574)*. 107
- Rozo, E., et al. (2007a). Cosmological Constraints from SDSS maxBCG Cluster Abundances. *Preprint (arXiv:astro-ph/0703571)*. 46, 57, 59
- Rubano, C., & Barrow, J. D. (2001). Scaling solutions and reconstruction of scalar field potentials. *Phys. Rev. D*, 64(12), 127301–+. 74
- Ruhl, J. E., et al. (2003). Improved Measurement of the Angular Power Spectrum of Temperature Anisotropy in the Cosmic Microwave Background from Two New Analyses of BOOMERANG Observations. *Astrophys. J.*, 599, 786–805. 38
- Ryckman, T. (Fall 2008). Early philosophical interpretations of general relativity. In E. N. Zalta (Ed.) *The Stanford Encyclopedia of Philosophy*.
URL <http://plato.stanford.edu/archives/fall2008/entries/genrel-early/> 70
- Sachs, R. K., & Wolfe, A. M. (1967). Perturbations of a Cosmological Model and Angular Variations of the Microwave Background. *Astrophys. J.*, 147, 73–+. 38
- Sahlén, M., Liddle, A. R., & Parkinson, D. (2005). Direct reconstruction of the quintessence potential. *Phys. Rev. D*, 72(8), 083511–+. 77, 78, 79, 81, 82, 88, 91, 94, 95, 105, 106
- Sahlén, M., Liddle, A. R., & Parkinson, D. (2007). Quintessence reconstructed: New constraints and tracker viability. *Phys. Rev. D*, 75(2), 023502–+. 78
- Sahni, V. (2002). The cosmological constant problem and quintessence. *Class. Quantum Grav.*, 19, 3435–3448. 66
- Sahni, V. (2005). Cosmological Surprises from Braneworld models of Dark Energy. *Preprint (arXiv:astro-ph/0502032)*. 67
- Sahni, V., & Starobinsky, A. (2000). The Case for a Positive Cosmological Λ -Term. *Int. J. Mod. Phys. D*, 9, 373–443. 66
- Sahni, V., & Starobinsky, A. (2006). Reconstructing Dark Energy. *Int. J. Mod. Phys. D*,

- 15, 2105–2132. [66](#)
- Saini, T. D. (2003). A Regularized Free Form Estimator for Dark Energy. *Mon. Not. R. Astron. Soc.*, *344*, 129. [28](#)
- Saini, T. D., Padmanabhan, T., & Bridle, S. (2003). Response of distance measures to the equation of state. *Mon. Not. R. Astron. Soc.*, *343*, 533–538. [28](#)
- Saini, T. D., Raychaudhury, S., Sahni, V., & Starobinsky, A. A. (2000). Reconstructing the Cosmic Equation of State from Supernova Distances. *Phys. Rev. Lett.*, *85*, 1162–1165. [77](#)
- Saini, T. D., Weller, J., & Bridle, S. L. (2004). Revealing the nature of dark energy using Bayesian evidence. *Mon. Not. R. Astron. Soc.*, *348*, 603–608. [106](#)
- Sarkar, S. (2008). Is the evidence for dark energy secure? *Gen. Relativ. Gravit.*, *40*, 269–284. [61](#)
- Schäfer, B. M., & Koyama, K. (2008). Spherical collapse in modified gravity with the Birkhoff theorem. *Mon. Not. R. Astron. Soc.*, (pp. 130–+). [46](#)
- Schmidt, B. P., et al. (1998). The High- Z Supernova Search: Measuring Cosmic Deceleration and Global Curvature of the Universe Using Type IA Supernovae. *Astrophys. J.*, *507*, 46–63. [31](#)
- Schrödinger, E. (1944). *What is Life?*. Cambridge University Press. [3](#)
- Scott, P. F., et al. (2003). First results from the Very Small Array – III. The cosmic microwave background power spectrum. *Mon. Not. R. Astron. Soc.*, *341*, 1076–1083. [38](#)
- Seljak, U., & Zaldarriaga, M. (1996). A Line-of-Sight Integration Approach to Cosmic Microwave Background Anisotropies. *Astrophys. J.*, *469*, 437–+. [19](#)
- Shaw, L. D., Weller, J., Ostriker, J. P., & Bode, P. (2006). Statistics of Physical Properties of Dark Matter Clusters. *Astrophys. J.*, *646*, 815–833. [152](#)
- Sievers, J. L., et al. (2003). Cosmological Parameters from Cosmic Background Imager Observations and Comparisons with BOOMERANG, DASI, and MAXIMA. *Astrophys. J.*, *591*, 599–622. [38](#)
- Sievers, J. L., et al. (2007). Implications of the Cosmic Background Imager Polarization Data. *Astrophys. J.*, *660*, 976–987. [38](#)
- Silk, J. (1967). Fluctuations in the Primordial Fireball. *Nature (London)*, *215*, 1155–+. [38](#)

- Silk, J. (1968). Cosmic Black-Body Radiation and Galaxy Formation. *Astrophys. J.*, 151, 459–+. [38](#)
- Simon, J., Verde, L., & Jimenez, R. (2005). Constraints on the redshift dependence of the dark energy potential. *Phys. Rev. D*, 71(12), 123001–+. [77](#)
- Simpson, F., & Bridle, S. (2005). Illuminating dark energy with cosmic shear. *Phys. Rev. D*, 71(8), 083501–+. [28](#)
- Simpson, F., & Bridle, S. (2006). Redshift sensitivities of dark energy surveys. *Phys. Rev. D*, 73(8), 083001–+. [28](#)
- Singh, S. (2004). *Big Bang*. Fourth Estate. [11](#)
- Skordis, C., & Albrecht, A. (2002). Planck-scale quintessence and the physics of structure formation. *Phys. Rev. D*, 66(4), 043523–+. [103](#)
- Smoot, G. F., et al. (1992). Structure in the *COBE* differential microwave radiometer first-year maps. *Astrophys. J.*, 396, L1–L5. [38](#)
- Spiegel, D. N., et al. (2003). First-Year *Wilkinson Microwave Anisotropy Probe (WMAP)* Observations: Determination of Cosmological Parameters. *Astrophys. J. Suppl. Ser.*, 148, 175–194. [38](#)
- Spiegel, D. N., et al. (2007). Three-Year *Wilkinson Microwave Anisotropy Probe (WMAP)* Observations: Implications for Cosmology. *Astrophys. J. Suppl. Ser.*, 170, 377–408. [38](#), [77](#), [82](#), [83](#)
- Stanek, R., Evrard, A. E., Böhringer, H., Schuecker, P., & Nord, B. (2006). The X-Ray Luminosity–Mass Relation for Local Clusters of Galaxies. *Astrophys. J.*, 648, 956–968. [119](#)
- Stanford, S. A., et al. (2006). The *XMM* Cluster Survey: A Massive Galaxy Cluster at $z = 1.45$. *Astrophys. J.*, 646, L13–L16. [111](#), [149](#)
- Starobinsky, A. A. (1998). How to determine an effective potential for a variable cosmological term. *JETP Lett.*, 68, 757–763. [77](#)
- Steinhardt, P. J., Wang, L., & Zlatev, I. (1999). Cosmological tracking solutions. *Phys. Rev. D*, 59(12), 123504–+. [74](#), [75](#), [76](#), [77](#), [105](#)
- Stephan–Otto, C. (2006). Optimized supernova constraints on dark energy evolution. *Phys. Rev. D*, 74(2), 023507–+. [28](#)
- Stewart, J. (1993). *Advanced General Relativity*. Cambridge University Press. [12](#)

- Sugiyama, N. (1995). Cosmic Background Anisotropies in Cold Dark Matter Cosmology. *Astrophys. J. Suppl. Ser.*, 100, 281–+. [19](#)
- Sunyaev, R. A., & Zeldovich, Y. B. (1970). Small-Scale Fluctuations of Relic Radiation. *Astrophys. Space Sci.*, 7, 3–19. [35](#)
- Szalay, A. S., et al. (2003). Karhunen–Loève Estimation of the Power Spectrum Parameters from the Angular Distribution of Galaxies in Early Sloan Digital Sky Survey Data. *Astrophys. J.*, 591, 1–11. [125](#)
- Szydlowski, M., & Godłowski, W. (2006). Which cosmological model – with dark energy or modified FRW dynamics? *Phys. Lett. B*, 633, 427–432. [86](#)
- Szydlowski, M., Kurek, A., & Krawiec, A. (2006). Top ten accelerating cosmological models. *Phys. Lett. B*, 642, 171–178. [86](#)
- Tang, J.-Y., Weller, J., & Zablacki, A. (2006). Probing modified gravity by combining supernovae and galaxy cluster surveys. *Preprint (arXiv:astro-ph/0609028)*. [46](#)
- Tegmark, M. (2007). *Universe or Multiverse?*, chap. 7, (pp. 99–126). Cambridge University Press. [69](#)
- Tegmark, M. (2008). The Mathematical Universe. *Found. Phys.*, 38, 101–150. [69](#)
- Tegmark, M., Aguirre, A., Rees, M. J., & Wilczek, F. (2006a). Dimensionless constants, cosmology, and other dark matters. *Phys. Rev. D*, 73(2), 023505–+. [70](#)
- Tegmark, M., Eisenstein, D. J., Hu, W., & Kron, R. (1998). Cosmic complementarity: probing the acceleration of the Universe. *Preprint (arXiv:astro-ph/9805117)*. [28](#), [29](#)
- Tegmark, M., et al. (2004). Cosmological parameters from SDSS and WMAP. *Phys. Rev. D*, 69(10), 103501–+. [52](#)
- Tegmark, M., et al. (2004). The 3D power spectrum of galaxies from the SDSS. *Astrophys. J.*, 606, 702–740. [27](#), [57](#)
- Tegmark, M., et al. (2004). The Three-Dimensional Power Spectrum of Galaxies from the Sloan Digital Sky Survey. *Astrophys. J.*, 606, 702–740. [125](#)
- Tegmark, M., et al. (2006b). Cosmological constraints from the SDSS luminous red galaxies. *Phys. Rev. D*, 74(12), 123507–+. [35](#)
- Tipler, F. J. (1994). *The physics of immortality : modern cosmology, God, and the resurrection of the dead*. Doubleday. [3](#)
- Tipler, F. J. (2007). *The Physics of Christianity*. Doubleday. [3](#)

- Tonry, J. L., et al. (2003). Cosmological Results from High- z Supernovae. *Astrophys. J.*, *594*, 1–24. [31](#)
- Trotta, R. (2007). Applications of Bayesian model selection to cosmological parameters. *Mon. Not. R. Astron. Soc.*, *378*, 72–82. [49](#), [61](#)
- Trotta, R. (2008). Bayes in the sky: Bayesian inference and model selection in cosmology. *Preprint (arXiv:0803.4089)*. [48](#)
- Tsujikawa, S. (2005). Reconstruction of general scalar-field dark energy models. *Phys. Rev. D*, *72*(8), 083512–+. [77](#)
- Tsujikawa, S. (2006). General analytic formulas for attractor solutions of scalar-field dark energy models and their multifield generalizations. *Phys. Rev. D*, *73*(10), 103504–+. [74](#)
- Upadhye, A., Ishak, M., & Steinhardt, P. J. (2005). Dynamical dark energy: Current constraints and forecasts. *Phys. Rev. D*, *72*(6), 063501–+. [29](#)
- Ureña-López, L. A., & Matos, T. (2000). New cosmological tracker solution for quintessence. *Phys. Rev. D*, *62*(8), 081302–+. [74](#)
- Vaidman, L. (Fall 2008). Many-worlds interpretation of quantum mechanics. In E. N. Zalta (Ed.) *The Stanford Encyclopedia of Philosophy*.
URL <http://plato.stanford.edu/archives/fall2008/entries/qm-manyworlds/>
[70](#)
- Verde, L., Haiman, Z., & Spergel, D. N. (2002). Are Clusters Standard Candles? Galaxy Cluster Scaling Relations with the Sunyaev–Zel’dovich Effect. *Astrophys. J.*, *581*, 5–19. [141](#), [146](#), [150](#)
- Verde, L., et al. (2003). First-Year *Wilkinson Microwave Anisotropy Probe* (WMAP) Observations: Parameter Estimation Methodology. *Astrophys. J. Suppl. Ser.*, *148*, 195–211. [51](#)
- Viana, P. T. P. (2006). Private communication. [26](#)
- Viana, P. T. P., Kay, S. T., Liddle, A. R., Muanwong, O., & Thomas, P. A. (2003). The power spectrum amplitude from clusters revisited: σ_8 using simulations with pre-heating and cooling. *Mon. Not. R. Astron. Soc.*, *346*, 319–326. [115](#), [116](#), [118](#), [119](#)
- Viana, P. T. P., & Liddle, A. R. (1996). The cluster abundance in flat and open cosmologies. *Mon. Not. R. Astron. Soc.*, *281*, 323–+. [45](#)
- Viana, P. T. P., & Liddle, A. R. (1999). Galaxy clusters at $0.3 < z < 0.4$ and the value of Ω_0 . *Mon. Not. R. Astron. Soc.*, *303*, 535–545. [26](#), [45](#), [136](#)

- Vikhlinin, A. (2006). Predicting a Single-Temperature Fit to Multicomponent Thermal Plasma Spectra. *Astrophys. J.*, *640*, 710–715. [116](#), [148](#)
- Vikhlinin, A., Kravtsov, A., Forman, W., Jones, C., Markevitch, M., Murray, S. S., & Van Speybroeck, L. (2006). *Chandra* Sample of Nearby Relaxed Galaxy Clusters: Mass, Gas Fraction, and Mass–Temperature Relation. *Astrophys. J.*, *640*, 691–709. [115](#), [116](#)
- Vikhlinin, A., Van Speybroeck, L., Markevitch, M., Forman, W. R., & Grego, L. (2002). Evolution of the Cluster X-Ray Scaling Relations since $z > 0.4$. *Astrophys. J.*, *578*, L107–L111. [117](#)
- Vilenkin, A. (1998). Unambiguous Probabilities in an Eternally Inflating Universe. *Phys. Rev. Lett.*, *81*, 5501–5504. [69](#)
- Voit, G. M. (2005a). Expectations for evolution of cluster scaling relations. *Advances in Space Research*, *36*, 701–705. [115](#)
- Voit, G. M. (2005b). Tracing cosmic evolution with clusters of galaxies. *Rev. Mod. Phys.*, *77*, 207–258. [116](#)
- Walker, A. G. (1937). On Milne’s Theory of World-Structure. *Proc. Lond. Math. Soc.*, *s2-42*(1), 90–127. [12](#)
- Wang, L., & Steinhardt, P. J. (1998). Cluster Abundance Constraints for Cosmological Models with a Time-varying, Spatially Inhomogeneous Energy Component with Negative Pressure. *Astrophys. J.*, *508*, 483–490. [46](#)
- Wang, S., Haiman, Z., Hu, W., Khoury, J., & May, M. (2005). Weighing Neutrinos with Galaxy Cluster Surveys. *Phys. Rev. Lett.*, *95*(1), 011302–+. [46](#)
- Wang, S., Khoury, J., Haiman, Z., & May, M. (2004a). Constraining the evolution of dark energy with a combination of galaxy cluster observables. *Phys. Rev. D*, *70*(12), 123008–+. [46](#), [108](#), [126](#), [142](#), [146](#), [152](#)
- Wang, W., & Feng, B. (2003). Early Tracking Behavior in Small-field Quintessence Models. *Chinese Journal of Astronomy and Astrophysics*, *3*, 105–112. [74](#)
- Wang, Y., Kratochvil, J. M., Linde, A., & Shmakova, M. (2004b). Current observational constraints on cosmic doomsday. *J. Cosmol. Astropart. Phys.*, *12*, 6–+. [81](#)
- Wang, Y., & Mukherjee, P. (2006). Robust Dark Energy Constraints from Supernovae, Galaxy Clustering, and 3 yr *Wilkinson Microwave Anisotropy Probe* Observations. *Astrophys. J.*, *650*, 1–6. [82](#)
- Wang, Y., & Mukherjee, P. (2007). Observational Constraints on Dark Energy and Cosmic

- Curvature. *Phys. Rev. D*, 76, 103533. [43](#)
- Warren, M. S., Abazajian, K., Holz, D. E., & Teodoro, L. (2006). Precision Determination of the Mass Function of Dark Matter Halos. *Astrophys. J.*, 646, 881–885. [45](#), [152](#)
- Weller, J., Battye, R. A., & Kneissl, R. (2002). Constraining Dark Energy with Sunyaev–Zel’dovich Cluster Surveys. *Phys. Rev. Lett.*, 88(23), 231301–+. [46](#)
- Weller, J., & Lewis, A. M. (2003). Large-scale cosmic microwave background anisotropies and dark energy. *Mon. Not. R. Astron. Soc.*, 346, 987–993. [43](#)
- Wetterich, C. (1988). Cosmology and the Fate of Dilatation Symmetry. *Nucl. Phys. B*, 302, 668. [72](#), [74](#)
- Wetterich, C. (2003a). Crossover quintessence and cosmological history of fundamental “constants”. *Phys. Lett. B*, 561, 10–16. [43](#), [103](#)
- Wetterich, C. (2003b). Probing quintessence with time variation of couplings. *J. Cosmol. Astropart. Phys.*, 10, 2–+. [43](#), [103](#)
- Wetterich, C. (2004). Phenomenological parameterization of quintessence. *Phys. Lett. B*, 594, 17–22. [77](#)
- Weyl, H. (1923). Zur allgemeinen Relativitätstheorie. *Phys. Z.*, 24, 230–232. [11](#)
- White, M. (2002). The Mass Function. *Astrophys. J. Suppl. Ser.*, 143, 241–255. [126](#)
- Wilkinson, R. H. (1963). A method of generating functions of several variables using analog diode logic. *IEEE Transactions on Electronic Computers*, EC12, 112–129. [71](#)
- Wilson, O. C. (1939). Possible Applications of Supernovae to the Study of the Nebular Red Shifts. *Astrophys. J.*, 90, 634–+. [30](#)
- Wittman, D., Dell’Antonio, I. P., Hughes, J. P., Margoniner, V. E., Tyson, J. A., Cohen, J. G., & Norman, D. (2006). First Results on Shear-selected Clusters from the Deep Lens Survey: Optical Imaging, Spectroscopy, and X-Ray Follow-up. *Astrophys. J.*, 643, 128–143. [107](#)
- Wood–Vasey, W. M., et al. (2007). Observational Constraints on the Nature of Dark Energy: First Cosmological Results from the ESSENCE Supernova Survey. *Astrophys. J.*, 666, 694–715. [31](#), [59](#)
- Wright, E. L. (2007). Constraints on Dark Energy from Supernovae, Gamma-Ray Bursts, Acoustic Oscillations, Nucleosynthesis, Large-Scale Structure, and the Hubble Constant. *Astrophys. J.*, 664, 633–639. [84](#)

- Xia, J.-Q., Zhao, G.-B., Feng, B., Li, H., & Zhang, X. (2006). Observing dark energy dynamics with supernova, microwave background, and galaxy clustering. *Phys. Rev. D*, *73*(6), 063521–+. [95](#)
- Yadav, A. P. S., & Wandelt, B. D. (2008). Evidence of Primordial Non-Gaussianity (f_{NL}) in the *Wilkinson Microwave Anisotropy Probe* 3-Year Data at 2.8σ . *Phys. Rev. Lett.*, *100*(18), 181301–+. [27](#)
- Younger, J. D., Haiman, Z., Bryan, G. L., & Wang, S. (2006). Breaking Cosmological Degeneracies in Galaxy Cluster Surveys with a Physical Model of Cluster Structure. *Astrophys. J.*, *653*, 27–42. [152](#)
- Zadeh, L. A., et al. (1996). *Fuzzy Sets, Fuzzy Logic, Fuzzy Systems*. World Scientific Press. [71](#)
- Zaldarriaga, M., Spergel, D. N., & Seljak, U. (1997). Microwave Background Constraints on Cosmological Parameters. *Astrophys. J.*, *488*, 1–+. [40](#)
- Zhang, X. (2006). Dynamical vacuum energy, holographic quintom, and the reconstruction of scalar-field dark energy. *Phys. Rev. D*, *74*(10), 103505–+. [77](#)
- Zhang, Y.-Y., Böhringer, H., Finoguenov, A., Ikebe, Y., Matsushita, K., Schuecker, P., Guzzo, L., & Collins, C. A. (2006). X-ray properties in massive galaxy clusters: *XMM-Newton* observations of the REFLEX-DXL sample. *Astron. Astrophys.*, *456*, 55–74. [47](#), [107](#), [115](#), [116](#), [117](#), [119](#)
- Zlatev, I., & Steinhardt, P. J. (1999). A tracker solution to the cold dark matter cosmic coincidence problem. *Phys. Lett. B*, *459*, 570–574. [74](#)
- Zlatev, I., Wang, L., & Steinhardt, P. J. (1999). Quintessence, Cosmic Coincidence, and the Cosmological Constant. *Phys. Rev. Lett.*, *82*, 896–899. [74](#)

Appendix A

Reconstruction of Quintessence

A.1 Uncertainty in Tracker Bayes Factor Estimates

For simplicity of notation we define $E \equiv \ln B_{12}$ in this Section, with B_{12} defined by Eq. (5.67) on p. 88. The uncertainty in our estimate of E will consist of two components: Poisson noise from sampling the distribution, and model uncertainty. The Poisson noise goes as

$$\sigma_{f_{\text{pri}}}^2 = f_{\text{pri}}/N_{\text{pri}}, \quad (\text{A.1})$$

$$\sigma_{f_{\text{post}}}^2 = f_{\text{post}}/N_{\text{post}}, \quad (\text{A.2})$$

where N_{pri} and N_{post} are the total numbers of samples drawn from the prior and posterior distribution respectively. The quantities f_{pri} and f_{post} are defined on p. 88. Accordingly, using standard error propagation with Eq. (5.67), we have that

$$\sigma_{B_{12}}^2 = D^2\sigma_C^2 + C^2\sigma_D^2 + 2B_{12}\text{cov}(C, D), \quad (\text{A.3})$$

with $C = f_{\text{post}}/(1 - f_{\text{post}})$ and $D = (1 - f_{\text{pri}})/f_{\text{pri}}$ so that $B_{12} = CD$. Additionally, we have

$$\sigma_C^2 = \frac{\sigma_{f_{\text{post}}}^2}{(1 - f_{\text{post}})^4}, \quad (\text{A.4})$$

$$\sigma_D^2 = \frac{\sigma_{f_{\text{pri}}}^2}{f_{\text{pri}}^4}. \quad (\text{A.5})$$

In the absence of knowledge about the covariance between C and D , we can place an upper limit on the Poisson uncertainty,

$$\sigma_{B_{12}}^2 \leq (D\sigma_C + C\sigma_D)^2. \quad (\text{A.6})$$

We use this upper limit as our estimate for the Poisson uncertainty. The corresponding uncertainty in E is then

$$\begin{aligned}\sigma_E &= \frac{\sigma_C}{C} + \frac{\sigma_D}{D} \\ &= \frac{\sigma_{f_{\text{post}}}}{f_{\text{post}}(1 - f_{\text{post}})} + \frac{\sigma_{f_{\text{pri}}}}{f_{\text{pri}}(1 - f_{\text{pri}})}.\end{aligned}\quad (\text{A.7})$$

The model average of E over M models is given by (note that this quantity is denoted $\langle \ln B_{12} \rangle$ in the main text)

$$\bar{E} = \frac{\sum_i E_i}{M} \quad (\text{A.8})$$

with an associated uncertainty

$$\sigma_{\bar{E}} = \sqrt{\frac{\sum_i (\bar{E} - E_i)^2}{M(M-1)}}. \quad (\text{A.9})$$

We will now have an ‘error on the error’ from the Poisson uncertainty, given by

$$\sigma_{\sigma_{\bar{E}}} = \sqrt{\frac{\sum_i (\bar{E} - E_i)^2 \sigma_{E_i}^2}{M(M-1) \sum_i (\bar{E} - E_i)^2}}, \quad (\text{A.10})$$

so our final estimate of E will be

$$\begin{aligned}E &= \bar{E} \\ &\pm \left[\sqrt{\frac{\sum_i (\bar{E} - E_i)^2}{M(M-1)}} + \sqrt{\frac{\sum_i (\bar{E} - E_i)^2 \sigma_{E_i}^2}{M(M-1) \sum_i (\bar{E} - E_i)^2}} \right].\end{aligned}\quad (\text{A.11})$$

A.2 Tracker Probability Distributions

Here we briefly describe a possible extension of the tracker analysis carried out in this work, though we believe application to present data would be premature.

To address the model uncertainty in the Bayes factor model average, we consider the probability distributions of the parameters that determine whether a model is classed as a tracker. In more detail, we can define three different ‘tracker functions’

$$C_1[\mathbf{z}_{\text{tr}}] = \min_{z \in \mathbf{z}_{\text{tr}}} (\Gamma(z) - 5/6), \quad (\text{A.12})$$

$$C_2[\mathbf{z}_{\text{tr}}] = \max_{z \in \mathbf{z}_{\text{tr}}} \left| \Gamma(z)^{-1} \frac{d\Gamma(z)}{d \ln a} \right|, \quad (\text{A.13})$$

$$C_3[\mathbf{z}_{\text{tr}}] = \max_{z \in \mathbf{z}_{\text{tr}}} |w_\phi(z) - w_{\text{tracker}}(z)|, \quad (\text{A.14})$$

where \mathbf{z}_{tr} is the redshift range for which the field is required to exhibit tracker behaviour, and record their values for all elements in our MCMC chains. The quantities defining these functions are introduced in detail in Sects. 5.1.2 & 5.4.3. Note that we do not include a function corresponding to the constraint $w_\phi < 0$, as $\max w_\phi(z)$ will be

a function of C_1 and C_3 . From this we obtain the posterior probability distribution $P(C_1, C_2, C_3 | \Pi(\Theta))$ given the prior distribution $\Pi(\Theta)$ for our *primary* cosmological parameters Θ . Running the MCMC for the prior distribution as well, we obtain the prior distribution $\Pi(C_1, C_2, C_3 | \Pi(\Theta))$.

We are then in a position to do *importance sampling* (see e.g. Appendix B in [Lewis & Bridle, 2002](#) for a brief introduction) using the prior and posterior we have calculated. We can change priors for C_1, C_2, C_3 from those induced by $\Pi(\Theta)$ to whichever we like and obtain the corresponding new posterior distribution, since we only need to divide out the prior distribution and multiply by the prior of our choice (with the exception of for parts of parameter space cut out by the primary prior $\Pi(\Theta)$ or very poorly sampled). A potential problem with this approach is that optimal sampling of the posterior distribution in C_1, C_2, C_3 is not necessarily achieved by optimal sampling in the primary parameters, and sufficient statistics may take a long time, i.e. many chain elements, to accumulate.

Setting natural priors for these new parameters may be perceived as difficult (although not manifestly more arbitrary than for other phenomenological parameterizations). A simple way of setting the priors is to argue that we should be equally likely to draw a parameter value that fulfils the corresponding tracker criterion, as one that doesn't. For instance, if we assume Gaussian priors, we get

$$P(C_1) = \frac{1}{\sqrt{2\pi}\sigma_{C_1}} \exp\left[-\frac{C_1^2}{2\sigma_{C_1}^2}\right], \quad (\text{A.15})$$

$$P(C_2) = \frac{2}{\sqrt{2\pi}\sigma_{C_2}} \exp\left[-\frac{C_2^2}{2\sigma_{C_2}^2}\right] \theta(C_2), \quad (\text{A.16})$$

$$P(C_3) = \frac{2}{\sqrt{2\pi}\sigma_{C_3}} \exp\left[-\frac{C_3^2}{2\sigma_{C_3}^2}\right] \theta(C_3), \quad (\text{A.17})$$

where θ is the Heaviside step function (C_2 and C_3 are restricted to non-negative values by definition). The standard deviations σ_{C_2} and σ_{C_3} are set by then demanding

$$\int_{C_2 \leq \epsilon} P(C_2) dC_2 = \int_{C_2 > \epsilon} P(C_2) dC_2, \quad (\text{A.18})$$

$$\int_{C_3 \leq \delta} P(C_3) dC_3 = \int_{C_3 > \delta} P(C_3) dC_3. \quad (\text{A.19})$$

The case of C_1 is different, since we only have one inequality to fulfil ($\Gamma > 5/6$). Hence, we need to put a cut-off at some value to determine the standard deviation. One could of course assign, for example, flat priors in the same fashion.

Using this method, we can thus obtain a posterior distribution $P(C_1, C_2, C_3)$ for a given prior distribution $\Pi(C_1, C_2, C_3)$ of our choice, thus allowing a removal of correlation biases intrinsic to particular parameterizations, which should reduce model uncertainty. This

method allows us to perform parameter estimation on C_1, C_2, C_3 as well as model selection by calculating the Bayesian evidence. It is of course applicable to general dynamical cosmological properties one might wish to study. Carrying this out in practice can however be involved since we might not be sampling efficiently in the MCMC, and performing model selection in a robust manner would require specialized code to address the sampling inefficiency and to handle the use of a binned distribution.

Appendix B

Forecast Constraints from Galaxy Clusters in the XCS

B.1 Cluster Number Count Equations

B.1.1 Ideal Measurements

The expected number of clusters with temperatures between T_1 and T_2 at redshifts between z_1 and z_2 when measurements are assumed to be exact is given by

$$N_{\text{ideal}}(T_1, T_2, z_1, z_2) = \int_{z_1}^{z_2} \int_{T_1}^{T_2} n_{\text{ideal}}(T, z) dT dz, \quad (\text{B.1})$$

where n_{ideal} is the actual number density of clusters in temperature and redshift (see Eq. (6.9) on p. 126), given by the convolution of the mass function $n(M_t, z)$ with cluster scaling relations, their scatter (through $p(L_t, M_t)$), cosmic volume dV/dz and the survey selection function f_{sky} (including sky coverage):

$$n_{\text{ideal}}(T, z) = \int_{M_t} \int_{L_t} n(M_t, z) f_{\text{sky}}(L_t, T, z) p(L_t, M_t | L(T, z), M(T, z)) \times \frac{dV}{dz} dL_t dM_t. \quad (\text{B.2})$$

The scaling-relation scatter probability distributions are assumed to be statistically independent,

$$p(L_t, M_t | L(T, z), M(T, z)) = p(L_t | L(T, z)) \times p(M_t | M(T, z)), \quad (\text{B.3})$$

each having a log-normal form:

$$\begin{aligned}
p(M_t|M(T, z), T, z) dM_t &= p(T_t^M(M_t)|T, z) \frac{dM_t}{dT_t^M} dT_t^M = \\
&= \frac{1}{\text{erf}(m_T/\sqrt{2})\sqrt{2\pi}\sigma_{\log T}} \exp\left[-\frac{1}{2} \frac{(\log_{10} T - \log_{10} T_t^M)^2}{\sigma_{\log T}^2}\right] \\
&\quad \times \Theta(m_T\sigma_{\log T} - |\log_{10} T - \log_{10} T_t^M|) \frac{dM_t}{dT_t^M} d\log_{10} T_t^M, \quad (\text{B.4}) \\
p(L_t|L(T, z)) dL_t &= \frac{1}{\text{erf}(m_L/\sqrt{2})\sqrt{2\pi}\sigma_{\log L_X}} \exp\left[-\frac{1}{2} \frac{(\log_{10} L(T, z) - \log_{10} L_t)^2}{\sigma_{\log L_X}^2}\right] \\
&\quad \times \Theta(m_L\sigma_{\log L_X} - |\log_{10} L(T, z) - \log_{10} L_t|) d\log_{10} L_t. \quad (\text{B.5})
\end{aligned}$$

The parameters m_T , m_L , $\sigma_{\log T}$ and $\sigma_{\log L}$ are described further in Sects. 6.3.2 and 6.3.3 as well as Table 6.4 (p. 130).

B.1.2 Measurement Errors

When treating the case of measurement errors in T and z , we must distinguish observed and true temperature. The expected number of clusters between *observed* temperatures T_1 and T_2 , and redshifts z_1 and z_2 , is given by

$$N_{\text{obs}}(T_1, T_2, z_1, z_2) = \int_{z_1}^{z_2} \int_{T_1}^{T_2} \bar{n}(T, z) dT dz, \quad (\text{B.6})$$

where \bar{n} represents the cluster distribution marginalized over the probability distribution for measurements, i.e.

$$\begin{aligned}
\bar{n}(T, z) &= \int_{z_t} \int_{T_t} n_{\text{ideal}}(T_t, z_t) p(T, z|T_t, z_t) dT_t dz_t \\
&= \int_{z_t} \int_{T_t} n_{\text{ideal}}(T_t, z_t) p\left(T \left[\frac{1+z_t}{1+z}\right] \middle| T_t, z_t\right) p(z|z_t) \left(\frac{1+z_t}{1+z}\right) dT_t dz_t, \quad (\text{B.7})
\end{aligned}$$

where z_t and T_t are true redshift and temperature, and in the last step the relation $T_{\text{obs}} = (1+z_{\text{obs}})T_t/(1+z_t)$ was used to go from observed to true temperature. The temperature measurement probability distribution is modelled by

$$p(T|T_t, z_t) dT = \frac{1}{\sqrt{\pi/2}(\sigma_T^- + \sigma_T^+)} \exp\left[-\frac{1}{2} \frac{(T - T_{\text{med}}(T_t, z_t))^2}{\sigma_T(T_t, z_t)^2}\right] dT \quad (\text{B.8})$$

with

$$\begin{aligned}
T_{\text{med}}(T_t, z_t)/T_t &= \alpha_c + \alpha_T T_t + \alpha_z z_t + \alpha_{zz} z_t^2 + \alpha_{TT} T_t^2 + \alpha_{zT} z_t T_t \\
\sigma_T(T_t, z_t) &= \begin{cases} \sigma_T^+ = T_t (\beta_c^+ + \beta_T^+ T_t + \beta_z^+ z_t + \beta_{zz}^+ z_t^2 + \beta_{TT}^+ T_t^2 + \beta_{zT}^+ z_t T_t), & T_t \geq T_{\text{med}}(T_t, z_t); \\ \sigma_T^- = T_t (\beta_c^- + \beta_T^- T_t + \beta_z^- z_t + \beta_{zz}^- z_t^2 + \beta_{TT}^- T_t^2 + \beta_{zT}^- z_t T_t), & \text{otherwise.} \end{cases}
\end{aligned}$$

where the α and β are determined from simulations (see Sect. 6.3.5)

Realistic T errors	Worst-case T errors
Eq. (B.8)	Eq. (B.8) with std. dev. $3 \times \sigma_T$

Table B.1: Temperature error specifications.

The redshift measurement probability distribution is modelled by

$$\begin{aligned}
p(z|z_t) dz &= \frac{1}{N_z^{\text{rand}}(z_t)(1 - f_{\text{cat}}) + N_z^{\text{cata}}(z_t)f_{\text{cat}}} \left\{ (1 - f_{\text{cat}}) \exp \left[-\frac{1}{2} \frac{(z - z_t)^2}{\sigma_0^2(1 + z_t)^2} \right] + \right. \\
&\quad \left. f_{\text{cat}} \exp \left[-\frac{1}{2} \frac{(z - z_t)^2}{c^2 \sigma_0^2(1 + z_t)^2} \right] \Theta(|z - z_t| - nc\sigma_0(1 + z_t)) \Theta(z) \right\} dz \\
N_z^{\text{rand}}(z_t) &= \sqrt{\frac{\pi}{2}} \sigma_0(1 + z_t) \left[1 + \text{erf} \left(\frac{z_t}{\sqrt{2}\sigma_0(1 + z_t)} \right) \right] \\
N_z^{\text{cata}}(z_t) &= \sqrt{2\pi} c \sigma_0(1 + z_t) \times \\
&\quad \left(\text{erfc} \left(\frac{n}{\sqrt{2}} \right) - \frac{1}{2} \min \left[\text{erfc} \left(\frac{z_t}{\sqrt{2}c\sigma_0(1 + z_t)} \right), \text{erfc} \left(\frac{n}{\sqrt{2}} \right) \right] \right) \quad (\text{B.9})
\end{aligned}$$

The temperature error assumptions made in this work are described further in Sect. 6.3.5 and summarized in Table B.1. The redshift error assumptions for parameters f_{cat} , n , c and σ_0 are described further in Sect. 6.3.4 and Table B.2. Note that the probability distributions of *true* temperatures and redshifts, the Bayesian "inverses" of the above, are weighted by the cluster distribution and given by

$$p(T_t|T, z_t) dT_t = \frac{p(T|T_t, z_t) n_{\text{ideal}}(T_t, z_t) dT_t}{\int p(T|T', z_t) n_{\text{ideal}}(T', z_t) dT'} \quad (\text{B.10})$$

$$p(z_t|T_t, z) dz_t = \frac{p(z|z_t) n_{\text{ideal}}(T_t, z_t) dz_t}{\int p(z|z') n_{\text{ideal}}(T_t, z') dz'} \quad (\text{B.11})$$

B.2 Expected Likelihood

In order to evaluate the expected constraints from a survey, one needs to consider some ensemble of possible outcomes and from that calculate, by ensemble averaging or otherwise (given a specification of 'expected'), the expected constraints. We have chosen a type of smoothed Maximum Likelihood (ML) estimate, that captures the most likely shape and size of constraint contours but removes the offset associated with a traditional ML point estimate. In the following we show in detail that our expected constraints can be obtained accurately without averaging over many data realizations, but rather by using only an 'average catalogue'.

Parameter	Description	Realistic z errors	Worst-case z errors
σ_0	Standard deviation at $z = 0$	0.05	0.10
c	Catastrophic standard deviation in units of σ_0	4	4
n	Min. deviation from mean in units of $c\sigma_0$ for catastrophic redshifts	1	1
f_{cat}	Fraction of catastrophic redshifts	0.05	0.10

Table B.2: Redshift error specifications.

Having an expression for the single-catalogue likelihood, we seek to estimate the expected constraints for the survey. We define this as the expected constraints for a set consisting of a certain fraction ε most likely catalogues. We start by setting up some formalism and prove our central theorem, and then go on to use this for our application.

Definition 1. Let $\{C_j\}$ denote a set of catalogues indexed by j . Let N be the number of bins of a catalogue. Let N_i or N_i^j be the observed number count for bin i , in catalogue j where superscript present. Let λ_i be the Poisson mean for bin i at which the likelihood is evaluated, and λ_i^* the same for the fiducial model used to generate the catalogues. Let $\delta_i^j \equiv N_i^j - \lambda_i^*$ measure the deviation of the observed number count from the fiducial-model mean.

Definition 2. Let the expected likelihood for the fraction ε most likely catalogues in a Poisson ensemble be given by

$$\langle \mathcal{L} \rangle_\varepsilon \equiv \prod_i e^{-\lambda_i} \left\langle \prod_i \left[\frac{\lambda_i^{N_i}}{N_i!} \right] \right\rangle_\varepsilon, \quad (\text{B.12})$$

where the product runs over the N bins in a catalogue, and $\langle \cdot \rangle_\varepsilon$ denotes a Poisson ensemble average restricted to catalogues C_j such that $\sum_j P(C_j) \Theta(P(C_j) - P_\varepsilon) = \varepsilon$ (with Θ the Heaviside step function). This expression also defines the probability threshold P_ε .

Corollary 1. It follows from the above definition and the Poisson distribution that

$$\begin{aligned} \langle \mathcal{L} \rangle_\varepsilon &= \prod_i e^{-\lambda_i} \sum_j \frac{P(C_j)}{\varepsilon} \prod_i \left[\frac{\lambda_i^{N_i^j}}{N_i^{j!}} \right] \Theta(P(C_j) - P_\varepsilon) = \\ &e^{-\sum_i (\lambda_i + \lambda_i^*)} \frac{1}{\varepsilon} \sum_j \prod_i \frac{(\lambda_i \lambda_i^*)^{\lambda_i^* + \delta_i^j}}{[(\lambda_i^* + \delta_i^j)!]^2} \Theta(P(C_j) - P_\varepsilon). \end{aligned} \quad (\text{B.13})$$

Definition 3. Let

$$\mathcal{C}_\pm \equiv \left\{ \{\delta_i\}_{i=1}^N \mid \delta_i \in \{[\lambda_i^*] - \lambda_i^*, [\lambda_i^*] - \lambda_i^*\} \forall i \right\}, \quad (\text{B.14})$$

the set of catalogues consisting of the 2^N catalogues between the most likely catalogue (for which $\delta_i = [\lambda_i^*] - \lambda_i^* \forall i$) to the catalogue with probability P_ε (for which $\delta_i = \lceil \lambda_i^* \rceil - \lambda_i^* \forall i$). Here, $\lceil \cdot \rceil$ and $\lfloor \cdot \rfloor$ are the ceiling and floor operators respectively.

Remark 1. The choice of this set of catalogues will be convenient and is suitable to define a smoothed ML estimate.

We now come to the central theorem:

Theorem 1. For the catalogue set \mathcal{C}_\pm ,

$$\langle \mathcal{L} \rangle_\varepsilon = \sum_i \left(\lceil \lambda_i^* \rceil - \frac{1}{2} \right) \ln \lambda_i - \lambda_i + \mathcal{O}(\delta^3) + \text{const.} \quad (\text{B.15})$$

Proof. The probability level ε for the catalogue set \mathcal{C}_\pm can be estimated through

$$\prod_i \frac{(\lambda_i^*)^{\lceil \lambda_i^* \rceil}}{\lceil \lambda_i^* \rceil!} \leq \frac{\varepsilon}{2^N e^{-\sum_i \lambda_i^*}} \leq \prod_i \frac{(\lambda_i^*)^{\lfloor \lambda_i^* \rfloor}}{\lfloor \lambda_i^* \rfloor!}. \quad (\text{B.16})$$

We approximate

$$\varepsilon \approx 2^N e^{-\sum_i \lambda_i^*} \prod_i \frac{(\lambda_i^*)^{\lambda_i^*}}{\Gamma(1 + \lambda_i^*)}, \quad (\text{B.17})$$

where we have used the gamma function as a continuation of the factorial, effectively extending the Poisson distribution to the gamma distribution for non-integer values of N_i , something we will use throughout. We can now write

$$\langle \mathcal{L} \rangle_\varepsilon = 2^{-N} e^{-\sum_i \lambda_i} \sum_j \prod_i \frac{(\lambda_i)^{\lambda_i^* + \delta_i^j} (\lambda_i^*)^{\delta_i^j}}{[(\lambda_i^* + \delta_i^j)!]^2} \Gamma(1 + \lambda_i^*), \quad (\text{B.18})$$

where the catalogues (indexed by j) are now restricted to those in \mathcal{C}_\pm . To proceed, we first take the logarithm of the likelihood to separate out the catalogue-set-dependent normalization, which is of no consequence for our discussion. We can thus write

$$\ln \langle \mathcal{L} \rangle_\varepsilon = -N \ln 2 + \sum_i [-\lambda_i + \lambda_i^* \ln \lambda_i + \ln \Gamma(1 + \lambda_i^*)] + \ln \widehat{\Sigma}, \quad (\text{B.19})$$

where we have defined

$$\widehat{\Sigma} \equiv \sum_j \prod_i \frac{(\lambda_i \lambda_i^*)^{\delta_i^j}}{[(\lambda_i^* + \delta_i^j)!]^2}. \quad (\text{B.20})$$

Taylor expanding in δ_i^j (since $|\delta_i^j| < 1$ for our catalogues) we find

$$\begin{aligned} \ln \langle \mathcal{L} \rangle_\varepsilon &= -N \ln 2 + \sum_i [\lambda_i^* \ln \lambda_i - \lambda_i + \ln \Gamma(1 + \lambda_i^*)] + \ln \widehat{\Sigma} \Big|_{\delta=0} + \\ &\sum_{i,j} \left(\frac{1}{\widehat{\Sigma}} \frac{d\widehat{\Sigma}}{d\delta_i^j} \right) \Big|_{\delta=0} \delta_i^j + \\ &\frac{1}{2} \sum_{i,j,k,l} \left[\frac{1}{\widehat{\Sigma}} \left(\frac{d^2 \widehat{\Sigma}}{d\delta_i^j d\delta_k^l} - \frac{1}{\widehat{\Sigma}} \frac{d\widehat{\Sigma}}{d\delta_i^j} \frac{d\widehat{\Sigma}}{d\delta_k^l} \right) \right] \Big|_{\delta=0} \delta_i^j \delta_k^l + \mathcal{O}(\delta^3), \end{aligned} \quad (\text{B.21})$$

where ‘ $\delta = 0$ ’ denotes $\delta_i^j = 0 \forall i, j$. Inserting $\widehat{\Sigma}$ and the derivatives

$$\frac{d\widehat{\Sigma}}{d\delta_i^j} = \ell(\lambda_i, \lambda_i^*) \prod_k \frac{(\lambda_k \lambda_k^*)^{\delta_k^j}}{[(\lambda_k^* + \delta_k^j)!]^2}, \quad (\text{B.22})$$

$$\frac{d^2 \widehat{\Sigma}}{d\delta_i^j d\delta_k^l} = \ell(\lambda_i, \lambda_i^*) \ell(\lambda_k, \lambda_k^*) \prod_m \frac{(\lambda_m \lambda_m^*)^{\delta_m^j}}{[(\lambda_m^* + \delta_m^j)!]^2} \tilde{\delta}_{jl}, \quad (\text{B.23})$$

where $\ell(\lambda, \lambda^*) \equiv \ln(\lambda\lambda^*) - 2\Psi(1 + \lambda^*)$ (the digamma function Ψ coming from the factorial as gamma function), we obtain

$$\begin{aligned} \ln \langle \mathcal{L} \rangle_\varepsilon &= \sum_i (\lambda_i^* \ln \lambda_i - \lambda_i) + \sum_i \ell(\lambda_i, \lambda_i^*) 2^{-N} \sum_j \delta_i^j + \\ &\quad \frac{1}{2} \sum_{i,j,k,l} 2^{-N} \left[\ell(\lambda_i, \lambda_i^*) \ell(\lambda_k, \lambda_k^*) \tilde{\delta}_{jl} - 2^{-N} \ell(\lambda_i, \lambda_i^*) \ell(\lambda_k, \lambda_k^*) \right] \delta_i^j \delta_k^l + \\ &\quad \mathcal{O}(\delta^3) \end{aligned} \tag{B.24}$$

$$\begin{aligned} &= \sum_i (\lambda_i^* \ln \lambda_i - \lambda_i) + \sum_i \ell(\lambda_i, \lambda_i^*) 2^{-N} \sum_j \delta_i^j + \\ &\quad \frac{1}{2} \sum_{i,k} \ell(\lambda_i, \lambda_i^*) \ell(\lambda_k, \lambda_k^*) \left[2^{-N} \sum_j \delta_i^j \delta_k^j - 2^{-2N} \sum_{j,l} \delta_i^j \delta_k^l \right] + \\ &\quad \mathcal{O}(\delta^3), \end{aligned} \tag{B.25}$$

where $\tilde{\delta}_{ij}$ is the Kronecker delta. We can evaluate the δ -sums using our knowledge of the set of catalogues \mathcal{C}_\pm :

$$\sum_j \delta_i^j = 2^{N-1} ([\lambda_i^*] + [\lambda_i^*] - 2\lambda_i^*) = 2^N \left(\Delta_i^* - \frac{1}{2} \right), \tag{B.26}$$

$$\sum_{j,l} \delta_i^j \delta_k^l = 2^{2N} \left(\Delta_i^* - \frac{1}{2} \right) \left(\Delta_k^* - \frac{1}{2} \right) = 2^{2N} \left[\Delta_i^* \Delta_k^* - \frac{1}{2} (\Delta_i^* + \Delta_k^*) + \frac{1}{4} \right], \tag{B.27}$$

$$\begin{aligned} \sum_j \delta_i^j \delta_k^j &= \frac{2^N}{4} [\Delta_i^* \Delta_k^* + \Delta_i^* (\Delta_k^* - 1) + (\Delta_i^* - 1) \Delta_k^* + (\Delta_i^* - 1) (\Delta_k^* - 1)] = \\ &\quad 2^N \left[\Delta_i^* \Delta_k^* - \frac{1}{2} (\Delta_i^* + \Delta_k^*) + \frac{1}{4} \right], \end{aligned} \tag{B.28}$$

where we have defined $\Delta_i^* \equiv [\lambda_i^*] - \lambda_i^*$ and excluded the possibility that $[\lambda_k^*] = [\lambda_k^*] = \lambda_k^*$. Inserting (B.27) and (B.28) in (B.25) we find that the second-order term is zero due to cancellation between its two constituent terms. Hence, also inserting (B.26), we finally arrive at

$$\ln \langle \mathcal{L} \rangle_\varepsilon = \sum_i \left[\lambda_i^* \ln \lambda_i - \lambda_i + \ell(\lambda_i, \lambda_i^*) \left(\Delta_i^* - \frac{1}{2} \right) \right] + \mathcal{O}(\delta^3) \tag{B.29}$$

$$\begin{aligned} &= \sum_i \left[\left([\lambda_i^*] - \frac{1}{2} \right) \ln \lambda_i - \lambda_i + \left(\Delta_i^* - \frac{1}{2} \right) (\ln \lambda_i^* - 2\Psi(1 + \lambda_i^*)) \right] + \\ &\quad \mathcal{O}(\delta^3). \end{aligned} \tag{B.30}$$

□

The theorem states that a good approximation to $\langle \mathcal{L} \rangle_\varepsilon$ is given by using $N_i = [\lambda_i^*] - 1/2$ in a single-catalogue likelihood \mathcal{L} . This expression, however, does give rise to an offset in the best-fitting values away from the true means, associated with shot noise. As we are

using the catalogue construction as a way of defining a meaningful expected likelihood which is not just an arbitrary point estimate, we are not really interested in this offset (and would like to separate it from sources of bias); rather the variance is what concerns us. Therefore, we propose using the very similar expression

$$\langle \ln \mathcal{L} \rangle = \sum_i (\lambda_i^* \ln \lambda_i - \lambda_i) + \text{const.} \quad (\text{B.31})$$

The best-fitting values for λ_i of this expression are equal to the true means λ_i^* . However, how do the standard deviations compare? The standard deviations are given by

$$\sigma_{\varepsilon,i} = \sqrt{\lceil \lambda_i^* \rceil - 1/2}, \quad \sigma_{\text{mean},i} = \sqrt{\lambda_i^*}, \quad (\text{B.32})$$

where $\sigma_{\varepsilon,i}$ is the standard deviation of Eq. (B.30) and $\sigma_{\text{mean},i}$ the standard deviation of Eq. (B.31). Upper and lower limits for their ratio can then be given as

$$\frac{1}{\sqrt{1 + 1/2\lambda_i^*}} < \frac{\sigma_{\text{mean},i}}{\sigma_{\varepsilon,i}} < \frac{1}{\sqrt{1 - 1/2\lambda_i^*}}. \quad (\text{B.33})$$

It is clear that for $\lambda_i^* < 1$ the relative error will become large as λ_i^* decreases. Again, this is due to shot noise. One could always make bins large enough that at least a few elements fall in each bin, ensuring only moderate relative errors in the standard deviations. Such a binning might however not be optimal or even close to, and thus reflect the underlying distribution poorly. It appears that no general conclusion can be drawn here. However, if we specify a dependence $\lambda_i = \lambda_i^*(\theta/\theta^*)^{a_i}$ for the λ_i 's on some parameter θ , as is typically the case and certainly here, we can write the following:

$$\begin{aligned} \langle \ln \mathcal{L} \rangle &= \sum_i (\lambda_i^* \ln \lambda_i - \lambda_i) + \text{const.} = \ln \theta \sum_i a_i \lambda_i^* - \sum_i \lambda_i^* \left(\frac{\theta}{\theta^*} \right)^{a_i} + \\ &\text{const.} \end{aligned} \quad (\text{B.34})$$

$$\begin{aligned} \ln \langle \mathcal{L} \rangle_\varepsilon &= \sum_i \left[\left(\lceil \lambda_i^* \rceil - \frac{1}{2} \right) \ln \lambda_i - \lambda_i \right] + \text{const.} = \\ &\ln \theta \sum_i a_i \left(\lceil \lambda_i^* \rceil - \frac{1}{2} \right) - \sum_i \lambda_i^* \left(\frac{\theta}{\theta^*} \right)^{a_i} + \text{const.} \end{aligned} \quad (\text{B.35})$$

Clearly, the only difference between $\ln \langle \mathcal{L} \rangle_\varepsilon$ and $\langle \ln \mathcal{L} \rangle$ comes from the difference in the first sum. Naively, we would not expect this to differ much between the two cases, particularly for a binning that represents the distribution well. What would be the expected value? Consider the following quantity:

$$s_{\text{rel}} \equiv \frac{\sum_i a_i \lambda_i^*}{\sum_i a_i (\lceil \lambda_i^* \rceil - \frac{1}{2})} = \frac{\sum_i a_i \lambda_i^*}{\sum_i a_i (\lambda_i^* + (\lceil \lambda_i^* \rceil - \lambda_i^*) - \frac{1}{2})}. \quad (\text{B.36})$$

One would generally expect that $(\lceil \lambda^* \rceil - \lambda^*) \in U(0, 1)$ or at least a similarly symmetric distribution across the bins, so that $\langle \lceil \lambda^* \rceil - \lambda^* \rangle = 1/2$. We thus expect

$$\langle s_{\text{rel}} \rangle = \frac{\sum_i a_i \lambda_i^*}{\langle \sum_i a_i (\lceil \lambda_i^* \rceil - \frac{1}{2}) \rangle} = \frac{\sum_i a_i \lambda_i^*}{\sum_i a_i \lambda_i^*} = 1. \quad (\text{B.37})$$

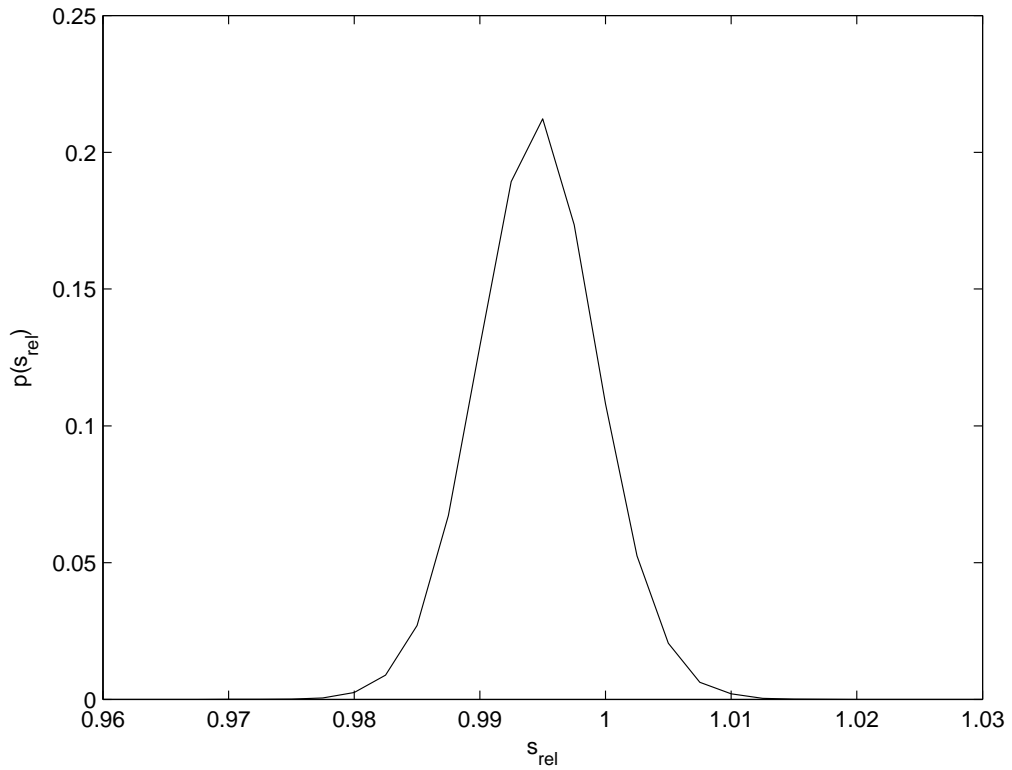


Figure B.1: The probability density function for s_{rel} for a typical XCS catalogue with $a_i \in U(-5, 5)$.

For typical XCS catalogues, even if we assign uncorrelated random exponents a_i , the probability distribution for s_{rel} is quite generally very sharply peaked at or close to $s_{\text{rel}} = 1$. An example is shown in Fig. B.1, for which $a_i \in U(-5, 5)$. Furthermore, finding typical a_i 's for the various XCS models, we find that $s_{\text{rel}} = 1 + \mathcal{O}(10^{-2})$.

In conclusion, the likelihood $\langle \ln \mathcal{L} \rangle$ of the average catalogue is a good approximation to the average likelihood $\ln \langle \mathcal{L} \rangle_\varepsilon$ of our set of catalogues \mathcal{C}_\pm , and can also generally be expected to be a good approximation in other similar applications. We have confirmed this by explicitly comparing to the likelihoods for a Poisson sample of catalogues, as shown in Fig. 6.6 (p. 128) in the main text.